Multi-Scale Measurements in Blood Rheology

by

Andy Vinh Le

Thesis submitted to the University of Ottawa and Université de Montpellier
in partial fulfillment of the requirements for the
Doctorate in Philosophy degree in Mechanical Engineering

Ottawa-Carleton Institute for Mechanical and Aerospace Engineering
Faculty of Engineering
University of Ottawa

Centre de Biologie Structurale
I2S - Information, Structures et Systèmes
Université de Montpellier

© Andy Vinh Le, Ottawa, Canada, 2025

Examining Committee

The following served on the Examining Committee for this thesis.

External Member(s):	Sylvie Lorthois CNRS Research Director, Porous and Biological Media group Institut de Mécanique des Fluides de Toulouse
	Anne Juel Professor, School of Physics & Astronomy University of Manchester
Carleton Member:	Edgar Matida Professor, OCIMAE Carleton University
UO Internal Member:	Catherine Mavriplis Professor, OCIMAE University of Ottawa
UM Internal Member(s):	Simon Mendez CNRS Research Associate HDR, ACSIOM research group Université de Montpellier
	Benoit Charlot CNRS Research Director HDR, M2N research group Université de Montpellier

Supervisor(s): Marianne Fenech
Professor, Department of Mechanical Engineering
University of Ottawa

Manouk Abkarian
CNRS Research Director HDR, Physics and Mechanics of Biological Systems
Université de Montpellier

Declaration of Authorship

I hereby certify that this thesis is entirely my own original work except where otherwise indicated. I am aware of the University of Ottawa regulations concerning plagiarism, including those regarding consequent disciplinary actions. Any use of the works of any other author, in any form, is properly acknowledged at their point of use.

Abstract

The English abstract follows.

Résumé: La rhéologie sanguine, régie par le comportement collectif des globules rouges (GR) déformables en suspension dans le plasma, est encore incomprise dans son ensemble. Ce travail explore les phénomènes d'écoulement sanguin à plusieurs échelles afin de mieux les comprendre. Il s'intéresse plus précisément à l'interaction entre les GR et la géométrie d'un réseau, ainsi qu'à l'interaction entre GR et le transport de masse des solutés dans la phase liquide. Nous explorons, finalement, une nouvelle technique pour caractériser les profils de vitesse dans les suspensions denses.

À l'échelle des vaisseaux capillaires, le transport du sang dans des réseaux uniformes est étudié. L'objectif de cette étude est d'examiner dans quelle mesure l'interaction entre les cellules et les nœuds individuels du réseau affecte l'efficacité globale de la perfusion. La perfusion de GR sains à différentes fractions volumiques à travers le réseau est effectuée dans diverses géométries et topologies. Cela permet de montrer comment l'excès de résistance relative du réseau évolue de manière non linéaire en fonction du débit mesuré. En définissant un nombre capillaire basé sur la vitesse locale des cellules et l'élasticité moyenne de cisaillement dans le plan de la membrane, une loi d'échelle pour l'excès de résistance relative en fonction de la fraction volumique locale de GR et de la topologie du réseau est proposée. Les premières observations suggèrent que ces propriétés de transport sont probablement corrélées au comportement local des GR et à la mécanique de leur membrane.

À l'échelle artériolaire, l'influence des GR sur le mélange des macromolécules en écoulement est examinée. Les GR, qu'ils soient agrégés ou non-agrégés, améliorent la diffusion effective pour des débits et des hématocrites croissants, avec un maximum près d'une fraction volumique de GR de 30%. Les molécules plus grosses bénéficient également davantage du mélange induit par les GR, ce qui démontre que ces derniers facilitent activement le transport de masse dans le fluide de suspendant sans dépendre d'une migration axiale prononcée.

Enfin, pour relever le défi de la mesure des champs de vitesse dans les suspensions denses de GR et pour développer une véritable hémophysique du sang, une technique de corrélation de fluorescence à deux foyers (2f FCS) est proposée. Validée avec des fluides transparents, newtonien et rhéofluidifiant, et appliquée à des suspensions physiologiquement denses de GR agrégées et non agrégées, cette techinique permet de capturer les profils de vitesse et de révéler la transition d'un écoulement parabolique à un écoulement en forme de bouchon dans diverses conditions. Bien que les mesures directes de l'hématocrite local

restent difficiles avec la cette technique, notre approche pose les bases d'une application en hémorhéologie.

Collectivement, ces résultats font progresser la compréhension de la rhéologie sanguine en reliant la déformation, la distribution et le mélange des GR à plusieurs échelles et en fournissant de nouvelles stratégies de mesure pour les suspensions denses et complexes.

Mots-clés : globule rouge, non-newtonien, microfluidique, réseau microfluidique, résistance hydrodynamique, transport de masse, mélange, corrélation de fluorescence à deux foyers, vélocimétrie.

Abstract: Blood rheology, governed by the collective behavior of deformable red blood cells (RBCs) suspended in plasma, remains incompletely understood. This work examines blood flow phenomena at multiple scales, focusing on the interplay between RBCs and network geometry, RBCs and solute mass transport, and innovative velocity-measurement techniques in dense suspensions.

At the scale of the capillary vessels, the transport of blood in uniform networks is explored. The aim of this study is to investigate how the interaction between cells with the individual nodes of the network affects the overall macroscopic transport. Measurements of healthy density-controlled RBCs through the network are completed in varying geometry and topology, showing how the excess relative resistance of the network scales non-linearly with the measured flow rate. Defining a capillary number through the local velocity of the cells and an average membrane in-plane shear elasticity, a scaling law for the excess relative resistance as a function of the local volume fraction of RBCs and the topology of the network is proposed. The first observations show that these transport properties are likely correlated to the local behavior of RBCs and their membrane mechanics.

At the arteriolar scale, the influence of RBCs on macromolecular mixing in flow is examined. Both aggregated and non-aggregated RBCs enhance effective diffusion for increasing flow rates and hematocrit with a maximum near a RBC volume fraction of 30%. Larger molecules also benefit more from RBC-induced mixing, demonstrating that RBCs actively facilitate mass transport in their suspending fluid without relying on pronounced axial migration.

Finally, to address the challenge of measuring velocity fields in dense RBC suspensions and to develop a real hemorheophysics of blood, a two-foci fluoresence correlation spectroscopy (2f FCS) technique is introduced. Validated with Newtonian and transparent shear-thinning fluids, and applied to physiologically dense suspensions of aggregated and non-aggregated RBC, 2f FCS captures velocity profiles and reveals the transition from parabolic to plug-like flow under varying conditions. Although direct local hematocrit measurements remain challenging, this approach identifies key measurement limitations and lays the groundwork for refined techniques in hemorheology.

Collectively, these findings advance the understanding of blood rheology by linking RBC deformation, distribution, and mixing at multiple scales and by providing new measurement strategies for dense, complex suspensions.

Keywords: red blood cell, non-Newtonian, microfluidics, microfluidic network, hydrodynamic resistance, mass transport, mixing, two-foci fluorescence fluctuation, velocimetry.

Acknowledgements

Completing this PhD thesis has been a long and challenging journey, and it would not have been possible without the guidance, support, and encouragement of many individuals.

First and foremost, I would like to express my deepest gratitude to my two advisors, Dr. Marianne Fenech and Dr. Manouk Abkarian, for their invaluable guidance, patience, and mentorship throughout this process. Their expertise and constructive feedback have been instrumental in shaping my research and helping me grow as a scientist.

I am also profoundly grateful to my committee members, Dr. Catherine Mavriplis, Dr. Edgar Matida, Dr. Simon Mendez, Dr. Benoit Charlot, Dr. Sylvie Lorthois, and Dr. Anne Jules, for their insightful suggestions and support, which enriched my work and broadened my perspectives.

Special thanks to my lab colleagues at the Centre de Biologie Structurale in Montpellier, Arianna, Anaïs, Lisa, Andreas, Marion, Team 8 PhysMechBio, and all the members of the halls at CBS60 for an incredible source of collaboration, inspiration, and camaraderie. The shared moments made the lab an enjoyable and stimulating environment at the CBS. I am also very grateful to all the people that I have met through the Fenech's Lab group; the conversations about various research and work have been enlightening. A special thanks to Maya and Tatianna for their help in Montpellier using the 2f FCS and the network project.

I would also like to acknowledge all the help from Dr. Viviana Clavería for providing her insight and collaboration on the mixing project, Dr. Muriel Giansily-Blaizot and the Département d'hématologie biologique at the CHU Montpellier for the acquisition of samples, Dr. Emmanuel Margeat for providing his expertise and guidance on FCS, Dr. Jean-Bernard Fiche for his guidance on the confocal microscope, Dr. Benoit Charlot and Audrey Sebban for the manufacturing of the microfluidic wafers and the wonderful time in the clean room at the IES, and all the previous master students that have made these projects possible.

I owe a special debt of gratitude to my family and friends for their unwavering support, love, and encouragement. To my partner, Kevin, thank you for your endless patience and understanding, especially during the challenging times.

Finally, I would like to thank all the funding agencies for supporting this research and the administrative and technical staff at the University of Ottawa and Université de Montpellier for their assistance throughout my doctoral journey.

This thesis is a reflection of the collective support, knowledge, and inspiration I have received from all of you. I am deeply grateful and forever indebted.

Table of Contents

List of Tables **xiv**

List of Figures **xvi**

Abbreviations **xxi**

List of Symbols **xxii**

Introduction **1**

Research Question and Objectives 1

Thesis Structure Overview 4

1 Scientific Background **5**

1.1 What is blood? 5

1.1.1 Red Blood Cells 6

1.1.2 Plasma 7

1.2 Blood Rheology 7

1.2.1 Viscosity of Fluids: Principles and Practical Measurements 8

1.2.2 Blood Viscosity in Classical Rheology 11

1.2.3 Blood Rheology at the Vessel Scale 13

1.2.4 Aggregation of Red Blood Cells 16

1.3 Insights into Blood Rheology from Capillaries to Bulk Flow 19

2 General Methodology **20**
2.1 Microfluidic Device Fabrication . . . 20
2.1.1 PDMS Microfludic Device . . . 20
2.1.2 Glass Capillary Microfluidic Device . . . 22
2.1.3 Glass-PDMS Sandwich Microfluidic Device . . . 24
2.2 Sample Preparation . . . 25
2.2.1 Blood Separation . . . 25
2.2.2 Non-Aggregating Red Blood Cells . . . 25
2.2.3 Aggregating Red Blood Cells . . . 26

3 Blood Flow Through a Uniform Network **27**
3.1 Introduction . . . 27
3.2 Background . . . 28
3.2.1 Rheology in Simple Geometries . . . 29
3.2.2 Network Rheology . . . 31
3.2.3 Collective Behaviour Through Network Topologies . . . 35
3.2.4 Deformation and Morphological Effects . . . 36
3.3 Objective . . . 39
3.4 Material and Methods . . . 40
3.4.1 Microfluidic Device . . . 40
3.4.2 Sample Preparation . . . 43
3.4.3 Experimental Setup . . . 46
3.4.4 Analysis of Macroscopic Measurement . . . 47
3.4.5 Analysis of High-Speed Video Microscopy . . . 51
3.5 Results . . . 56
3.5.1 Verification of Macroscopic Responses . . . 56
3.5.2 RBC Suspension . . . 64
3.5.3 Role of RBC Local Dynamics . . . 71

3.5.4 Deformability effects . . . 82
3.6 Discussion . . . 87
3.6.1 Macroscopic Response Considerations without Cells . . . 87
3.6.2 Healthy RBC Suspension . . . 88
3.6.3 Role of RBC Local Dynamics . . . 95
3.6.4 Deformability Effects . . . 99
3.7 Conclusions and Future Work . . . 100
3.8 Key Takeaways . . . 102

4 Mixing in Microcirculation **104**
4.1 Introduction . . . 104
4.2 Background . . . 105
4.2.1 Microcirculatory Blood Transport and Mixing . . . 106
4.2.2 Mass Transport Scaling for Single Phase Fluids . . . 107
4.3 Objective . . . 109
4.4 Methods . . . 109
4.4.1 Microfluidic Device . . . 109
4.4.2 Sample Preparation . . . 110
4.4.3 Experimental Setup . . . 111
4.4.4 Data Acquisition and Analysis . . . 111
4.5 Results . . . 115
4.5.1 Diffusion Length as a Function of Time . . . 115
4.5.2 Aggregation Effects . . . 117
4.5.3 Transport of Molecules of Increasing Molecular Weight . . . 118
4.5.4 Cell Axial Diffusivity . . . 122
4.5.5 Interface Location (3:1 vs 1:1) . . . 123
4.6 Discussion . . . 124
4.6.1 Diffusion Length Scale . . . 124

4.6.2 Aggregability . . . 125
4.6.3 Transport of Molecules of Increasing Molecular Weight . . . 125
4.6.4 Mechanisms . . . 126
4.7 Conclusions . . . 129
4.8 Key Takeaways . . . 131

5 Two-Foci Fluorescence Correlation Spectroscopy 132
5.1 Introduction . . . 133
5.2 Background . . . 133
5.2.1 Techniques in Blood Rheology to Measure Velocity . . . 135
5.2.2 Velocity Measurement from 2f FCS . . . 137
5.2.3 Velocity Measurements of Blood in Vitro . . . 138
5.2.4 Viscosity Models of Whole Blood in Bulk . . . 141
5.3 Objective . . . 142
5.4 Material and Methods . . . 142
5.4.1 Microfluidic Device . . . 143
5.4.2 Sample Preparation . . . 143
5.4.3 Experimental Setup . . . 145
5.4.4 Analysis Methods . . . 150
5.5 Results . . . 153
5.5.1 Velocity Profile Measurements . . . 153
5.5.2 Hematocrit Approximation . . . 158
5.5.3 Limitations and Considerations . . . 160
5.6 Discussion . . . 165
5.6.1 Velocity Profile Measurement . . . 165
5.6.2 Hematocrit Approximation . . . 167
5.6.3 Considerations and Limitations . . . 168
5.7 Conclusions and Future Work . . . 171
5.8 Key Takeaways . . . 172

6 General Conclusions and Perspectives **174**

References **178**

APPENDICES **191**

A Blood Flow Through a Uniform Network **192**

A.1 Approximating Channel Resistance 192

A.2 Porosity, Permeability and Tortuosity 195

A.3 Network Clogging 202

A.4 Velocity Field Matrix 204

A.5 Cell Trajectories 211

A.6 Cell Cluster Distribution 216

A.7 Morphological Variations 219

A.8 Hematocrit Measurement Errors 224

A.9 Experimental Matrix 226

B Mixing in Microcirculation **227**

B.1 Alternative Experimental Setup 227

B.2 Fitting Models to Characterize Flow 229

B.3 Diffusion Length Function of Time 231

B.4 Relative Effective Diffusion Coefficient Function of Position 231

B.5 Experiment Matrix 234

C Two-Foci Fluorescence Correlation Spectroscopy **236**

C.1 High Speed Camera Imaging of Linear Actuation 239

C.2 Tracer Selection 242

C.3 Symmetry Across Channel Height 244

D Mini Review **246**

List of Tables

3.1 Mechanical properties of RBC membranes 37
3.2 Uniform Network Design Summary 43
3.3 Hexagonal Network Geometric Properties 43
3.4 Summary of $\Delta P - Q$ polynomial fits 58
3.5 Summary of $\Delta P - Q$ polynomial fits for Channel 4 subsets 61
3.6 Summary of relative excess relative resistance magnitude fitting parameter 68
3.7 Summary of power-law exponent fitting parameter 69

5.1 Summary of fitting power-law index 155
5.2 Summary of relative measurement error 164

A.1 Summary of network tortuosity 201
A.2 Summary of network permeability 201
A.3 Summary of glutaraldehyde treatment map 202
A.4 Experimental Matrix: healthy RBC trials 226
A.5 Experimental Matrix: diamide and treated RBC trials 226
A.6 Experimental Matrix: glutaraldehyde treated RBC trials 226

B.1 Experimental Matrix: aggregation and cell-mask 234
B.2 Experimental Matrix: molecular weight 234
B.3 Experimental Matrix: measurement positions 235
B.4 Experimental Matrix: flow rate 235

C.1 Summary of constant velocity calibration 239

List of Figures

1 Snapshot of project questions 3

1.1 Electron microscope imaging of a red blood cell. 6
1.2 Example velocity profile between parallel plates 8
1.3 Example schematic of rotational rheometers and measurement curve 10
1.4 Representation of Poiseuille's equation 10
1.5 Bulk blood relative viscosity curve 12
1.6 Example Cell Free Layer 14
1.7 Fåhræus Effect 15
1.8 Fåhræus-Lindqvist Effect 17
1.9 Example of aggregated RBC in plasma. (Obtained in-house, University of Ottawa) 18

2.1 Example SU8 master wafer for PDMS fabrication 21
2.2 Schematic: glass capillary microfluidic device 23
2.3 Schematic: glass-PDMS microfluidic device 24

3.1 Examples of vasculature of tissues in different organs. 28
3.2 Example $\Delta P - Q$, $\dot{\gamma}$ and η in straight tubes 30
3.3 RBC shape change and theoretical pressure loss 31
3.4 Variation of intrinsic viscosity, K_t, with cell velocity u_o 32
3.5 RBC morphology and normalized flow resistance function of normalize velocity 33

3.6 In vivo example of pressure-flow dynamics through microcirculatory network 34
3.7 In vitro example of pressure-flow dynamics through microcirculatory network 35
3.8 RBC distribution in square network 36
3.9 Schematic of RBC membrane-cytoskeleton interaction and coupling 37
3.10 Example of RBC distribution map in straight channel 38
3.11 Schematic: Hexagonal Network 41
3.12 Relative rigidity of treated RBC 45
3.13 Schematic: network experimental setup 46
3.14 Schematic: network flow configuration 48
3.15 Analysis: example settling flow rate 50
3.16 Analysis: background and channel detection pipeline 52
3.17 Analysis: cell detection pipeline 54
3.18 Analysis: example of cell morphologies 55
3.19 Results: example Newtonian $\Delta P - Q$ curve 57
3.20 Results: summary of $\Delta P - Q$ of each network 59
3.21 Results: summary of $\Delta P - Q$ of Channel 4 subsets 60
3.22 Results: example healthy RBC sequence and $\Delta P - Q$ 62
3.23 Results: example macroscopic imaging of RBC passage 63
3.24 Result: example $\Delta P - Q$ and $R_{exc} - Ca$ for healthy RBC 65
3.25 Result: summary of $R_{exc} - Ca$ for healthy RBC in log-log 67
3.26 Result: summary of $R_{exc} - Ca$ fitting parameter for healthy RBC 68
3.27 Result: summary of $R_{exc} - Ca$ for healthy RBC in log-log in high Ca regime 69
3.28 Result: summary of $R_{exc} - Ca$ fitting parameter for healthy RBCs in high Ca regime 70
3.29 Results: example normalize cell velocity distribution 72
3.30 Results: example normalize cell area distribution 74
3.31 Results: relative proportion of cell cluster size as function of Ca 75
3.32 Results: relative proportion of cell cluster size as function of ϕ 76

3.33 Results: example RBC morphologies 77
3.34 Results: $EI - Ca$ for low hematocrit 78
3.35 Results: example RBC morphologies in Channel 3 79
3.36 Results: relative distribution of cell morphologies in Channel 3 and 4 . . . 81
3.37 Results: $R_{exc} - V$ for glutaraldehyde treated RBC 83
3.38 Results: $R_{exc} - Ca$ for glutaraldehyde treated RBC 84
3.39 Results: power-law fitting parameter for glutaraldehyde treated RBC . . . 85
3.40 Results: $R_{exc} - V$ for diamide treated RBC 86
3.41 Results: example diamide treated RBC 86
3.42 Results: parameter of power-law fits organized by porosity 91
3.43 Literature: $R_{exc} - Ca$ from Quéguiner and Barthes-Biesel 93
3.44 Literature: $R_{exc} - V$ from Secomb et al. 94
3.45 Literature: $R_{exc} - V$ from Lingard 95

4.1 Example laminar microfluidic device and biomimic microcirculation 106
4.2 Schematic of co-flow microfluidic in mixing processes 108
4.3 Schematic: co-flow microfluidic device 110
4.4 Schematic: mixing in microcirculation syringe experimental setup 112
4.5 Analysis: measurement pipeline 113
4.6 Results: total spread as function of advection time 116
4.7 Results: total spread as function of advection time fitting parameter 117
4.8 Results: normalized effective diffusion as function of hematocrit 119
4.9 Results: normalized effective diffusion as function of flow rate 120
4.10 Results: normalized effective diffusion as function of Stokes Radius 121
4.11 Results: cell mask effective diffusion as function of hematocrit 122
4.12 Results: normalized effective diffusion by interface position 123
4.13 Literature: trajectories indicate minimal axial dispersion 126
4.14 Literature: granular suspension exhibit turbulence-like structures 127

4.15 Literature: RBC time sequence indicate rotation 128

5.1 Schematic: components to develop a constitutive law of blood 134
5.2 Schematic: configuration of the confocal volume 136
5.3 Schematic: sample correlation function for simplified model 138
5.4 Compilation of velocity measurements of blood in vitro 140
5.5 Schematic: example microfluidic devices 143
5.6 Viscosity curves of PEO 144
5.7 Schematic: experimental setup 146
5.8 Schematic: experimental setup optical path 148
5.9 Schematic: sample data acquisition trace 149
5.10 Schematic: flow generation configuration 151
5.11 Analysis: cross-correlation peak time extraction 152
5.12 Results: velocity profile through different solutions 154
5.13 Results: velocity profile of non-aggregating RBC - Poiseuille flow 156
5.14 Results: velocity profile of non-aggregating RBC - Constant velocity 157
5.15 Results: fluorescent fluctuation intensity 159
5.16 Results: cross-correlation amplitude 160
5.17 Results: depth penetration measurements 162
5.18 Results: wall effects and multi lag time 163
5.19 Schematic: confocal volume entering microfluidic device 168
5.20 Schematic: confocal volume calibration 170

A.1 Schematic: hexagonal network partitioned into subsections 193
A.2 Schematic: CAD of hexagonal network mask 196
A.3 Schematic: hexagonal network porosity approximation 197
A.4 Schematic: tortuosity interpretation 199
A.5 Schematic: tortuosity ordering 199

A.6 Example network clogging . . . 203
A.7 Results: normalized cell velocity Channel 3, $\phi = 13\%$ . . . 205
A.8 Results: normalized cell velocity Channel 3, $\phi = 28\%$ . . . 206
A.9 Results: normalized cell velocity Channel 4, $\phi = 12\%$ . . . 207
A.10 Results: normalized cell velocity Channel 4, $\phi = 24\%$ . . . 208
A.11 Results: normalized cell velocity Channel 6, $\phi = 13\%$ . . . 209
A.12 Results: normalized cell velocity Channel 6, $\phi = 26\%$ . . . 210
A.13 Results: sample trajectories, $\phi = 10\%$ . . . 212
A.14 Results: sample trajectories, $\phi = 40\%$ . . . 213
A.15 Results: measured tortuosity and track angle, $\phi = 10\%$ . . . 214
A.16 Results: measured tortuosity and track angle, $\phi = 40\%$ . . . 215
A.17 Results: measured absolute value of projected cell area . . . 216
A.18 Results: example normalize cell area distribution, Channel 4 . . . 217
A.19 Results: example normalize cell area distribution, Channel 6 . . . 218
A.20 Results: example $EI - V$ heat map at $\phi = 10\%$ . . . 220
A.21 Results: example $EI - V$ heat map at $\phi = 20\%$ . . . 221
A.22 Results: example morphology in Channel 3, straight 0° . . . 222
A.23 Results: example morphology in Channel 3, bifurcation . . . 223
A.24 Results: hematocrit approximation . . . 225

B.1 Schematic: mixing in microcirculation pressure experimental setup . . . 228
B.2 Results: total spread as function of time (all) . . . 232
B.3 Results: normalized effective diffusion as function of position (all) . . . 233

C.1 Schematic: error using Hele-Shaw approximation . . . 238
C.2 Analysis: approximating constant velocity configuration . . . 240
C.3 Schematic: calibration of constant velocity configuration . . . 241
C.4 Results: example tracers . . . 242
C.5 Results: symmetry measurements . . . 245

Abbreviations

μPIV micro-particle image velocimetry

2f FCS two-foci fluoresence correlation spectroscopy

AFM atomic force microscope

APD avalanche photodiode

CFL cell free layer or cell depleted layer

CR confinement ratio

EI elongation index

FCS fluoresence correlation spectroscopy

KOH potassium hydroxide

PBS phosphate buffered saline

PDMS polydimethylsiloxane

PEO polyethylene oxide

PLL-PEG poly(L-lysine)-poly(ethylene glycol) methyl ether

RBC red blood cell

WBC white blood cell

List of Symbols

α Power-law exponent parameter 66, 90, 101

δ Diffusion length 114, 115, 124, 231

η Dynamic viscosity 8, 13, 42, 49, 64, 192, 194, 195

η_{45} Dynamic viscosity at 45% hematocrit 16

η_{app} Apparent viscosity 9, 31

η_{rel} Relative viscosity 16

$\dot{\gamma}$ Shear rate 8, 125, 133

κ_B Bending modulus 36

ϕ Hematocrit 53, 66, 89, 115, 133

ϱ Porosity 42, 43, 66, 195, 198

τ Characteristic time scale 47

τ Shear Stress 8, 133

τ_D Characteristic diffusion time 137

τ_F Characteristic advection flow time 137

A Second ordercomponent of hydraulic resistance from polynomial fit 49

A_c Cross-sectional Area 195, 200

B Linear component of hydraulic resistance from polynomial fit 49, 87

$\mathbb{C}$ Fluorescent concentration 114, 229, 230

$\mathbb{C}_1$ Initial low fluorescent concentration 114

$\mathbb{C}_2$ Initial high fluorescent concentration 114

Ca Capillary number 64, 66, 68, 73, 78, 79, 89, 96, 219

D Diffusion coefficient 114, 115, 125, 137, 229, 230

d Diameter 13, 15, 16

f Excess resistance magnitude 66, 83, 89, 90, 92, 93, 96, 101

G_s Membrane surface shear modulus 36, 64, 82, 83

h Height 42, 114, 141, 152, 194, 230, 237

k Permeability 42, 43, 195, 198

K_t Intrinsic viscosity 31, 89

l Length 13, 42, 49, 192, 194, 195, 197, 224, 229

N Average molecule number 137

ΔP Pressure drop 13, 47, 49, 192, 195

Q Flow rate 13, 47, 49, 152, 192, 195, 237

$\vec{R}$ Distance between foci 137, 145

r Radius 49, 192, 224

R Hydraulic Resistance 47, 49, 192

R_{equ} Equivalent Hydraulic Resistance 192

R_{exc} Excess Relative Hydraulic Resistance 47, 50, 64, 66, 68, 89, 96

R_{rel} Relative Hydarulic Resistance 49

t Mean advection time 115, 124

T Tortuosity 42, 43, 66, 197, 200

V Velocity 114, 115, 195, 229, 230, 237

V_p Velocity in axis of plane 137

w Width 42, 114, 152, 194, 198, 230, 237

Introduction

Research Question and Objectives

The field of hemorheology is not solely concerned with the biological function of blood within the circulatory system. It has implications for a number of biomedical applications where precise control of blood flow is essential, including dialysis, blood transfusion, and the development of next-generation diagnostic tools [1].

Understanding blood rheology, however, is still in its infancy. Blood is classified in the family of suspensions that are particularly complex to study; it is a dense suspension of highly deformable red blood cells (RBCs), suspended in a macromolecule-rich aqueous phase known as plasma, which induces reversible aggregation between cells at low shear stresses [2, 3]. Research in hemorheology performed in the last 50 years has either been descriptive when focusing on microcirculation, such as revealing local RBC concentration to be heterogeneous in flow [4], or classical, such as showing how blood apparent viscosity decreases with increasing shearing of the flow [5].

Despite these pioneering discoveries, the absence of new approaches to deciphering the role of blood structure in its bulk flow and in microcirculatory conditions represents a significant obstacle to the advancement of the study of blood rheology. In this work, I aim to address blood rheological questions by combining bulk rheological measurements of blood flow with the characterization of local microstructure phenomena occurring when blood flows through both simple and complex geometries. I propose to discuss blood flow at three distinct levels, addressing three key questions during my doctoral studies outlined as follows:

- Firstly, at the capillary scale of the microcirculation, where nutrient and gas exchanges occur, **we ask how do the cells interact with individual nodes and channels of a microfluidic network and how does this contribute to the overall transport**

through the network? To investigate this network rheology, RBCs are flowed through different uniform hexagonal networks with varying channel lengths, while maintaining the same overall hydrodynamic resistance (Figure 1A). The preliminary results indicate that an increase in the applied peripheral pressure results in a reduction in the relative apparent viscosity, which is dependent on both the volume fraction of RBCs and the topology of the hexagonal network. This study aims to elucidate the influence of the local hydrodynamic interaction of RBCs in a uniform network on the global measurement of blood flow through such a network.

- Secondly, at the arteriolar level, the mixing process in blood is not fully understood, despite its primary function being the transport of nutrients and gases in a well-mixed state to and from the capillary fields. **We ask how does the presence of RBCs affect mixing at the scale of the microcirculation?** This study aims to discuss the importance of blood being a concentrated suspension of RBCs in the mixing process that occurs in the body every day. Using rectangular-cross-sectional polydimethylsiloxane (PDMS) microchannels (Figure 1B), we investigate the mixing of fluorescent macromolecules of varying molecular weight in a suspension of RBCs with different volume fractions and at various flow rates around the physiological value.

- Lastly, in bulk, where blood suspensions are typically measured using classical rheometric methods such as plate-cone rheometers, linear velocity profiles are assumed when measuring the viscosity of the fluid of interest (Figure 1C). **We ask if it is still true for the case of suspensions such as blood due to the heterogeneous distribution of RBCs in flow.** To connect the macroscopic measurements of viscosity with the microstructure we explore the use of two-foci fluoresence correlation spectroscopy (2f FCS) to obtain the velocity field and uncover the true velocity profile and its distribution that occurs in the bulk suspension when sheared in a rheometer.

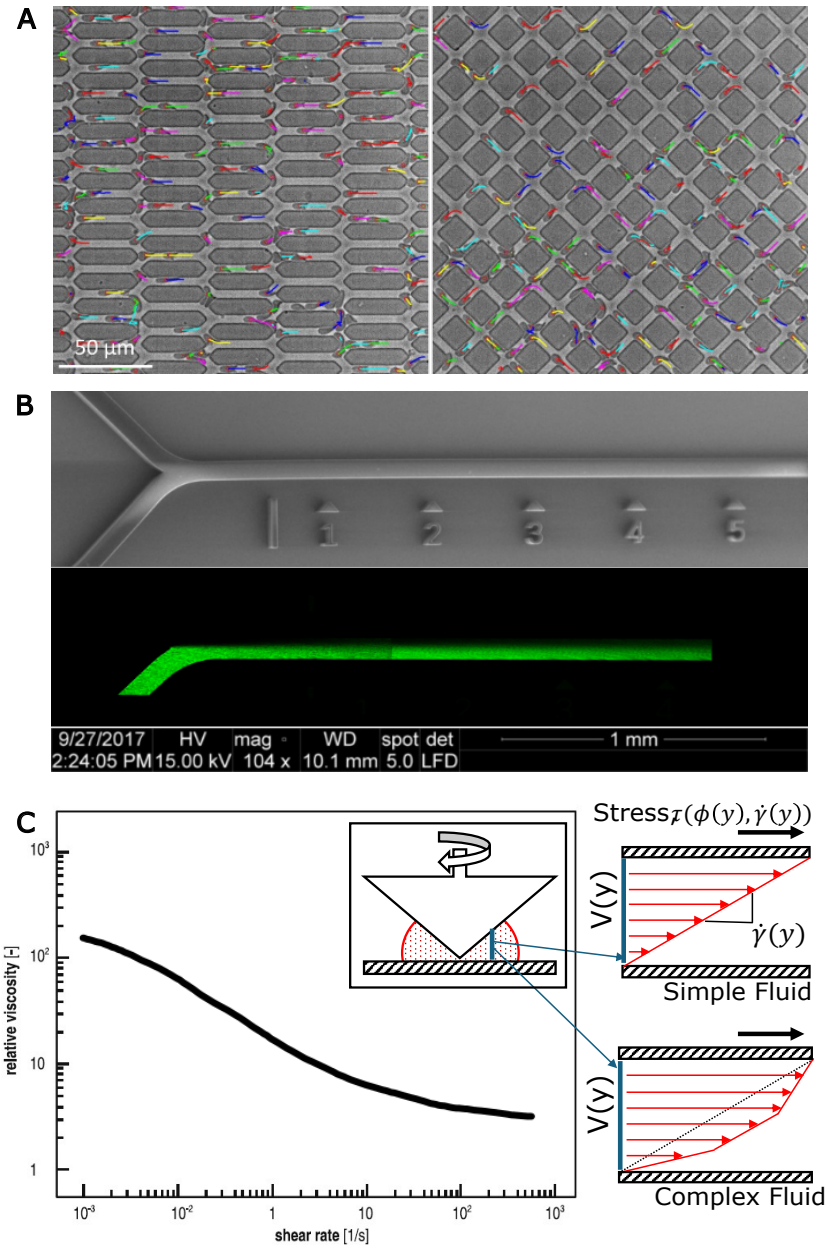


Figure 1: (A) Uniform networks with varying channel lengths with superimposed RBC trajectories. (B) Co-flow channel with confocal fluorescent imaging showing diffusion of Alexa 488 through bulk suspension. (C) Bulk rheological measurement of relative viscosity as function of shear rate using a rotational rheometer assuming a linear deformation. Schematic represents an exaggerated plate-cone rheometer with a fluid solution indicated as a dotted pattern.

Thesis Structure Overview

The thesis document is organized as follows:

Chapter 1, "Scientific Background," introduces general key concepts necessary for understanding this thesis.

Chapter 2, "General Methodology," introduces the shared methodologies used in microfluidic fabrication of PDMS channels and RBC preparation.

The main body of the thesis is then divided into three chapters, each focusing on different aspects of blood flow. Each chapter follows a consistent structure: a chapter abstract, introduction, background information, objectives, methods, results, and discussion.

Chapter 3, "Blood Flow Through a Uniform Network," examines the macroscopic rheological dynamics of blood flow through a uniform hexagonal network and explores how local cell dynamics influence overall flow behavior.

Chapter 4, "Mixing in Microcirculation," investigates the enhancement of mass transport of solutes in the suspending phase, emphasizing the effects of both non-aggregating and aggregating RBCs.

Chapter 5, "Two-Foci Fluorescence Correlation Spectroscopy," explores the novel application of 2f FCS to measure local velocity and volume fraction, aiming to develop a constitutive law for blood flow.

Each chapter is designed to provide a comprehensive and structured understanding of the respective topics. The thesis then concludes with:

Chapter 6, which highlights key findings and contributions of this work and perspectives for future investigations.

The manuscript also includes supplementary material in the Appendices such as an auxiliary analysis, results, supporting images, and the experimental matrix summary for the study on "Blood Flow Through a Uniform Network" (Appendix A), "Mixing in Microcirculation" (Appendix B), and "Two-Foci Fluorescence Correlation Spectroscopy" (Appendix C).

Chapter 1

Scientific Background

This chapter provides the general scientific background and bibliography necessary to comprehend the work presented in the remainder of the manuscript. For enhanced readability, this section offers only a general introduction to blood rheology; more detailed literature reviews will be presented in the respective chapters, each focusing on the different studies discussed in this thesis.

1.1 What is blood?

Blood is a vital type of connective tissue that serves a number of functions, including the transport of dissolved gases of respiration, protection against invading microorganisms, coagulation from injuries, and regulation of various bodily processes. Given the significance of blood in the human body, it is crucial to develop an understanding of blood flow phenomena, particularly in the context of designing biomedical applications such as microfluidic devices and gaining insights into micro-vascular disorders like sickle cell disease. However, due to the complex composition and behavior of blood, there is still much to be discovered regarding its flow properties [6].

Whole blood is a heterogeneous fluid comprising formed elements suspended in a liquid intercellular matrix. The formed elements are composed of red blood cells (RBCs), white blood cells (WBCs), and platelets. Meanwhile, the suspending liquid, more commonly designated as plasma, contains a multitude of dissolved substances, including proteins, electrolytes, minerals, and fats. RBCs, which constitute approximately 40-45% of the total volume of whole blood, most commonly referred to as the hematocrit, contain hemoglobin,

a protein that facilitates the transportation of 99% of oxygen from the lungs to the rest of the body and carbon dioxide from the body to the lungs [7]. WBCs, comprising monocytes, lymphocytes, neutrophils, eosinophils, and basophils, play a pivotal role in defending the body against foreign invaders and infectious diseases. Platelets, which are fragments of cytoplasm derived from megakaryocytes in the bone marrow, are responsible for initiating the coagulation cascade that results in the formation of blood clots at sites of injured blood vessels. Lastly, plasma serves as a transport medium for blood cells, nutrients, waste products, hormones, proteins, and carbon dioxide throughout the body [7].

1.1.1 Red Blood Cells

RBCs are specialized cells whose primary function is the transport of oxygen. During the formation of the RBC, the nucleus is shed from the erythroblast prior to its entry into the bloodstream. A typical healthy human RBC exhibits biconcave disk morphology with a diameter of approximately 8 µm and a thickness that ranges from 1 µm to 2 µm, with the thinnest region situated at the center of the thickest region at the periphery. An example RBC is depicted in Figure 1.1. This biconcave shape provides a high surface area to volume ratio for maximizing oxygen exchange with the surrounding tissue. Furthermore, the deformable nature of the RBC membrane enables it to traverse narrow vessels [8]. The RBC membrane can be described as a thin, highly deformable viscoelastic shell comprising an outer lipid bilayer and a mesh-like network of proteins forming the cytoskeleton and lining the inner surface of the bilayer.

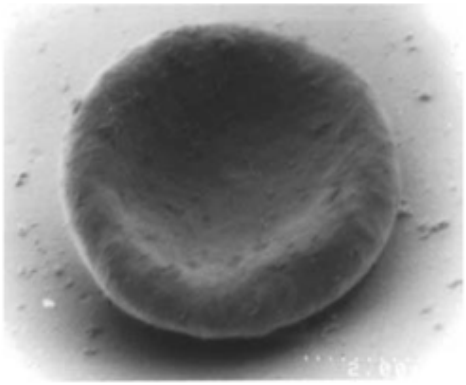


Figure 1.1: Electron microscope imaging of a red blood cell. (Reproduced from [7])

The bilayer is made of phospholipids which are amphiphilic molecules. Their dual interaction with water organizes them into a bilayer structure, with its hydrophilic heads and

hydrophobic tails, creating a stable barrier that resists area changes which would expose the hydrophobic tails to the aqueous environment, ensuring the membrane's integrity and functionality. Consequently, the cell membrane behaves like an incompressible fluid material in two dimensions [6]. The fluidity of the lipid bilayer allows the cytoskeleton to move relative to the bilayer when a portion of the membrane is stretched [6, 9]. The RBC cytoskeleton, primarily composed of spectrin, actin, and associated proteins, provides mechanical stability and elasticity essential for RBC deformability. Together the RBC membrane has a composite structure where the lipid bilayer provides a bending resistance while the underlying spectrin network, which is anchored to the proteolipid membrane, provides a shear elasticity that allows the cell to survive in microcirculation for more than 120 days. The thickness of the RBC membrane is less than 10 nm [6, 10].

1.1.2 Plasma

The plasma is a dilute electrolyte solution of proteins suspending the formed elements of blood. Approximately 8% of plasma by weight is composed of fibrinogen, globulin, and albumin proteins. Fibrinogen is the principal protein involved in the formation of blood clots, whereby it undergoes polymerization to form insoluble fibrin during coagulation. Globulin serves as a carrier of lipids and other water-soluble substances and contains antibodies that resist infection from bacteria and viruses. Albumin is a type of protein that plays a pivotal role in maintaining water balance within the body. It is the primary contributor to the overall osmotic pressure of plasma proteins. The presence of protein in plasma results in elevated osmotic pressure, facilitating the absorption of water from interstitial fluids into capillaries. Apart from the presence of plasma proteins, plasma has a composition identical to that of interstitial fluid [7].

1.2 Blood Rheology

Hemorheology is the scientific discipline concerned with the flow or deformation of blood and its formed elements, and its relationship with stresses. The rheological properties of blood depend upon a multitude of factors, including the shear stress, shear rate, the dimensions, and the geometry of the vessel through which the blood flows [11]. An understanding of the rheological properties of blood, including its non-Newtonian characteristics, has been gained through rheological studies using classical rotational viscometers where the fluid is unconfined and small glass capillaries where the fluid is confined [5, 11, 12]. However, the extrapolation of information from simple geometries to the prediction of rheological

properties and microstructures in complex situations in the microcirculation, where there are significant variations in vessel length, diameter, flow rate, and RBC volume fraction, represents an ongoing area of research.

1.2.1 Viscosity of Fluids: Principles and Practical Measurements

The term "viscosity" is used to describe the intrinsic property of a fluid that determines its response to deformation when subjected to shear stress. In order to gain an intuitive understanding of this property, it is useful to consider the following example: two flat, parallel plates with a finite distance between them and a fluid occupying the space between them. Upon the application of an external force to the upper plate, it will move with a constant velocity in a tangential manner to the other plate, thereby generating shear stress within the fluid. This results in the continuous deformation of the fluid. The velocity gradient between the plates, referred to as the strain rate or shear rate (Figure 1.2), is determined by the ratio of the incremental velocity change and the perpendicular distance change between the plates [7, 13]. It is common practice to emphasize the viscosity, which is a material property, as measurements from different rheometers should yield the same value under the same conditions.

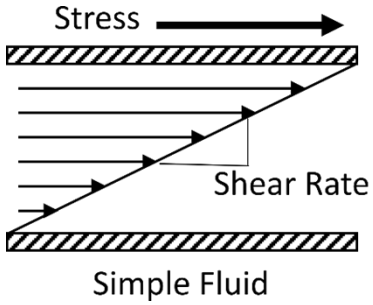


Figure 1.2: Example velocity profile between parallel plates (indicated by cross-hatch) where the top plate is displaced at a constant rate.

The dynamic viscosity (η) is then the proportionality factor between the shear stress (τ) and shear rate ($\dot{\gamma}$):

$$\tau = \eta \frac{\partial u}{\partial y} = \eta \dot{\gamma}. \tag{1.1}$$

η is constant for simple fluids which are described as Newtonian. In the case of non-Newtonian fluids, the ratio of shear stress and shear rate for any given measurement can

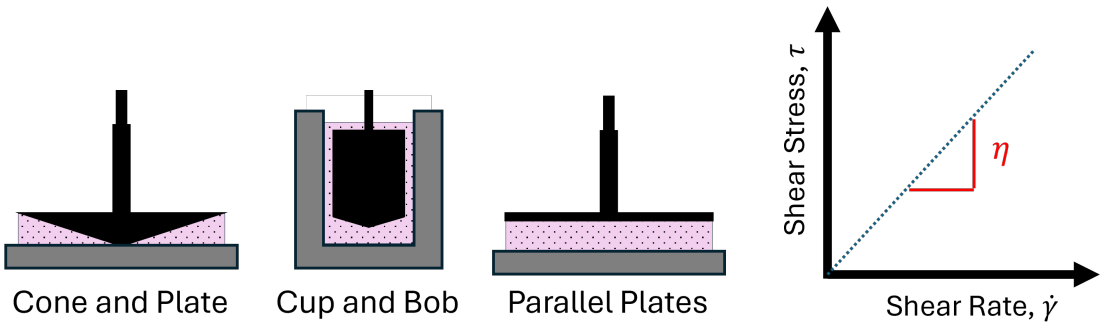
be used to define an apparent viscosity (η_{app}) which is a coefficient that depends on the shear rate. The apparent viscosity may then be described as:

$$\eta_{app} = \frac{\tau(\dot{\gamma})}{\dot{\gamma}}. \tag{1.2}$$

There are several classes of non-Newtonian fluids, including, for instance, shear-thickening fluids, shear-thinning fluids, thixotropic fluids, rheopectic fluids, and Bingham plastics [7, 13].

A number of techniques are available for measuring the rheological properties of fluids. The following section will highlight two principal categories of shear rheometers: rotational rheometers and capillary-based flow rheometers. Rotational rheometers comprise a "cup" containing the sample and a measuring "bob", which is placed in or on the fluid sample. The three most common geometries of cup and bob are the Couette (or coaxial cylinder), cone-plate, and parallel plates (Figure 1.3(a)). A rotational rheometer can be operated in two distinct ways: by rotating the measuring bob while the cup remains stationary (the Searle method) or by rotating the cup while the measuring bob is stationary (the Couette method) [14]. In either method, while the rotational speed of the bob or cup is predetermined, the torque required to rotate the bob or cup against the fluid's viscous forces exerted by the fluid is measured. Moreover, the precise definition of the geometries of the bob and its cup allows for the computation of the shear stress on the measurement bob [14]. To then extrapolate the viscosity of the fluid, it is common to assume that the shear rate in the rheometer is constant and the fluid inside is homogeneous in order to derive the viscosity of the sample of fluid (Figure 1.3(b)) .

In the case of pipe- or capillary-based rheometers, the fluid sample is forced through a tube with a constant cross-sectional area and well-known dimensions under laminar flow conditions. A capillary rheometer with an embedded pressure sensor can be utilized to determine the pressure drop across a known distance for a controlled flow rate, whereby Poiseuille's equation can be applied to extract the viscosity of the fluid sample (see Figure 1.4) [15]. An alternative methodology is through the utilization of optical viscometer techniques. In this method, two fluids are co-flowed together into a microfluidic Y-shaped chip, comprising the sample of interest and a reference fluid. The position of the interface between the two fluids is then observed by detecting a contrast difference or surface tension difference. The volume occupied by each fluid is contingent upon the sample viscosity, flow rates, and dimensions of the chip. By carefully controlling and measuring these parameters, the position of the interface provides valuable information. Specifically, the relationship between the flow rates, the known viscosity of the reference fluid, and the observed position of the interface can be used to calculate the viscosity of the sample fluid. [16].



(a) Rotational rheometers (b) Sample measurement curve

Figure 1.3: (a) Common geometries of rotational rheometers and (b) sample measurement curve expected to be extracted from a cone-plate rotational rheometer for a Newtonian fluid.

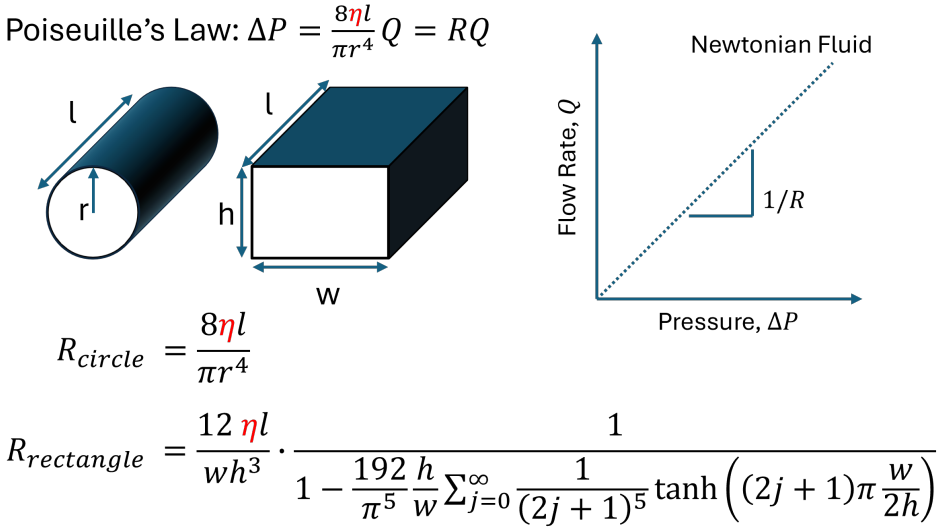


Figure 1.4: Poiseuille's law describes the relation between flow rate and pressure for an incompressible and Newtonian fluid in laminar flow through a long round channel with constant cross section. The hydraulic resistance, R, encompassing the viscosity and geometric terms can be extrapolated for different cross-sectional geometries.

1.2.2 Blood Viscosity in Classical Rheology

In whole blood, classical rheological methods such as rotational viscometers have revealed the non-Newtonian shear-thinning characteristic of blood [5]. The classical depiction of whole blood's shear-thinning behavior of the relative viscosity of blood as a function of shear rate, as demonstrated by Chien from results using a coaxial rheometer, is illustrated in Figure 1.5 . The relative viscosity is defined as the apparent viscosity normalized by the viscosity of the suspending fluid of the bulk blood.

The non-Newtonian behavior of blood in bulk is largely due to three aspects of RBC behavior: their ability to aggregate and form 3D structures at low shear rates, their deformability, and complex flow dynamics. When whole blood is tested under low shear rate conditions, the relative viscosity exhibits a marked increase. This phenomenon can be attributed to the tendency of RBCs to form reversible aggregates at low shear rates (illustrated in the following section), which are disaggregated with increasing shear rates. Without aggregation, the increase in relative viscosity in the lowest measured shear rate regime has been found to be an order of magnitude lower as demonstrated by Chien using albumin-Ringer with whole blood to inhibit cell aggregation as illustrated in Figure 1.5 [5]. Further reduction in the relative viscosity at high shear rate is associated with the deformability of the RBCs and its complex dynamics of cell transition, including tumbling, rolling, orientation, and the formation of highly deformed polylobed shapes [7, 13, 17]. In the work of Chien, hardened cells resulted in elevated relative viscosity that was constant with the shear rate [5]. Over the past century, numerous constitutive relationships have been proposed in the field of blood rheology. These studies have concentrated on two principal independent variables, namely the hematocrit and the shear rate, which are known to exert an influence on viscosity. In the initial investigations into blood viscosity, the emphasis was on the hematocrit dependence of the suspension, with the equations being primarily limited to high shear rates within the regime where blood viscosity remains unchanging with shear rate. These models were empirical and semi-empirical extensions to Einstein's equation for the viscosity of dilute suspensions of rigid particles or Taylor's equation for deformable liquid droplets [19]. Models that focused on shear rate dependence at a given hematocrit followed classical rheological models for non-Newtonian fluids, such as the power law [20] or the Casson equation [21]. An empirical constitutive model was proposed by Zydney, Oliver, and Colton [19] that accounted for shear rate, hematocrit, and suspending phase viscosity. However, despite the extensive work completed on the viscosity of red cell suspensions, the constitutive laws proposed tend to be limited to specific ranges of shear rates, hematocrit, geometries, and steady flow.

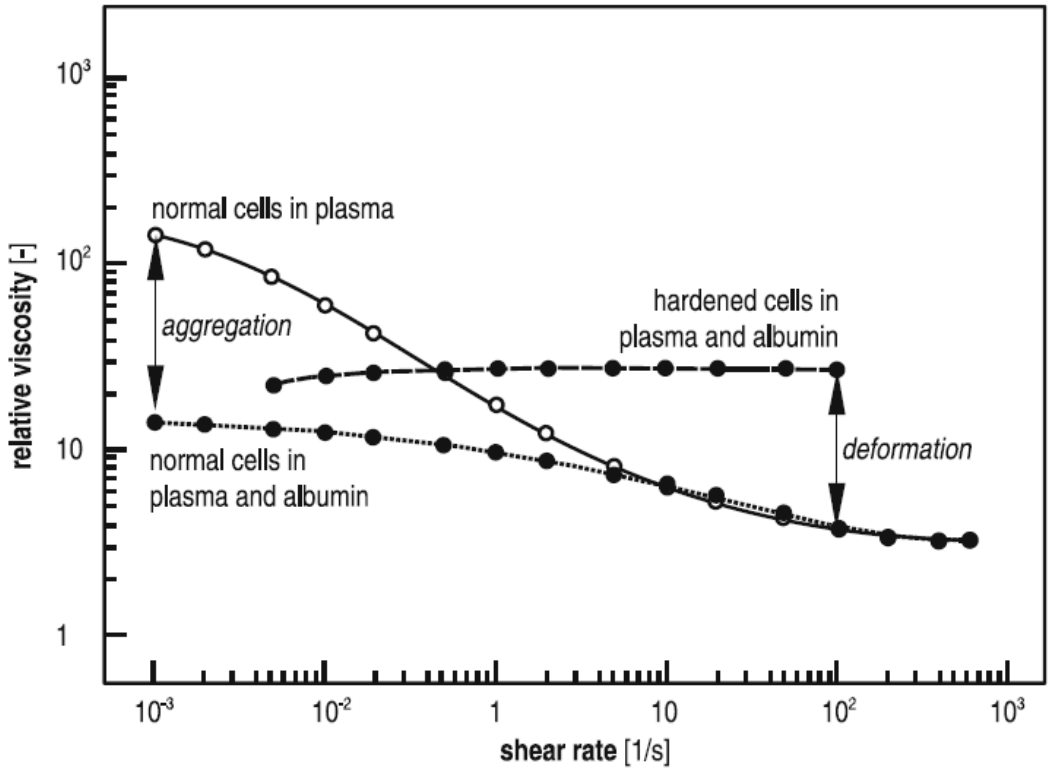


Figure 1.5: Relative viscosity relationship to shear rate for three types of human blood suspensions at 45% hematocrit. The albumin-Ringer solution at 11% did not result in aggregation. Each point represents the mean of four to six experiments (Reproduced from [5, 18])

1.2.3 Blood Rheology at the Vessel Scale

When looking at blood flow through vessels, we can consider our focus on the regime of flow encountered in physiological conditions at the capillary level. With diameters typically ranging from about 5 µm to 100 µm in the limit of large shear rates with time average spatial mean velocity between 0.5 mm/sec to 1 mm/sec [22–24]. In this regime, the Reynolds[1] number is in the range of 0.0015, and the Womersley[2] number is in the range of 0.003-0.007, indicating that the blood flow through the vessel is steady and governed by the pressure gradient and viscous shear stress and not by inertial forces [23]. Furthermore, in this regime of vessel size, the size of the RBCs is not negligible compared to the size of the vessels. The concept of apparent viscosity of blood in a given vessel (which differs from the apparent viscosity of the bulk blood as outlined in Equation (1.2)) is considered the viscosity of an equivalent Newtonian fluid flowing through the same tube with the same flow rate when the same pressure difference is applied at both ends. For a round tube, the viscosity of a Newtonian fluid can be described by Poiseuille's law which is given by [6]:

$$\eta = \frac{\pi d^4 \Delta P}{128 l Q} \tag{1.3}$$

where η is the viscosity, d is the tube diameter, l is the tube length, ΔP is the pressure difference across the tube and Q is the average flow rate through the tube. The apparent viscosity measured in vessels is not an intrinsic property of the fluid but a property of the blood and blood vessel interaction [24].

Cell Free Layer

When blood flows through microvessels, an intriguing phenomenon occurs whereby RBCs tend to migrate away from the vessel walls and towards the center. This migration results in the formation of two distinct phases within the vessel: a core of RBCs in the center and a cell free layer or cell depleted layer (CFL) near the wall. An example CFL is illustrated in Figure 1.6. The formation of the CFL has the effect of reducing the resistance to flow in comparison to what would be expected based solely on the viscosity of blood [6, 25].

[1] Reynolds number relates the inertial forces to viscous forces in a fluid flow. Commonly expressed as $Re = \rho V l/\eta$, where ρ is the density, V is the characteristic velocity, l is the characteristic length, and η is the dynamic viscosity.

[2] Womersley number is the dimensionless number that relates the unsteady inertial forces to viscous forces in a fluid flow. Commonly expressed as $\alpha = l\sqrt{\omega\rho/\eta}$, where l is the characteristic length, ω is the angular frequency of pulsatile flow, ρ is the fluid density, and η is the dynamic viscosity.



Figure 1.6: Flowing a RBC suspension in a round microchannel with an inner diameter of 50 µm, a cell-free layer is observed close to the channel wall and a dense core of RBCs in the center of the channel. (Adapted from video provided by Manouk Abkarian, Montpellier)

The radial distribution of RBCs and the formation of the CFL are influenced by a number of underlying phenomena. Due to the finite size of the RBC, there is a limit on the proximity of the cell's center to the boundary of the wall, resulting in a size exclusion effect [6]. Additionally, when placed close to a boundary wall, deformable particles and RBCs migrate away from the solid boundaries in a linear shear flow [26, 27]. A distinct mechanism from the migration of deformable particles from a boundary in linear shear, another mechanism for migration arises from the curvature of the velocity profile where the velocity gradient increases from the center of the channel to the wall. The migration effect due to a curved velocity has been demonstrated numerically in an unbounded Poiseuille flow in the work of Kaoui and colleagues, which reported the migration of vesicles towards the centerline [28]. Lastly, in vivo, an additional effect that promotes a CFL is the presence of a glycocalyx matrix and endothelial surface layer that results in a biological exclusion zone for flowing RBCs. In concentrated suspensions, however, frequent cell-to-cell interactions cause RBCs to migrate away from regions of high concentration at the core, leading to shear-induced diffusion or dispersion [29]. Consequently, CFL width reflects the balance between center-ward migration (cell–wall interactions) and wall-ward migration (cell–cell interactions), shaping RBC distribution and blood flow behavior.

Fåhræus Effect

One consequence of the CFL results in what is known as the Fåhræus effect. The Fåhræus effect is defined as a decrease of the volume fraction of RBCs (tube hematocrit) observed in blood flowing in a narrow tube relative to the volume fraction of RBCs (discharge hematocrit) that is discharged from the tube. This phenomenon can be attributed to the concentration of RBCs in the channel, which enables the cells to travel at a faster rate than the surrounding plasma in the CFL. Consequently, the cells reach the end of the channel in a shorter time [6]. Based on experimental data, a parametric model of the Fåhræus effect

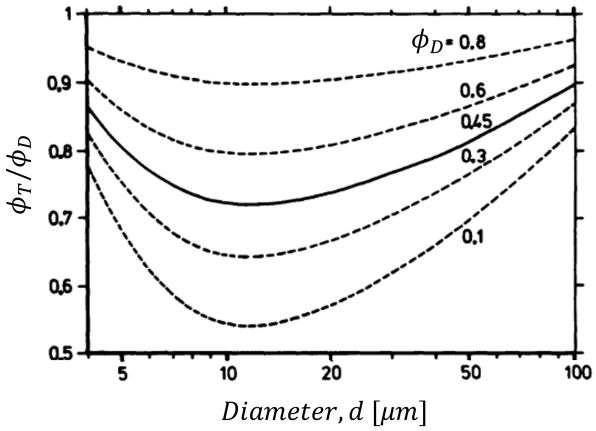


Figure 1.7: Parametric model description of the Fåhræus effect, showing the ratio of tube hematocrit (ϕ_T) to discharge hematocrit (ϕ_D) as a function of tube diameter (d) with representation at different discharge hematocrit. (Adapted from [31])

is described as follows [30]:

$$\frac{\phi_T}{\phi_D} = \varphi_D + (1 - \phi_D)(1 + 1.7e^{-0.415d} - 0.6e^{-0.011d}) \tag{1.4}$$

where ϕ_T is the tube hematocrit, ϕ_D is the discharge hematocrit, and d is the diameter of the tube. The parametric model of the Fåhræus effect is illustrated in Figure 1.7.

Fåhræus-Lindqvist Effect

The outcome of the CFL is a notable reduction in flow resistance. In the glass capillary viscometer experiment conducted by Fåhræus and Lindqvist [12], it was determined that the viscosity of blood in cylindrical channels with a diameter of less than 300 µm could not be accurately determined using Poiseuille's law due to the considerable influence of the CFL. The Fåhræus-Lindqvist effect describes the manner in which the relative apparent viscosity is altered in response to changes in the diameter of the tube in question. The relative apparent viscosity is observed to decrease with decreasing tube diameter, reaching a minimum at approximately 10 µm due to the increased relative effect of the CFL on reducing the average relative viscosity. A minimum in the relative apparent viscosity is observed between 6 µm to 10 µm where the relative thickness of the CFL is at its maximum and the inversion of the Fåhræus-Lindqvist effect occurs below 6 µm where it can

be understood as the single-file motion of RBCs being maximally deformed to the channel dimensions [24, 32].

A number of analytical models have been developed with the objective of defining the apparent viscosity of blood in straight channels. These models describe the relationship between blood flow and pressure drop, and they capture the Fåhræus-Lindqvist effect [33, 34]. However, these models provide predictions for limited diameters or hematocrit ranges, which limits their applicability to the study of blood flow in networks. In contrast, experimental results in glass tubes have facilitated the development of empirical relationships that describe the dependence of the relative apparent viscosity (η_{rel}) on the tube diameter and hematocrit [31].

$$\eta_{rel} = 1 + (\eta_{45} - 1)\frac{(1-\phi_D)^C - 1}{(1-0.45)^C - 1} \tag{1.5}$$

where η_{45} is the relative apparent *in vitro* viscosity for a discharge of 45% hematocrit, ϕ_D is the discharge hematocrit and the parameter C is the curvature of the relationship between relative apparent viscosity and hematocrit for a given tube diameter. The relative apparent viscosity at 45% is given by:

$$\eta_{45} = 220e^{-1.3d} + 3.2 - 2.44e^{-0.06d^{0.645}} \tag{1.6}$$

while parameter C is given by:

$$C = (0.8 + e^{-0.075d})(-1 + \frac{1}{1 + 10^{-11}d^{12}}) \tag{1.7}$$

where d is the diameter of the channel in micrometers. The empirical relationship proposed by Pries and colleagues captures the relationship between viscosity and hematocrit below 6 µm where the relationship is expected to be linear with sufficiently small hematocrit, while for larger tubes, the viscosity increases faster with hematocrit [31]. The Fåhræus-Lindqvist effect is represented in Figure 1.8.

1.2.4 Aggregation of Red Blood Cells

The phenomenon of RBC aggregation occurs in human blood under low shear conditions and in the presence of specific macromolecules, where RBCs aggregate into linear arrays (as illustrated in Figure 1.9), or even three-dimensional aggregate structures [11]. RBC aggregation should not be mistaken for blood clotting or coagulation, which is the trapping

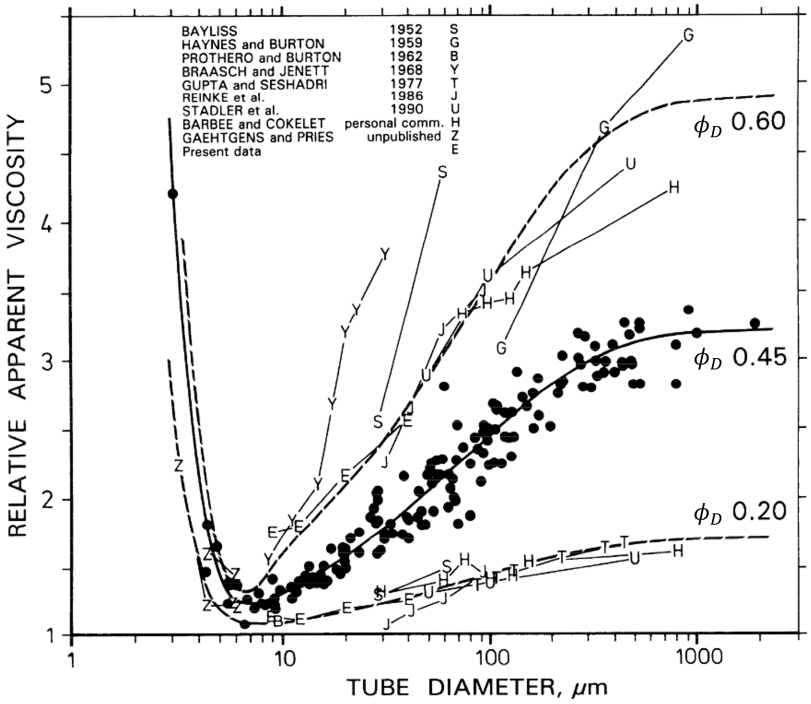


Figure 1.8: Relative apparent viscosity (η_{rel}) as a function of tube diameter for blood flowing at different discharge hematocrit (ϕ_D). Data points are experimental measurements, while (Reproduced from [31])

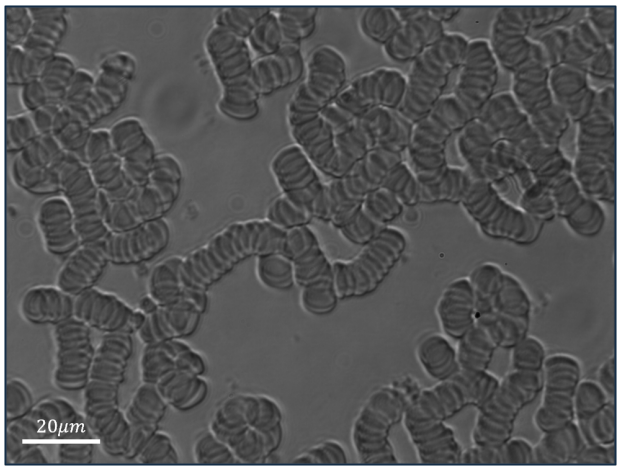


Figure 1.9: Example of aggregated RBC in plasma. (Obtained in-house, University of Ottawa)

of RBCs in a fibrin network following platelet activation. RBC aggregation is a reversible process, with disaggregation occurring under the influence of increasing shear stress. The reversibility of RBC aggregation is a principal factor influencing the shear-thinning property of blood, whose effect is most pronounced in shear rates lower than $100\,s^{-1}$, with cell deformability representing the other determining element [5, 11].

Fåhræus demonstrated RBC aggregation formation at low shear rates in both physiological and pathological conditions [35]. Increased RBC aggregation has been observed in a variety of pathological conditions and states such as sickle cell anemia, diabetes mellitus, myeloma, and many more [36]. However, it is believed that in normal blood microcirculation, the shear rates are too high to allow the formation of aggregates with the exception of some veins and venules [11,37]. Studies of RBC aggregation in tube flow have demonstrated the intricate relationships between the viscosity of RBC aggregates and the augmentation of the CFL thickness [38]. An increase in aggregation can result in a blunt velocity profile, leading to an augmented apparent viscosity. However, conversely, it can also give rise to enhanced axial migration of cells, resulting in a larger CFL at the wall, thereby exerting an opposing effect [11].

Two molecular models have been proposed to explain the formation of aggregates: the bridging model and the depletion model. The bridging model, as proposed by Chien and Jan [39], describes the formation of aggregates due to the adsorption of long-chain macromolecules, such as fibrinogen or dextran, onto cell surfaces, which then leads to a bridging effect between cells [37]. The depletion model posits that the reduction of

macromolecule concentration in the vicinity of RBCs diminishes the osmotic forces exerted on them, prompting fluid to move away and increasing the likelihood of cell adhesion [40, 41]. The configuration of aggregates is contingent upon several local conditions, including the shear rate and hematocrit, and can assume a multitude of intricate forms, ranging from single or branching rouleaux to spheroids [37].

1.3 Insights into Blood Rheology from Capillaries to Bulk Flow

In summary, the study of blood rheology reveals a field of remarkable complexity, where the interplay of cellular interactions, suspension dynamics, and flow behaviors continues to challenge our understanding. While advances in the rheology of suspensions and flow in porous media provide a valuable framework, significant opportunities for discovery remain. The following chapters delve into this intricate topic by exploring key aspects across multiple scales.

At the capillary scale, we investigate how RBCs interact with microfluidic networks, shaping overall transport dynamics and the apparent viscosity of blood. At the arterial level, we examine how the unique suspension properties of blood influence mixing processes critical for nutrient and gas exchange. Finally, at the bulk scale, we explore how heterogeneous RBC distribution impacts the classical assumptions of rheometry, seeking to bridge macroscopic viscosity measurements with microscopic velocity profiles.

Together, these studies illuminate the intricate mechanisms governing blood flow and open new avenues for understanding and modeling its behavior across diverse biological and physical contexts.

Chapter 2

General Methodology

The following chapter examines the fabrication process of the polydimethylsiloxane (PDMS) and glass microfluidic devices, and it describes the preparation of the blood samples for both non-aggregating and aggregating red blood cell (RBC) samples.

2.1 Microfluidic Device Fabrication

In this work, microfluidic devices were used to explore blood rheology. Three main categories of devices were fabricated, which are the PDMS channels, glass capillary channels, and glass-PDMS channels. The microfluidic device made in PDMS allowed for the replication of complex designs, which first starts with the design that is made into a master wafer mold, in which the design can be replicated using soft lithography. In contrast, the microfluidic devices made using either glass capillary or glass-PDMS channels were simple straight channels with constant cross-sectional area and were fabricated by piecing commercially available components together to create an enclosed microfluidic device.

2.1.1 PDMS Microfludic Device

Wafer fabrication

The fabrication of the silicon wafer copy used as molds of either the network pattern or the diffusion co-flow design was completed in the clean room of the Institut d'Electronique et des Systèmes (UMR5214, CNRS, Montpellier) by Audrey Sebban through classical optical

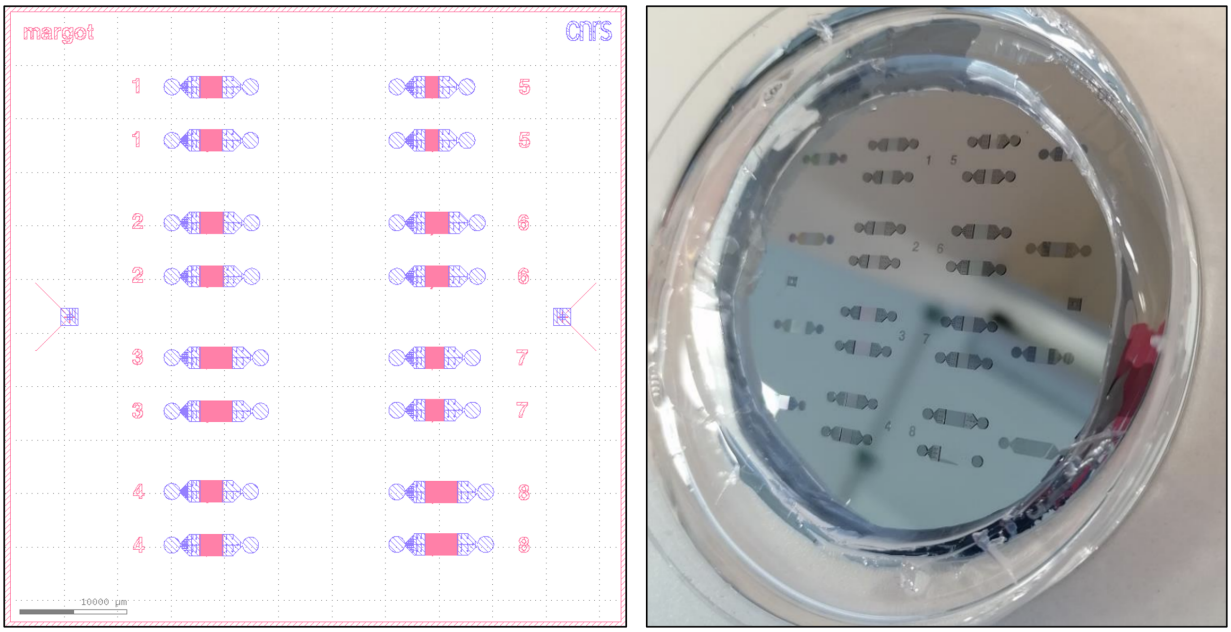


Figure 2.1: (Left) Sample CAD design of the microfluidic network. (Right) Manufactured SU8 master wafer used to mold the microfluidic networks in PDMS. (Images provided courtesy of Benoit Charlot and Clara Bollaërt)

photolithography [42]. The purpose of photolithography is to transfer a pattern from a photomask to a wafer which is used for the fabrication of PDMS copies. This process begins with applying a coating of photosensitive material called a photoresist (SU8) to the silicon wafer substrate through spin coating. The thickness of the coating is dependent upon a number of factors, including the rotation speed of the spin coating apparatus and the viscosity of the photoresist. Once the optimal thickness has been achieved, the photoresist-coated wafer is subjected to a soft bake to eliminate any residual photoresist solvent. Subsequently, the photomask, which contains the pattern, is aligned and positioned over the photoresist, and then exposed to UV light. Subsequently, a post-exposure bake is conducted to facilitate the smoothing of any residual irregularities. If a multilayered design is required, a second layer of photoresist coating, accompanied by a soft bake, mask alignment, and exposure, is then completed for the second layer of the pattern design. Upon completion of all layers, the wafer is placed in a developer solution, which effectively removes any remaining excess photoresist not cured by UV exposure. Finally, a post-developer bake of the wafer is performed to stabilize the features of the mold. An example mask design and the finished SU8 master are presented in figure 2.1.

Channel fabrication

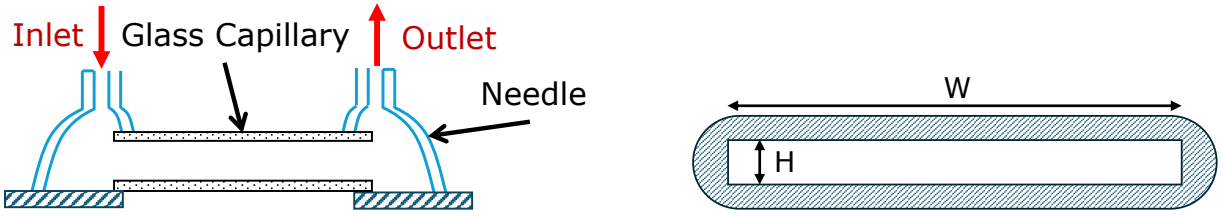
To produce PDMS chips, two-part PDMS elastomer and curing agent (RTV615 A+B, Momentive Performance Materials GmbH) are mixed in a 10:1 ratio for 5 min in a 50 mL falcon tube until fully combined and opaque through the introduction of air bubbles. The mixture is then placed into a bucket centrifuge (Centrifuge 5810 R, Eppendorf) for a preliminary degassing step of 2 min in the original mixing container. After degassing, the mixture is poured onto the master pattern mold and degassed again for 1 h in a vacuum chamber to remove bubbles that form between the hexagonal pillars. Subsequently, the mold is placed into an oven set at 70 °C for 2 h and left to rest for 24 h. The PDMS copy is removed from the mold with a scalpel to avoid any tearing. Inlet and outlet holes are punched into each microchannel using a 1.5 mm diameter Integra Miltex biopsy punch (Ted Pella Inc., USA). The surfaces of the PDMS channels are cleaned and sealed with clear Scotch tape to prevent contamination from dust. The PDMS chip is closed by placing the PDMS copy on a glass slide to form the final wall.

To clean the glass slide, standard 1 mm glass slides are placed in a glass slide holder with 1 mol/L potassium hydroxide (KOH) solution and sonicated for 30 min in the KOH solution. Any residue is rinsed off with 1 L of MiliQ water. Lastly, to bond the PDMS copy to the glass slide, the PDMS and glass slide are placed in a plasma surface etcher (Femto, Diener electronic GmbH & Co. KG) for 1 min to functionalize the surface of the PDMS and glass slide, and sandwiched together once plasma treated. The final chip is placed on a 90 °C hot plate to complete the bonding between the PDMS copy and glass slide. To avoid RBC adhesion to the glass or PDMS, the channels are flushed with poly(L-lysine)-poly(ethylene glycol) methyl ether (PLL-PEG) (0.1 mg/mL solution in HEPES) for 1 h and then rinsed with phosphate buffered saline (PBS). The PLL backbone interacts electrostatically with the PDMS substrate while the PEG side chains extend into the channel from the PDMS surface to act as polymeric bristles to prevent RBC adhesion. PLL-PEG treated PDMS chips are stored in the refrigerator until they are used.

2.1.2 Glass Capillary Microfluidic Device

Glass capillary microfluidic devices are made using commercially available glass capillaries (CM Scientific Ltd., UK) with defined nominal geometry to create simple straight channels. Glass capillaries come in both rectangular and circular cross-sectional areas and are fabricated from borosilicate glass, clear fused quartz, or synthetic fused silica. Borosilicate glass hollow rectangular capillaries (CM Scientific Ltd., UK) with inner cross-sectional dimensions of 200 µm by 2.00 mm and 100 µm by 1.00 mm are used. To create a glass capillary

microfluidic device, the glass capillary is supported by two glass slides and capped with two syringe needles (20-gauge, BD PrecisionGlide Needle, USA) using a quick 5-minute epoxy (G14250, Thorlabs Inc, USA). The cross-sectional view of a completed glass capillary microfluidic device is represented in Figure 2.2(a) in which the inlet and outlet are enclosed by the syringe needles and glass slides.



(a) Channel cross-section (b)Capillary cross-section

Figure 2.2: (a) Schematic of glass microfluidic device using glass borosilicate rectangular channels with 10:1 width (W) to height (H) aspect ratio. The ends capped with 20-gauge syringe needles using 5 min quick epoxy on 1 mm glass slides. (b) Capillary cross-section have rounded outer dimensions and rectangular inner dimensions.

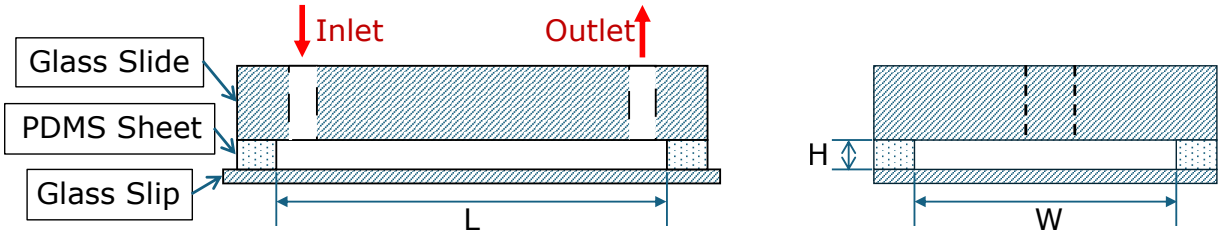
The fabrication of a microfluidic device commences with the cleaning and treatment of the glass components. The glass slides and capillaries are placed in a glass holder containing 1 mol/L KOH and subjected to ultrasonication for a period of 30 min. The KOH is then discarded, and the glass is rinsed with Milli-Q water to remove any residuals. The glass components are then dried using compressed argon gas and placed in a plasma chamber (Femto, Diener electronic GmbH & Co. KG) for one minute to functionalize the surface with PLL-PEG. An alternative to the use of KOH for cleaning the glass capillary is the use of a piranha solution (a solution of 70:30 sulfuric acid (H_2SO_4) and hydrogen peroxide (H_2O_2)), which both cleans and prepares the inner surface for bonding with PLL-PEG polymers. The treatment protocol is completed identically to that of the glass slides of the PDMS microfluidic device. The glass slides and capillary are then dried in a vacuum chamber and ready to be assembled as an enclosed device.

The glass capillary is affixed to two glass slides at both openings with a small droplet of Norland Optical Adhesive 63 (NOA63, Thorlabs, USA) and cured with UV light. This serves to prevent sliding of the capillary and the glass slides before the ends of the capillary are capped using the syringe needles. Syringe needles are prepared by blunting the ends and bending the needle 90 degrees for ease of connection with tubing. The syringe needle cap end is cut shorter to reduce the total reservoir size and notched to account for the glass capillary. NOA63 is used to temporarily bond the syringe needles to the ends of the glass capillary and glass slide such that the center of the syringe needle cap is centered over the

entrance of the glass capillary. The edge of the syringe needle cap and glass slide is coated with several layers of a 5-minute epoxy that cures rapidly to create a watertight seal.

2.1.3 Glass-PDMS Sandwich Microfluidic Device

A secondary channel design that is employed is a hybrid glass-PDMS microfluidic device wherein the bottom and top surfaces of the channel are glass with a nominal channel cross-sectional area of 100 µm by 3000 µm. The objective of this channel design is to fabricate channels with a greater aspect ratio than that of glass capillaries currently available on the market, or which cannot be manufactured using traditional PDMS copies without the formation of buckling. To manufacture a glass-PDMS microfluidic device, a 1 mm thick 76 mm by 24 mm glass slide with drilled port holes (RS FRANCE, France), a #1 24 mm by 60 mm glass slip (Carl-Roth, Germany) and a 100 µm PDMS sheet (SiMPore, USA) are employed. The cross-sectional view of a completed glass-PDMS microfluidic device is depicted in Figure 2.3.



(a) Channel cross-section (b) Capillary cross-section

Figure 2.3: The schematic of a glass-PDMS sandwich microfluidic device illustrates the use of prefabricated PDMS sheets with a known height, glass slides, and glass slips for the top and bottom surface, respectively. PDMS blocks are employed to support FEP tubing for fluid injection. The channel, with a nominal cross-sectional dimension of 100 µm (H) by 3 mm (W) and channel length of 5 cm (L).

First, the glass slide is perforated with port holes using a diamond-tipped drill bit, water, and a Dremel tool. The glass slide and slip are then cleaned by placing the glass in a glass holder with 1 mol/L KOH and sonicating it for 30 min. The glass is subsequently rinsed off with Milli-Q water and air dried using compressed argon gas. The channel pattern with nominal dimensions of 3 mm by 5 cm is cut on the PDMS sheet, whose top and bottom surfaces are protected by two acetate surface liners. The top surface liner is removed with the center of the channel pattern and the PDMS is cleaned with Scotch

tape. Subsequently, the PDMS sheet and glass slide are subjected to plasma treatment using a Corona Plasma Treater (Elveflow, France). The plasma treated glass slide is placed over the cut-out channel design, ensuring that the drilled port holes are over the cut-out channel design. Subsequently, the bonded PDMS and glass sheet are then placed onto a hot plate at 90 °C for 10 min to remove any excess water produced. To connect tubes to the ports, simple PDMS blocks are bonded on the top glass over the port holes and punched with 1.5 mm biopsy punches. Finally, to achieve a complete closure of the channel, the aforementioned procedure is repeated for the bottom glass slip surface, ensuring that the glass slip fully covers the cut-out channel pattern.

2.2 Sample Preparation

2.2.1 Blood Separation

Discarded whole blood samples are obtained from our collaborator from CHU Montpellier hematology lab. The samples range from 500 µL to 2 mL. Whole blood is separated into its constituent components by a series of washes in PBS and glucose. The procedure starts by filtering the samples through an Acrodisc WBC Syringe Filter with Leukosorb Membrane (Cytiva, USA) which removes the white blood cells (WBCs) leaving the RBCs and platelets. The blood sample is centrifuged (NF 048, Nuve, Turkey) at 5000 RPM, or equivalently 2320 RCF, for 5 min which separates the sample by density, and the suspending plasma of the sample can be removed with any residual buffy coat. The isolated RBCs are then re-suspended with PBS, gently mixed, and centrifuged again. The PBS layer is discarded and replaced with fresh PBS. This is repeated for a total of five washes in which any WBCs or platelets should be removed, and the separated RBC pellet should be close to 100% hematocrit. Blood is suspended in the final hematocrit in either a PBS and OptiPrep solution or plasma and OptiPrep solution to produce a non-aggregating sample or aggregating sample, respectively.

2.2.2 Non-Aggregating Red Blood Cells

To prepare blood in a non-aggregating state, it is suspended in a solution of PBS, OptiPrep, and glucose. PBS is prepared by combining tablets (P4417, Sigma-Aldrich, Germany) with 200 mL of Milli-Q water using a magnetic mixer for 30 min to make the x1 PBS solution. OptiPrep (Ref. D1556, Sigma-Aldrich, Germany) is a commercial gradient density medium

that is mixed with PBS to modify the density of the suspending fluid solution to reduce RBC sedimentation. The use of OptiPrep was found to have a low impact on the mechanical properties of the cells [43]. The addition of glucose in the final suspending fluid solution allows the RBC to produce energy through glycolysis to maintain the vital cell functions. The suspending fluid solution consists of 68.5% PBS to 31.5% OptiPrep by volume with 0.9 mg/mL of glucose. The pH of the solution is measured using an inoLab pH 7110 lab pH meter (Xylem, USA) in a 500 mL flask and adjusted to be between 7.3-7.4 pH by pipetting concentrated HCl or NaOH. The solution is subsequently filtered with a 0.2 µm filter (Nylon, Non-Sterile, Fisher Scientific, Ireland) and stored in the fridge prior to use.

2.2.3 Aggregating Red Blood Cells

To make an aggregating sample of blood, RBCs are suspended in a density-adjusted plasma solution to reduce their sedimentation. To create a density-matched suspending solution with native plasma collected from blood washing, 330 µL of OptiPrep is dried in an oven at 60 °C to powder form overnight. The powder is then cooled and mixed with 1 mL of native plasma using a magnetic stirrer. Similar to the non-aggregating RBC suspending solution, the pH of the solution is then measured using a lab pH meter and is adjusted to be between 7.3-7.4 pH. Then the final solution of plasma and OptiPrep suspending media is filtered with a 0.2 µm filter. Since the native plasma solution is from the blood sample, the concentration of salts, proteins, or anticoagulant agents is not controlled.

An alternative to plasma induced aggregation, a PBS, OptiPrep, and dextran-70 solution can be used instead. To prepare the solution with the macromolecules that mimic healthy levels of fibrinogen, 20 mg of dextran-70 were diluted in 1 mL of PBS and OptiPrep solution [44].

Chapter 3

Blood Flow Through a Uniform Network

Chapter Abstract

In this work, the transport of blood in uniform networks is explored. The aim of this study is to investigate how the interaction between cells with the individual nodes and segments of the network affects the overall perfusion efficiency. Measurements of healthy density-controlled red blood cells (RBCs) through the network are completed in varying geometry and topology, showing how the relative resistance of the network scales non-linearly with the measured flow rate. Defining a Capillary number through the local velocity of the cells and an average in-plane shear elasticity, a scaling law for the excess relative resistance as a function of the local volume fraction of RBCs and the topology of the network is proposed. The first observations show that these transport properties are likely correlated to the local behavior of RBCs and their membrane mechanics.

3.1 Introduction

Blood provides an impressive number of essential physiological functions including nutrient supply and waste disposal, oxygen delivery, homeostasis, temperature regulation, and transport of immunity soldiers. To do so, blood has to circulate in a complex plumbing system of vessels, 80000 km long, half of which composes the so-called microcirculation. There is a hierarchy of vessels smaller than a few hundred microns called the arterioles

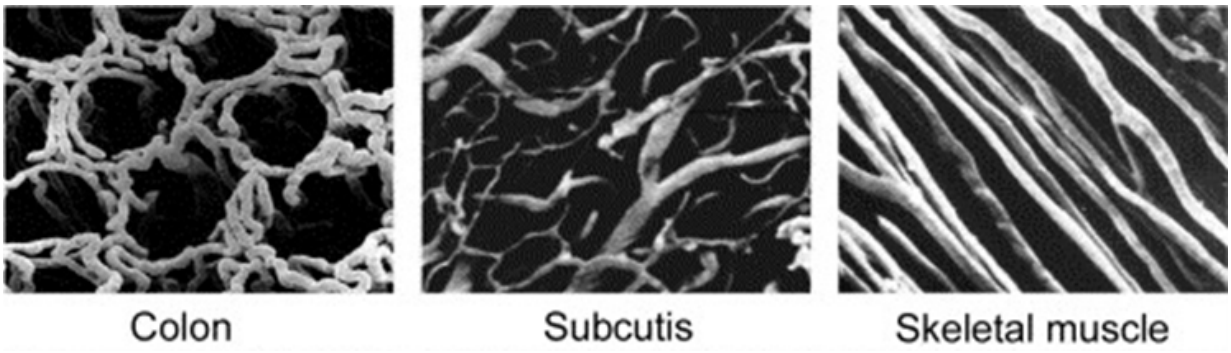


Figure 3.1: Examples of vasculature of tissues in different organs. (Reproduced from [45])

and venules that feed red blood cells (RBCs) to reticulated networks of tiny vessels, called the capillaries, whose sizes are of the order of RBCs' size and perfuse all the cells of the body at a distance of no more than a hundred microns, allowing gas exchange with the surrounding tissue. The level of perfusion through such a reticulated network is a process that depends on the interactions between RBCs, the suspending fluid, and the geometry of the vessels whose complexity and connectivity depend on the organs being perfused [7, 24]. Figure 3.1 illustrates the diverse microcirculatory vasculature observed in different organs.

Cells' hydrodynamic interactions through the segments and nodes of the network result in significant spatial and temporal variations of the hematocrit, as well as a high degree of variability in suspension dynamics from vessel to vessel. Despite extensive research on microcirculatory heterogeneity, the fundamental mechanisms underlying its emergence at the microcirculatory network level remain largely unclear [46, 47]. These mechanisms entail a robust interconnection between the network architecture and blood flow dynamics. Consequently, a more profound comprehension of these mechanisms is of paramount importance for a comprehensive understanding of the underlying physiology of the microcirculatory system.

3.2 Background

Blood is a suspension of cells with a volume fraction of about 40 to 45%. Its rheology is mainly controlled by the RBCs which form the largest population of cells, compared to the white blood cells (WBCs) or the platelets. In comparison, for each WBC, there are about 50 platelets and 1000 RBCs, which are therefore considered as the major rheoactive

entities.

In the physiological regime of microcirculation, RBC flow occurs through vessel diameters ranging from 5 µm to 100 µm, at the limit of high shear rates. At this scale, Reynolds[1] and Womersley[2] numbers are significantly less than one, indicating that blood flow in each vessel is primarily governed by the local pressure gradient and viscous stresses. To comprehend the transport of blood flow at the single vessel or network scale, one common description uses the concept of relative apparent viscosity. It is defined as the apparent viscosity normalized by the viscosity of the suspending fluid and is utilized to represent the spatially and temporally averaged effective parameters characterizing the global viscous dissipation. It is important to note that apparent viscosity is not an intrinsic property of the fluid itself but rather a property of the blood and blood vessel interaction including the formation of a cell free layer or cell depleted layer (CFL) (see Section 1.2.3) results in the Fåhræus-Lindqvist effect (see Figure 1.8 in Section 1.2.3) [24].

3.2.1 Rheology in Simple Geometries

In bulk, blood is one of the classical examples of a shear thinning fluid, a feature demonstrated in the seminal works of Chien in hemorheology, using a rotational rheometer [5]. At low shear rates, RBCs tend to aggregate into linear arrays known as rouleaux, which results in a higher viscosity. These aggregates are reversible, disassembling at high shear rates and the cells are able to form a rich variety of dynamical shapes that further reduce the viscosity of the bulk fluid [17]. The primary determinant of bulk blood viscosity is the hematocrit, in which higher hematocrit levels increase viscosity [7].

In a tube, the variation in relative apparent viscosity as a function of tube diameter is described by the Fåhræus-Lindqvist effect (see Section 1.2.3). As in bulk rheological measurement of blood, the largest determinant in modifying the apparent viscosity measurement through capillary tubes is the hematocrit. However, in experiments completed in glass tubes by Reinke, Gaehtgens, and Johnson [48], it was found that the apparent viscosity of blood is approximately constant whenever the tube diameter is between 30.2 µm to 132.3 µm for pseudo-shear rates[3] between 1/s and 20/s while at lower shear regimes RBC

[1] At the capillary scale $Re \approx 0.0015$ considering a blood density of $1060\,\mathrm{kgm}^{-3}$ and blood viscosity of 3.5 mPa sec [23].

[2] At the capillary scale $\alpha \approx 0.003 - 0.007$ considering a blood density of $1060\,\mathrm{kgm}^{-3}$, blood viscosity of 3.5 mPa sec, and characteristic frequency of 1 Hz [23].

[3] Pseudo shear rate is defined as the ratio of the mean flow velocity to the cross-sectional area of the measuring tube.

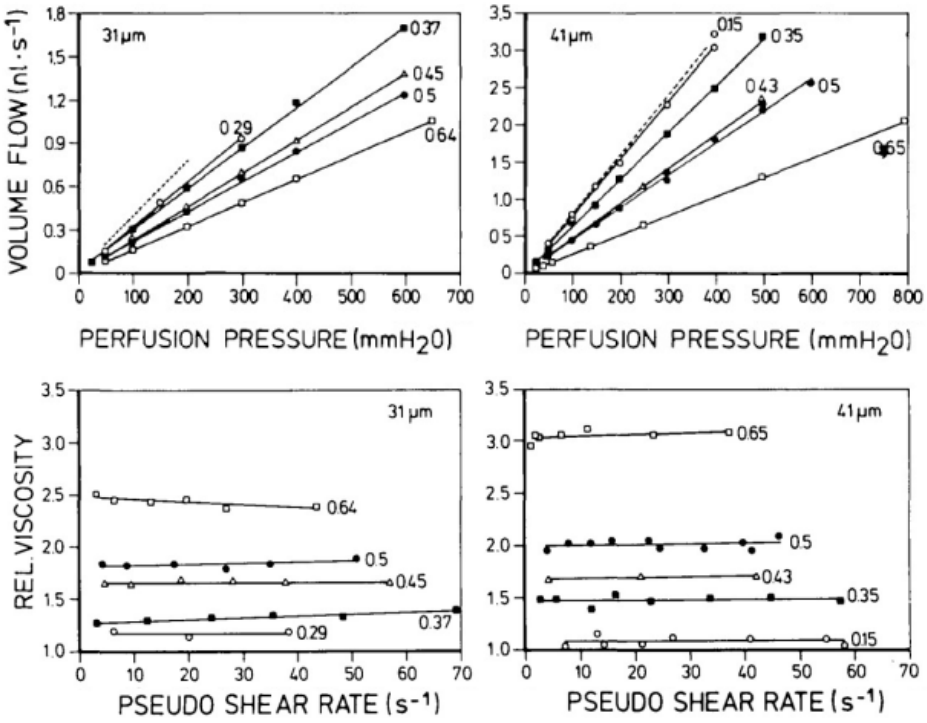


Figure 3.2: (Top row) Pressure-flow relations obtained in capillary tubes with plasma and blood samples with different feeding hematocrits. Dashed lines indicate linear regressions for plasma, solid lines for blood samples. (Bottom row) Relationship between pseudo shear rate and relative apparent blood viscosity. Linear regressions (solid lines) were calculated for all data. (Reproduced from [48])

aggregates begin to affect viscosity. A set of examples of the pressure-flow, pseudo-shear rates, and relative apparent blood viscosity are presented in Figure 3.2.

Constant apparent viscosity, however, is contrary to what is reported in confined single file motions found in vessel diameters less than 6 µm. In vessels with diameters comparable to cell sizes, analytical studies using lubrication theory have modeled axisymmetric membrane deformations in tube flow to approximate plasma flow in the narrow gaps between cells and vessel walls. These studies have examined how cell shape affects global capillary hydrodynamic resistance. For example, Secomb and colleagues demonstrated that as RBC velocity increases, the cell shape changes, causing the gap between the cell and vessel wall to widen, as illustrated in Figure 3.3 (left). This, in turn, reduces apparent viscosity and flow resistance [49]. The decrease in apparent viscosity with increasing velocity is corroborated

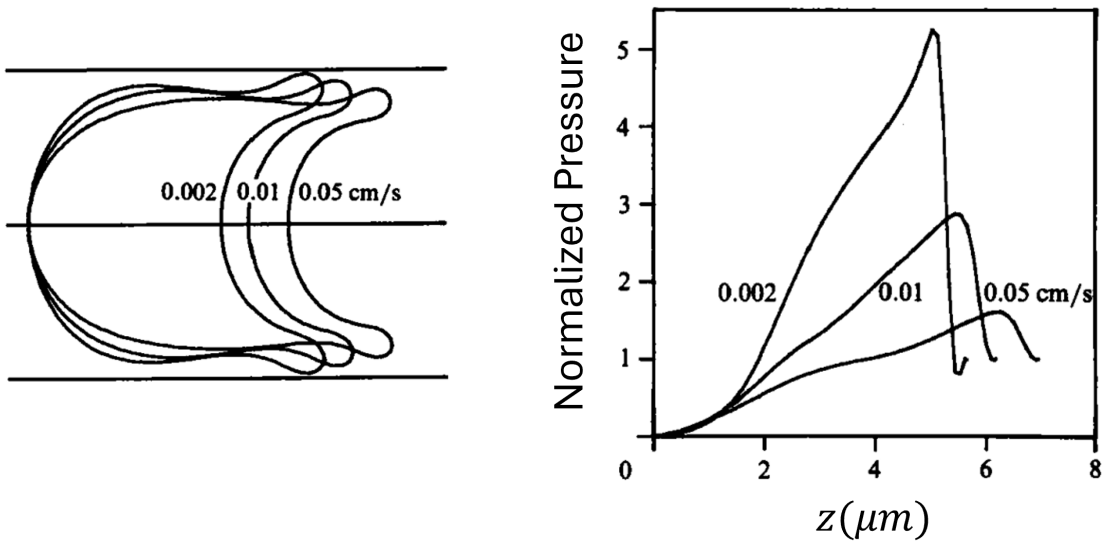


Figure 3.3: (Left) Cell shapes calculated from both shear and bending elasticity in a vessel of 6 µm diameter with increasing cell velocities. (Right) Variation of normalized pressure in the gap corresponding with the cell shape. (Reproduced from [49])

in numerical models of the flow of capsules [50], finite element results reported by Skalak and Tozeren [51], experimentally using model cells by Lee and Fung [52], and human cells in capillary arrays by Lingard [53]. The apparent viscosity (η_{app}) is said to scale proportionally to the hematocrit (ϕ) and the intrinsic viscosity (K_t) as follows $\eta_{app} = \eta(1 + \phi K_t)$. The behavior of the intrinsic viscosity which can be understood as the contribution of resistance of the cell with increasing cell velocity is represented in Figure 3.4.

For the case of asymmetric flowing RBC, it was concluded, however, that the cell's asymmetry itself did not strongly influence flow resistance [54]. This is further confirmed in simulation studies reported by Noguchi and Gompper, which demonstrate that as flow velocity increases, a model of the RBC transitions from a non-axisymmetric discocyte to an axisymmetric parachute shape, which results in a reduction in the flow resistance as demonstrated in Figure 3.5 [55].

3.2.2 Network Rheology

Microcirculation studies observing the macroscopic rheological behaviour at the network level have been reported both in vivo and in vitro. In vivo studies, typically completed

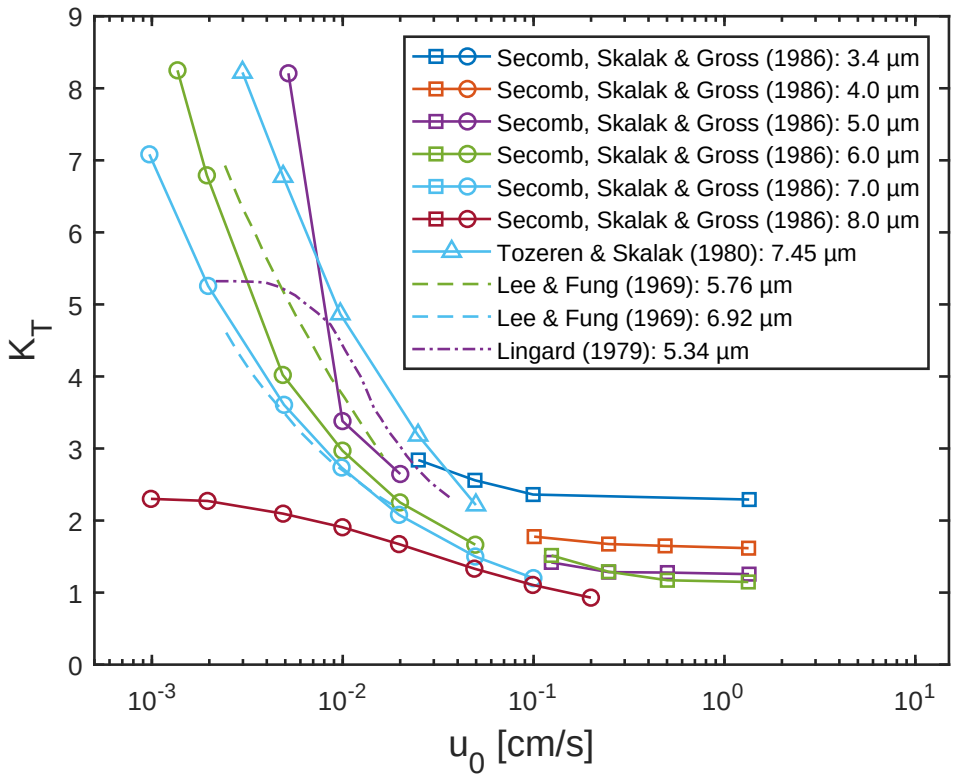


Figure 3.4: Variation of intrinsic viscosisty (K_t) with cell velocity (u_o) comparing a theoretical lubrication model in straight channels to experimental studies. The theoretical lubrication model described by Secomb, Skalak & Gross includes shear elasticity but neglects bending of are indicated by □, while results of the theoretical lubrication model that includes both shear elasticity and bending elasticity are indicated by ∘ [49]. Finite element results of Skalak & Tazeren are indicated in △ [51] . Experimental results of Lee & Fung using model cells are indicated by dashed lines [52], and those of the Lingard model through using human cells are indicated by dot and dashed lines [53]. (Reproduced from [49])

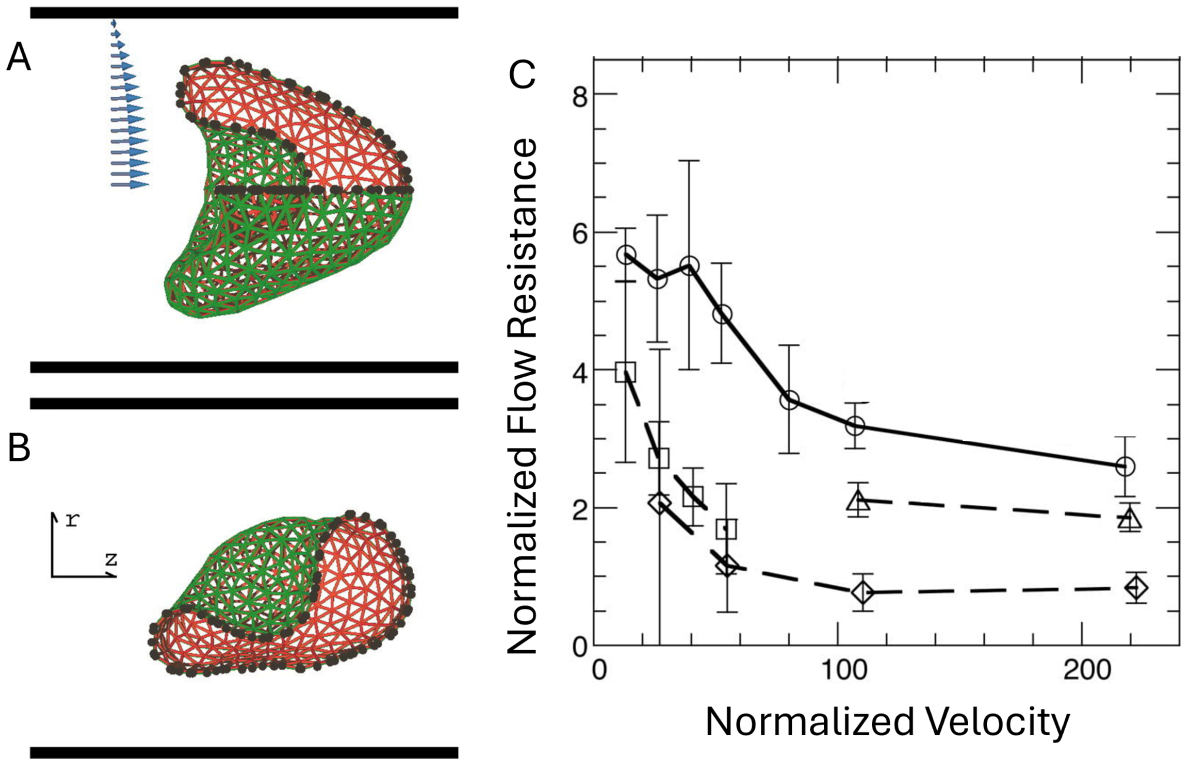


Figure 3.5: (A) RBC model with parachute shape at normalized velocity of 218, (B) RBC model with slipper-like shape at normalized velocity of 80 (C) Normalized velocity as a function of normalized flow resistance where the solid line corresponds to the RBC model and the dashed line to fluid vesicles model. (Reproduced from [55])

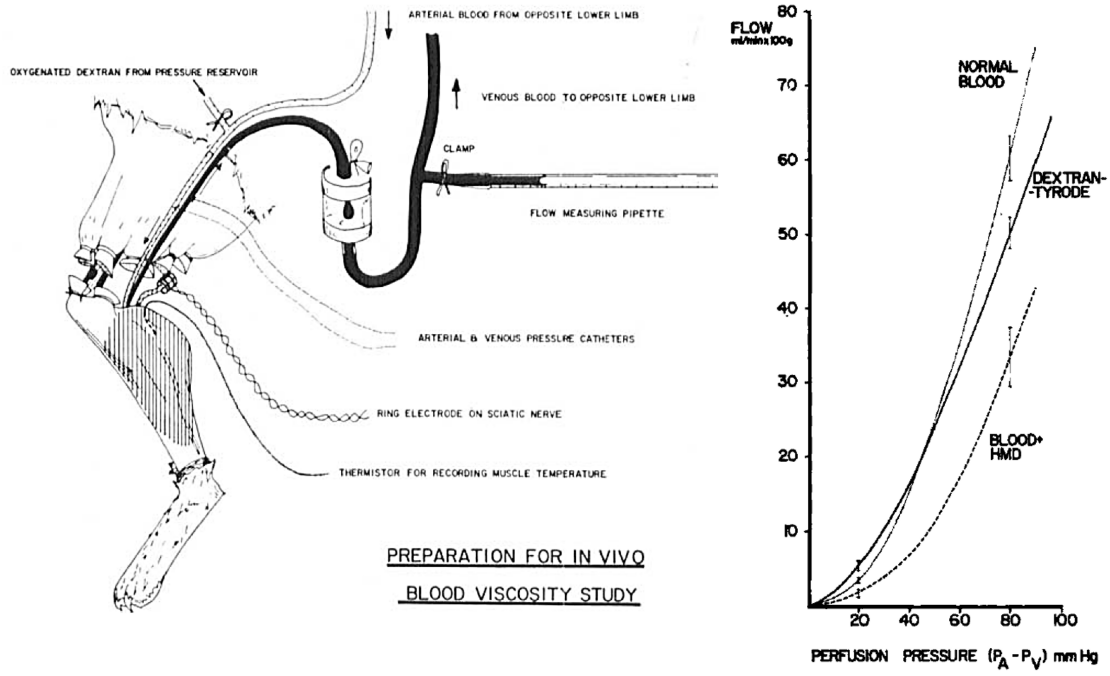


Figure 3.6: (Left) Schematic illustration of the biological viscometer through the calf muscle vascular bed of a cat. (Right) Pressure-flow curve of dilated calf muscle for normal blood, blood with dextran and dextran-Tyrode solution. (Reproduced from [56])

on whole vascular beds such as the calf muscles, are used to complete biological viscometric measurements of blood flow through a network of channels starting from the arterial level [56, 57]. These rheological studies of whole organ flow have indicated a non-linearity in the viscosity measurement of vascular beds as demonstrated in Figure 3.6 (right) [56,57]. In contrast, measurement of the macroscopic response of a pulmonary network array completed in vitro reported by Stauber and colleagues was found to produce a proportional relationship between measured pressure and flow rate, indicating a constant apparent viscosity as demonstrated in Figure 3.7 [58]. This discrepancy on whether a non-linearity is present or not may simply be associated with differences in the vascular dimension and the length scales that are present in vivo compared to in vitro, or with the small pressure gradient regime explored. Furthermore, biological phenomena such as passive vasodilation in which the vessel widens may be induced by increasing pressure and flow, which may further result in differences between in vivo and in vitro reporting.

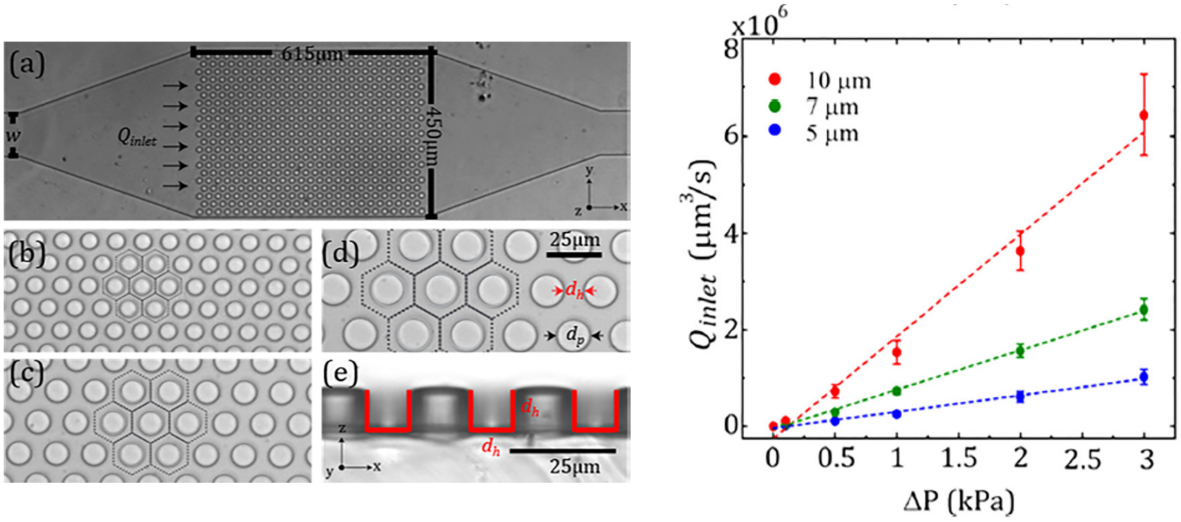


Figure 3.7: (Left) Bright-field imaging of the bio-mimetic microfluidic networks of pulmonary alveolar capillaries network. (Right) Flow rate as a function of pressure drop in the microfluidic network. (Reproduced from [58])

3.2.3 Collective Behaviour Through Network Topologies

There have been several recent investigations focusing on the collective behavior of RBCs in idealized networks, and the associated properties at the network scale [47, 58–61]. The advantage of a microfluidic system to model network flows is the ability to spatially resolve individual RBCs and control the network architecture without biological compensatory mechanisms such as short-term diameter variations. These advantages have provided an understanding of the physical mechanisms by which network architectures impact blood flow dynamics.

Studies in microcirculation tend to focus on understanding the highly heterogeneous distribution of RBCs in a network such as in a square microfluidic network demonstrated in Figure 3.8. For example, in vivo, the spatial arrangement of the feeding and draining vessels results in variation of RBC distribution close to the vessels to the region to be supplied, and the variation in length and diameter of microvascular pathways between the feeding and draining vessels results in dispersion in pressure drop per length along those pathways. Therefore, a higher flow rate is expected on shorter pathways [30]. To understand the impact on heterogeneous RBC distribution in networks, there has been a

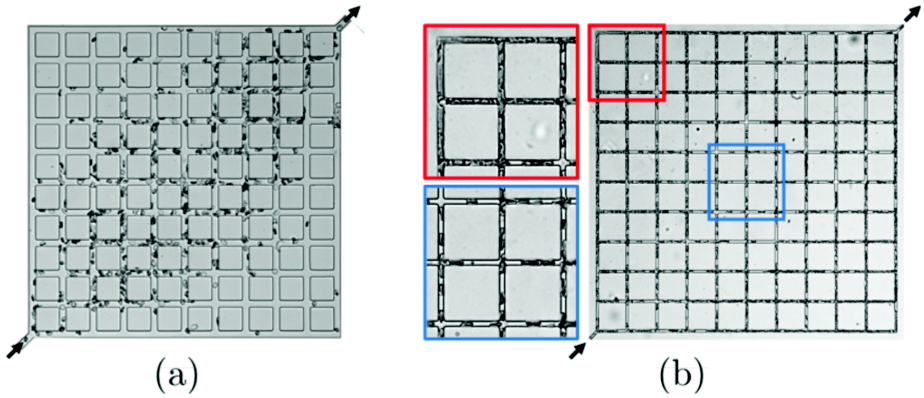


Figure 3.8: (a) Instantaneous snapshot of RBC distribution in a square network for (a) 10 µm and (b) 5 µm side channels. (Reproduced from [47])

focus on understanding individual bifurcation laws for modeling cell distribution in simple hexagonal networks with single inputs for channel diameters in the range of 10 µm [47, 59, 60]. However, in these studies, there is no reporting of macroscopic rheological responses induced by the presence of cells correlated with the local behavior of the cells.

3.2.4 Deformation and Morphological Effects

At rest, the RBCs are disk-shaped but can deform strongly when flowed in microcirculation in channels that are smaller than their resting diameter. This is attributed to the large surface area to volume ratio of the cells and the viscoelasticity of the membrane [2]. Specifically, the RBC membrane has a composite structure where the lipid bilayer provides a bending resistance while the underlying spectrin network, which is anchored to the proteolipid membrane, provides a shear elasticity that allows the cell to survive in microcirculation for more than 120 days. A resting RBC and schematic of the RBC membrane and attached cytoskeleton are depicted in Figure 3.9. Because the RBC membrane is extremely thin, three independent deformation modes are required to describe its mechanical state: isotropic stretching or compression, simple shear, and out-of-plane bending [2]. Correspondingly, the associated elastic moduli are the stretching modulus (κ_α), the shear modulus (G_s), and the bending modulus (κ_B). As summarized by Tomaiuolo [62], typical average values for these moduli are presented in the following table.

The ability of the RBC to deform and shape change is important to pass through vessels whose diameters are smaller than the largest diameter of the cell [11]. In capillaries

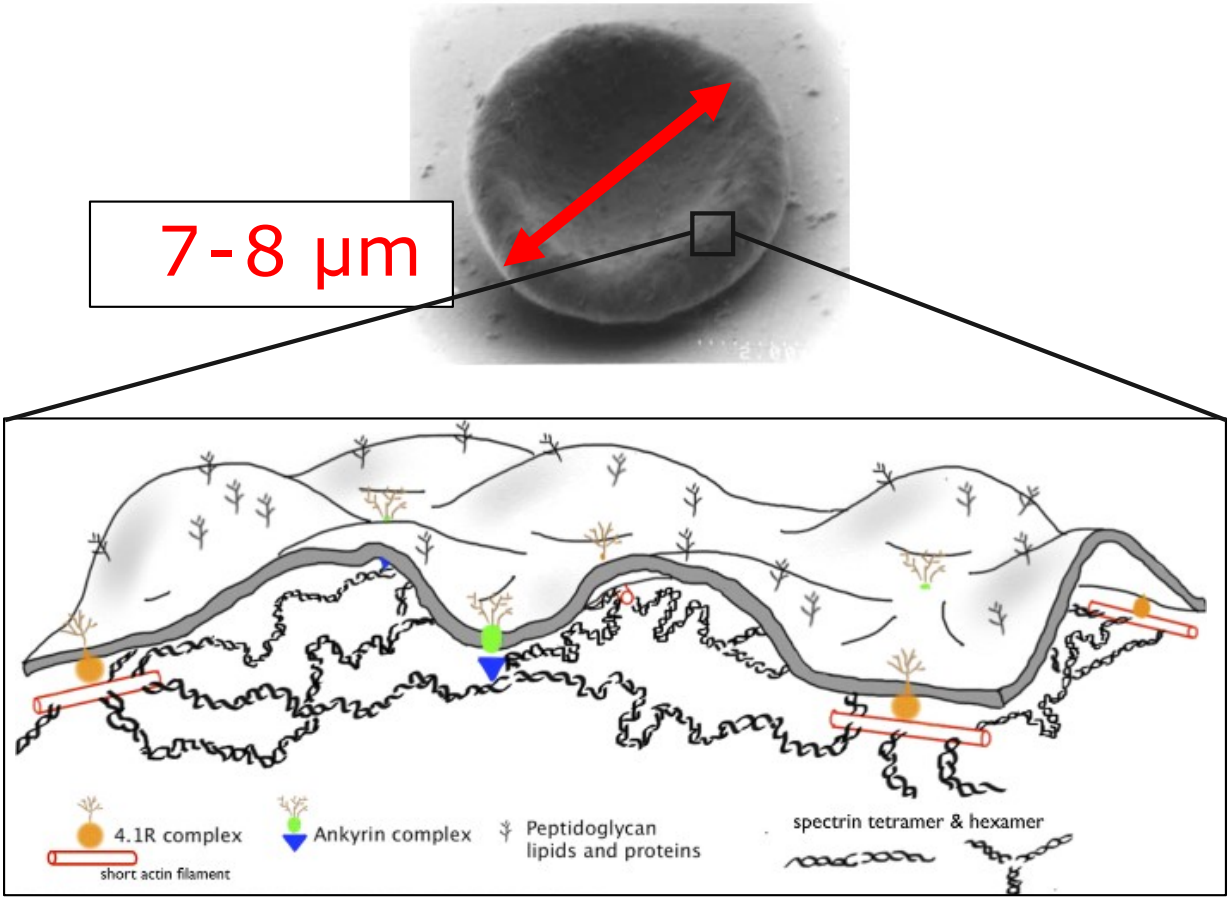


Figure 3.9: (Top) Scanning electron microscope imaging of a human RBC. (Reproduced from [7]) (Bottom) Schematic drawing of a RBC membrane-cytoskeleton interaction and coupling. (Reproduced from [2])

Table 3.1: Mechanical properties of RBC membranes from Tomaiuolo [62]

Modulus	Average value and dispersion in literature
Surface shear modulus, G_S, (μNm^{-1})	5.5 $\pm$ 3.3
Stretching modulus, κ_α, (mNm^{-1})	399 $\pm$ 110
Bending modulus, κ_B, (J)	28.75 $\pm$ 22.5
Surface shear viscosity, η_S, (μN sec m^{-1})	0.515 $\pm$ 0.39

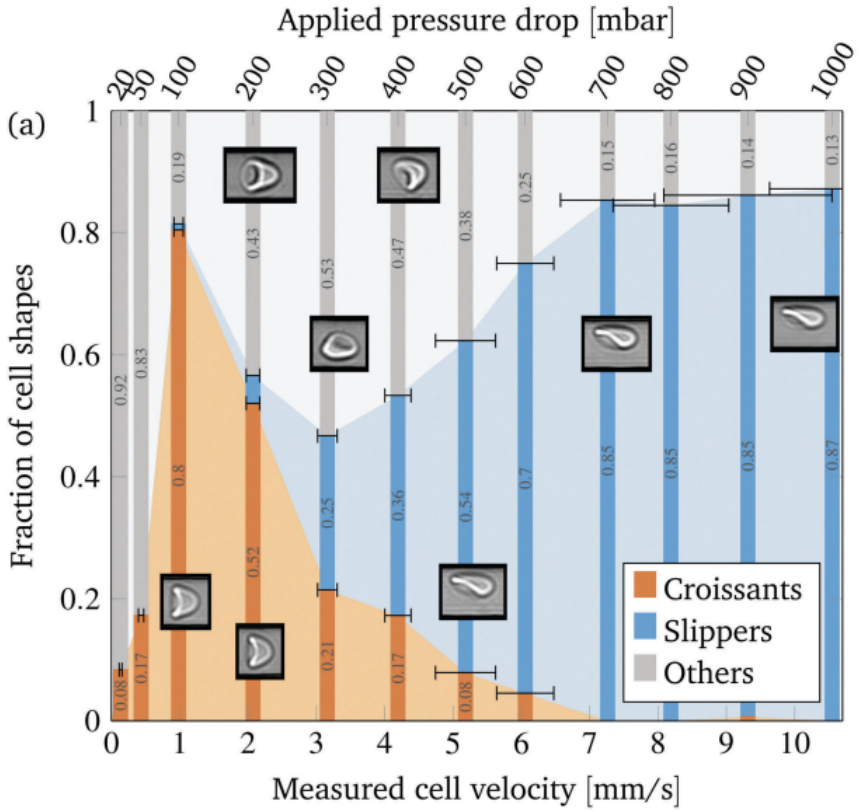


Figure 3.10: Experimental results showing fraction of observed cell shapes as a function of applied pressure drop and mean cell velocity in steady flow condition. Measurements are completed in a rectangular PDMS channel with dimensions of 11.9 µm by 9.7 µm cross-sectional area. (Reproduced from [67])

a RBC can achieve a variety of shapes due to its high deformability, and predicting its shapes requires understanding the relationship between flow conditions and the membrane mechanics. The steady state morphology of a RBC depends on the channel geometry, the flow velocity, the viscosity of the surrounding fluid, and the mechanical properties of the RBC itself [63,64]. The morphologies of a RBC flowing in straight capillaries have been extensively studied experimentally [64–68] and numerically [49,55,67,69]. Two morphologies that are observed in straight microcapillary channels are the parachute (axisymmetric) and slipper shape (asymmetric) which have been shown to depend on flow parameters. The experimental phase diagram, in rectangular channels, is shown as a function of input pressure drop and cell velocities in Figure 3.10.

The interplay between cellular morphologies and vascular network architecture raises several key questions about topologies. First, how does the transition from parachute-like to slipper-like morphologies, commonly observed in rectangular channels, change when analyzed in the complexity of a vascular network? Second, do varying network topologies produce distinct morphological phase maps based on their structural characteristics? Finally, at the network scale, does the distribution of individual cell morphologies correlate strongly with increased vascular resistance, influencing overall flow dynamics? Addressing these questions is critical for understanding how cellular behavior integrates with global rheological properties and vascular architecture.

3.3 Objective

This study aims to understand how cells interact with individual nodes of a microfluidic network and how these interactions contribute to overall macroscopic transport through the network. A gap in the current literature is the lack of observations of network designs with vessels below 6 µm, where the morphological shape of cells can significantly influence overall flow resistance and dynamics within such networks. To investigate this network rheology, RBCs were flowed through various uniform networks with different channel lengths while maintaining the same overall geometric hydrodynamic resistance. This approach enabled a study of how the local hydrodynamic interactions of RBCs with the channels in a uniform network affect the global resistance of blood flow. The specific objectives of this work are:

- Quantify the non-linearity of the global rheological behavior of blood through a confined network.
- Investigate how the global rheological behavior scales with different network geometries and topologies.
- Examine how the dynamic variation at the macroscopic scales is affected by the the feeding hematocrit and the geometric parameters of the network.
- Explore the local dynamics of cell passage including the volume fraction distribution, velocity field variation and morphological changes through the network and correlate it to the global rheological properties observed.
- Assess the effects of deformability on the global rheological response.

3.4 Material and Methods

The following section examines the general fabrication process of the microfluidic devices. It describes the preparation of the blood sample for both untreated and treated RBC. It then outlines the experimental setup and flow configuration for measuring the global rheological behavior and local RBC dynamics. Finally, it presents the analysis of the global macroscopic rheology and local high-speed imaging of the cells.

3.4.1 Microfluidic Device

PDMS channel design

The design of the microfluidic chip comprises two hierarchical levels, the entrance and exits, which are approximately 2 mm wide with a height of 100 µm, and a uniform network consisting of individual interconnecting channels with an approximate height of 4.9 µm and width of 5 µm. A total of eight networks was originally designed with varying ratios of channel length, resulting in topological changes from a hexagon to a square-like design, of which only a subset was tested. A schematic of the uniform network design is presented in Figure 3.11.

To achieve a quantitative understanding of micro-circulation under a well-defined geometry and regime of speeds that corresponds to a few hundred microns per second, a uniform network in polydimethylsiloxane (PDMS) is used. Although this network is not designed to replicate a particular micro-circulatory topology, it enables the quantitative assessment of micro-circulatory phenomena without the confounding influence of physiological phenomena such as short-term vessel diameter changes, which introduce an additional layer of complexity to the study of blood flow in micro-circulation. The hydraulic resistance of these networks was designed to be the same.

Hydraulic resistance

The circuit analysis to obtain the equivalent hydraulic resistance (R_{equ}) of the network is presented under Appendix A.1 where the equivalent hydraulic resistance, composed of the individual branching hydraulic resistances, is determined with the following equation:

$$R_{equ} = k\frac{(2R_1 + R_2)(R_1 + R_2)}{n(2R_1 + R_2) + m(R_1 + R_2)} + (k-1)\frac{R_2}{(n+1)} \tag{3.1}$$

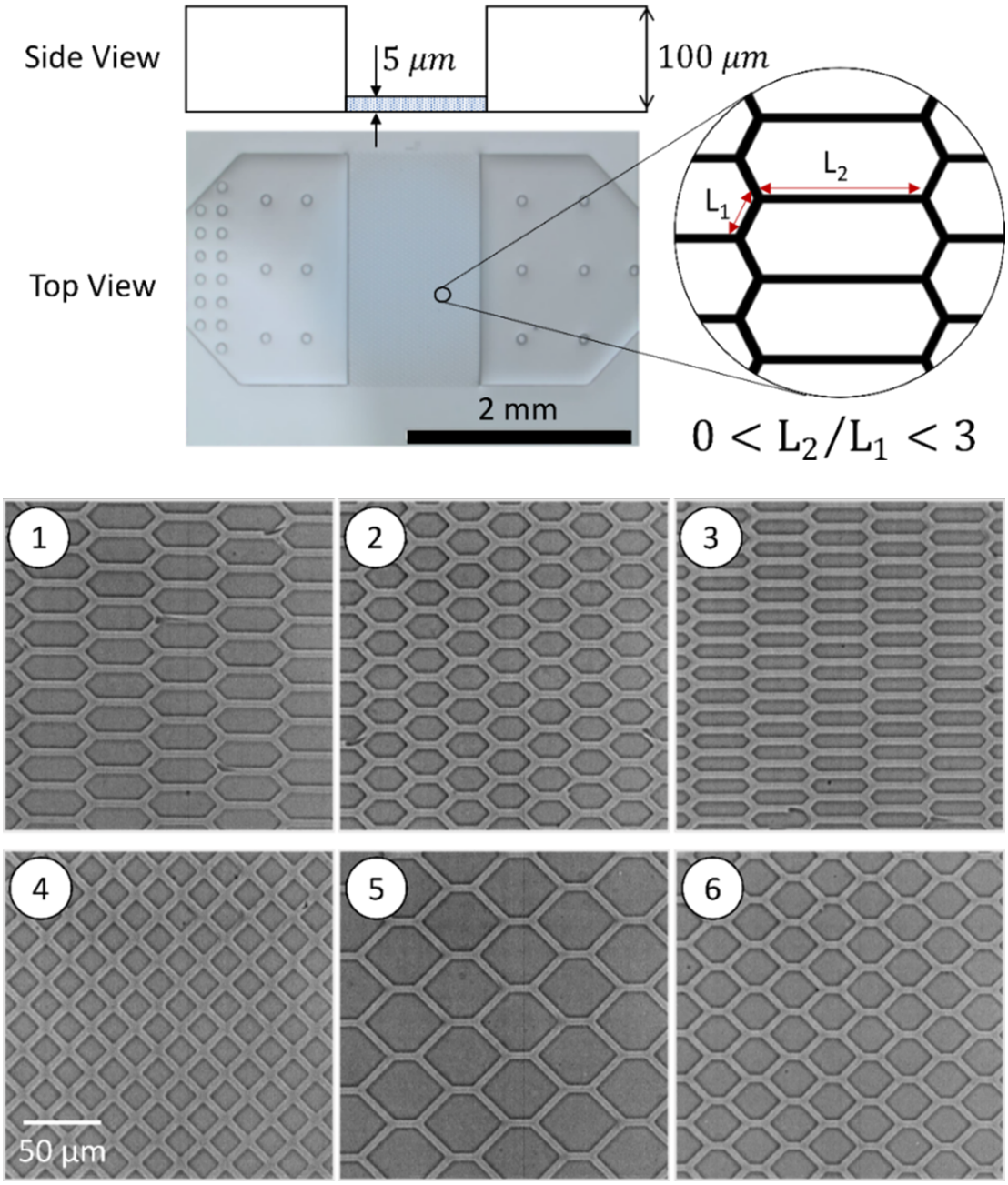


Figure 3.11: Side and top view of uniform network PDMS channel, the length ratio (l_1/l_2) of the channels range between zero to three to observe the effects of bifurcations on the blood flow. The angle of the bifurcation is constant at 90° for all topologies. Sample imaging of the uniform network designs with their different length ratio.

where R_1 and R_2 are the hydraulic resistance of the straight channels of length 1 and 2 respectively, as indicated in Figure 3.11, while k, n, and m are the number of columns and rows of the subsections of the network as outlined in Appendix A.1. For a single channel with rectangular cross-sectional area, the hydraulic resistance ($R_{rectangle}$) can be written as follows [70]:

$$R_{rectangle} = \left(\frac{12\eta l}{h^3 w}\right) \cdot \frac{1}{1 - \frac{192h}{\pi^5 w}\sum_{j=0}^{\infty}\frac{1}{(2j+1)^5} tanh((2j+1)\pi\frac{w}{2h})} \tag{3.2}$$

where η is the viscosity, l is the length of the channel, h is the height of the channel, and w is the width of an individual channel. If the cross-sectional area of individual channels can be assumed to be consistent throughout the network, the equivalent hydraulic resistance can be considered to be a linear function of the length of the two-channel branch and the configuration of the rows and columns. In doing so, an equivalent hydraulic resistance can be written that separates the viscosity, width, and height from the linear arrangement of the channel lengths.

$$R_l = k\left(\frac{(2l_1 + l_2)(l_1 + l_2)}{n(2l_1 + l_2) + m(l_1 + l_2)}\right) + \frac{(k-1)\, l_2}{(n+1)} \tag{3.3}$$

$$R_{equ} = \left(\frac{12\eta}{h^3 w}\right) \cdot \frac{R_l}{1 - \frac{192h}{\pi^5 w}\sum_{j=0}^{\infty}\frac{1}{(2j+1)^5} tanh((2j+1)\pi\frac{w}{2h})} \tag{3.4}$$

A summary of the different designs is shown in Table 3.2. The primary networks in which blood flow experiments are completed are in channels denoted Channel 3, 4, and 6 with length ratios of 1:3, 1:0, and 3:2, respectively. The table assumes an individual channel height and width of 4.88 µm. The hydrodynamic resistance of all the networks is the same.

Geometric porosity, permeability and tortuosity

Porosity (ϱ), permeability (k) and tortuosity (T) are three parameters that can play an important role in understanding the transport through a porous medium such as the uniform network. The porosity is the volume fraction of the void area where the fluid flows to the bulk volume. The permeability describes the ability of the medium to transport fluid, while the tortuosity characterizes the path of fluid transport through the medium. Furthermore, since the networks are engineered to be of a specific geometry, these parameters may be

Table 3.2: Design summary of uniform network with equivalent normalized resistance $R_{EqNorm} = R_{Equ}/\eta$

No.	l_1 (µm)	l_2 (µm)	l_1/l_2	$k(col)$	$n(row)$	$m(ends)$	R_l (µm)	R_{EqNorm} ($1/\mu m^3$)
1	15	30	1:2	25	94	1	19.45	0.98
2	15	15	1:1	42	94	1	19.78	0.99
3	10	30	1:3	40	141	1	19.52	0.98
4	20	0	1:0	71	71	2	19.72	0.99
5	30	15	2:1	17	47	2	20.87	1.05
6	15	10	3:2	54	94	1	19.84	1.00
7	20	10	2:1	72	141	1	20.25	1.00
8	10	25	2:5	47	141	1	19.70	0.99

For unit conversion, $\mu l/(min.mBar) = 166.7 \mu m^3/(mPa.s)$.

Table 3.3: Geometric characterization of porosity (ϱ), permeability (k), and tortuosity (T)

Channel	ϱ	k (µm^2)	T
1	0.342	0.617	1.11
2	0.406	0.545	1.17
3	0.467	0.662	1.08
4	0.497	0.420	1.41
5	0.244	0.482	1.25
6	0.449	0.511	1.21
7	0.427	0.353	1.47
8	0.515	0.571	1.16

described from the geometric parameters. The analysis of the porosity (ϱ), permeability (k) and tortuosity (T) of the different network topologies is presented in Appendix A.2. A summary of the key parameters is presented in Table 3.3.

3.4.2 Sample Preparation

In this work, healthy non-aggregating human RBCs are flowed in the network in which the preparation is described in Section 2.2. To test rigidified RBCs, two chemical treatments are used with differing results: diamide or glutaraldehyde, both of which are described to increase the membrane rigidity of RBCs by enhancing protein-to-protein associations, which in turn leads to the formation of inter- and intra-disulfide bonds [71–73]. In this

work, RBCs were found to become more spherical, losing their characteristic biconcave morphology with greater concentration of diamide with the selected incubation time, while the cells' morphology was maintained with glutaraldehyde.

Diamide treatment

The protocol for diamide treatment follows the work of Safeukui and colleagues [72]. To treat RBC samples with diamide, RBCs are first washed and prepared as a 10% hematocrit solution. The RBC sample is treated at three concentrations of diamide which were prepared in a PBS and glucose solution at 50 µM, 100 µM and 200 µM. These concentrations were selected due to the low relative rigidity of the RBCs when compared with untreated RBCs [72]. To treat the RBCs, 50 µL of RBCs were combined with 450 µL of the diamide concentration and placed in a test tube heater for one hour at 37 °C. After incubation, centrifugation was conducted at 400 RCF for 5 min and the surplus diamide was removed and the RBC pellet was re-suspended with the phosphate buffered saline (PBS), OptiPrep and glucose solution.

Glutaraldehyde treatment

RBCs are first washed and prepared as a 10% hematocrit solution. The glutaraldehyde 25% mother solution (G5882-1ml, Sigma-Aldrich, Germany) is diluted to a concentration of 0.01%, 0.005%, and 0.001% in a PBS solution through serial dilution. 100 µL of 10% hematocrit are then placed in 1 mL solution of diluted glutaraldehyde. The solution is mixed by gentle rotation and then centrifuged at 7000 RPM, or equivalently 3248 RCF, for 5 min. The glutaraldehyde solution is then removed, and the remaining RBC pellet is washed in a filtered solution of PBS with bovine serum albumin at 1 mg/mL. The RBCs are then centrifuged again, resulting in the separation of the RBC pellet. The RBC pellet is subsequently washed in filtered PBS with glucose solution for two additional washes. The treated RBCs are then ready to be re-suspended in the PBS and OptiPrep solution to the appropriate hematocrit. To achieve a total volume of 500 µL that is sufficient for testing, the treatment is scaled up to five individual Eppendorf vials with a ratio of 100 µL of 10% hematocrit RBCs to 1 mL glutaraldehyde. This avoids having to deal with a high concentration of cells that can clump during rigidification. Similarly, to create a final hematocrit of 20% of 500 µL solution, the treatment is completed on a total of 1000 µL of 10% hematocrit RBCs in 10 individual Eppendorf vials, and the final combined pellet is re-suspended to a bulk 20% hematocrit. A series of concentration and incubation time trials were conducted and summarized in Table A.3 presented in Appendix A.3. The selected

conditions were chosen to ensure that the RBCs remained sufficiently flexible to avoid clogging the network and is demonstrated in Figure A.6 presented in Appendix A.3.

Approximating rigidification

An adapted graphic of reported results is presented in Figure 3.12 where the relative rigidity defined as the ratio of the surface shear modulus of treated to untreated RBC from the work of Drochon [74] is presented with the reported relative rigidity from the work of Safeukui and colleagues [72]. A relative rigidity is approximated from glutaraldehyde experiments of Abay and colleagues reporting atomic force microscope (AFM) measurements of Young's elastic modulus of treated RBC assuming that the surface shear modulus is proportional to the Young's elastic modulus of the membrane in which the relative rigidity is the ratio of treated to untreated RBC. In the regime of diamide and glutaraldehyde tested, the change in the rigidity of the cells is approximately linear [73]. Using the fitted model, the approximate change in the surface shear modulus is assumed to be proportional to the change in relative rigidity as a coarse approximation.

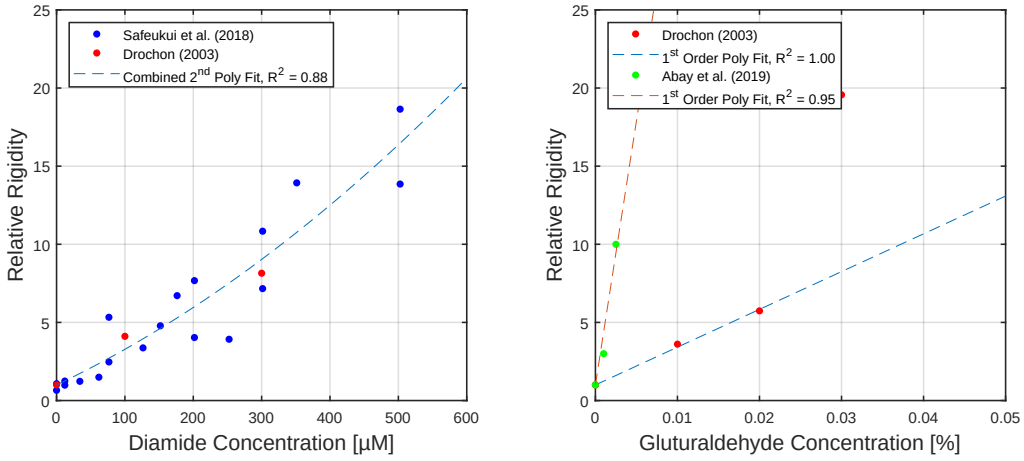


Figure 3.12: Relative rigidity of treated RBCs with diamide and glutaraldehyde. Fitted by 2nd and 1st order polynomial fit, respectively. (Adapted from [72–74])

3.4.3 Experimental Setup

To investigate the question of micro-circulatory flow, a microfluidic platform with a pressure control system is employed. Individual pressure controllers (Flow-EZ LU-FEZ-1000, Fluigent, France) are utilized to regulate the pressure gradient across the microfluidic network, which induces a flow rate that is quantified using a flow meter (Flow Unit FLU-S-D, Fluigent, France) that is placed in series with the microfluidic network. This approach enables the macroscopic measurement of pressure and bulk flow rate, which can be used to calculate the relative apparent viscosity of the blood sample that is flowed through the network. In addition to the bulk flow measurements, high-speed videos of the cell passage through the network are taken simultaneously using a high-speed camera, at 1400 fps for pressures below 250 mbar or 2000 fps for pressures greater than 250 mbar using a FASTCAM NOVA R5-4K (Photron, Japan) with the microfluidic system setup placed over an inverted microscope setup (Nikon Instruments Inc., Japan). Video microscopy is conducted in bright-field mode using both a 10x and 40x magnification air immersion objective lens. The experimental setup and sample measurements are presented in Figure 3.13.

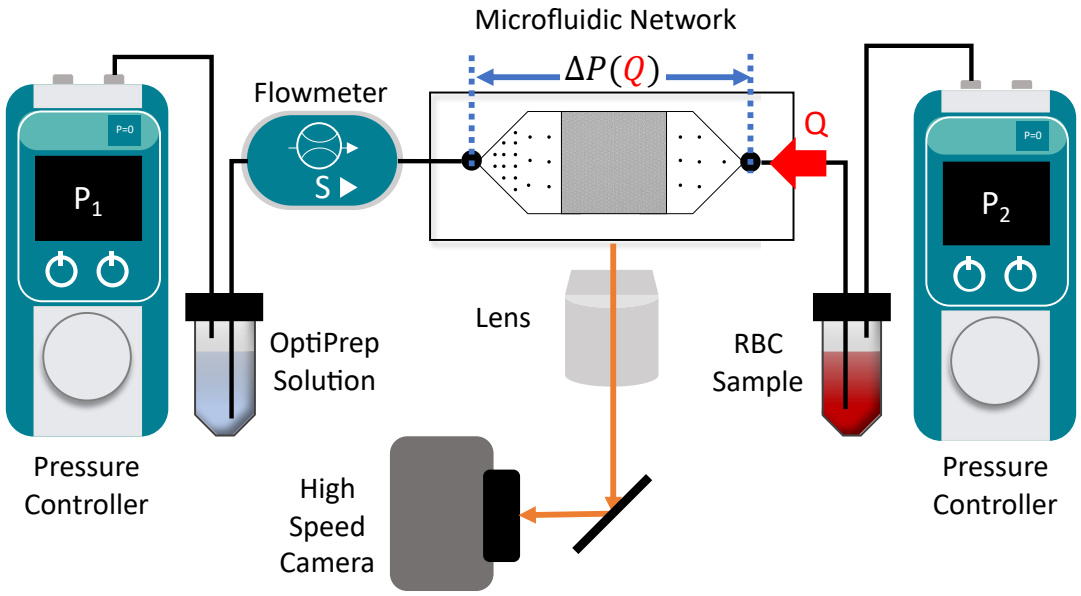


Figure 3.13: Schematic of PDMS microfluidic platform using pressure system and flow meter to drive fluid through the device while measuring with a high-speed camera.

Flow configuration

Measurements are first taken while flowing the suspending fluid through the network for an increasing and then decreasing ramp of pressures ranging from 10 mBar to 810 mBar, in increments of 50 mBar. Each pressure is held for approximately 10 s until the flow rate is stable. The suspending fluid is tested first to determine the hydrodynamic resistance of the network flowing a fluid of constant viscosity. Subsequently, the RBC sample is flowed in the reverse direction starting with a decreasing and then increasing ramp of pressures from 810 mBar to 60 mBar, in increments of 50 mBar. This sequence is completed twice; the first run is to ensure that the network reservoir is filled with the feeding RBC suspension and that there is minimal fluctuation in the bulk. For each pressure change, a video is taken of the passage of RBCs with the focus at the entrance of the microfluidic network at 10x magnification. The RBC flow is repeated the second time with the same pressure protocol to extract videos at the local scale with 40x magnification taken at the center of the network. It is assumed that the hydraulic resistance of the network measured from flowing the suspending fluid alone is the same between the different trials. The flow configuration of the typical suspending fluid and the RBCs are demonstrated in Figure 3.14 where the blue and orange curves represent the trace of the pressure and flow, respectively.

3.4.4 Analysis of Macroscopic Measurement

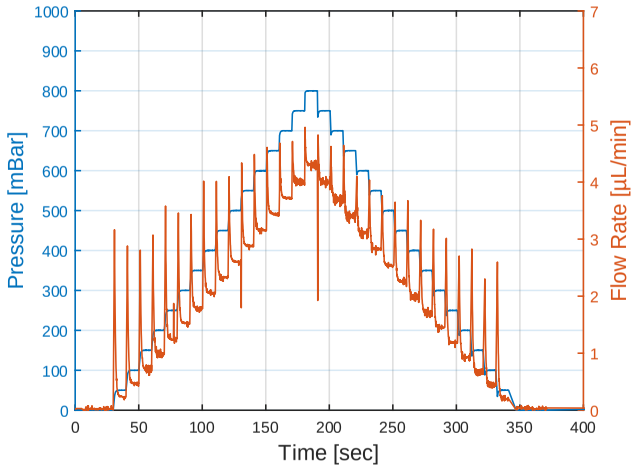
To analyze the macroscopic bulk flow measurement of the entire network, the mean flow rate at a given pressure is fitted to extract the settling flow rate, the hydraulic resistance R is calculated through the Q versus ΔP curves, and the excess relative resistance R_{exc} of the system is computed.

Settling flow rate

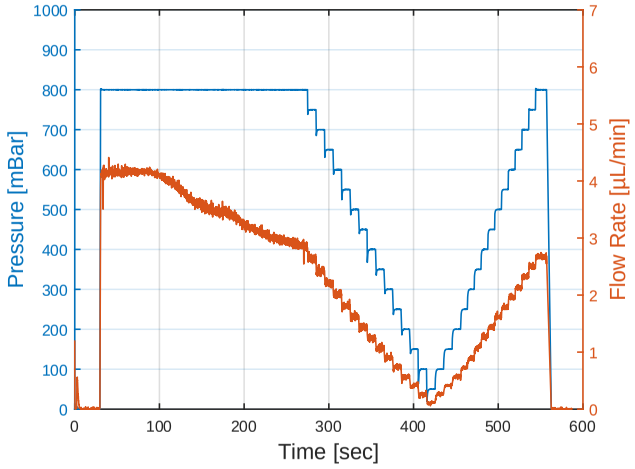
The PDMS microfluidic device is compliant and therefore there is a characteristic time for the flow rate to become steady. The flow response (Q) is modeled after a first-order system with a unit step pressure input which is modeled by:

$$Q(t) = Q_{SS} - Q_0 e^{t/\tau} \tag{3.5}$$

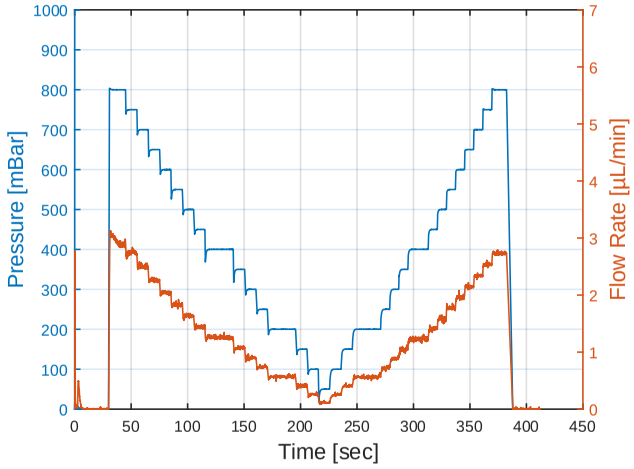
where Q_{SS} is the steady-state settling flow rate for the limiting case of $t \to \infty$, Q_0 is the starting flow rate, and τ is the system's characteristic settling time.



(a) PBS OptiPrep



(b) First RBC Run



(c) Second RBC Run

Figure 3.14: Example pressure and flow rate ramping direction for (a) the suspending fluid, and (b,c) the RBC suspension. Blue and orange curves represent the trace of the pressure and flow rate, respectively.

Hydraulic resistance

For a simple straight round channel, the hydraulic resistance (R) is well defined by the Hagen-Poiseuille equation:

$$Q = \left(\frac{\pi r^4}{8\eta l}\right)\Delta P = \frac{1}{R}\Delta P \tag{3.6}$$

where η is the fluid viscosity, l is the length of the channel, r is the radius of the channel, ΔP is the pressure drop, and Q is the flow rate. For a straight round channel, $R = \frac{8\eta L}{\pi r^4}$ and it can be extrapolated that R is dependent on the geometric properties of the channel itself and the viscosity of the fluid.

In practice, flow through a PDMS channel is not expected to be linear over the full range of applied pressure drops due to the material compliance. For elevated pressures, the channel cross-sectional area will increase, which will reduce the overall resistance. To deduce more precisely the hydrodynamic resistance, the deformability effect is included in the measurements by fitting a pressure drops-flow rate relationship with a second order polynomial model that passes through zero:

$$Q = A\Delta P^2 + B\Delta P. \tag{3.7}$$

The linear component (B) gives the resistance, while the second order term (A) includes non-linearity that is associated with channel deformation at the highest pressures. An example of the hydraulic resistance of the suspending fluid flowing through the network is represented in Figure 3.15. As a rule of thumb, the $\Delta P(Q)$ curves remain linear up to 500 mBar of pressure.

Excess relative hydraulic resistance

For simplicity, the following approach is presented using the well-known equations of Poiseuille flow in circular channels, but note that the reasoning is similar for the more complex network geometries. The relative hydraulic resistance (R_{rel}) is defined as the ratio of the resistance of the RBC suspension to the Newtonian suspending fluid.

$$R_{rel} = \frac{R_{RBC}}{R_{Opt}} = \frac{8\eta_{RBC} l}{\pi r^4}\frac{\pi r^4}{8\eta_{Opt} l}. \tag{3.8}$$

Assuming that the geometry of the channel changes minimally, the relative resistance approximately corresponds to the relative viscosity of the RBC suspension compared to

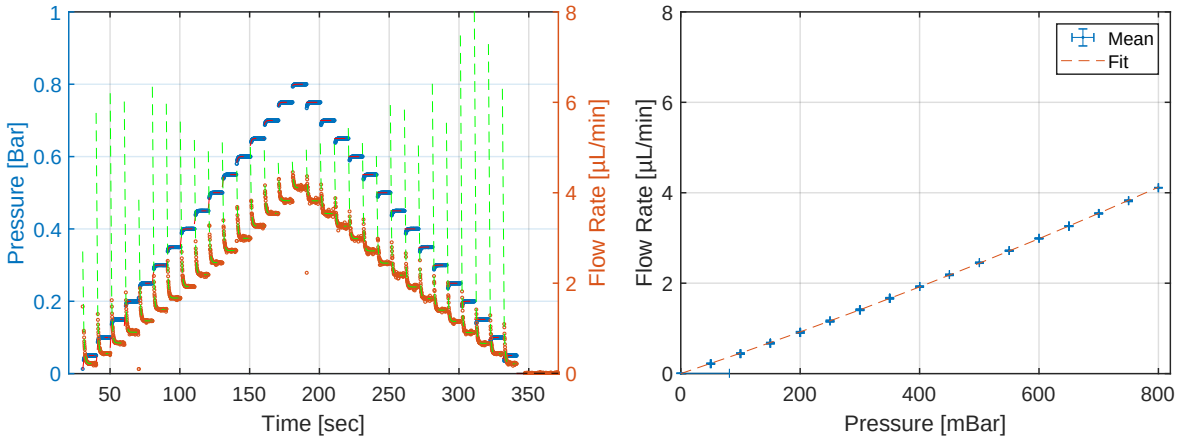


Figure 3.15: (Left) The settling flow rate is extracted using a first-order system approximation for each pressure and flow rate. Here, the blue points are the pressure measurement, the orange points are the flow rate measurement, the solid red line are fits for the settling pressure, and the dashed green line are the fit for the settling flow rate. (Right) The extracted settling flow rate as a function of settling pressure is fitted with a 2nd order polynomial indicated by a dashed red line. The error bars represents the 95% confidence interval of the fitted mean.

the Newtonian suspending fluid, $R_{RBC}/R_{Opt} = \eta_{RBC}/\eta_{Opt}$. It is a useful quantity allowing us to compare the different network channel designs as it accounts for their variation in the hydraulic resistance originating from manufacturing variations.

To compare the different experimental setups, the excess scaled relative hydraulic resistance (or excess relative resistance, R_{exc}, for short) is calculated as follows:

$$R_{exc} = \frac{R_{RBC}}{R_{Opt}} - 1 = \frac{\Delta P_{RBC}}{Q_{RBC}} \frac{Q_{Opt}}{\Delta P_{Opt}} - 1 = \frac{A\Delta P^2 + B\Delta P}{Q_{RBC}} - 1. \tag{3.9}$$

The excess relative resistance is analogous to the excess relative apparent viscosity. The excess relative apparent viscosity evaluated from the excess relative resistance is equal to the intrinsic viscosity times the hematocrit.

3.4.5 Analysis of High-Speed Video Microscopy

High-speed videos are analyzed to obtain the local hematocrit and the local dynamics of RBCs through the microfluidic network. This is completed by first identifying the channel, categorizing the channel sub-regions, detecting the cells, cell tracking, and morphological categorization. Image processing is completed using MATLAB 2019a with the Image Processing Toolbox.

Background and channel detection

The first step of the image processing is identifying the background image and the detection of the channels. The background image is achieved by taking the median gray-scale intensity value across all frames of the image sequence captured using the high-speed camera (see Figure 3.16 Median Filter). This process yields an image that represents a state of no cell flow and any potential deposition within the network as well as intensity gradients due to the illumination imperfections. The channel area is then defined in relation to the background image. To enhance the extraction of the channels, a Gaussian filter is applied to the background image and then a histogram equalization, with the objective of enhancing contrast. Subsequently, the image is binarized by thresholding with a threshold value derived from Otsu's method. Subsequently, small holes are filled, and objects with an area smaller than that of the network pillars are removed. The binary image is inverted, and the resulting image approximates the channel area (see Figure 3.16 Binarize-Registration). As this process is applied to the background image, it can be assumed that the detected channel area remains consistent throughout the duration of image acquisition.

The network is classified into two regions: the junction and the straight regions. Classification of the region is achieved by applying a skeleton process, using the MATLAB function "bwmorph" on the binary channel image and extracting the branch-point of the skeleton channel (see Figure 3.16 Skeletonize). The skeleton image is the result of removing the outermost pixels and, when applied to the binary channel image, results in a single pixel wide path that traces the center line of the channel. The joining and bifurcating junctions are identified as the branch-point of the skeleton channel, while the straight regions are the regions that are not the branch-points. Sample region labeling is identified for channels and junctions regions in the bottom row of Figure 3.16 for Channel 3 (1:3), 4 (1:0), and 6 (3:2). Regions are split by straights 0° and 45°, while junctions are classified by joining and bifurcations.

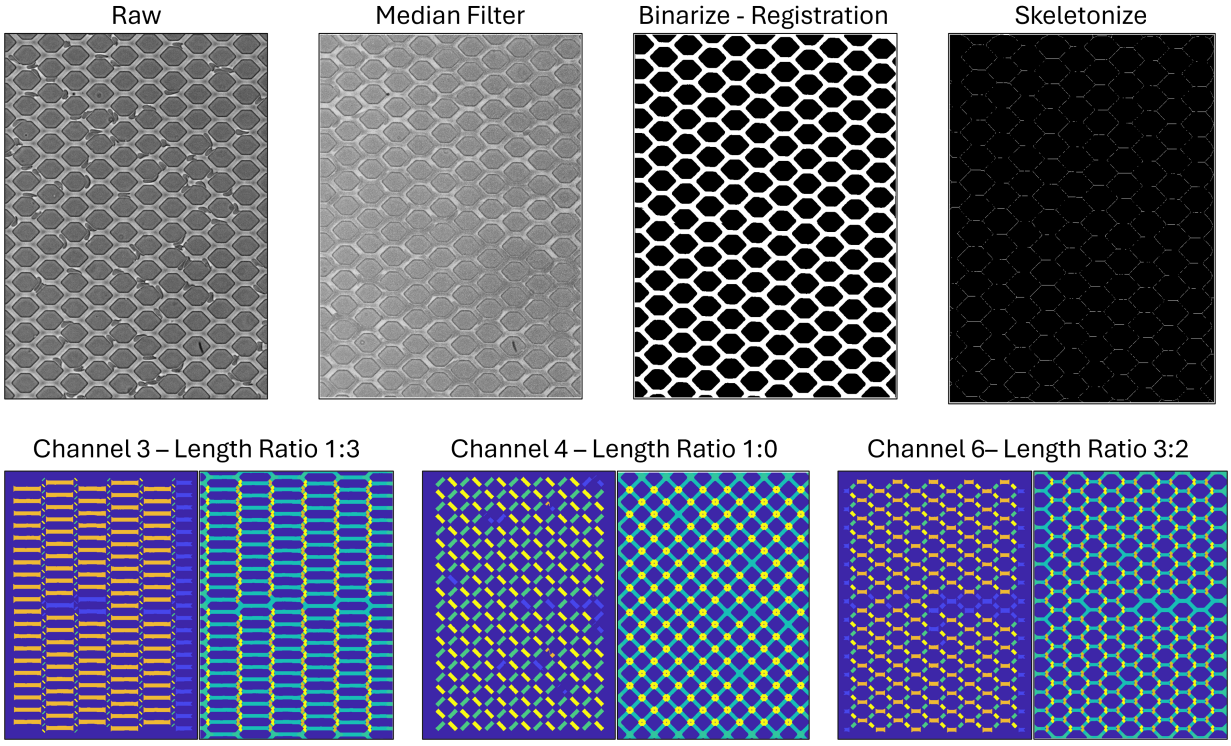


Figure 3.16: (Top row) General pipeline of channel detection from raw image sequence by median filtering, binarizing and skeletonizing for region detection. (Bottom row) Paired images represents the region labeling of Channel 3 (1:3), 4 (1:0), and 6 (3:2) for straight channels (left) and junctions (right). The left of the image pairs represents the regions split by straight aligned (orange) and straight 45 degrees (yellow and green). The right of the image pairs are split by bifurcations (yellow) and joining junctions (orange). Light blue regions are omitted areas that are filtered out from processing.

Cell detection

The process of cell detection is analogous to that of channel detection, but with the additional step of filtering out the network pillars. For each frame, the background image, which contains the pillars, is subtracted. To enhance the cell edge, the image is pre-processed by applying a Laplacian of Gaussian filter, which enhances the edge. The image is then binarized by thresholding the image with a fixed threshold value. The binarized images are then filled for holes, masked with the channel binary image, and small areas are removed. The binary label property of each cell object is extracted, such as the cell area, centroid, and sphericity. The local hematocrit (ϕ) approximation is then simply the ratio of total cell area over total channel area.

$$\phi \propto \frac{A_{totalcell}}{A_{channel}} \tag{3.10}$$

The calibration of the relationship between the local measured hematocrit and the feeding hematocrit is represented in Figure A.24 found in Appendix A.8. The local projected hematocrit is found to be greater than the nominal feeding hematocrit. This overestimation is expected to be primarily due to a projection error; however, secondary factors such as heterogeneity of the network, location and size of the region of interest, and quality of imaging can also affect the accuracy of estimating the local projected hematocrit.

Cell tracking

Cell tracking is achieved by applying Kalman filtering [75] and the Hungarian algorithm [76] on the high-speed imaging of the cell passage. The Kalman filter is a linear quadratic estimation algorithm that employs a series of measurements of the binary image over time to determine the most probable future state, which is then refined based on the noisy measurements of the future time step [75, 77]. Subsequently, the prediction is matched to the most probable object, thereby ensuring that the same object is tracked throughout the video acquisition process. This is achieved through the use of the Hungarian algorithm [76]. The initial implementation of cell tracking was conducted in MATLAB; however, it was subsequently transferred to TrackMate [78], a plugin on Fiji, as the primary platform for completion.

With the individual cells tracked, the local cell speed can be approximated. The relative displacement of the centroids is calculated:

$$|V| = \sqrt{(x_t - x_{t-1})^2 + (y_t - y_{t-1})^2} \tag{3.11}$$

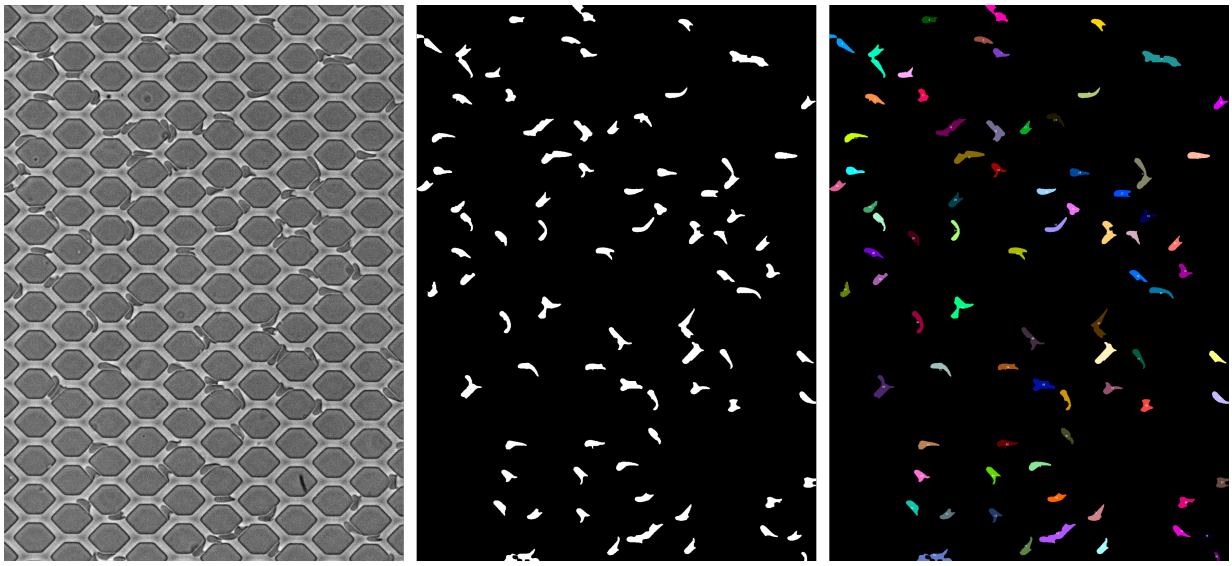


Figure 3.17: Example of local hematocrit approximation. Raw images (left) are binarized (middle) and individual cells are labeled (right). Binary parameters such as area, eccentricity, and major minor axis are extracted. Projected hematocrit is then the ratio of total cell area to total channel area from channel mask determined from channel detection.

where x and y are the centroid positions at time t and $t-1$. The speed of the cell is then the relative displacement per frame.

Cell morphology

The cell morphology present in the network is first described in general terms. Parameters such as the cell's eccentricity, circularity, size, major and minor length are characterized for each channel and flow rate. The secondary process implemented is the classification of the cells' morphology based off the binary image properties to auto sort them into the categories of slippers, parachute, bumping, and unclassified. Slippers are characterized by their elongated asymmetric shape with their center of mass away from the centerline of the channel, while parachutes are more symmetrical in their flow along straight channels. The case of bumping is for cells that have entered the joining bifurcation region of a channel and linger at the junction corner. Lastly, unclassified cells are cells that have clustered, forming long trains of cells and poorly segmented cells. Example schematic, raw imaging and outlined cells are presented in Figure 3.18. To classify the cells' morphology, a support

vector machine[4] classification model is developed using the MATLAB 2019a classification learning plugin [79]. This is accomplished by manually labeling cells with a GUI pipeline that randomly selects an assortment of binarized images of RBC which are then hand categorized to develop a base database. Once a thousand samples of each category were identified, the model was applied to the rest of the set of images, which is primarily due to variations in the quality of images that result in variation in the parameters of the binary images of the cells.

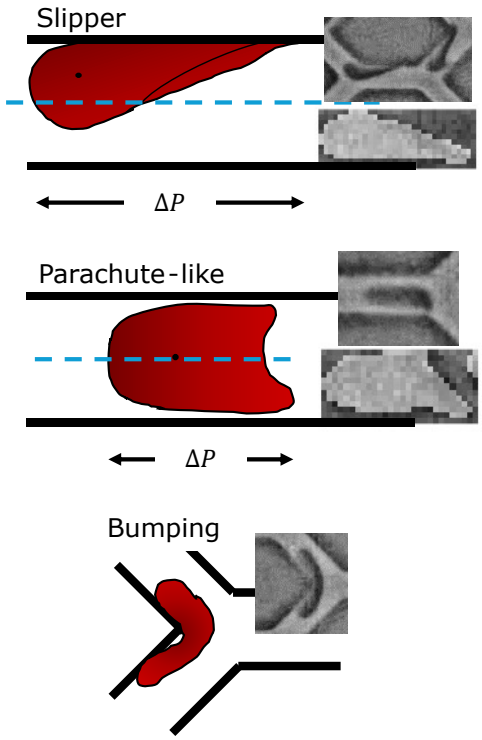


Figure 3.18: Examples of observed cell morphologies in the network. Three broad groups are categorized by (left) an asymmetric slipper-like cell, (center) an axisymmetric parachute-like cell, and (right) a bumping morphology where cells are stretched at the bifurcation and lingering.

[4]Support vector machine classification model is a machine learning algorithm that classifies data into different labels by finding an optimal line or hyperplane to maximize the separation between each classification.

3.5 Results

3.5.1 Verification of Macroscopic Responses

The initial set of results is centered on the observations regarding the macroscopic responses of the Newtonian suspending fluid and RBC suspensions flowing through the network. The nuances of the measurements are described in detail, including the non-linearity of the pressure and flow curve due to the compliance of PDMS at high pressure. The initial stabilization of the hematocrit in the network and clogging are discussed.

Flow of the Newtonian fluid through the network

As previously outlined in Section 3.4.3, the suspending fluid was first flowed into the network to determine the hydrodynamic resistance of the network for a Newtonian fluid. The flow rate as a function of pressure curve of the suspending fluid is presented in Figure 3.19 for Channel 3 (1:3). This figure depicts the results of experiments completed using this network geometry, with the average second-order polynomial fit and average linear fit presented as a solid black line and a dashed red line, respectively. In the pressure-flow rate curve, a non-linearity is observed while flowing the suspending fluid alone at pressures greater than 500 mBar.

Figure 3.20 is the compilation of the flow rate as a function of pressure measurements of the different network geometries for experiments completed prior to flowing the RBC suspensions. Each experiment is conducted on distinct manufactured PDMS microchannels with experiments spanning several months. The solid black line in Figure 3.20 represents the averaging of the suspending fluid pressure and flow rate polynomial curve fit, in which the average and standard deviation of the polynomial coefficients ($Q = A\Delta P^2 + B\Delta P$) are tabulated in Table 3.4. Experiments are primarily focused on measurements completed in network geometries with length ratios of 1:3, 1:0, and 3:2. Additionally, preliminary testing was conducted in network geometries with length ratios of 1:2, 1:1, and 2:1, though these results are not represented in the following analysis as there are few experiments completed and lacking measurements with the same blood samples. From the ensemble of tested networks, the difference in the linear region between the different network topologies is on average similar and within acceptable variability when accounting for manufacturing variance.

One network of note with greater variance than the other length ratio designs is Channel 4 (1:0). Dividing the network into four subgroups (denoted 4 A, 4 A bis, 4 B, and 4 B bis)

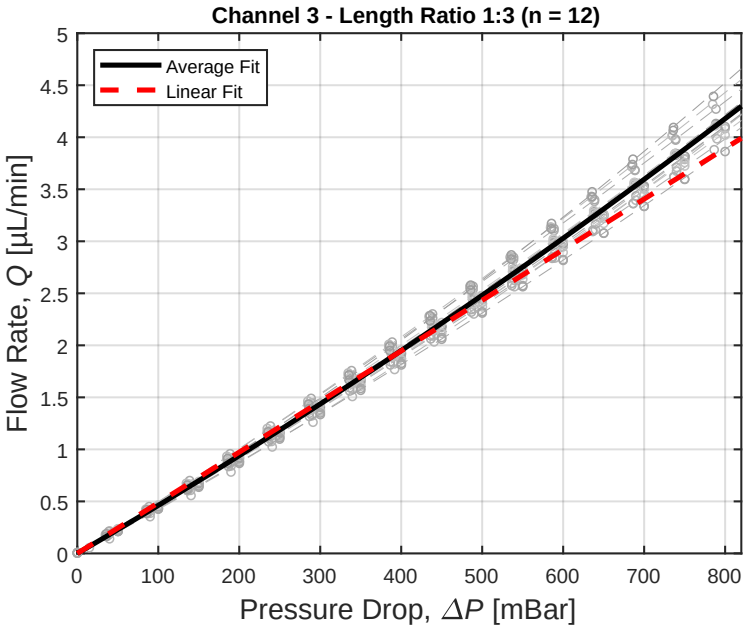


Figure 3.19: Newtonian, suspending fluid average flow rate and pressure curves for network length ratio of 1:3 (Channel 3) of the 2nd order polynomial fit in solid black line and the linear fit in dashed red line.

Table 3.4: Average and standard deviation of second order polynomial fits of different network geometries, the experimental equivalent resistance and theoretical equivalent height. (Corresponding to Figure 3.20)

Channel	1	2	3	4	5	6
Length Ratio	1:2	1:1	1:3	1:0	2:1	3:2
A $*(10^6)$	0.72 (0.17)	0.91 (0.19)	0.87 (0.23)	1.0 (0.31)	1.54 (0.35)	0.99 (0.42)
B $*(10^3)$	4.6 (0.23)	5.03 (0.51)	4.53 (0.24)	4.89 (0.34)	4.04 (0.67)	4.39 (0.35)
n	7	3	12	13	2	11
R_{eq}	1.29 (0.04)	1.18 (0.09)	1.31 (0.04)	1.22 (0.06)	1.47 (0.11)	1.36 (0.06)
h (µm)	5.25	5.39	5.23	5.34	5.17	5.21

Mean Coefficient (Standard Deviation), A [µL/min(mBar)^2], B [µL/min(mBar)], R_{eq} [mPas/µm^3]

by different SU8 master wafers (A and B) and network pairs (non-bis and bis), differences in hydrodynamic resistance were observed. The subgroups are depicted in Figure 3.21 and the polynomial fitting parameters tabulated in Table 3.5. The network equivalent hydraulic resistance from the linear portion of the polynomial fit and the approximate height of the network derived from the equivalent hydraulic resistance are also presented in the Table 3.5. Large variance in the network resistance is observed from sub-micrometer changes in the theoretical height of the channel, which results in large variance in pressure-flow rate dynamics at high pressure gradients.

Flow of the RBC suspension through the network

In contrast, the flow sequence of the RBC suspension is completed in reverse of the suspending fluid alone, beginning with a high pressure to bring the cells as fast as possible into the network until a stationary local hematocrit is reached. Figure 3.22 depicts the pressure and flow rate curves as a function of time for a typical experiment, illustrating the first and second sequences with the resulting mean pressure and mean flow rate curves. The mean pressure and mean flow rate curves are separated into the direction of the ramp, with downward triangles representing the decreasing ramp and upward triangles representing the increasing ramp in pressures. The displayed fit is of the total sequence, presented as a dashed line with a matched color.

Flowing the blood sample twice through the same microfluidic chip does not significantly alter the pressure-flow rate curve, apart from the high-pressure segment of the decreasing ramp during the first run. This discrepancy is most likely associated with the

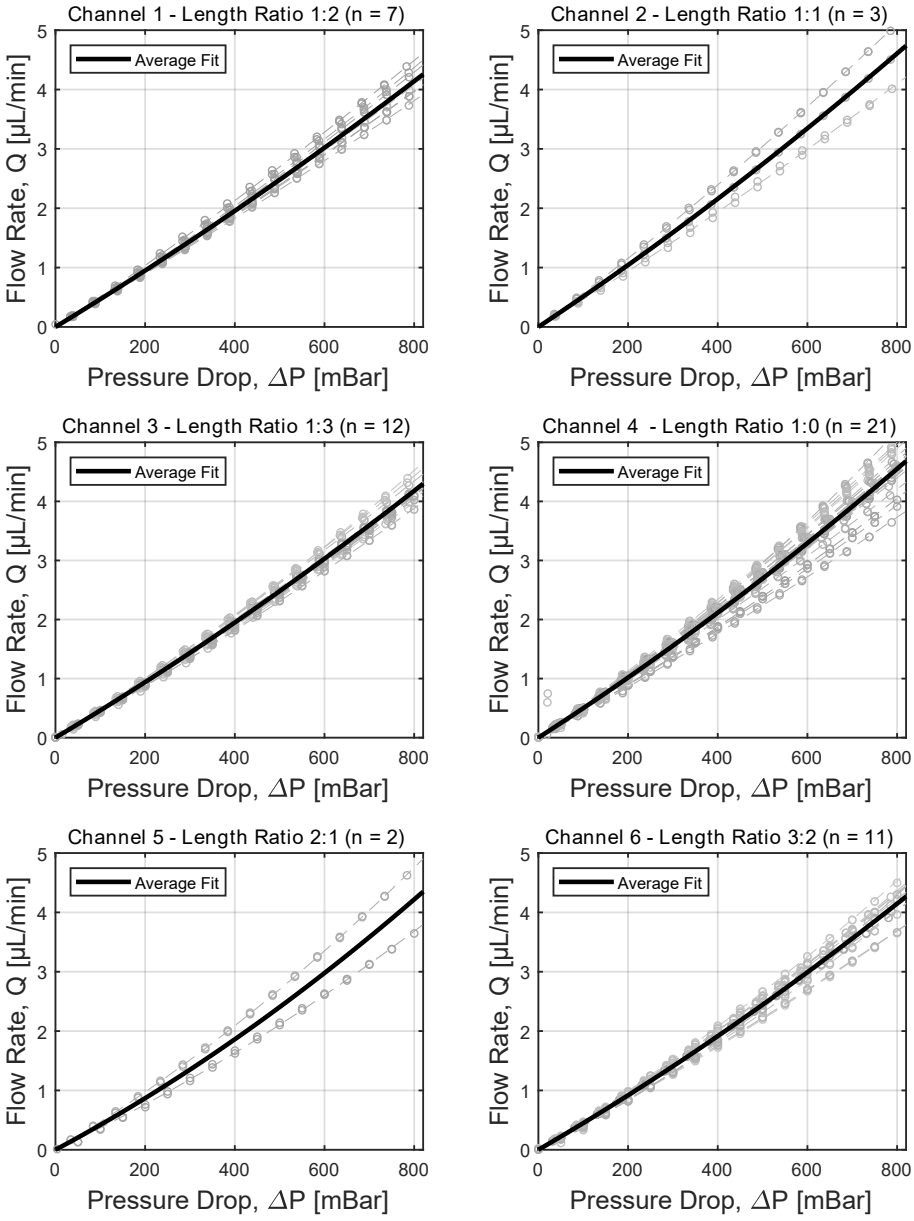


Figure 3.20: Measurement of pressure and flow rate of the suspending fluid indicated by open circle and their associated second order polynomial fit in dashed line for network length ratio of 1:2, 1:3, 1:0 and 3:2. The solid black line is the average of the polynomial fit of all tests.

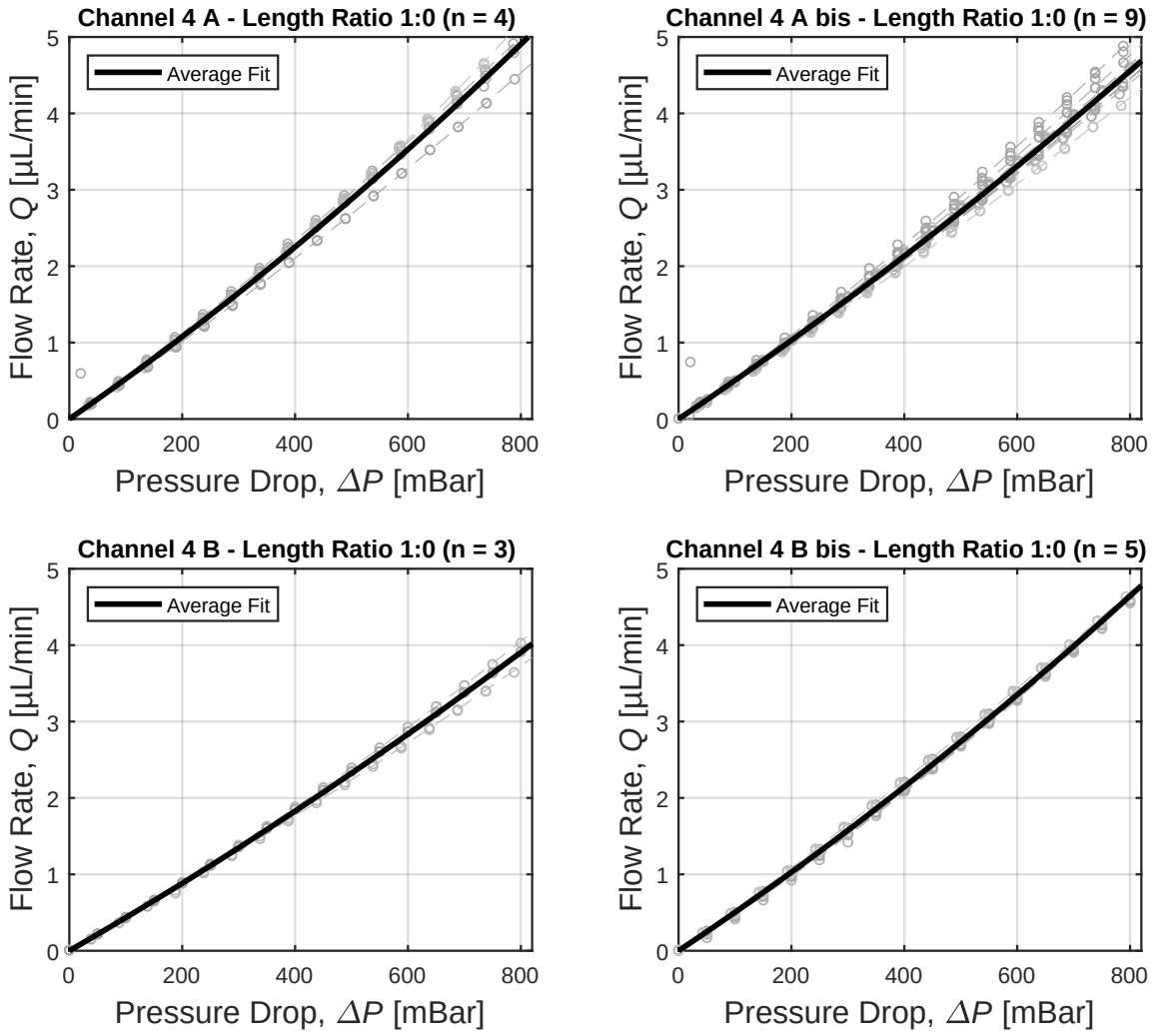


Figure 3.21: Measurement of pressure and flow rate of the suspending fluid indicated by open circle and their associated second order polynomial fit in dashed line for network length ratio 1:0 grouped by wafer (A and B) and secondary network. The overlaying solid black line is the average of the fit of all tests.

Table 3.5: Average and standard deviation of second order polynomial fits of Channel 4 split by subgroup of wafer (A, B) and network pair, the experimental equivalent resistance and theoretical equivalent height. (Corresponding to Figure 3.21)

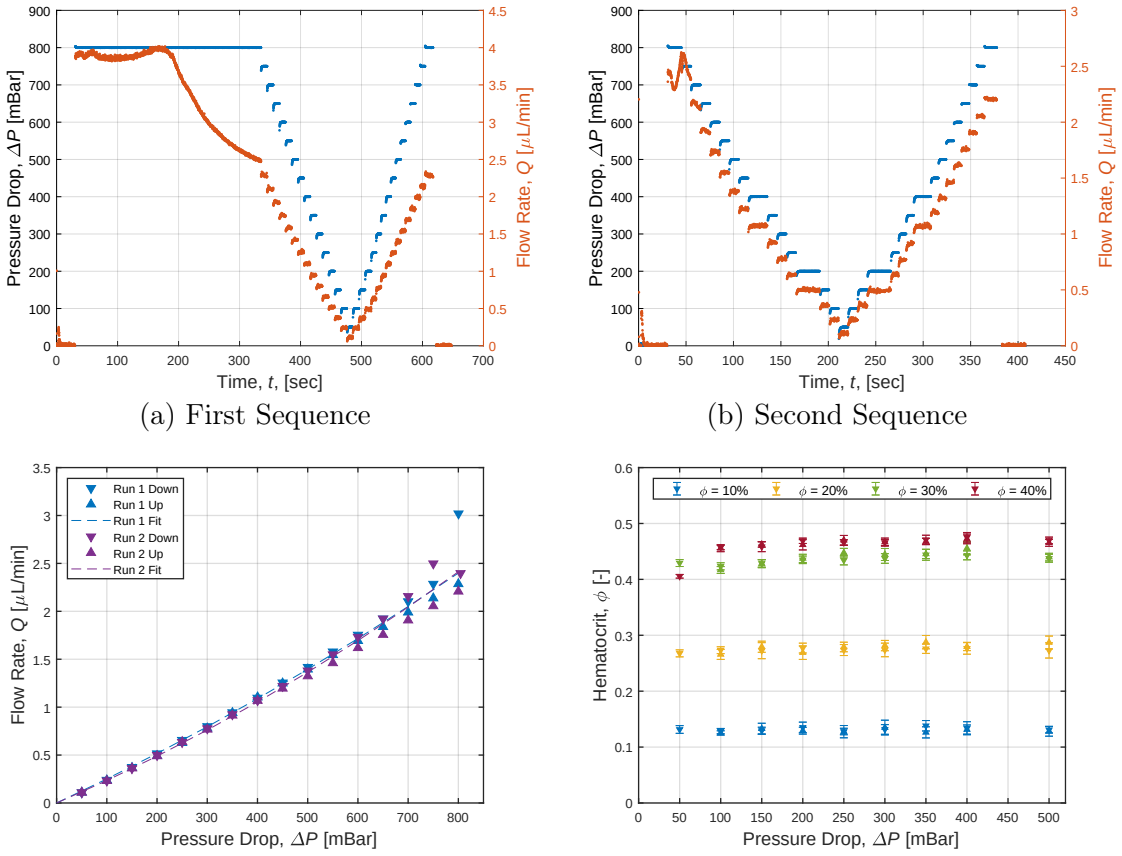
Channel	4 A	4 A bis	4 B	4 B bis
Length Ratio	1:0	1:0	1:0	1:0
A $*(10^6)$	1.24 (0.47)	0.91 (0.16)	0.78 (0.15)	1.10 (0.36)
B $*(10^3)$	5.13 (0.27)	4.97 (0.16)	4.26 (0.09)	4.92 (0.31)
n	4	9	3	5
R_{eq}	1.16 (0.05)	1.2 (0.03)	1.4 (0.02)	1.21 (0.05)
h (µm)	5.41	5.36	5.16	5.35

Mean Coefficient (Standard Deviation), A [µL/min(mBar)^2], B [µL/min(mBar)], R_{eq} [mPas/µm^3]

initial introduction of cells into the network, where a decrease in flow rate towards a plateau is observed.

It is also important to consider the possibility of local clogging occurring over the course of the experiment. Figure 3.23 depicts the standard deviation of background-subtracted images taken at 10x magnification at the entrance of the network for the decreasing and increasing ramps at 800 mBar, 400 mBar, and 100 mBar during the first sequence for the matching experiment of Figure 3.22. The number of frames is matched for the characteristic distance for cells to traverse the network and is scaled by the mean flow rate through the network. For this example of Channel 3 (1:3), the flow rate decreases from 2.25 µL/min, 1.00 µL/min and 0.25 µL/min which requires 10 frames, 25 frames, and 100 frames, respectively.

Localized transitory clogging within the network is evidenced by the appearance of dark channels, indicating regions where no cells have passed. Qualitative observations suggest that the number of dark channels increases between the initial downward ramp and the upward ramp at the same pressure. Additionally, lower pressure gradients lead to more void channels, underscoring the sensitivity of clog formation to pressure drop.



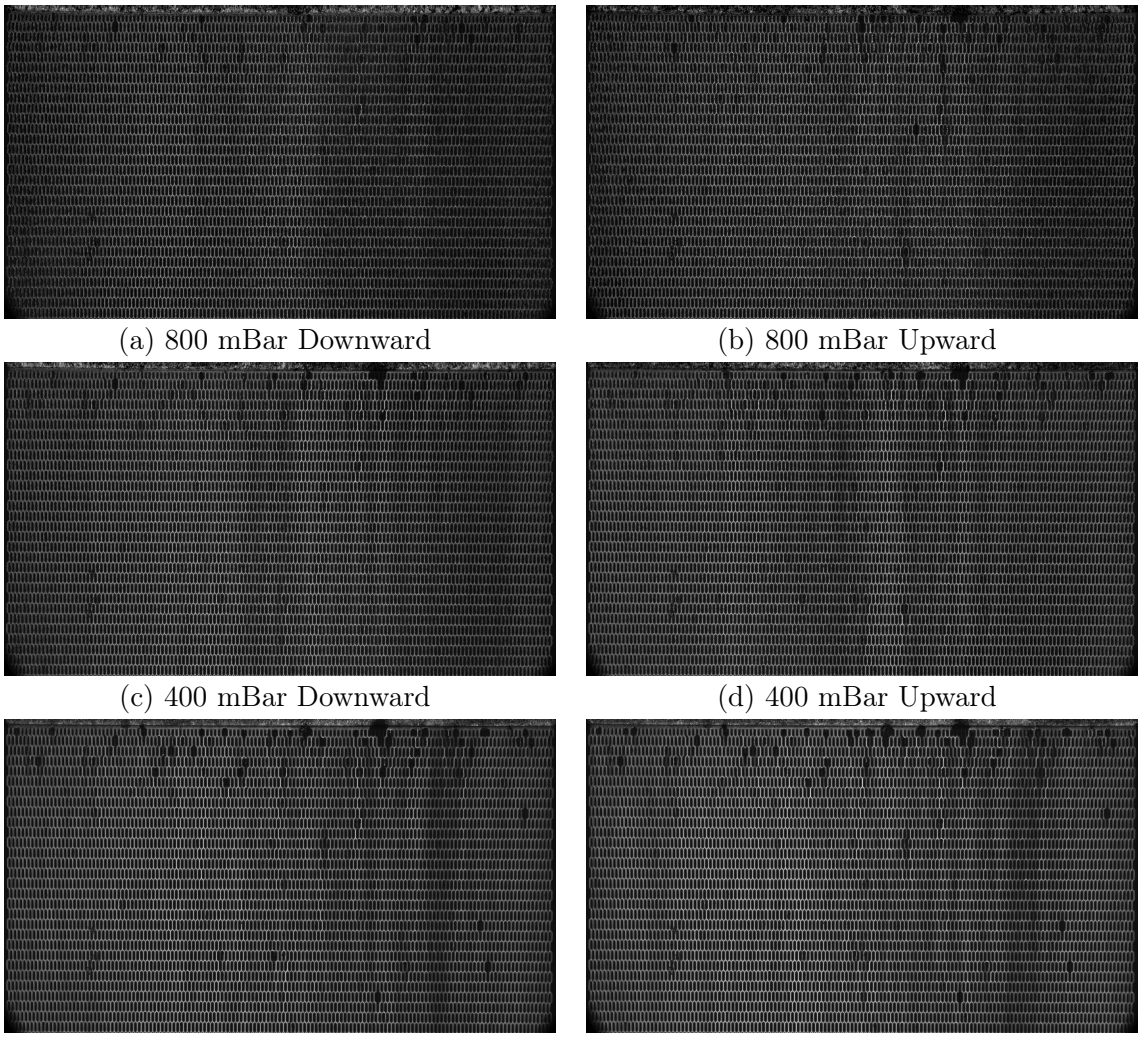
(a) First Sequence

(b) Second Sequence

(c) Mean Flow Rate vs Pressure

(d) Hematocrit vs Pressure

Figure 3.22: (a-c) Example first and second sequence of the RBC suspension completed sequentially and the resulting average flow rate as a function of pressure for a 30% hematocrit sample through a 1:3 length ratio network. Blue data points represent the pressure while orange data points represent the flow rate. (d) The projected hematocrit extracted from the local 40x magnification imaging of the RBCs passage as a function of the pressure drop of different nominal feeding hematocrit.



(a) 800 mBar Downward (b) 800 mBar Upward

(c) 400 mBar Downward (d) 400 mBar Upward

(e) 100 mBar Downward (f) 100 mBar Upward

Figure 3.23: Standard deviation image of background subtracted images using 10, 25, and 100 frames taken for 800 mBar, 400 mBar and 100 mBar pressure measurements, respectively. Darkened regions indicate areas that lack the passage of cells. In these images, flow is entering from the top. Downward indicates measurements taken during the down ramp from 800 mBar to 100 mBar, while upward indicates measurements taken during the up ramp from 100 mBar to 800 mBar.

3.5.2 RBC Suspension

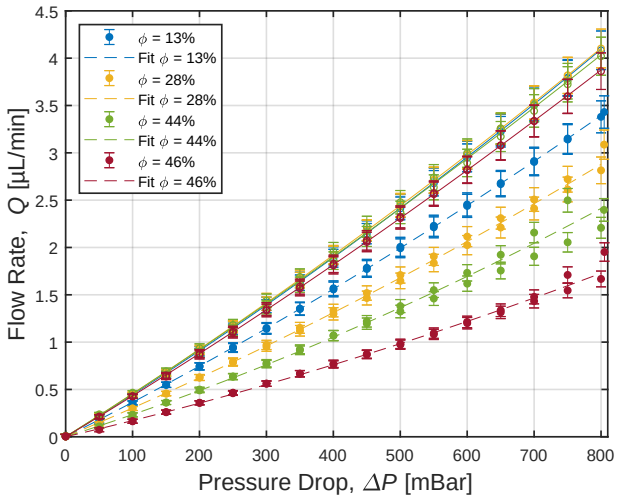
With the general understanding of the dynamics of flowing both the Newtonian fluid and the RBC suspension in the network system, the normalization of the pressure-flow curve is presented and a scaling law of the RBC suspension transport is proposed. The effects of increased hematocrit of healthy untreated RBC suspension through different uniform networks are explored and comparisons are made between our measurements and those found in the literature.

Healthy untreated RBC flow

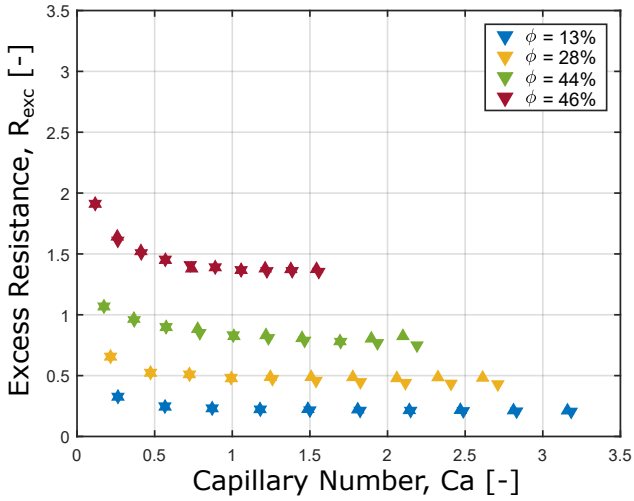
Data for healthy RBC suspensions in PBS and OptiPrep, shown in Figure 3.24(a), illustrate how feeding hematocrit affects flow rate curves in Channel 3 (1:3). Steady-state flow rates are plotted against the applied pressure drop for nominal feeding hematocrits of 10% to 40%. Each data point indicates the mean flow rate, with a 5% measurement uncertainty from the flow meter. Open markers represent the Newtonian suspending fluid, while filled markers depict the RBC suspension; dashed lines show second-order polynomial fits. All experiments were conducted on the same day using the same blood sample to minimize biological variability, with serial dilution reducing the volume fraction from 40% down to 10%.

To compare and contrast the experimental flow rate curves, the data are rescaled as excess relative resistance (R_{exc}). Determining this scaling requires understanding RBC deformation dynamics, quantified by the Capillary number (Ca), which balances viscous drag and in-plane elastic forces. Ca is defined as $\eta V/G_s$, where η is approximately 1.77 mPa s the viscosity of the suspending fluid, V is the mean convective velocity, and G_s is approximated to be 5.5 µN/m the membrane surface shear modulus of an average RBC [62]. The pressure-flow curves from Figure 3.24(a) are re-plotted as excess relative resistance versus the Capillary number in Figure 3.24(b).

Two key findings emerge: the first, flow rate at a given pressure decreases with increasing hematocrit, and the second, the pressure-flow rate relationship becomes non-linear at higher pressures. Upon rescaling the pressure–flow rate curves, an expected "squeezing" of the x-axis is observed, since higher-hematocrit samples exhibit slower flow rates than low-hematocrit samples. Consistent with the original curves, non-linear behavior in the excess relative resistance emerges with decreasing Ca, growing more pronounced at higher hematocrit levels. As shown in Figure 3.24(b), two regimes appear: for low Ca, R_{exc} decreases sharply, while for $Ca \gtrsim 1$, the drop in resistance begins to level off and may even reach a plateau.



(a) Steady state flow rate



(b) Scaled relative resistance

Figure 3.24: (a) Steady state flow rate for given pressure drop depicting increasing measured projected hematocrit (ϕ) in Channel 3 (1:3). Second order polynomials are fitted to pressure vs flow data for suspending fluid marked with open marker and solid line and RBC suspension with closed marker with dashed lines of matched color scheme. (b) The flow rate and pressure drop is rescaled as the excess relative resistance as a function of Capillary number. The direction of the triangles represent the directionality of the measurement, i.e. downward triangles represent a measurement during the downward ramp.

Proposal of a scaling law for the transport properties of the networks.

A natural question that arises from observing the excess relative resistance as a function of the Capillary number is whether the dynamics of the RBCs through the network can be normalized. Plotting R_{exc} versus Ca in log-log seems to present linear regions indicative of a power-law behavior, as shown in Figure 3.25 for Channel 3 (1:3), 4 (1:0), and 6 (3:2) and for nominal feeding hematocrits between 10 to 40% and from several different blood samples. The experiments completed using the same blood sample are matched by marker shape in all the subplots, while the color gradient of the markers represents the local projected hematocrit measured from the local high-speed microscopy imaging. Experiments that do not exhibit any discernible clogging, fiber, or debris in the microfluidic network are deemed suitable for inclusion.

A first observation that can be made is the relationship of the hematocrit with the magnitude of the excess relative resistance, which is represented by the shift in the y-axis in Figure 3.25. We propose here a first approach with a simple power-law with the Capillary number and parameters depending on the hematocrit (ϕ) as a first approach, with the following general form:

$$R_{exc} \sim f(\phi, \varrho) Ca^{-\alpha(\phi)}, \tag{3.12}$$

where f is the excess relative resistance magnitude, and α is the power-law exponent representing the stiffness of the resistance decrease with the Ca. The f could also be dependent on geometric parameters of the network itself such as the porosity (ϱ) or tortuosity (T).

The R_{exc} versus Ca are then fitted with the proposed power-law over the solid markers which represent the regime of low Capillary number, and the resulting parameters are extracted and plotted against the measured local projected hematocrit in Figure 3.26. These parameters themselves can be fitted by a simple law. For instance, a quadratic function in the form of $f(\phi, \varrho, c_1, c_2) = \phi(\varrho c_1 \phi + c_2)$ is to be used, where c_1 and c_2 are two constants. This model captures the effect where when $\phi \to 0$, the R_{exc} scales at approximately $c_2\phi$. In contrast, the power-law exponent itself is fitted with a power-law model in the form of $\alpha(\phi, a_1, a_2) = a_1\phi^{-a_2}$, where a_1 and a_2 are other constant parameters. The fits are tabulated in Table 3.6 and Table 3.7.

Note that the function f scales linearly with ϕ at low volume fraction, and the deviation from linear behavior is stronger for one type of channels compared to the two others, the main difference between them being their porosity.

The regime of high Ca is treated identically, and the parameters of the fit are shown in Figure 3.27. The experiments completed using the same samples are matched by marker

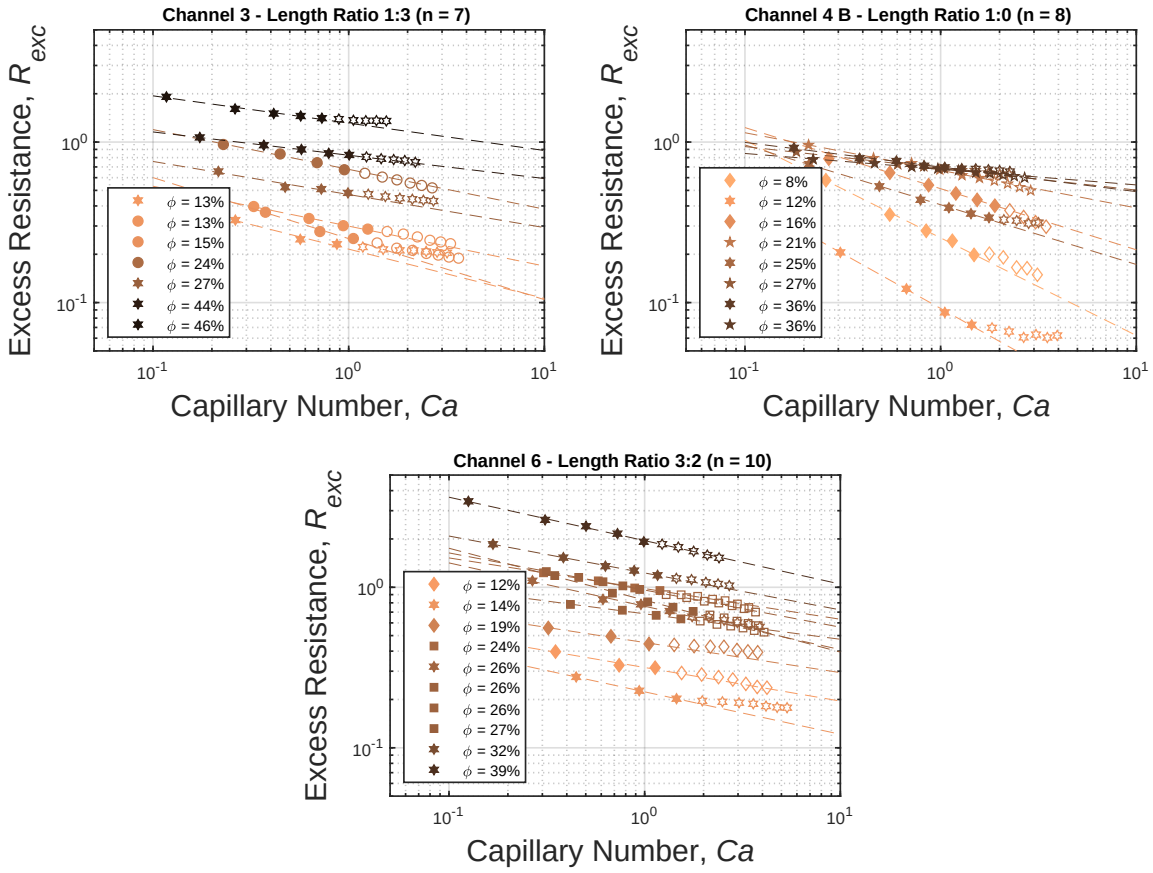


Figure 3.25: Excess relative resistance of healthy untreated RBCs as a function of Capillary number. Results are organized by network with length ratio 1:3, 1:0, and 3:2 during downward ramp scaled in log-log. Matched markers represent the same blood sample between channels and the color gradient is representative of the measured local projected hematocrit (ϕ). A power-law fit represented by dashed line is completed over solid markers representing the decay in the low capillary region, while the open markers are the high capillary region.

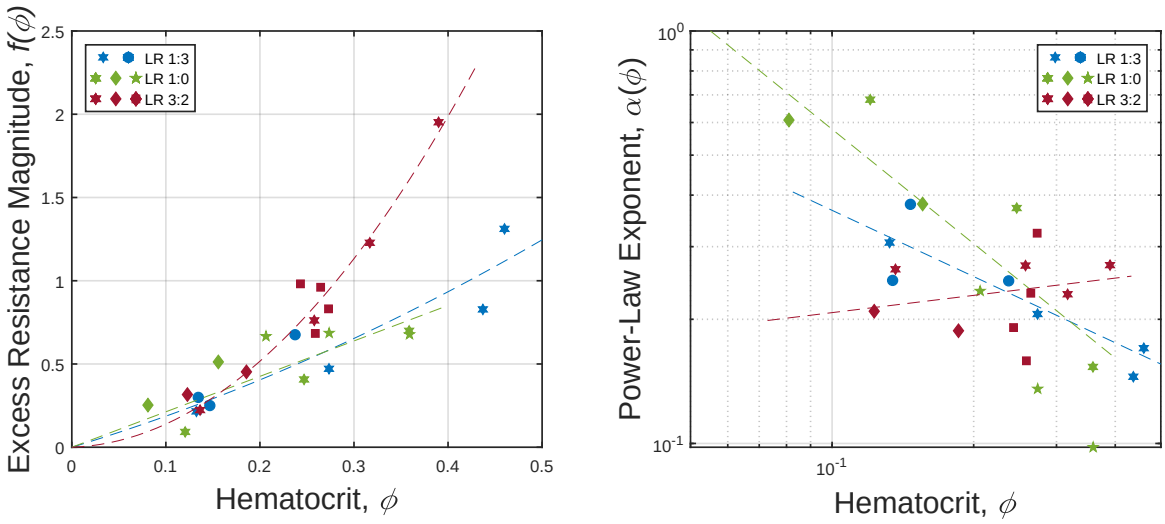
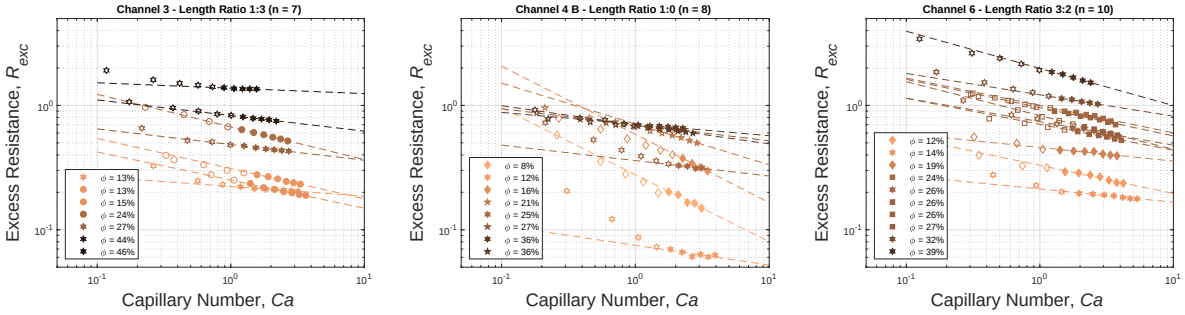


Figure 3.26: Extracted fitting parameter of power-law fits (left) excess resistance magnitude and (right) power-law exponent. Matched markers represent the same blood sample between channels and matched with Figure 3.25. LR is the length ratio of the network design.

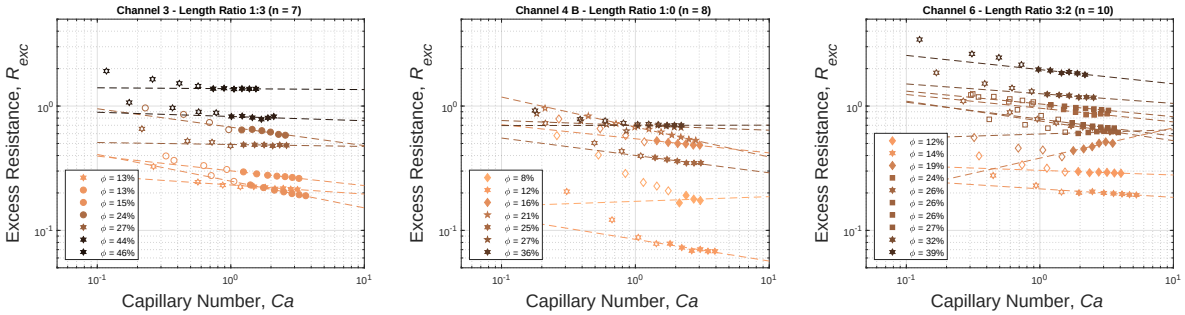
shape, with the gradient of the markers representing the hematocrit. The extracted fitting parameters are then plotted against the local projected hematocrit in Figure 3.28. Comparatively to the low Ca regime, the R_{exc} as a function of Ca is found to have a similar excess relative resistance magnitude but a decrease in the power-law exponent.

Table 3.6: Fitting Parameters ($f(\phi, \varrho, c_1, c_2) = \phi(\varrho c_1 \phi + c_2)$) of Excess Relative Resistance Magnitude

		Low Ca			High Ca Down			High Ca Up		
LR	Porosity (ϱ)	c_1	c_2	R^2	c_1	c_2	R^2	c_1	c_2	R^2
1:3	0.467	3.29	1.70	0.82	3.29	1.69	0.8	3.70	1.71	0.80
1:0	0.497	0	2.12	0.44	0	2.18	0.35	0	2.24	0.52
3:2	0.449	26.57	0.20	0.93	26.57	0.13	0.93	28.06	0	0.91



(a) Downward ramp

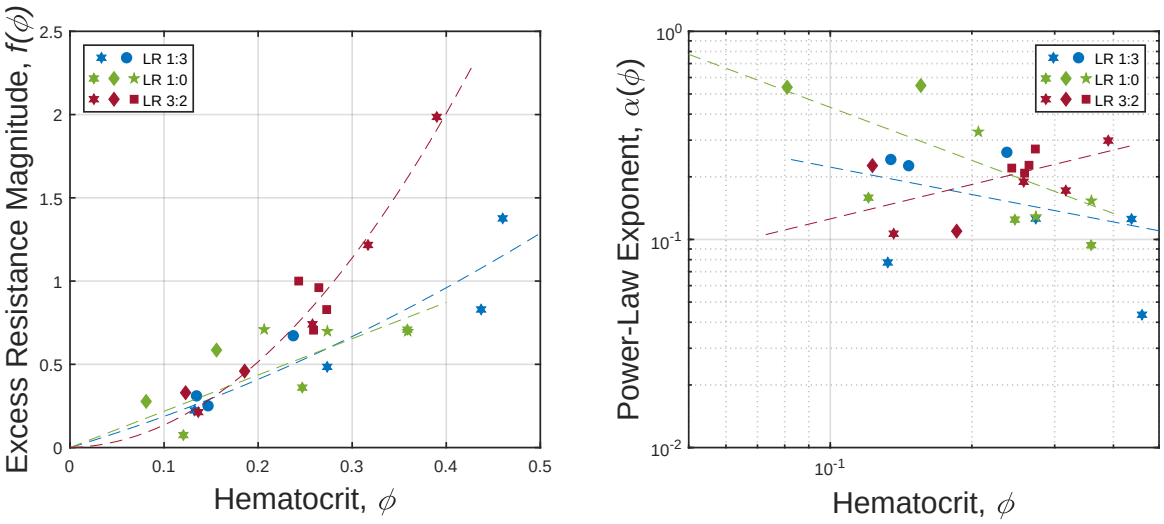


(b) Upward ramp

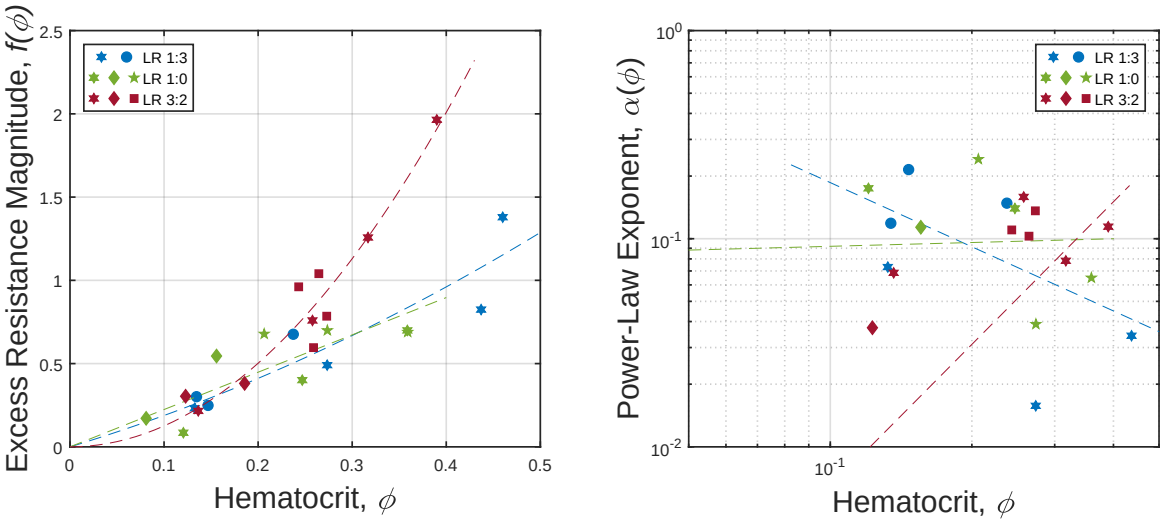
Figure 3.27: Relative resistance of healthy untreated RBC in network with length ratio 1:3, 1:0 and 3:2 during downward ramp upward ramp in high capillary regime. Matched markers represent the same blood sample between channels and the color gradient is representative of the projected hematocrit. A power-law fit is completed over solid markers representing the high capillary regime, while the open markers are the low capillary region.

Table 3.7: Fitting Parameters ($\alpha(\phi, a_1, a_2) = a_1\phi^{-a_2}$) of Power-law Exponent

		Low Ca			High Ca Down			High Ca Up		
LR	Porosity (ϱ)	a_1	a_2	R^2	a_1	a_2	R^2	a_1	a_2	R^2
1:3	0.467	0.11	0.53	0.70	0.08	0.44	0.20	0.02	1.02	0.40
1:0	0.497	0.07	0.92	0.76	0.06	0.85	0.49	0.11	-0.06	0
3:2	0.449	0.29	0.14	0.05	0.45	-0.55	0.34	1.21	-2.28	0.14



(a) Downward Ramp Fitting Parameter



(b) Upward Ramp Fitting Parameter

Figure 3.28: Power Law fitting parameter of healthy untreated RBCs in network with length ratio 1:3, 1:0 and 3:2 during downward ramp upward ramp in high capillary regime. Matched markers represent the same blood sample between channels and matched with Figure 3.27. LR is the length ratio of the network design.

3.5.3 Role of RBC Local Dynamics

In the following section, the local transport characteristics of the cells through the network are presented, such as the velocity distribution, cell cluster size, and morphology.

Velocity field comparison

Given the different network topologies, differences in the cell velocity are expected. Normalized velocity histograms of Channel 3 (1:3), 4 (1:0), and 6 (3:2) are presented in Figure 3.29 at a pressure of 50 mBar, separated by the region in the network. The normalized velocity is determined as the ratio of the cell velocity to the mean convective velocity through the network at the given imposed pressure. Examples of measured projected hematocrit of 13% and 28% are presented for Channel 3 (1:3) to observe the effect of increasing hematocrit, while 12% and 13% hematocrit examples are presented for Channel 4 (1:0) and 6 (3:2), respectively.

Comparing the velocity histogram across two projected hematocrits, a broadening of the velocity distribution is found with increasing hematocrit in the network. Analysis of velocity histograms across different geometries indicates that Channels 3 (1:3) and 6 (3:2) exhibit two distinct cell speed distributions depending on whether they are aligned with the flow (0°) or oriented at 45°. Aligned channels support roughly twice the flow rate because their cross-sectional area is twice as large as that of branched channels. Despite similar topological characteristics, the velocity distributions in aligned and branched sections of Channel 3 (1:3) and 6 (3:2) differ in skewness, highlighting localized regions of acceleration, deceleration, and a bimodal velocity profile. In contrast, Channel 4 (1:0) displays a more uniform velocity distribution in its 45° segment, indicating relatively consistent cell speeds. Compared to the hexagonal network channels, this square-like geometry maintains steadier flow conditions, resulting in less variation in cell velocity.

The matrices of normalized cell velocity organized by increasing pressure for each tested network can be found in Appendix A.4 for nominal feeding hematocrit of 10% and 20%. However, minimal changes in the normalized velocity histogram distribution were found with increasing pressure.

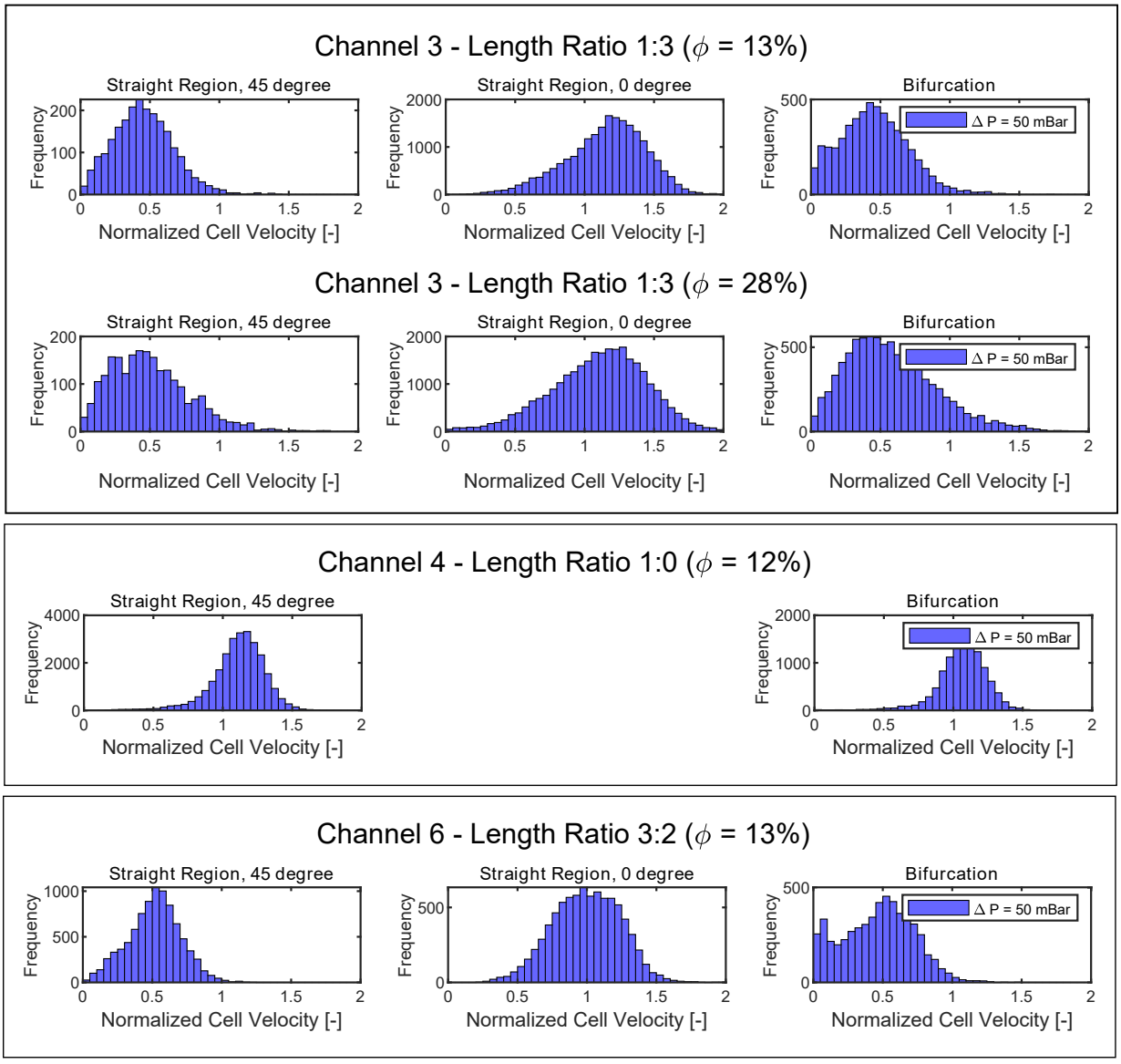


Figure 3.29: Normalized cell velocity distribution at 50 mBar in Channels 3, 4, and 6 for feeding hematocrit between 12 to 28%. Distribution is separated by individual channels either aligned to the flow indicated by 0° or at 45°, or at the bifurcation.

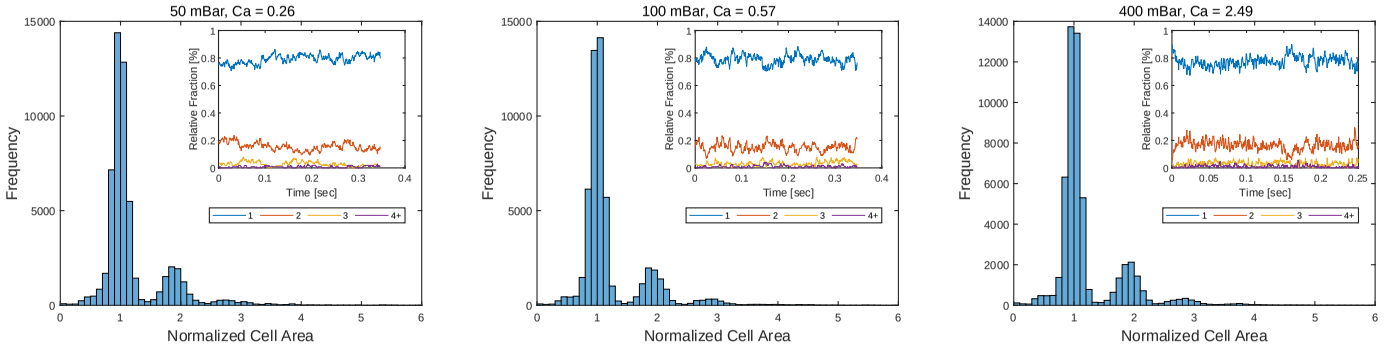
Hematocrit and cell cluster distribution

The change in the average cluster size of cell passage as a function of Capillary number across different network geometries is analyzed for increasing cell volume fractions. Histograms illustrate the total normalized projected cell area for healthy, untreated RBCs, with insets showing the relative proportion of cell area binned into clusters of 1, 2, 3, and 4 or more cells over time. These distributions are presented for nominal feeding hematocrit levels of 10%, 20%, and 40% in Channel 3 (1:3) at increasing capillary numbers in Figure 3.30. The normalized projected cell area is defined as the ratio of the measured projected cell area to the first peak of the projected cell area distribution. Histograms are smoothed using a kernel density estimator to identify peaks. The absolute value of the first peak of the projected cell area is plotted as a function of pressure drop (see Figure A.17), and the histograms for Channel 4 (see Figure A.18) and Channel 6 (see Figure A.19) are placed in Appendix A.6.

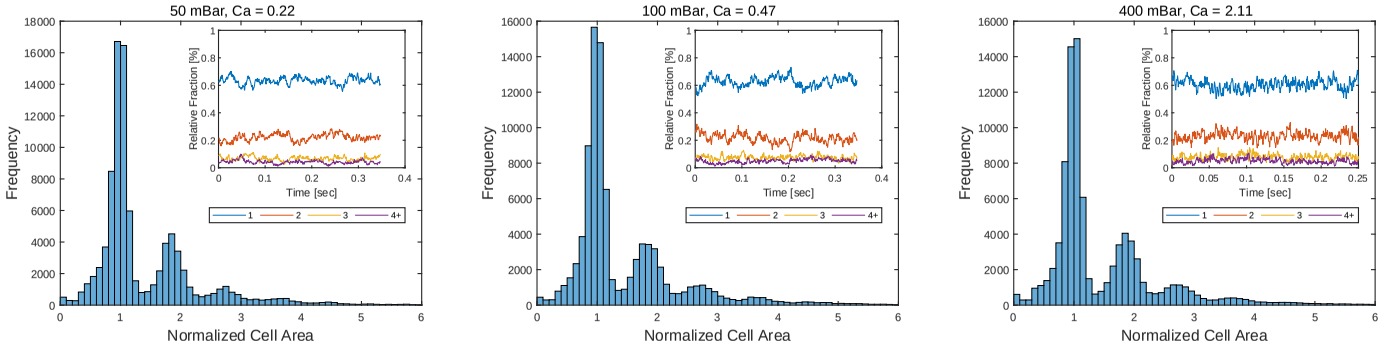
Multiple modes are observed in the histogram of total cell area, corresponding to varying sizes of cell clusters. The mean relative proportion of cell area binned to 1, 2, 3, and 4 or more cell clusters is then presented as a function of Ca and is represented in Figure 3.31. It is observed that the mean relative proportion of cell cluster size remains relatively unchanged with the Ca and over the short time scales where measurements are completed.

In contrast, as feeding hematocrit increases, the distribution skews towards a higher frequency of cell clustering size, indicated by the shift of the initial peak's frequency towards subsequent peaks, suggesting that a greater hematocrit tends to increase the likelihood of cell clustering. This can be alternatively represented by the mean relative proportion of cell area binned to 1, 2, 3, and 4 or more cell clusters as a function of projected hematocrit represented in Figure 3.32. The relative fraction of cluster size trends the same between the three tested network types.

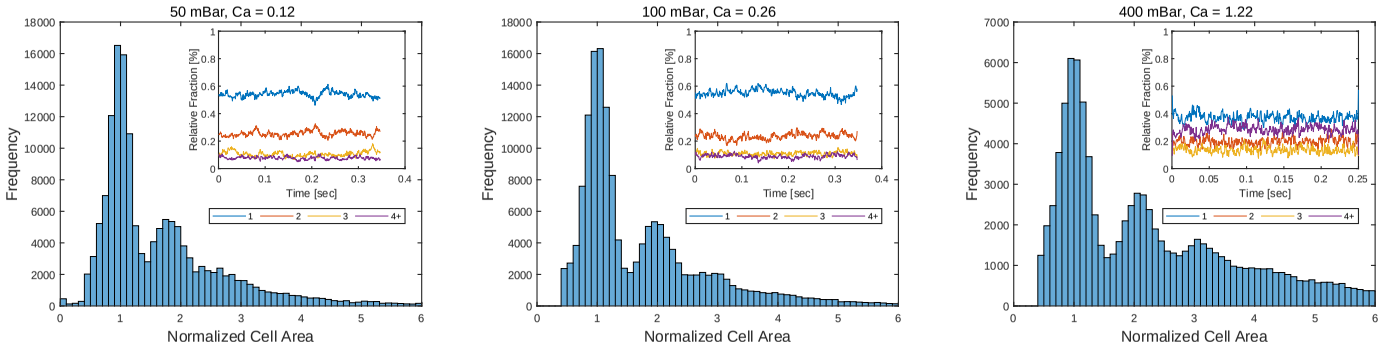
To visualize the cell clustering sizes which can constitute cells that are side-by-side or in train formation, example of cell clusters within different normalized projected cell area ranges is presented in Figure 3.33 taken from the aligned straight region of Channel 3 (1:3) with projected hematocrit of 13%. White boundaries represent the binary perimeter from image processing to segment the cells. The same blood samples are used between experiments but are completed over three experimental days. From the example, it can be observed that the normalized projected cell area does correlate with the number of cell objects. However, it does not necessarily distinguish between the type of clustering or the proximity of the objects.



(a) $\phi = 13\%$



(b) $\phi = 28\%$



(c) $\phi = 46\%$

Figure 3.30: Channel 3 with length ratio of 1:3 projected cell area distribution for increasing pressures of healthy untreated RBCs for increasing feeding hematocrit. Inset is the relative fraction of cell sizes binned by mode over acquisition time.

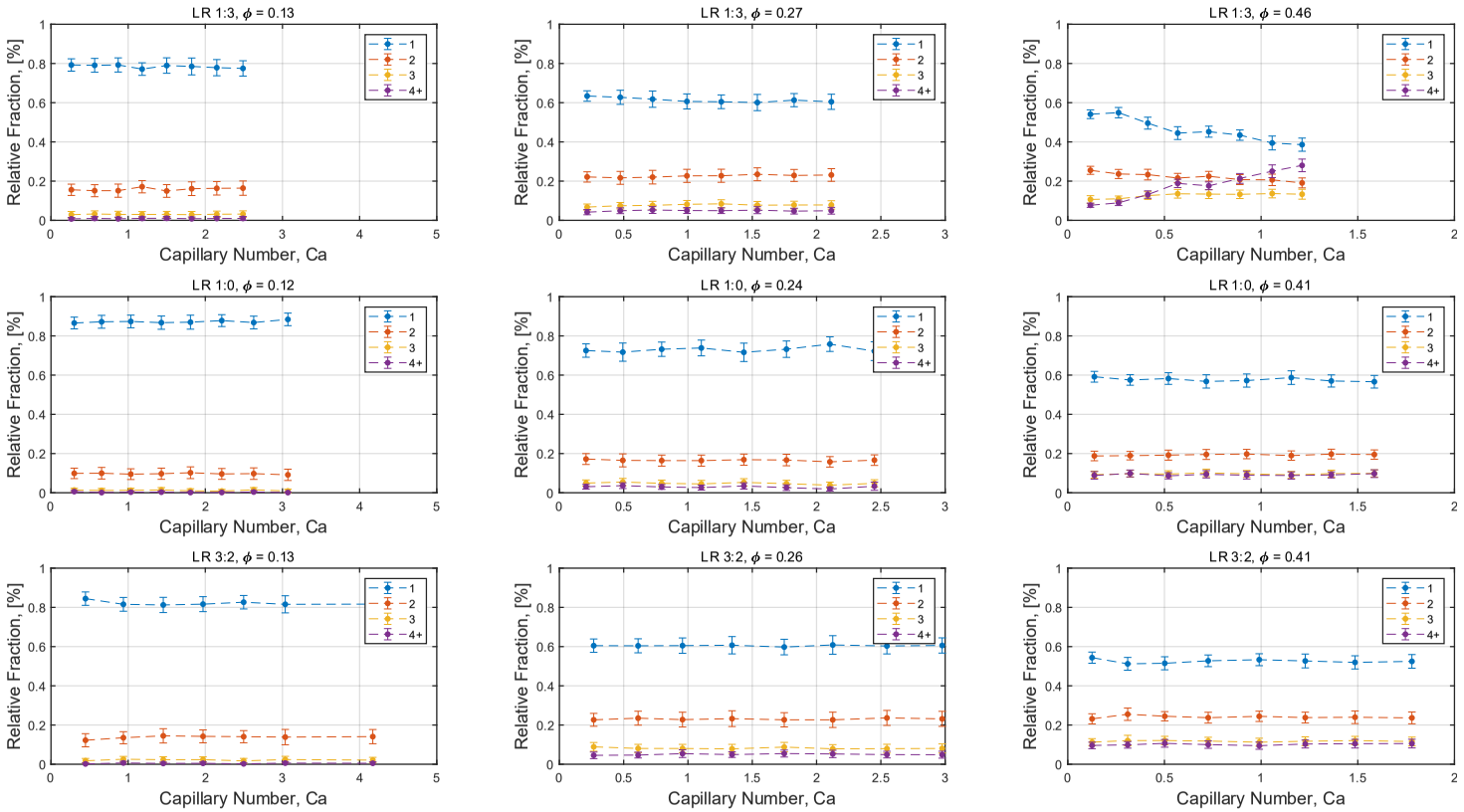


Figure 3.31: Mean and standard deviation of relative proportion of cell cluster size as a function of the Capillary number for increasing hematocrit samples in Channel 3 (top row), 4 (middle row), and 6 (bottom row). Connected dashed lines is present for clarity.

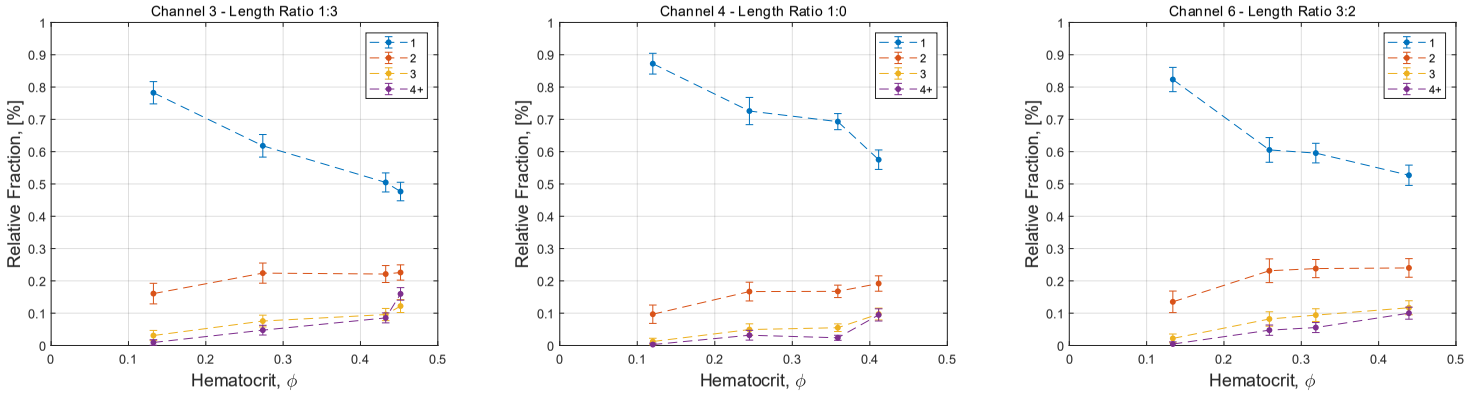


Figure 3.32: The mean and standard deviation of relative proportion of cell cluster size as a function of the projected hematocrit averaged over the full Capillary number range in Channel 3 (left), 4 (center), and 6 (right). Connected dashed lines is present for clarity.

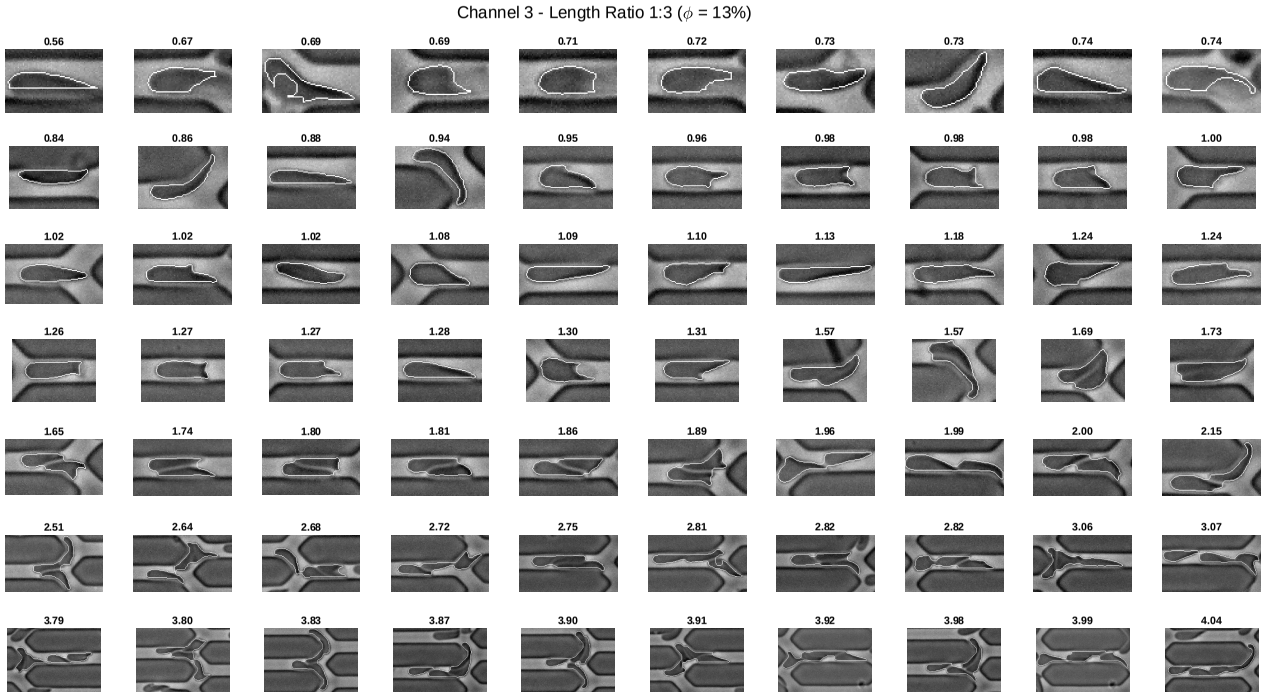


Figure 3.33: Example RBC morphologies found in binned projected cell area categories. Examples are from Channel 3 at a Capillary number of 1.18 with mean projected hematocrit of 13%. Examples are taken from straight channels aligned to flow. Images are scaled by rows within similar projected cell area bins. While the number above the image indicate the measured normalized projected area.

Morphological variations

It is hypothesized that the dynamics of RBC passage through the network and the resulting reduction in relative resistance in the network are due to a shape adaptation of the cells as they flow through the network. To quantify the elongation of the cells in the network, an elongation index (elongation index (EI)) is defined as follows:

$$EI = (MajorAxis - MinorAxis)/(MajorAxis + MinorAxis) \tag{3.13}$$

where EI is the ratio of the difference of major and minor axes and the sum of the major and minor axes of the binary image of a cell. The EI is plotted as a function of mean Ca in Figure 3.34, where the mean of all single cells in all straight channels is considered, and the Capillary number is defined as the value of the global Capillary number, which is approximated from the mean flow rate and cross-sectional area. It is observed that with increasing Ca the average elongation of the collective cells increases while approaching a plateau. Interestingly, this does not necessarily distinguish between different morphologies of the cells such as axisymmetric, slipper, or bumping morphologies.

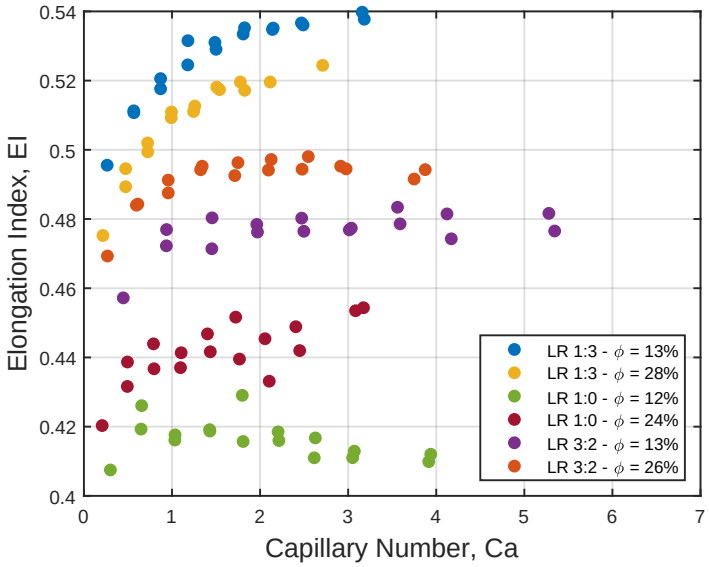


Figure 3.34: Mean elongation index as a function of mean network Capillary number in the network geometries 3 (1:3), 4 (1:0), and 6 (3:2) for nominal feeding hematocrit of 10% and 20%. The measured projected hematocrit are reported in the legend. LR is the length ratio of the network design.

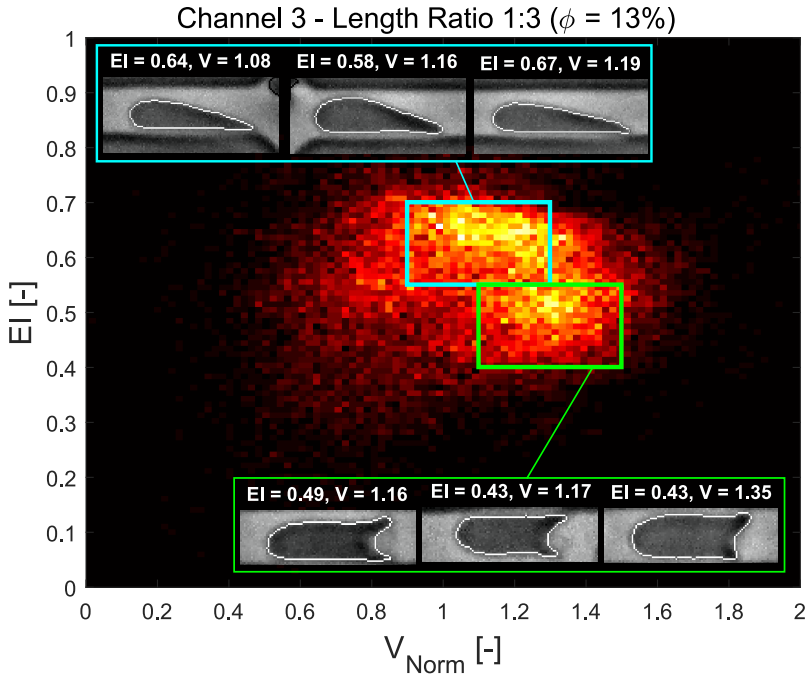


Figure 3.35: Heat map distribution of individual cell elongation index as a function of normalized cell velocity taken at a mean Capillary number of 1.18 (pressure drop 200 mBar) in the straight aligned channel from Channel 3 (1:3). Examples of RBC morphology are taken from the high incidence region observed by the yellow area.

This is clear when observing an individual point of Figure 3.34 and plotting the cell EI as a function of the individual normalized cell velocity. As an example Figure 3.35 represents a heat map of Channel 3 (1:3) at a mean Capillary number of 1.18 taken at the straight region aligned to the flow. There is a distribution of cell morphologies that are present in the different channels which questions if this changes with Ca. A wider representation of each network and cell morphology is presented in Appendix A.7.

Morphological distribution

In the low volume fraction regime, the relative distribution of cell morphology is presented as a function of the Capillary number for Channel 3 (1:3) and 4 (1:0), which have a relatively similar porosity but different geometric topology in Figure 3.36. The distribution of the relative cell morphology is taken from classifications taken at all locations (channels aligned, channels angled, and bifurcation) in the network. The example morphological distribution is presented for nominal feeding hematocrits of 10% and 20% using the same blood sample in which the measured local hematocrit is labeled.

Differences in the morphological distribution of red blood cells (RBCs) are evident between Channel 3 (Figure 3.36 A, C) and Channel 4 (Figure 3.36 B, D) despite having similar porosity. In Channel 3, a diverse distribution of cell morphologies is observed at both 13% and 23% hematocrit, including parachutes, slippers, and bumping cases, with a bias toward parachute morphologies at lower capillary numbers. In contrast, Channel 4 at low hematocrit (9%) is dominated by parachute morphologies, which show minimal variation with increasing Capillary number. However, at 23% hematocrit, the morphological distribution shifts to resemble that of Channel 3. What's interesting is a difference in the power-law index at low hematocrits where Channel 4 (1:0) had a larger power-law index compared to Channel 3 (1:3). While at higher hematocrit, where the distribution is more similar, the power-law index also becomes similar in range.

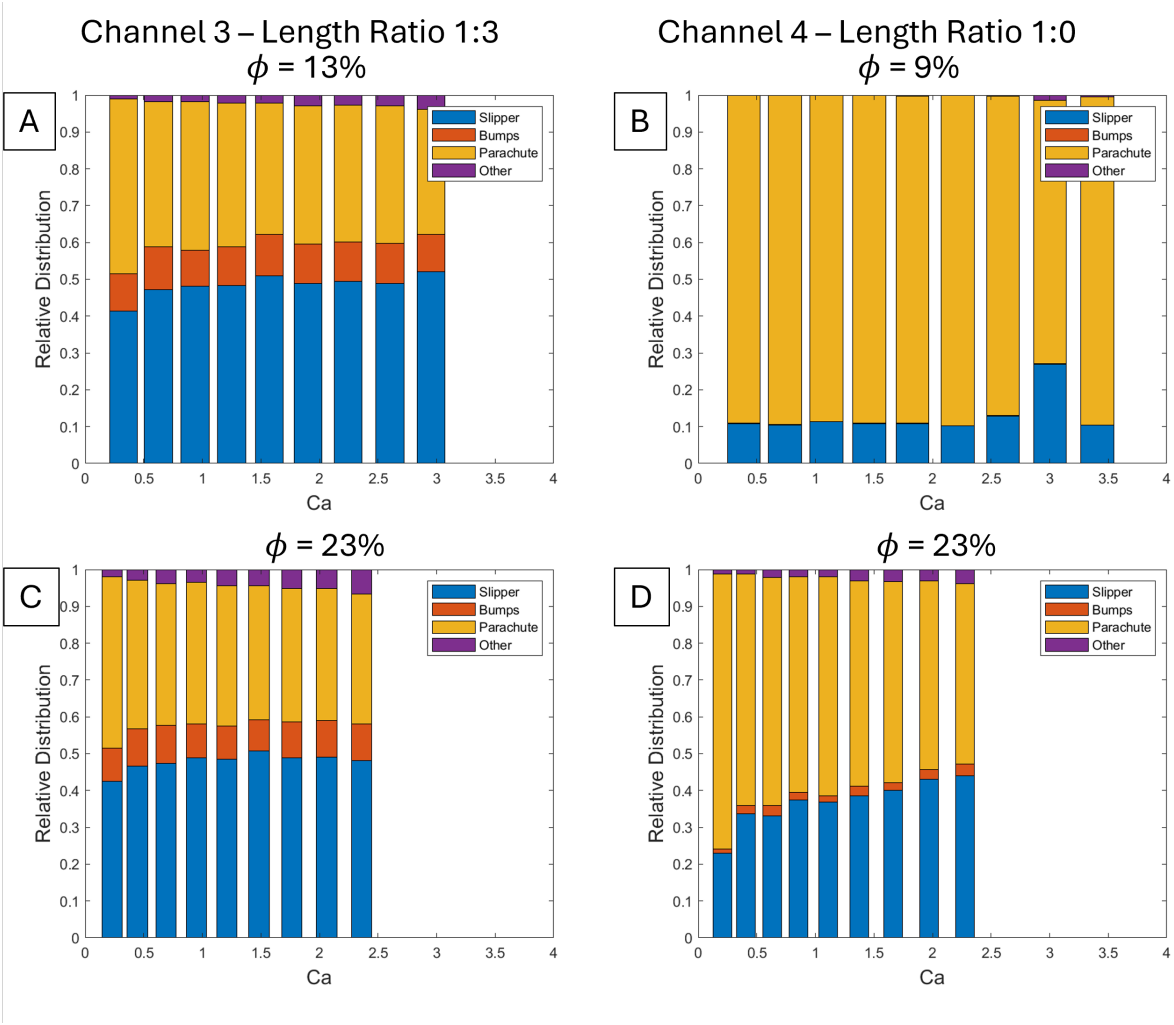


Figure 3.36: Relative distribution of cell morphology in Channel 3 (1:3) with measured projected hematocrit of (A) 13% and (C) 23%, and Channel 4 (1:0) with measured projected hematocrit of (B) 9% and (D) 23%.

3.5.4 Deformability effects

From the experiments completed in healthy untreated RBCs a general framework of the dynamics of RBC passage has been defined. The relative resistance appears to be dependent on both the hematocrit of the suspension and the network porosity. This dynamic is captured with a simple power-law that depends on the Capillary number that scales with the hematocrit, and so the following question is how the dynamic is modified when the cell membrane shear elasticity is modified. In this work, glutaraldehyde and diamide, which are two common chemical fixatives used in RBC studies, are implemented in modifying the cells' membrane mechanical property [71, 73, 74, 80].

Gluturaldehyde

Glutaraldehyde treated RBC at 0.01%, 0.005%, and 0.001% concentration and untreated RBC control in Channel 3 (1:3) network geometry flowing nominal feeding hematocrit of 20% samples in the network. The glutaraldehyde experiments were completed in a new SU8 master wafer due to wear of the previous wafers and had a measured height of approximately 4.76 µm. The excess relative resistance as a function of the mean convective velocity is depicted in Figure 3.37 in log-log. Markers that are matched are completed using the same sample of healthy RBC. Glutaraldehyde treatment at 0.005% and 0.001% resulted in minimal change to the relative resistance compared to RBC treated in 0.01% concentration of glutaraldehyde. The increase in excess relative resistance was observed to be greater than simply an increase in the hematocrit, which may be indicative that a modification of the surface shear modulus was accomplished.

However, at the current stage of this study, the exact change in the surface shear modulus of the treated RBC is not known from the lack of direct measurements. As a first approximation test, the Capillary number may be approximated from surface shear modulus measurements reported by Drochon on treated RBCs [74], and from elastic modulus measurements from atomic force microscope reported by Abay et al. [73]. A summary of the approximation is reported in the method Section 3.4.2. The change in the Capillary number is assumed to primarily be the result of the change in the surface shear modulus. The excess relative resistance as a function of Capillary number which is approximated from Drochon is presented in Figure 3.38 (a) while the Capillary number which is approximated from Abay et al. is presented in Figure 3.38(b). From the approximation, the excess relative resistance was not found to align when assuming the G_s values reported by Drochon. In contrast, assuming the G_s values reported by Abay et al., a separation of the excess relative resistance is observed such that the 0.01% treated and untreated sample

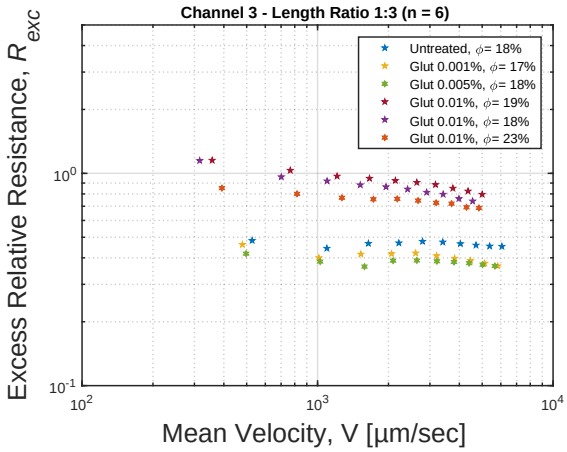


Figure 3.37: Excess relative resistance versus mean convective velocity in 1:3 network geometry. Markers indicate different blood sample.

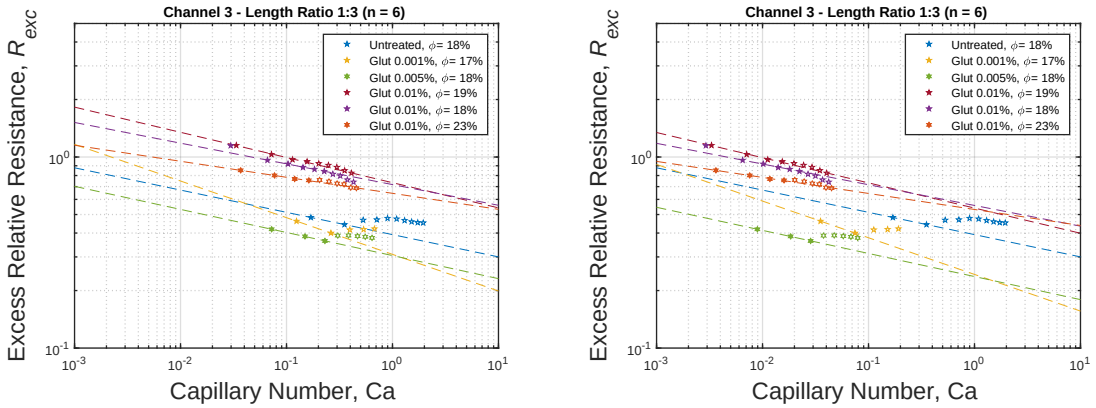
appears to align along a line in log-log, while the 0.001% and 0.005% samples begin to deviate.

Similar to the healthy samples presented earlier in this work, the excess relative resistance is fitted with a power-law function with parameters that depend on the hematocrit in the first linear region in log-log. The fitting parameters are extracted and plotted against the healthy RBC sample in Figure 3.39 while assuming the membrane surface shear modulus. The fitting parameter is plotted against the healthy samples from the previous section and is represented by dashed lines. But it should be noted that the control untreated healthy sample is considered separate from this curve.

Two observations can be made, the first is that using the approximate G_s from Drochon resulted in excess relative resistance magnitude that is elevated for the 0.01% treated sample, while using the approximate G_s from Abay et al. resulted in f that coincides with the results of healthy cells previously reported in this work. However, despite the similarity in the excess relative resistance magnitude, the power-law exponent was found to be significantly lower than the previous healthy cell, including the healthy control.

Diamide

Diamide treated blood measurements (completed by Tatiana Turcitu under supervision) were completed in Channels 3 (1:3), 4 (1:0), and 6 (3:2) network geometries flowing a nominal feeding 10% hematocrit samples into the channels. Experiments of blood samples

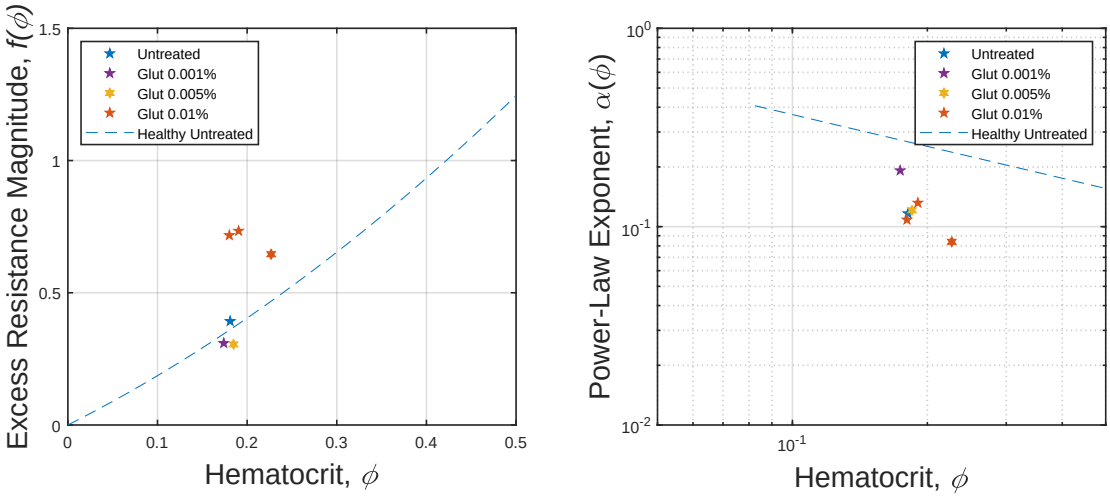


(a) Approximating G_S from Drochon (b) Approximating G_S from Abay et al.

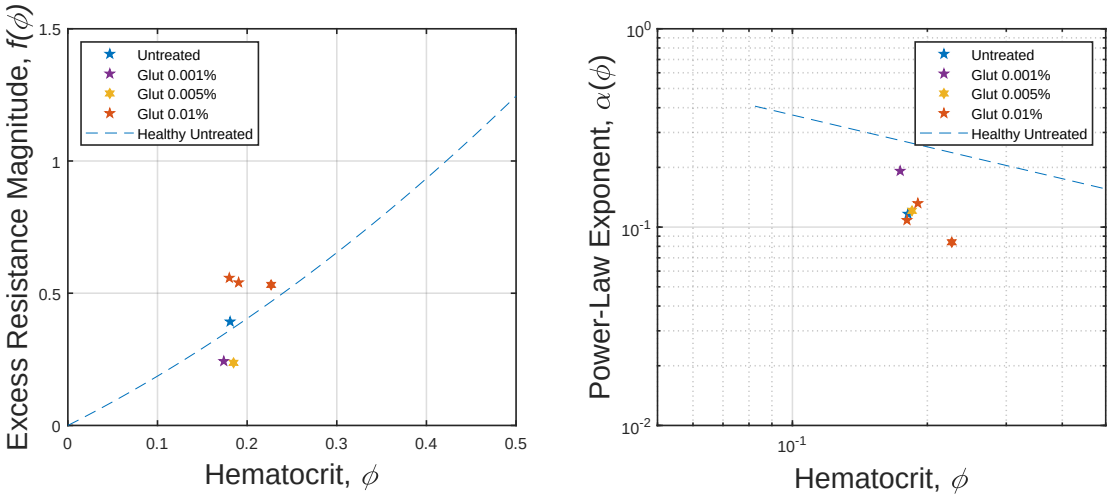
Figure 3.38: Relative resistance of treated RBC with glutaraldehyde as a function of Capillary number determined from approximating G_S from reported literature values (a) Drochon [74] and (b) Abay et al. [73]. Dashed lines represent power-law model fit over first linear region in log-log.

flowing through Channel 6 (3:2) and 4 (1:0) were completed sequentially over two days while blood samples flowing through Channel 3 (1:3) were from a different blood donor. The relative resistance as a function of mean convective velocity is presented in Figure 3.40(a) while the mean local projected hematocrit as a function of pressure drop is presented in Figure 3.40(b) for Channels 3 (1:3), 4 (1:0), and 6 (3:2).

A steep increase in the excess relative resistance is observed of several fold with an increase in the concentration of diamide treatment in all three tested channels while the hematocrit was low, lower than the 10% feeding hematocrit at injection as observed in Channel 4 (1:0) and 6 (3:2). The lower hematocrit was most probably caused by insufficient filling of the channel and not primarily due to a clogging issue, as imaging of the macroscopic view during the first run sequence shows entrances that are not fully filled and the free passage of RBCs through the channel. The fold increase in the excess relative resistance, however, cannot be solely associated with a change in surface shear modulus as the treatment of the RBC in diamide resulted in a loss of membrane that is not reported in the literature. Instead, this increase in excess relative resistance may be associated with the aspect ratio between the size of the cell and the channel size. Examples of the changed cell shape are represented in Figure 3.41 taken at the channel bifurcation.

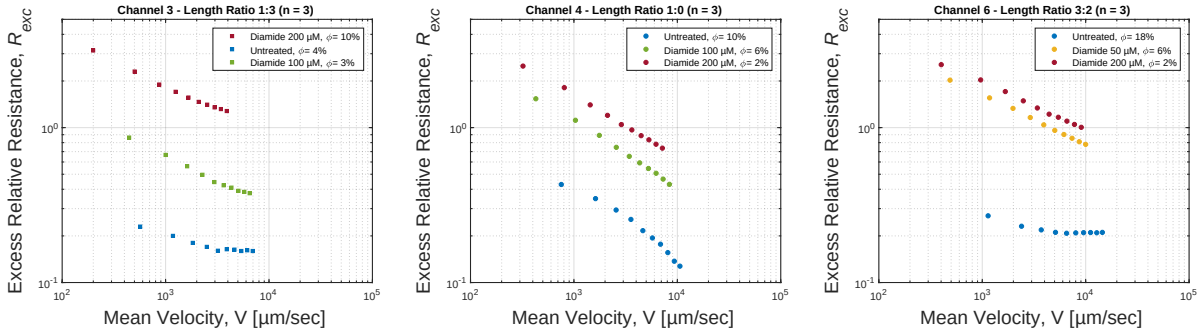


(a) Approximating G_S from Drochon

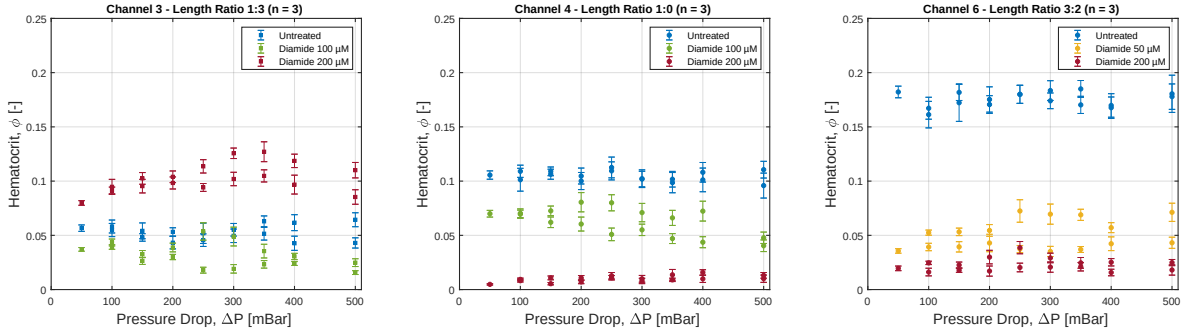


(b) Approximating G_S from Abay et al.

Figure 3.39: Extracted fitting parameter of power-law model for treated RBC with glutaraldehyde as a function of hematocrit, where the Capillary number is approximated from surface shear modulus reported in literature (a) Drochon [74] and (b) Abay et al. [73]. Dashed fit represents the fitted model of untreated healthy cells.



(a) Relative Resistance as function of Mean Convective Velocity



(b) Local Projected Hematocrit Measurements

Figure 3.40: Relative resistance versus mean convective velocity and mean local projected hematocrit flowed through with network Channels 3 (1:3), 4 (1:0), and 6 (3:2). Markers indicate difference in donor blood sample.

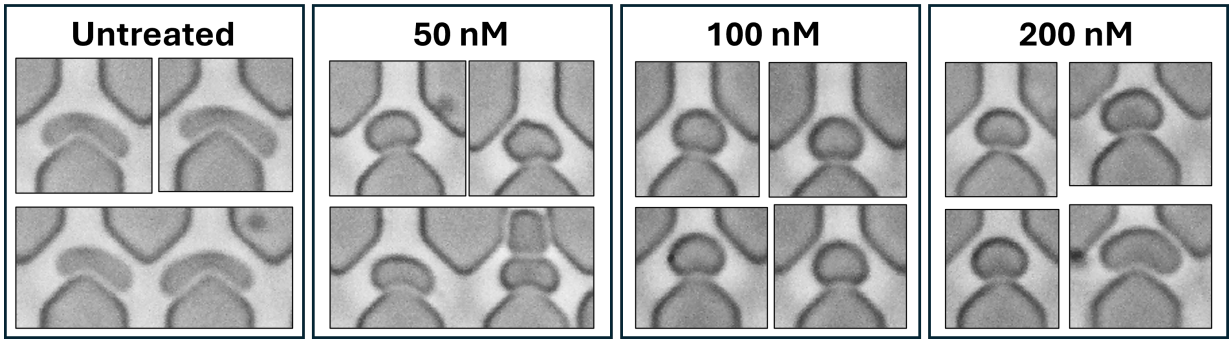


Figure 3.41: Cell deformation at bifurcation for increasing diamide treated RBCs.

3.6 Discussion

3.6.1 Macroscopic Response Considerations without Cells

The non-linear pressure-flow relationship observed in the Newtonian suspending fluid underscores the significant role of PDMS channel deformation at elevated pressures. Above 500 mBar, the relationship deviated from linearity (see Figure 3.19), which, according to Poiseuille's law, can be attributed to changes in fluid viscosity or network geometry. In this case, the non-linearity arose from changes in the network geometry rather than the fluid viscosity, as the increasing pressure caused the PDMS channel to deform, altering its cross-sectional area. Such deformation at the liquid-solid interface is well-documented for low aspect ratio rectangular channels [81] and compliant microchannels [82]. The resulting expansion of the channel cross-section reduces hydraulic resistance and alters the flow profile, leading to higher flow rates than would occur in a rigid channel under the same pressure gradient. To capture these effects, a second-order polynomial was employed to model the mean pressure-flow data within the tested pressure range, focusing on the quasi-linear region where deformation effects are minimal.

As evidenced by Figure 3.19, significant variability in the measured hydrodynamic resistance is observed even within channels of the same design. This variability likely stems from fabrication-related factors, such as minor inconsistencies in the PDMS mix ratio, curing temperature and duration, and small manufacturing imperfections. These factors influence the compliance properties of PDMS, altering its response to pressure and potentially affecting network geometry. Additionally, variability in the preparation of the suspending fluid batches could further contribute to experimental inconsistencies. Such manufacturing and material discrepancies raise important questions about the reproducibility of results and the extent of variability between different network designs. Understanding and mitigating these sources of variability is crucial for ensuring reliable comparisons across experiments.

The maximum difference of 11% in the fitting parameter (B) for the linear portion of the polynomial fit is between Channel 4 (1:0) and 6 (3:2). This variation in the hydrodynamic resistance is within acceptable limits, given potential manufacturing inconsistencies and the use of the SU8 master wafer. Notably, even minor alterations of a few hundredths of a micrometer in channel height can significantly affect hydrodynamic resistance, as it scales with the cube of the height. The impact of manufacturing variations on pressure and flow rate responses is further highlighted by differences observed between wafers, particularly within Channel 4 (Figure 3.20). Splitting this network into two categories, based on the master wafer and specific network pairs on the wafer, demonstrates the significant influence

of these variations. To enable meaningful comparisons across experiments and account for variability in Newtonian resistance, the excess relative resistance will be considered.

In contrast to the flow sequence of the Newtonian fluid, the RBC suspension flow sequence is conducted in reverse. As shown in Figure 3.22, the sample sequence and mean flow rate as a function of pressure reveal differences in flow dynamics between the first and second runs, particularly at higher pressures. These differences are attributed to variations in hematocrit stability during the initial feeding sequence. By the second run, the hematocrit distribution, estimated from the projected hematocrit, stabilizes. This stabilization is supported by Figure 3.23, which shows a progressive increase in homogeneous brightness across the network, indicating a uniform distribution of cell passage.

Localized transitory clogging, initially a concern, was observed predominantly near the network entrance and was found to be influenced by the pressure gradient. As depicted in Figure 3.23, clogging zones were significantly more prevalent at 100 mBar compared to 800 mBar. This difference due to pressure may be associated with the deformability of the channel itself, as the channel would be at its largest at 800 mBar comparatively to at 100 mBar. However, despite the presence of these localized clogs, the second flow run of the blood sample produces pressure-flow curves that closely follow the trajectory of the first run in the realm of low pressure at which the focus of analysis is made. This finding suggests that localized clogging has a gradual or negligible impact on the overall pressure-flow rate relationship.

3.6.2 Healthy RBC Suspension

Macroscopic rheological response

As evidenced in Figure 3.24(a), an increase in hematocrit results in a reduction in flow rate for a given pressure. This decrease in flow rate for a given pressure with increasing hematocrit is an intuitive result as the introduction of more and more cells in the network adds local viscous "resistors," which increase the overall resistance to the flow. This decrease in flow rate must scale with hematocrit for low hematocrit. Such a type of resistance decrease has been observed in the literature in straight tube flows of varying sizes, from 30 µm to 100 µm [48] and in straight capillary arrays (not connected, in parallel) with channel diameters of approximately 5 µm [83]. However, in contrast to the behavior observed in large straight capillary tubes [48] or large pulmonary networks [58] and more similar to that observed in confined straight capillary arrays [49, 50, 83], the relationship between pressure and flow rate observed in this work in the tested pressure range is non-linear.

This non-linearity is illustrated in Figure 3.24(b) which depicts two distinct regimes: for low Ca, there is a sharp decrease in R_{exc}, while for $Ca \gtrsim 1$, the drop in resistance seems to slow down and may even reach a plateau. Theoretical work in straight narrow capillaries with diameters ranging from 5 µm to 8 µm by Secomb et al. has demonstrated a non-linear relationship between intrinsic apparent viscosity associated with single RBC passage and flow rate. In their theoretical framework that accounts for both the shear and bending elasticity, the shape and apparent viscosity of cells are found to be independent of flow rate at moderate to high velocities [49]. Conversely, at low velocities, membrane shear and bending stresses become significant factors in defining the cells' shape and the associated apparent viscosity [49]. The theoretical predication of Secomb and colleagues showed good qualitative agreement with the observed shape transition observed experimentally by Tomaiuolo and colleagues in straight capillaries where, at low RBC velocity, a rim protruding outwards is found at the trailing end which transitions to an elongated asymptotic configuration at increasing velocity [64]. Furthermore, experimental work using human RBC in glass capillary arrays supports a similar non-linear relationship [83]. The non-linearity is attributed to the cells' ability to squeeze through capillaries: as the velocity of the cells increases, the resistance to movement is expected to decrease due to the deformation of red cells caused by lubrication pressures and drag forces in the lubrication film that separates the cells from the capillary wall. In the following section, the focus will primarily be on the low capillary regime where the largest decrease in excess relative resistance is observed.

Scaling of excess relative resistance magnitude with hematocrit

Fitting the R_{exc} versus Ca (Figure 3.25) with a simple power-law provides a means of understanding how the dynamics of the RBC through the network may be normalized between the different network topologies and the hematocrit that flows through it.

The excess relative resistance magnitude (f) was found to scale linearly with ϕ at low volume fraction as observed in Figure 3.26. At the lower limit of hematocrit, where there are no cells present, it can be postulated that f in the absence of cells should approach zero. This is based on the principle that the same fluid flowing through the same network should yield identical pressure and flow rate curves, and therefore no excess resistance. This is similarly described in the work of Secomb et al. where the contribution of the volume fraction of cells to the apparent viscosity is said to be proportional to the volume fraction and the intrinsic viscosity (K_t) of the cell in the fluid ($\eta_{app} = \eta(1 + k_t\phi)$) [49].

Fitting f with a quadratic function reveals that channels with a 3:2 length ratio deviate more from linear behavior than those with ratios of 1:3 or 1:0. The fit quality varies

significantly depending on the blood sample, yielding R squared values of 0.44, 0.83, and 0.93 for network Channel 4 (1:0), 3 (1:3), and 6 (3:2), respectively. Channel 4 (1:0) is better represented by a linear model, as the second-order parameter (c_1) approaches zero. In contrast, Channel 3 (1:3) and 6 (3:2) show a non-linear increase in f with Channel 6 responding more strongly at lower hematocrit. Notably, this trend in f is also observed in the high Capillary number regime (Figure 3.28).

Despite similar hydrodynamic resistances under Newtonian flow, the three network geometries differ in porosity. Channel 6 (3:2) has a porosity of 0.332 ($\pm$0.004), while Channel 3 (1:3) and 4 (1:0) have higher and similar porosities of approximately 0.392 ($\pm$0.001) and 0.404 ($\pm$0.001), respectively. As shown in Figure 3.42, the channels are grouped according to their projected porosity and demonstrate very similar trends. Taking insight from porous media, the relationship between porosity and permeability is often not so straightforward and is commonly described with empirical correlations, the most popular being the Kozeny-Carman correlation, which describes that the permeability through a porous medium scales to the cube of the porosity [84,85]. It is probable that the difference in porosity may give rise to non-linearity. However, further exploration will be required that explores further into characterizing the effects of porosity on the transport of RBC. This may be completed by testing a wider range of network porosity while maintaining the same hydrodynamic resistance, such as the other network topologies which have a range of porosity of 0.24 to 0.52 for channels with a length ratio of 2:1 and 2:5, respectively.

Scaling of power-law exponent with hematocrit

A second observation concerns the relationship between hematocrit and the power-law exponent (α) in the low Capillary number regime. This exponent, defined by the slope of the excess relative resistance scaled by the Capillary number in log-log, was fitted with a power-law to approximate the observed non-linear decrease with increasing hematocrit. The results show that Channel 3 (1:3) and 4 (1:0) experience a decrease in the power-law exponent as hematocrit increases, whereas Channel 6 (3:2) exhibits a more constant trend with the hematocrit (Figure 3.26, left).

Under low hematocrit conditions in the low capillary regime, where cells traverse the network individually, the power-law exponent varies from 0.2 to 0.7 depending on the network geometry. As hematocrit approaches 50%, the exponent converges to a narrower band between 0.1 and 0.3. This stands in contrast to the high capillary regime, where all three tested geometries display a decrease in the power-law exponent comparatively to the low capillary regime. Such a decrease suggests that the excess relative resistance plateaus at higher capillary numbers, implying a possible lower limit to the excess relative

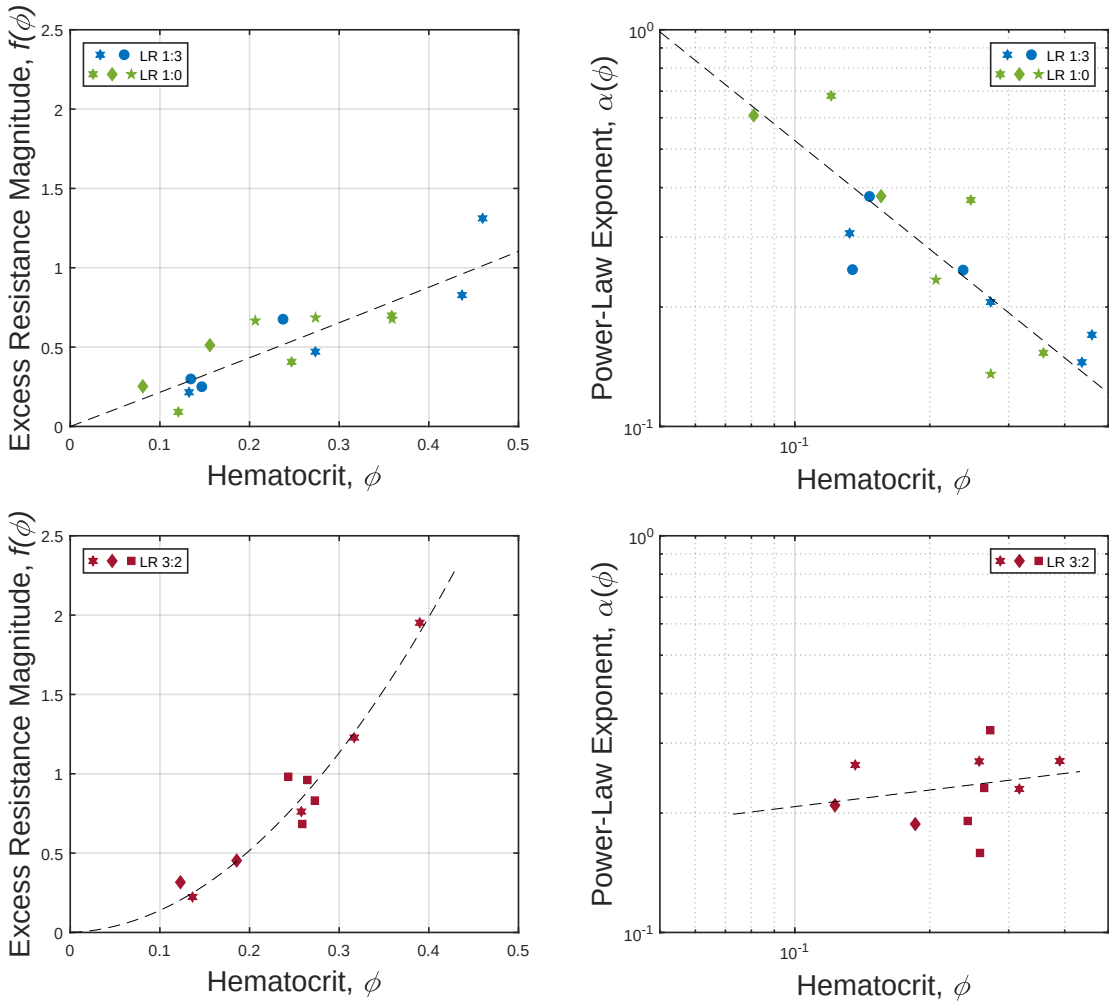


Figure 3.42: Parameter of power-law for relative resistance scaled by Capillary number. The rows of graphs represent the two identified porosity of 0.4 (top row) and 0.34 (bottom), markers represent same RBC sample and the color represents the specific geometry. Dashed line is the fit through the combined data set.

resistance. As discussed previously, this plateauing of the excess relative resistance is most likely associated with shape adaptation of the cells becoming independent of the flow rate at moderately high velocities as described by Secomb et al. [49] and Tomaiuolo [64], and observed in Figure 3.34.

The effects of confinement are a critical factor in determining flow resistance in microchannels. Numerical work on single capsules flowing through long cylindrical pores by Quéguiner and Barthes-Biesel demonstrated that increasing confinement ratio (CR), which is the ratio of the radius of an equivalent spherical particle to the radius of the channel cross-section, results in an increase in the excess relative resistance when flowing capsules through capillaries. Their observations were modeled using a spherical neo-Hookean capsule, showing that the associated excess relative resistance scales as a power-law with the Capillary number until the capsule ruptures due to overstretching [50]. An adapted figure of the experiment reported from Quéguiner and Barthes-Biesel is represented in Figure 3.43, left. What is interesting is that a non-linear decrease of the excess relative resistance with Capillary number is observed, which depends on the confinement ratio of the cells and the network. Fitting a power-law model of the excess relative resistance demonstrates that they observe that an increase in confinement ratio results in a linear increase in the power-law exponent while a non-monotonic change in the f, as demonstrated in Figure 3.43, right.

Theoretical predictions by Secomb et al. also indicate that confinement influences the intrinsic apparent viscosity (which is proportional to the excess relative resistance) with increasing cell velocity. A rough fitting of the excess relative resistance with a power-law model and extracting the fitting parameter indicates a power-law exponent that ranges from 0.2 to 0.7 for channel sizes ranging from 5.0 µm to 8.0 µm. The excess relative resistance and the associated scaling of the power-law exponent with confinement ratio is presented in Figure 3.44 [49].

The experimental results of Quéguiner and Barthes-Biesel and the theoretical lubrication model of Secomb and colleagues define a bound at which the power-law index can be expected at low hematocrit conditions. In this study, the measurements of RBC volume were conducted indirectly from the image analysis. The approximations based on imaging suggest an average RBC volume of 74.8 fL, corresponding to an equivalent nominal radius of 2.62 µm for a spherical equivalent cell. The resulting confinement ratio is approximately 0.99, and so the power-law exponent expected from the work of Quéguiner and Barthes-Biesel, and Secomb et al. are 0.25 and 0.66, respectively. Under low hematocrit conditions and in the low capillary regime, where cells traverse the network individually, we found the power-law exponent to range from 0.2 to 0.7 depending on the network geometry, which is within the bands of power-law exponents reported by Secomb et al. as well as Quéguiner and Barthes-Biesel [49, 50].

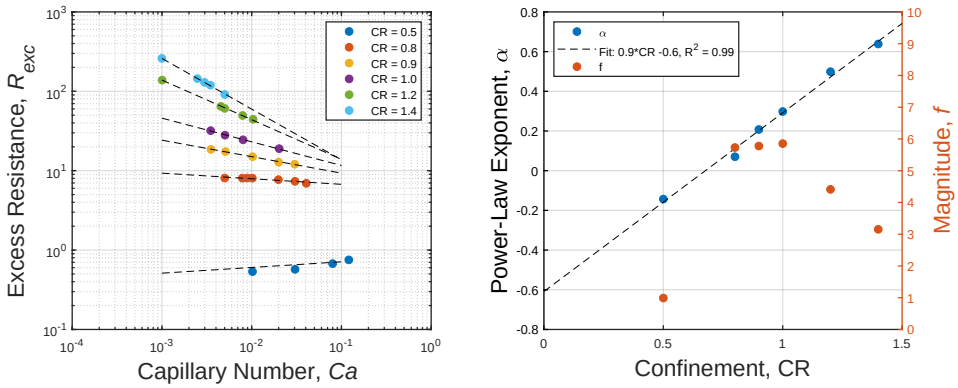


Figure 3.43: (Left) Excess resistance as a function of Capillary number for spherical neo-Hookean spheres at increasing confinement ratio (CR) between 0.5 and 1.4. Dashed lines are power-law model fits. (Right) Extracted fitting parameter of power-law model that scales with the Capillary number. The blue points represent the power-law exponent and orange points represent the excess relative resistance magnitude. The power-law exponents is fitted with a linear equation to interpolate for an expected power-law exponent for a CR of 1. [50] (Adapted graphic).

In contrast, in the high hematocrit range where literature results are more limited, experimental data from Lingard for straight parallel capillary arrays with individual channels in the range of 5 µm report similar non-linearity. The results of Channel 3 (1:3) are placed in parallel to the results of Lingard for straight capillary arrays in Figure 3.45 as the 1:3 length ratio shares the closest topologies to straight channels from entrance to exit. It is noted that f is found to increase with increasing hematocrit. There are differences between the rate at which the excess relative resistance magnitude increases with hematocrit between the work of Lingard and this study, which may be due to the methodology imposed for determining the hematocrit. As the one reported by Lingard are nominal hematocrits while the network is marked with the local projected hematocrit values [53].

Fitting the region after the plateau with a power-law model, a power-law exponent between 0.2 and 0.5 was obtained for feeding hematocrits between 22% and 84% (recreated in Figure 3.45, right). The power-law exponent was found to be non-monotonic with a low point at approximately 40% hematocrit. This contrasts with the monotonous decrease in the power-law exponent of Channel 3 (1:3) and in Channel 4 (1:0). These findings are within the range of the power-law exponent extracted from the observation of excess relative resistance as a function of velocity from Lingard's work. However, with the limitation in the quantity of reported values, the certainty of the trends of a decrease in the

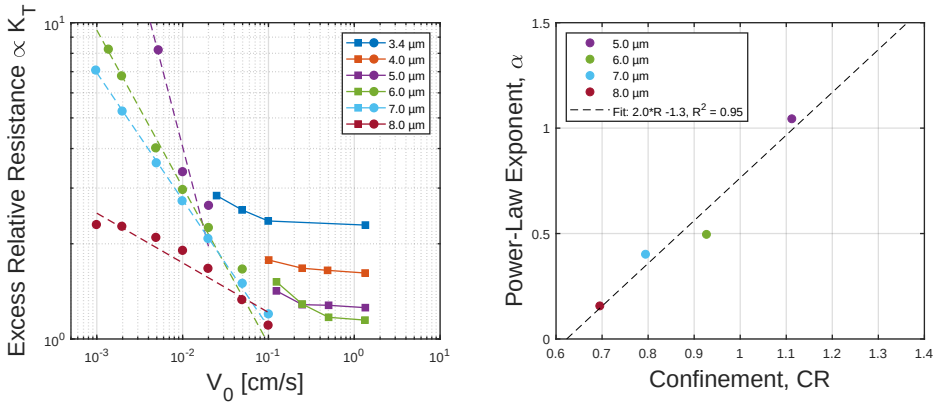


Figure 3.44: (Left) Variation of intrinsic viscosity (K_t) with cell velocity (v_o) using theoretical lubrication model in straight channels. Theoretical lubrication model described by Secomb, Skalak & Gross that includes shear elasticity but neglect bending of are indicated by □, while theoretical lubrication model that includes both shear elasticity and bending elasticity of are indicated by ○. Power-law model fits over the initial decrease in excess relative resistance is represented by dashed lines, while solid line are to connect the high velocity regime for clarity. [49]. (Adapted graphic). (Right) Extracted power-law index from fitted power-law index from change in intrinsic viscosity as a function of confinement assuming an average cell volume of 97 fL and spherical radius of 2.85 µm.

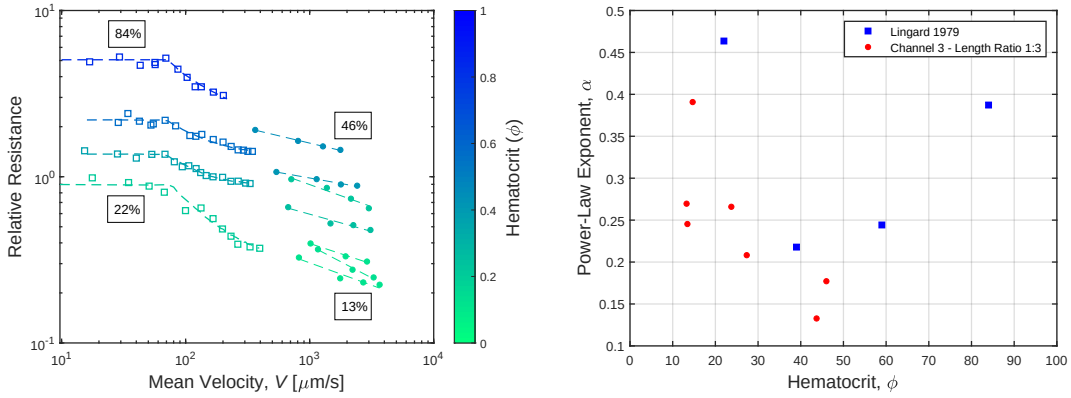


Figure 3.45: (Left) Comparison of 1:3 length ratio network design (○) with the results of straight capillary array of Lingard (□). The results of Lingard was extracted and scaled with $Gs = 5.5\,\mu\text{N/m}$ and η =2.2 mPa sec. (Right) Extracted fitting power-law exponent for power-law model.

power-law exponent can be further explored. This work demonstrates that confinement, hematocrit, and network geometry significantly influence the power-law scaling of relative resistance in microvascular networks. The scaling of the power-law exponent is consistent with theoretical and experimental studies.

3.6.3 Role of RBC Local Dynamics

A question that arises is if the scaling of the relative resistance can be associated to a local dynamic of the cells' passage through the network with increasing feeding hematocrit into the network channels. The following section will discuss the correlation of the transport characteristics with the local dynamics of the cells, such as their distribution in the network or their morphological variations throughout the network.

Velocity field variation

At low volume fractions, network geometry exerts a strong influence on the cell velocity distribution (Figure 3.29). Channel 4 (1:0) exhibits a narrow distribution in both straight sections and bifurcations, contrasting with the broader distributions seen in Channel 3 (1:3) and 6 (3:2). In these hexagonal networks, velocity distributions at bifurcations skew toward zero, reflecting an increased likelihood of "bumping" at the junction. In the square

network of Channel 4, however, bifurcation velocities resemble those in the straight region, suggesting that cells remain more centrally aligned and are less prone to stopping. They zigzag along the network, not bumping at junctions.

Despite these observed differences, the difference in volume fraction does not correlate with the excess relative resistance magnitude (f) as the three tested network configurations resulted in a similar level magnitude of f at low volume fractions. In contrast, there could be a correlation to the difference in magnitude of the power-law exponent as Channel 4 (1:0) does exhibit a larger decrease in R_{exc} with increasing Ca compared to Channel 3 (1:3) and 6 (3:2). In simple straight rectangular channels, the distribution of cell morphology is found to depend on the velocity of the cell passage in which faster velocities tend to transition cells' passage from axisymmetric croissant to slipper-like morphology [67, 68]. However, in the case of the network flow, there is the additional presence of bumping cases where the cells adhere and linger to the channel bifurcation. The question of then how do different morphologies contribute to the resistance is explored in the following section.

Lastly, comparing the effect of increasing the hematocrit in the same network design, a broadening of the normalized single cell velocity is observed in all three network geometry length ratios. This would indicate that the cells are transported at wider velocities and are experiencing a broader distribution of shape adaptation. A broadening of the velocity distribution can give rise to preferential flow paths, which is significant because it can lead to a non-uniform distribution of cells and potentially affect the overall flow dynamics and flow response of the system. Further exploration of a larger region of interest that spans a larger fraction of the network would be worth exploring to observe large-scale dispersion or heterogeneity of the cell velocity.

Hematocrit and cell cluster distribution

The macroscopic rheological response of network flow depends on hematocrit, as the formation of multi-cell clusters in the network can influence overall flow behavior. Even at low hematocrit, occasional clusters of two or three cells are observed (Figure 3.30). Interestingly, cluster-size distribution appears largely independent of the Capillary number (Figure 3.31). This would indicate that the observed decrease in the excess relative resistance with the Capillary number is not correlated to a change in the distribution of cell clusters with the Capillary number. What is interesting to further explore is how much elongation of the collective of cells in a system that is predominately single cell compares to one that is made of cell clusters composed of two or more cells?

In contrast, Figure 3.32 shows that higher hematocrit reduces single-cell occurrences

and increases multi-cell clusters, underscoring the role of cell volume fraction in determining the quantity of clustering within microchannel networks. The shift from single cell to clusters or trains of cells may actually be beneficial in reducing the total excess relative resistance to the network. In the experimental work of Abkarian et al., excess pressure of the passage of RBC in a high-speed microfluidic differential manometer demonstrates that the excess pressure of cell passage does not proportionally increase with the size of the train [66]. Instead, a reduction in excess pressure was observed, suggesting that the excess pressure is most likely not additive. Despite this, the relative fraction of clusters sizes are found to be similar between the three network topologies and so it is unlikely that the excess relative resistance magnitude is solely a result of changes in the fraction of clusters in the network.

This, however, does not separate cluster size from the potential effect on the porosity of the system itself. It is interesting to consider that the relative effect of larger cluster size on a network of channels that are already less porous would have a much greater effect on its permeability.

Morphological variations

From a macroscopic observation of the elongation of the RBCs as a function of the Capillary number, similar observations can be made compared to the works completed by Tomaiuolo in straight capillaries [64] and in theoretical analysis by Secomb, Skalak, and Gross [49]. With increasing Capillary number, the single cells become increasingly elongated. In the interpretation of Figure 3.34 the increase in mean cell elongation is described for a collective of all single cell passage. This makes intuitive sense, as cells are experiencing increasing shear stresses with increased pressure gradients; the cells stretch with the flow. What is interesting, however, is that there appears to be a plateauing in the shift in the elongation index with increasing plateau, further indicating that there may be a regime after which the cells stretching to the flow is minimal. This independence with the Capillary number is observed at the macroscopic rheological response as the excess relative resistance approaches a plateau in the high capillary regime (Figure 3.27) which results in power-law exponents that tend towards zero.

From the morphological distribution (Figure 3.36), an observation of a shift in morphologies is observed. As the Capillary number increases, cells transition from an axisymmetric parachute morphology to a slipper-like morphology, a behavior consistent with previous studies in straight square and rectangular capillaries under steady flow [67, 68]. However, unlike in straight capillaries, the presence of bifurcations in the network topolo-

gies gives rise to a tertiary morphology: the bump. Cells may deform on the bifurcations, resulting in a bumping morphology and, upon dislodging, rotate into a slipper morphology.

Furthermore, differences in the RBC morphology distribution between Channel 3 (1:3) and 4 (1:0) may give rise to the observed differences at the macroscopic scale. At low hematocrit, axisymmetric parachutes dominate as the primary cell morphology in Channel 4 compared to Channel 3, which has a bias towards slipper-like morphology. This shift in dominance appears to be rooted in the fact that there are bumping morphologies in Channel 3 compared to Channel 4 at a nominal feeding hematocrit of 10%. With increasing hematocrit, the change in morphological distribution observed in Channel 4 is likely due to increased cell-cell interactions, which raise the probability of cluster formation and subsequent interactions with bifurcations. These increased interactions at higher hematocrit in Channel 4 indicate that morphological shifts are driven more by collective dynamics than by individual cell responses. The enhanced interactions result in a greater likelihood of cells engaging with bifurcations, ultimately altering the morphological distribution observed in the network. This shift in morphological distribution in the network may be correlative to what is observed at the macroscopic scale, as Channel 4 at low hematocrit exhibits a much greater power-law exponent compared to Channel 3, which begins to converge with increasing hematocrit.

The results of morphological distribution, however, are counterintuitive to the expected macroscopic response. In the work of Noguchi and Gompper, dynamics of fluid vesicles and RBC in cylindrical capillary flow are studied by using a three-dimensional mesoscopic simulation approach. The authors found that non-axisymmetric discocytes transit to an axisymmetric parachute shape with increasing flow rate [55]. Similar resistance reduction is observed by McWhirter and colleagues when observing the collection of cells aligned to the flow compared to a zig-zag configuration [86]. Slipper-like shapes were observed around transition velocities, and the overall shape transition reduced the flow resistance. If morphological shape was simply the only factor that modulated the macroscopic resistance of the network, an increase in the resistance would be expected as there is an observed decrease in parachute-like morphology. What may be concluded then is that the elongation effect of increased flow rate supersedes the effect of resistance reduction that is imposed from morphological changes.

As previously observed in the morphological variations, an increase in the overall length indicated by the elongation index is observed and has been demonstrated analytically in the works of Secomb and colleagues to result in a reduction in pressure loss [49]. However, the contribution of extended parachute lengths to extended slippers is not well known.

3.6.4 Deformability Effects

Gluturaldehyde

In the experiments with glutaraldehyde (Figure 3.38), the scaling of the velocity with surface shear modulus for a given glutaraldehyde treatment from the works of Drochon [74] did not result in a singular universal excess relative resistance curve as a function of Capillary number. Compared to untreated control, 0.001% glutaraldehyde treated and 0.005% glutaraldehyde treated cells produced excess relative resistance that is within the regime of excess relative resistance magnitude of previously tested untreated RBC. While 0.01% glutaraldehyde treated cells were observed to result in an increase in the relative resistance an order of magnitude greater than the untreated sample.

In order to have the relative resistance of the 0.01% glutaraldehyde treated cells to approach a similarly scaled relative resistance, the rigidity of the cells must be an order of magnitude greater than that deduced from the work of Drochon. Using the approximation of change in surface shear modulus from the work of Abay and colleagues, an approximate 34-fold increase of the surface shear modulus compared to 3.4 observed in the works of Drochon, the excess relative resistance magnitude is found to trend closer to the untreated samples as shown in Figure 3.39. This variation in modifying the surface shear modulus can arise from the ratio of monomers and polymers in different glutaraldehyde batches, which has a significant influence on the fixation properties [73]. What is clear is that in order to properly characterize the effects of modulating the surface shear modulus on the relative resistance, an auxiliary measurement of the surface shear modulus is necessary.

A secondary effect observed in the glutaraldehyde experiments is a marked decrease in the power-law exponent. Based on current understanding, parameters known to influence the power-law exponent include the degree of cell confinement within the channels. Hydraulic resistance measurements for a Newtonian fluid indicate that the channel height is approximately 4.7 µm, which is slightly smaller than the height of 5.2 µm measured for the previous master wafer. This suggests that cells passing through channels produced from the new wafer should experience greater confinement, theoretically resulting in a higher power-law exponent.

The observed discrepancy might arise from the experimental conditions, particularly the regime of flow rates tested. It is possible that the flow rates have reached a saturation point in terms of cell deformation, placing the system in a regime where further increases in flow rate no longer elicit additional deformation of the glutaraldehyde-treated cells. Such saturation would diminish the sensitivity of the power-law exponent to confinement effects, thereby explaining the unexpected reduction in its value. Further investigation into the

specific deformation behavior of treated cells under varying flow conditions is needed to clarify this phenomenon.

Diamide

In order to compare transport in this case compared to the healthy cells, the excess relative resistance should be plotted as a function of the Capillary number. However, normalization of the mean velocity with the diamide experiment is complicated as the RBC morphology has changed with the protocol used to treat the cells with diamide (see Figure 3.41). In contrast with the findings reported in the existing literature [72], the application of the protocol resulted in a notable alteration of the cellular morphology, manifesting as an increased spherical shape. Diamide treatment induced significant morphological changes in the RBCs, as evident in a notable alteration in their surface area-to-volume ratio. Local imaging of treated cells reveals vesiculation and pinched membranes during passage through the network, indicating substantial structural changes. Since the surface area-to-volume ratio is crucial for cellular deformability, these changes likely impact the cells' ability to navigate confined channels. This is consistent with the behavior of capsules in confined channels, where confinement significantly affects deformability and flow dynamics.

Another factor to consider is the effect of diamide on the distribution of changes in surface shear modulus, which remains incompletely characterized. Prior work by Safeukui et al. suggests that diamide treatment skews the distribution of the Young's modulus, resulting in a heterogeneous population of cells with varying deformability. The macroscopic rheological response of a mixed population of deformable objects in a networked system remains unclear, particularly in terms of interactions between subsets of cells with differing mechanical properties [72]. Understanding how such heterogeneity influences flow resistance and network dynamics requires further investigation.

3.7 Conclusions and Future Work

In this work, the transport dynamics of RBCs in uniform microvascular networks are explored, emphasizing how interactions between cells and network nodes correlate with perfusion efficiency. First examining the macroscopic rheological response through the different network channels, a non-linear relationship between the excess relative resistance and Capillary number was observed. Two regimes are identified: a low capillary regime represented by a sharp decrease in the excess relative resistance and a high capillary regime represented by a plateauing of the excess relative resistance. The excess relative resistance

as a function of low Capillary number was found to scale with a simple power-law, with parameters dependent on the hematocrit and the porosity.

At low volume fractions, the excess relative resistance magnitude (f) scales linearly with hematocrit, but diverges more strongly from linearity in Channel 6 (3:2) than in Channel 3 (1:3) or 4 (1:0), with the main difference between them being the network porosity. At the local scale, variations in the velocity distribution and cell morphological distribution appear unrelated to changes in f. Additionally, cell cluster-size distributions remain independent of the Capillary number across all channels and are generally similar between the three channels. Nonetheless, the impact of cluster size on flow, particularly at higher hematocrit levels, warrants further study, as f differs more prominently under these conditions.

The power-law exponent (α) in the low-capillary regime decreases non-linearly with increasing hematocrit for Channel 4 (1:0) and 3 (1:3), converging to a constant value, but remains nearly constant for Channel 6 (3:2). At low hematocrit, Channel 4 exhibits the highest exponent, falling within expected literature ranges given the cell confinement ratio. The disparity between Channel 4 and Channel 3 and 6 at low volume fraction correlates with velocity field variations and differing cell morphologies. In Channel 4, cells display a narrow velocity distribution and fewer bifurcation interactions, resulting in more parachute-like shapes in its morphological distribution. By contrast, Channel 3 features frequent "bumping," producing more slipper morphologies. As hematocrit increases, an increase in cell-cell interaction results in bumping morphologies in Channel 4 becoming more similar to Channel 3. Interestingly, their α begins to converge with increasing hematocrit. In the high-capillary regime, α is notably lower, aligning with the observation that cell elongation plateaus at higher velocities.

The effects of RBC rigidification were also preliminarily investigated. Glutaraldehyde-treated cells exhibited elevated excess relative resistance, yet scaling the flow rate by a Capillary number that incorporated an estimated surface shear modulus brought the f close to that of healthy controls. Rigidified cells also displayed a reduced power-law exponent, indicating a possible saturation in deformability. However, further verification is needed since these tests were performed in new channels. By contrast, diamide treatment altered the RBC membrane surface area-to-volume ratio, inadvertently affecting flow resistance beyond mere changes to the shear modulus, thus complicating normalization. Overall, these results suggest that changes in RBC deformability may be captured using capillary-number scaling, but caution is required when surface area-to-volume ratios are also modified.

This work provides a framework in understanding the interplay between the local dynamics of cell passage in a microfluidic network and their contribution to overall macro-

scopic transport through the network. However, many open questions still need to be explored. In native blood, RBC are able to form reversible aggregates which are known to increase the bulk viscosity at low shear rates. Although trains of cells are observed at higher hematocrit in this study, these formations of trains appear to be associated with the geometric nature of the network. If cell aggregability were to be present in the network, would an excess relative resistance be observed similar to that of bulk viscosity measurements at low shear rates? Understanding the effects of aggregability will bring further insight on the microcirculatory flow and how it plays a role in influencing perfusion efficiency in physiological conditions.

Considering a wider biological context,from an evolutionary perspective, birds and mammals appear to have evolved two distinct strategies for ensuring efficient blood circulation in their high-metabolism tissues [87]. Birds typically have smaller genomes, which contribute to smaller RBCs that navigate microvasculature more easily. Mammals, on the other hand, produce enucleated RBCs with exceptionally resilient membranes, enabling high deformability and effective microcirculatory flow despite the lack of major internal repair mechanisms.The key question emerging from these observations is whether the evolutionary loss of RBC nuclei in mammals indeed confers superior flow properties in microcirculation. Answering this would involve comparing blood flow under identical conditions across species, thereby isolating the effects of RBC size, nucleus presence, and membrane properties. The framework of this study, which observes the interplay between local dynamics of cell passage with overall perfusion efficiency, can be further extended to explore and clarify how different evolutionary solutions influence microvascular efficiency.

3.8 Key Takeaways

Macroscopic Flow Response of Healthy RBC Suspension

Increasing the hematocrit reduces the flow rate at a given pressure due to the higher proportion of RBCs, lowering fluid mobility. Rescaling pressure and flow as excess relative resistance versus Capillary number reveals two regimes: a sharp decrease at low capillary numbers likely due to significant RBC deformation, and a plateau at high capillary numbers, indicating steady-state behavior.

Scaling of Macroscopic Response

The excess relative resistance follows a simple power-law model that scales with the Capillary number. The excess relative resistance magnitude is found to not only depend on the hematocrit, but also on the porosity of the network geometry, while the power-law exponent is dependent on the confinement ratio of the cells' passage, which shows good agreement with values from the literature.

Velocity Distribution

The local cell velocity distribution is primarily dictated by the topologies of the network, which broadens with increasing hematocrit. At low hematocrit, differences in velocity distribution are not correlated to the excess relative resistance magnitude but potentially to the power-law exponent due to changes in cell morphological distribution with increasing cell velocity.

Cell Clustering Effect

The cell cluster-size distributions remain independent of the Capillary number across all channels and are generally similar between the three channels. Furthermore, the cluster distribution shifts from single cell to multi-cell with increasing hematocrit.

Morphological Effects

The observed plateauing in the high capillary region appears to be correlated with the plateauing of the elongation of the cells, indicating a maxima to the cells' deformation. Morphological distribution differences at low hematocrit are correlative with differences observed in the power-law exponent between Channel 3 (1:3) and 4 (1:0).

Deformability Effects

Initial experiments on cell deformability indicate that an increase in cell rigidity using glutaraldehyde-treated cells results in an increase in the excess relative resistance. However, direct measurement of the surface shear modulus will be essential in scaling the excess relative resistance. In contrast, diamide-treated cells also resulted in an increase in excess relative resistance, but through the means of modifying the cells' surface area to volume ratio.

Chapter 4

Mixing in Microcirculation

Chapter Abstract

This study explores how the concentrated suspension of RBCs impacts the mixing of fluorescent macromolecules in the suspending phase. The goal is to determine whether the presence of RBCs enhance mixing in a suspension. Using a PDMS microfluidic co-flow device, experiments were conducted under varying RBC aggregability, volume fraction, and flow rates. Results show that both aggregating and non-aggregating RBCs enhance normalized effective diffusion, with an optimality at a nominal feeding hematocrit of 30%, which increases at higher flow rates. The enhancement in mass transport was also observed for molecules with increasing molecular weights. However, this augmentation does not appear to result from axial RBC translation, as the cells' effective diffusion does not correlate with the solute's enhanced diffusion in the fluid phase. Despite large axial migrations not being observed, cell-cell interactions and individual rotations have been shown to improve mixing in granular suspensions. These first observations show that RBC are not only essential bodies for the transport of oxygen but are also fundamental entities acting directly on the improvement of macromolecule mixing present in their liquid suspending phase.

4.1 Introduction

Rapid mixing is of essential importance in many microfluidic applications such as during homogenization of solutions of reagents used in chemical reactions, sequencing or synthesis of nucleic acids or protein crystallization. However, it is notoriously difficult to mix fluids

in microchannels at low Reynolds number conditions of laminar flow where molecular diffusion is usually insufficient to mix fluids in large channel sizes on the time scale of their usual residence time. Mixing is then more difficult for solutions containing macromolecules that have diffusion coefficients one or two orders of magnitude lower than that of ordinary small molecules [88, 89]. Figure 4.1(A) illustrates the minimal mixing that occurs in a microfluidic channel under laminar flow, a property used in microfluidics. This mixing problem is crucial in blood flow in particular. Blood transports oxygen by red blood cells (RBCs) as well as proteins, glucose, mineral ions, and hormones to all the cells of the body through the microcirculation, and a well-mixed state is essential for these transfers.

Furthermore, physiological activities such as the formation of thrombi and atherosclerotic plaques are directly influenced by the transport of macromolecules. Gaining insights into the transport rates of these macromolecules is therefore vital for comprehending the underlying mechanisms of complex pathological processes [90]. In parallel, during the past few decades, synthetic micro- and nano-particles have also been transported by the blood stream used as drug, gene, and/or imaging delivery vehicles [91], and their mixing and availability near the vessel walls are a prerequisite to their function.

Quantitative insights into mixing scales, influenced by factors such as Brownian diffusivity, shear rate, particle properties, particle dispersion, channel topologies, and aggregation, are valuable for advancing diagnostic tools and designing artificial organs. Figure 4.1(B) illustrates an in vitro microcirculatory network, showing minimal axial migration across streamlines as cells converge into a venule channel similar to that observed in a single-phase laminar flow microfluidic device.

4.2 Background

At the microcirculatory scale, the transport of blood typically resides in the limit of low Reynolds and high Péclet [1] numbers regime. This limitation makes the isolation of solutes in micro-devices simple and enables laminar flow-patterning techniques, but for situations where the mixing of solutes is essential, this limitation is a challenge. This has given rise to studies of chaotic advection applied to microfluidics where the flow field through the device is designed to increase mixing by using deterministic flow fields to amplify local mixing by diffusion [88]. Unless microfluidic devices are designed specifically to generate

[1] Péclet number is the dimensionless number that relates the advective transport rate to diffusive transport rate. Commonly expressed as $Pe = lV/D$, where l is the characteristic length, V is the characteristic velocity, and D is the mass diffusion coefficient.

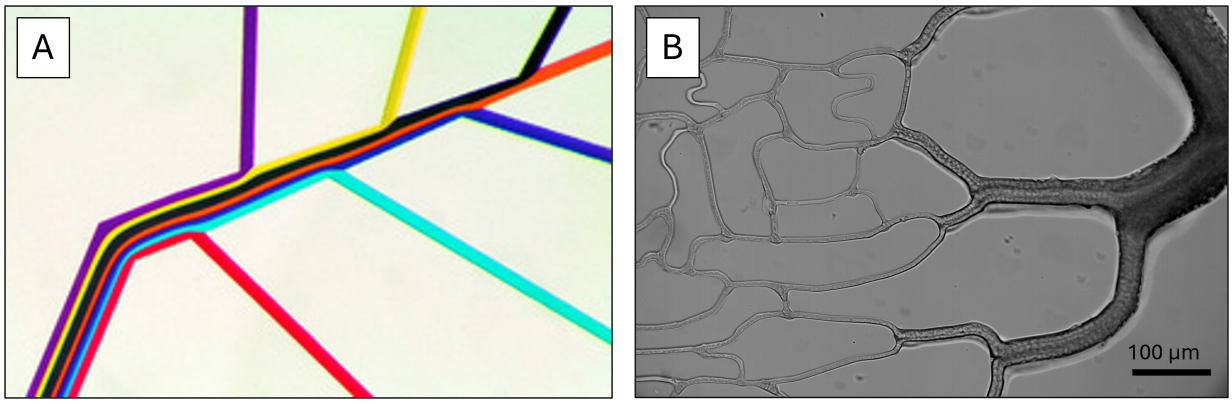


Figure 4.1: (A) A visual representation of fluid mixing in a microfluidic channel under laminar flow demonstrates minimal mixing (Reproduced from [92]). (B) An in vitro illustration of a microcirculatory network of branching channels illustrates the minimal extent of cell diffusion, as indicated by the prolonged streaks of heterogeneous distribution. The streak-line showcase the lack of mixing between two RBC streams (Reproduced from [93]).

flow structures that can shorten diffusion length scales, mixing is often a slow process at the mesoscale.

Experimental evidence in suspension rheology strongly suggests that the presence of a velocity gradient enhances heat and mass transfer within the suspension [90, 94, 95]. In the case of suspensions composed of rigid particles, two primary mechanisms have been proposed to explain this phenomenon. The first mechanism involves particle rotation, which induces local mixing within the surrounding fluid. As the particles rotate, they create disturbances and fluid motion that enhance the transfer of heat and mass within the suspension. The second mechanism is known as shear-induced collision diffusion. In this mechanism, particle interactions or collisions result in a net lateral displacement of the particles, accompanied by associated motions in the suspending phase. These interactions and motions contribute to improved mass transfer throughout the suspension; however, only shear-induced diffusion can cause migration the particles themselves [90, 96].

4.2.1 Microcirculatory Blood Transport and Mixing

Augmenting the mass transport through blood suspension is of great interest due to the function of blood in the cardiovascular system as well as the development of extracorporeal devices such as dialyzers and blood oxygenators where mixing is of the essence in the functionality. Mass transport augmentation in RBC suspensions has been studied observing

the transport of ferricyanide [90], urea [95], bovine serum albumin [97, 98], oxygen [99], and platelets [100].

In the study by Wang and Kellert [90], the mass transport of ferricyanide was measured normal to the direction of the bulk flow in a Couette flow using a Couette cell with a gap width of 460 µm to the surface of the cell. Blood samples of human, bovine, and rabbit in the form of normal, hardened, and ghost RBCs were observed. In this work, it was found that the augmentation (A) of the mass transport is correlated with the Péclet number (Pe), and their data was well described by $A = \alpha * Pe^{\beta}$ where the α and β coefficients are dependent on the particle volume fraction and rigidity of the RBC. For volume fractions up to 10%, particle deformability was not found to augment mixing significantly, while for more concentrated suspensions, the normalized augmentation increases for hardened cells, while it decreases for normal and ghost cells [90]. This is in contrast to the study by Cha and Beissinger [98], where bovine serum albumin was measured at the surface using a total internal reflection fluorescence method to determine the effective diffusivity through a rectangular channel in a ghost cell suspension. It was found that the augmentation of the mass transport, scaled with the Péclet number as found in previous studies, while the normalized augmentation increased with volume fraction to a maximum at 45% RBC hematocrit, after which a decrease was observed. This observed optimality was explained as a reduction of rotational and translational motion of the RBCs due to increased particle-particle collisions at higher volume fraction.

In the current literature of mass transport of macromolecules through RBC suspension, the focus has been primarily on the transport from the bulk RBC suspension to the surface where the absorption of the macromolecule of interest can be measured. What currently lacks in the study of mass transport is the observation of the transport through the bulk itself where mixing occurs between the RBCs. Furthermore, there also is a lack of studies looking at the effect of mixing in the context of RBC aggregation as in physiological conditions the presence of proteins, primarily fibrinogen, in the suspending phase allows for the formation of linear RBC aggregates.

4.2.2 Mass Transport Scaling for Single Phase Fluids

In the work of Ismagilov and colleagues, diffusion of low molecular weight species is experimentally and theoretically quantified across the interface between two aqueous single-phase solutions in a pressure-driven laminar flow microchannel at high Péclet numbers and low Reynolds number demonstrated in Figure 4.2 [101]. At steady state, the width of the mixing region at the interface adjacent to the wall of the channel and transverse to the

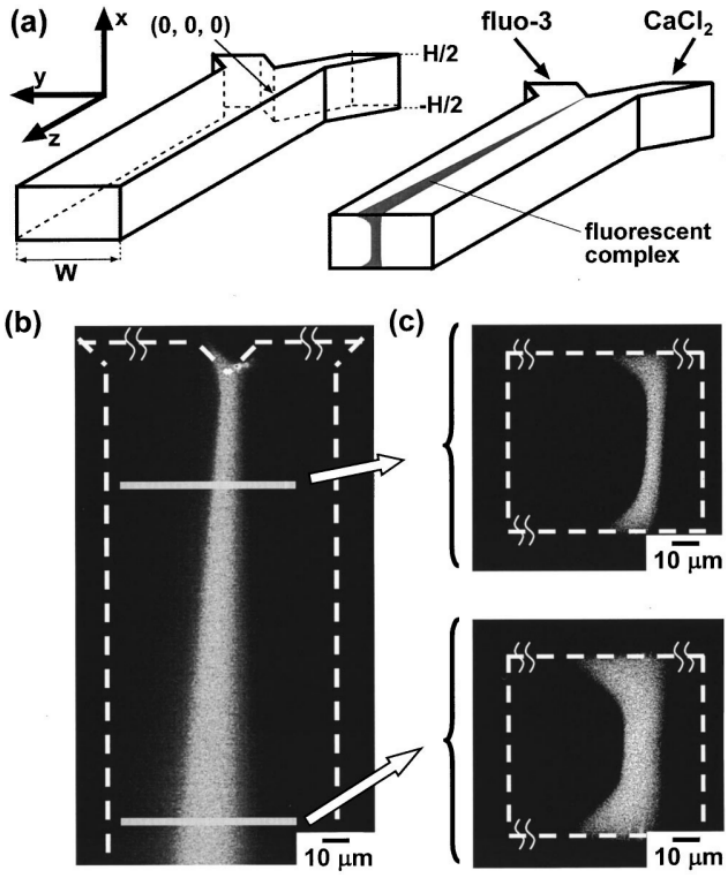


Figure 4.2: (a) Schematic of the co-flow microfluidic design to generate fluorescence gradient. (b) and (c) indicate fluorescence data by confocal fluorescence microscopy in y-z and x-y planes, respectively. (Reproduced from [101])

flow scales as one third power of the axial distance and the average velocity of the flow, while at the center of the channel the width of the mixing region scales as the one half power of the axial distance and the average velocity. The difference in the scaling law when comparing the broadening of the mixed region at the walls compared to at the center of the channel can be attributed to a skewed diffusive distribution, which is a direct consequence of the three-dimensional hydrodynamics of pressure-driven channel flow. The scaling of the mass transport is confirmed with numerical simulation by Kamholz and Yager, which further confirms that secondary concentration gradients yield variation in the scaling behaviour [102].

4.3 Objective

Despite blood's primary role in transporting nutrients and gases, the mechanisms of mixing within blood remain poorly understood. This study investigates how the concentrated suspension of RBC influences the mixing process in the body. Using rectangular polydimethylsiloxane (PDMS) microchannels, we examine the mixing of fluorescent macromolecules in RBC suspensions at varying volume fractions and flow rates near physiological conditions. The study evaluates the enhancement of mass transport in both non-aggregating and aggregating RBCs configurations, addressing how the RBCs presence impacts mixing at the microcirculatory scale. To address this question, the following objectives are pursued:

- Investigate the effects of non-aggregating and aggregating cells, hematocrit, and flow rate on augmenting the mixing of the solute in the suspending fluid.
- Explore the mechanism behind the augmentation of the mass transport through the bulk suspension.
- Investigate the impact of increasingly higher molecular weight molecules on transport through a dense suspension.

4.4 Methods

This section details the design of the PDMS channel, the specific preparation of RBC samples under both non-aggregating and aggregating conditions, and the experimental setup for the confocal microscope. Additionally, the 2D advection-diffusion model used to determine the effective diffusion coefficient is presented.

4.4.1 Microfluidic Device

A PDMS microfluidic co-flow channel design with a rectangular cross-sectional area schematic of PDMS junction channel design with 67 µm width (W) and 40 µm height (H) cross-sectional area. An example wafer and a schematic of the microfluidic channel design are presented in Figure 4.3 and the general fabrication methodology using PDMS is reported in Section 2.1.1.

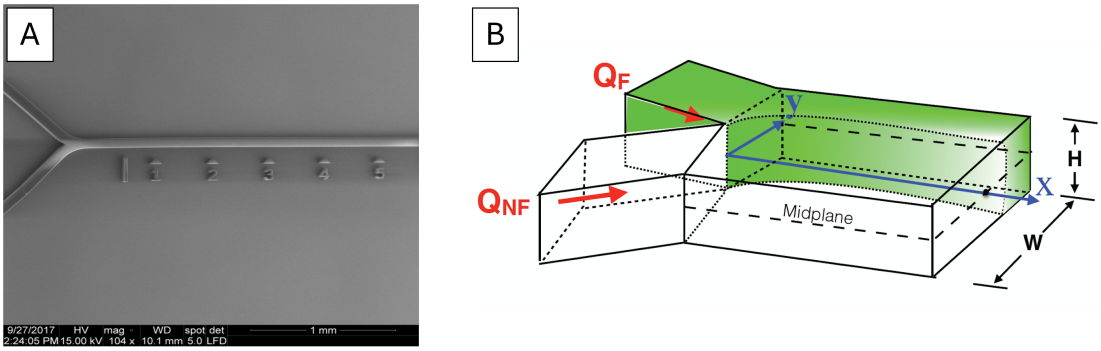


Figure 4.3: (A) Imaging of the SU8 master wafer and (B) schematic of the microfluidic co-flow design. The nominal cross-sectional area of the straight joined channel is designed to have a width (W) of 67 µm and height (H) of 40 µm.

4.4.2 Sample Preparation

In this work, both healthy non-aggregating and aggregating human RBC are flowed in the co-flow channel at a nominal feeding hematocrit between 10% and 60%. The preparation of the blood sample is described in Section 2.2. The preparation of the fluorescent dye or fluorescent dextran, and cell mask are presented in this section.

Fluorescent dye or fluorescent dextran

To quantify the mixing process through a dense suspension, fluorophore dye specifically Alexa 488 or fluorescent dextran (with molecular weight of 10 kDa, 70 kDa,150 kDa, or 2000 kDa) is added to half the sample. To inoculate the sample with the dye and measure the fluorescent intensity profile, 20 µL of 50 µmol/L dye is added to 1 mL sample solution and gently mixed by rocking the Eppendorf.

Cell mask

To quantify the axial migration of the cells, the RBC membrane is stained with a solution of CellMask plasma membrane stain (C37608, ThermoFisher). This is accomplished by preparing a fresh solution of the CellMask plasma stain in a warmed phosphate buffered saline (PBS) solution, submerging the cell suspension into the staining solution for 5 to 10 minutes at 37 °C. Followed by washing the RBC in PBS solution three times. The stained cells are then re-suspended to the appropriate feeding hematocrit to be tested immediately.

4.4.3 Experimental Setup

A PDMS microfluidic co-flow channel design with a rectangular cross-sectional area is used to quantify mixing in blood at different RBC hematocrits. Using a confocal microscopy setup, two RBC samples of identical volume fraction (where one was dyed with Alexa 488) are flowed together in the channel, and the fluorescent intensity of the profile is measured along the length of the channel.

Experiments are completed on a Zeiss LSM800 confocal microscope setup equipped with a water immersion 63x objective lens. The microfluidic device is clipped to the microscope on a piezo-controlled electronic stage in which the focus of the microscope is automatically set to be the mid-plane of the microfluidic device by using the built-in autofocus with offset function of the Zeiss Zen application. For this study, the two fluids are injected into the channel using two independent syringe pumps with a flow ratio of 1:3 where the fluorescent dyed sample is flowing at the slower flow rate. The result is that a quarter of the total fluid is fluorescent (either using Alexa 488, red blood cell mask, or fluorescent dextran) at the junction as it flows into the rectangular PDMS chips that are approximately 67 µm in width 40 µm in height. Measurements are taken at seven positions (outlined in Appendix B.5) up to 10 mm along the length of the channel relative to the entrance junction. At each position, a 2048 by 1280 pixel scan is taken at the mid-plane and 1 µm above and below the mid-plane. The Zeiss microscopy stage is programmed to return to the preset positions to complete measurements at the same position for different flow conditions. A schematic of the experimental setup is composed in the following Figure 4.4. An alternative experimental setup using a pressure control system and flow meter is proposed in Appendix B.1.

4.4.4 Data Acquisition and Analysis

As described previously, measurements of the intensity profile are completed at seven positions along the length of the channel relative to the channel junction. The position of each gradation taken is summarized in Table B.3 in Appendix B.5. Measurements are completed for nominal feeding hematocrits between 0% and 60%. The fluorescent and non-fluorescent sides are matched to have the same blood and volume fraction of cells and are flowed into the channel in a 1:3 ratio. This is done for total input flow rates between 25 µL/h and 400 µL/h. Given the dimensions of the channel and total input flow rate, the Péclet number of the system ranges from 156 to 2493. A summary of the experimental configuration is outlined in Appendix B.5.

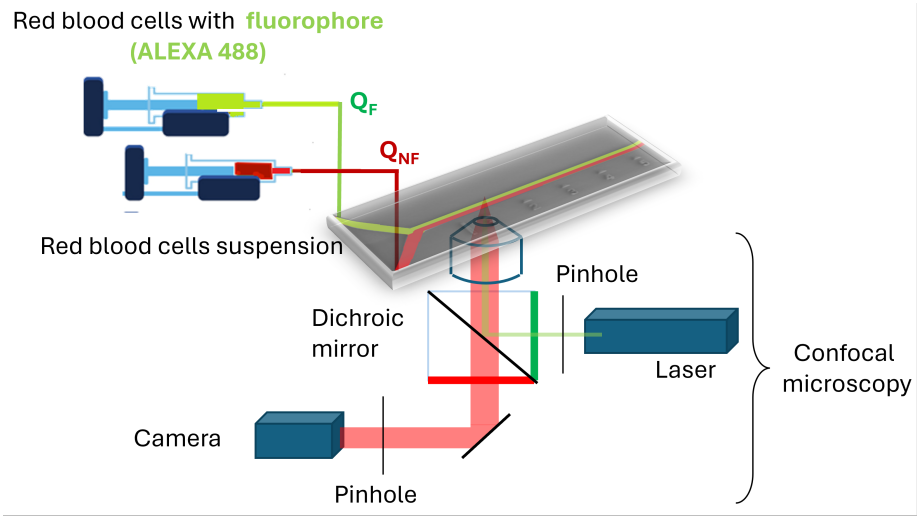


Figure 4.4: A PDMS microfluidic coflow channel with a rectangular cross section area to quantify mixing in blood at different cell volume fraction are used. Two samples of identical volume fraction of RBCs with one dyed with Alexa 488 that is flowed together in the channel and measure the fluorescent intensity profile at different positions along the length using a confocal microscopy setup.

Fluorescent intensity imaging at each position consists of a 2048 by 1280 pixel scan taken at the mid-plane and 1 µm above and below the mid-plane. To extrapolate a spatially averaged fluorescent intensity profile for a given position away from the junction, the three images are rotated to have the channel alignment to be horizontal. The three images taken at the different heights around the mid-plane are averaged to create an average fluorescent intensity image, which is then averaged along the length of the channel. The result is a spatially averaged fluorescent intensity as a function of the width of the channel that integrates the small variation in channel height and along a length of the channel. An example of the confocal scanning fluorescent imaging in the co-flow channel is depicted in Figure 4.5(A). A schematic of the mid-plane of the channel and an example of a spatially averaged intensity over the width are presented in Figure 4.5(B) and Figure 4.5(C), respectively. Due to wall effects, the confocal scan close to the channel walls has a reduction in intensity as observed at $y = 0.5W$ in Figure 4.5(C). Each position along the length of the channel has a spatially averaged fluorescent intensity image that is then individually fitted with a fitting model to extract a characteristic diffusion length and the effective diffusion coefficient. An example of the spatially averaged fluorescent intensity of the seven positions and the associated fits is presented in Figure 4.5(D).

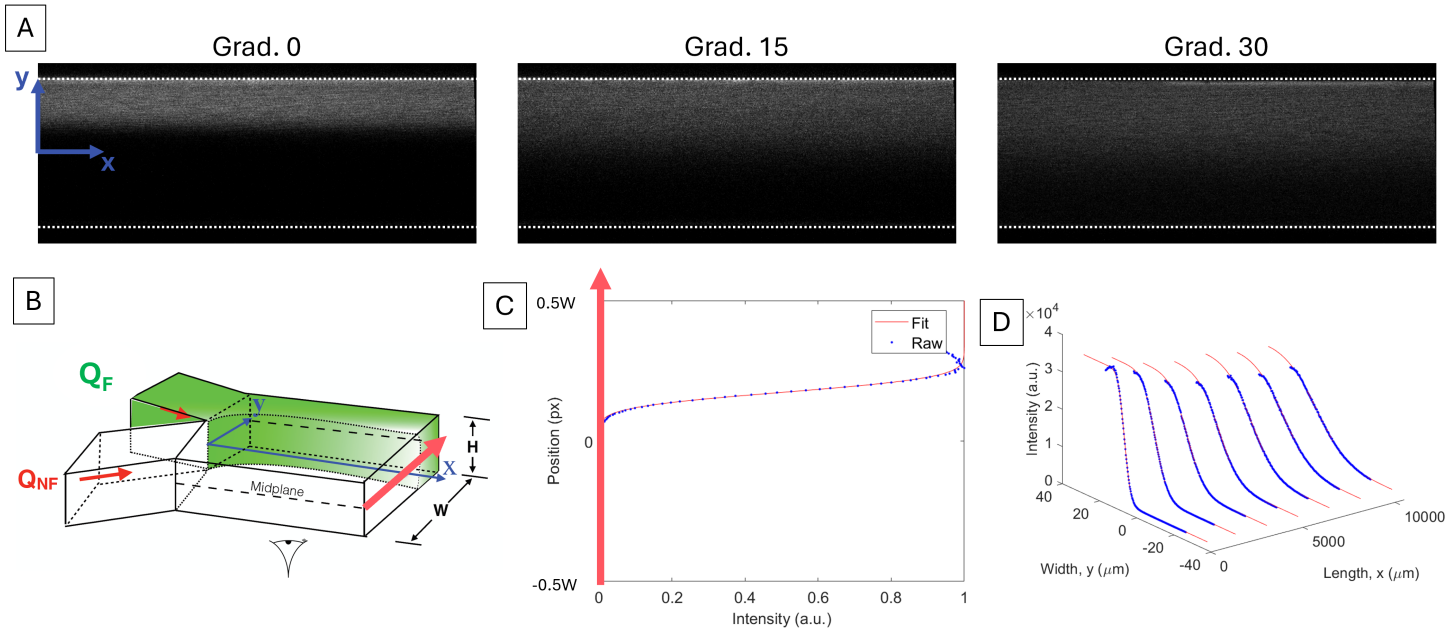


Figure 4.5: (A) An example of raw fluorescent imaging of the cells taken at different graduations along the length of the channel with walls marked out as dotted white line and the reference position of measurement. (B) Schematic of PDMS junction channel design with 67 µm width (W) and 40 µm height (H) cross-sectional area. The input through both branches share the same blood feeding hematocrit, however the input of the fluorescent labeled fluid (either using Alexa 488 in the suspending fluid or marking the red blood cells) enters at an input flow rate (Q_F) that is 1/3 the rate of the non-fluorescent fluid input fluid rate (Q_{NF}). A confocal microscope scans the light intensity at the mid-plane of the channel at different positions along the length (x) of the channel. The reference position is taken as the junction point of the two branches. (C) The spatially averaged fluorescent intensity along the width of the channel (y direction) are fitted with a 2D analytical model of the advection-diffusion transport described in Equation (4.2). (D) The spatially average fluorescent intensity of the different positions are plotted together with the fits indicated as solid blue line. The change in fluorescent intensity showcases the mixing through the non-fluorescent sample with increasing x.

Modeling the mass transport

To simplify the mass transport equation (as described in Appendix B.2) the following assumptions are applied. In a shallow microfluidic device where the width is much larger than the depth of the channel, the flow can be approximated as a Hele-Shaw flow, and so velocity variation is only dependent on the depth. The solute diffusion in the direction of the flow can also be neglected in an advection-dominated regime in the stream-wise direction, as indicated by an estimated Péclet number between 156 and 2493. Furthermore, the solute concentration is assumed to be diffused across the channel depth and becomes independent of the depth. Thus, the mass transport equation simplifies to:

$$V\frac{\partial \mathbb{C}}{\partial x} = D\frac{\partial^2 \mathbb{C}}{\partial y^2} \tag{4.1}$$

where $\mathbb{C}$ is the concentration of the solute in the fluid, V is the velocity along x, and D is the diffusion coefficient.

For parallel co-flowing channels where the fluorescent dye occupies a portion of the channel width, the initial condition is $\mathbb{C}(x=0,y) = \mathbb{C}_1 + (\mathbb{C}_2 - \mathbb{C}_1)\ H(y)$, where H is the Heaviside step function, $\mathbb{C}_1$ and $\mathbb{C}_2$ are the initial fluorescent concentrations of the low and high steps, and the boundary condition assumes no-flux through the surface walls. The solution of the simplified mass transport can be solved using the method of images, also known as the method of reflection and superposition, discussed in the works of Crank for a finite system under an enclosed boundary [89]. The concentration field ($\mathbb{C}$) can be described as:

$$\mathbb{C}(x,y) = \mathbb{C}_1 + \frac{\mathbb{C}_2 - \mathbb{C}_1}{2}\sum_{k=-\infty}^{\infty}\left[erf\left(\frac{y - \frac{w}{4} + 2wk}{\sqrt{\frac{4\ \mathbf{D}x}{V}}}\right) - erf\left(\frac{y - \frac{3w}{4} + 2wk}{\sqrt{\frac{4\ \mathbf{D}x}{V}}}\right)\right] \tag{4.2}$$

where $\mathbb{C}_1$ and $\mathbb{C}_2$ are the initial fluorescent concentrations at the entrance where the two fluids interface, w and h are the width and height of the channel, D is the effective diffusion coefficient, and V is the velocity in the x direction.

As a simplification, the terms in the denominator of the error function can be written as a function of the diffusion length (δ) that describes the width or the dispersion of the error function. The diffusion length provides a measure of how the concentration has propagated in the channel. The diffusion length can thus be written as:

$$\delta \propto (Dt)^{\alpha} \propto \left(\frac{Dx}{V}\right)^{\alpha} \tag{4.3}$$

where D is the effective diffusion coefficient and t is the mean advection time defined as the ratio of the position along the length of the channel (x), and the mean velocity (V). The mean velocity is then defined as the ratio of total input flow rate to the total cross-sectional area. The width of the mixing region at the interface adjacent to the wall of the channel and transverse to the flow is expected to scale as one third power of the axial distance and the average velocity of the flow, while at the center of the channel the width of the mixing region is expected to scale as the one half power of the axial distance and the average velocity as described in the work of Ismagilov and colleagues [101].

For each position along the length of the channel, a spatially averaged fluorescent intensity as a function of the width (y) is fitted to extract a diffusion length (δ) at that given position. The diffusion length can then be described as a function of the mean advection time for each position at a given total input flow rate. Furthermore, assuming a scaling of one half ($\alpha = 0.5$), an effective diffusion coefficient (D) is extracted for each position.

4.5 Results

The following section presents the results on the scaling observed for the diffusion length as a function of advective time in the co-flow channel. Then the effects of aggregation on augmenting the mixing transport and how it differs for solutes of different molecular weights are presented.

4.5.1 Diffusion Length as a Function of Time

The first observation is on how the width of the mixing region increases over time. The width represented by the diffusion length (δ) as a function of mean advection time (t) in log-log format presents linear regions indicative of a power-law behavior as shown in Figure 4.6 for three sample configurations: non-aggregating RBCs, aggregating RBCs with plasma, and aggregating RBCs with dextran-70 for hematocrits ranging between 0% and 60%.

The δ can then be fitted with a simple power-law model with t and parameters that depend on the hematocrit (ϕ) in the following general form:

$$\delta \sim A(\phi) \cdot t^{n(\phi)} \tag{4.4}$$

where the extracted scaling factor (A) and power-law index (n) are dependent on the hematocrit (ϕ) and represent the rate at which mixing is achieved with t.

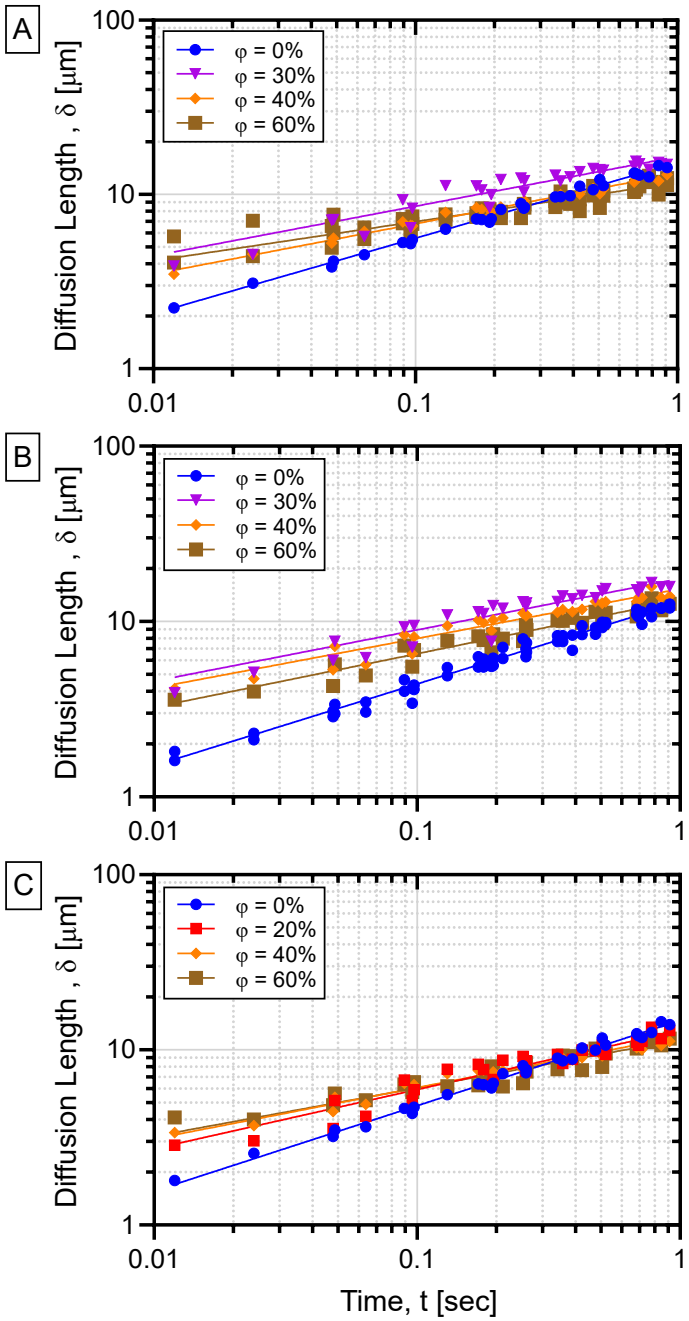


Figure 4.6: The diffusion length (δ) as a function of mean advection time (t) for the suspending fluid and RBC suspension at increasing hematocrit (ϕ) for (A) non-aggregating, (B) aggregating in plasma and (C) aggregating RBCs in dextran-70. Each hematocrit which contains the diffusion length of all input flow rate and position is fitted with a power-law model (indicated by the solid line) up to $t = 1$.

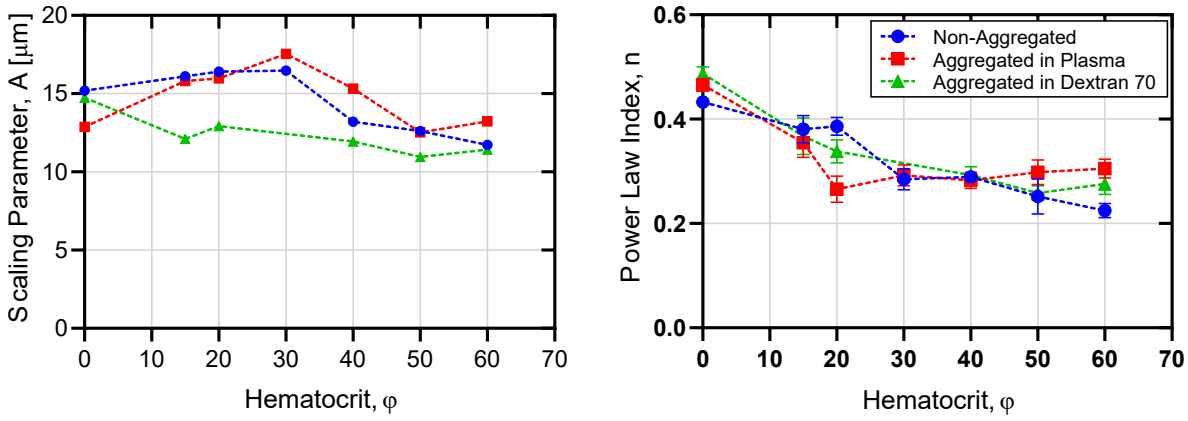


Figure 4.7: The fitted parameter of power-law model of Figure 4.6 is presented for the scaling factor, A, and the power coefficient, n, over the total diffusion length measurement. The fits are extracted over the diffusion length as a function of mean advection time that consists of all flow rates and position up to $t = 1$. The error bar represents the standard error while the dashed line between data points is for clarity.

The extracted fitting parameter with the proposed power-law for the three fluid configuration is plotted against the nominal feeding hematocrit in Figure 4.7. The error bar represents the standard error measurement, and the dashed line is presented for clarity of the trend. The scaling factor is found to have a non-monotonic increase for non-aggregating and aggregating samples in plasma, while a general decrease is observed for the aggregating sample in dextran-70 . The power-law index, on the other hand, presents a decrease in magnitude with increasing hematocrit for the non-aggregating and both aggregating samples. The power-law evolves between n $\approx$ 0.5 to n $\approx$ 0.3 or 0.2 depending on the aggregating medium.

4.5.2 Aggregation Effects

To contrast the augmentation to the mass transport between the different hematocrit, the spatially averaged normalized effective diffusion coefficient is presented as a function of the feeding hematocrit in Figure 4.8 for increasing input flow rate. The spatially averaged normalized effective diffusion is the ratio of the effective diffusion coefficient obtained at the given hematocrit to the effective diffusion coefficient obtained without cells ($\phi = 0$). The spatially averaged normalized effective diffusion coefficients are organized by non-

aggregating and aggregating RBC samples. The spatially averaged normalized effective diffusion coefficient reveals that there is a non-monotonic increase between the mass transport of the solutes in the suspending phase, with an optimality around the 30% hematocrit. The augmentation of the spatially averaged normalized diffusion coefficient is observed to increase with increasing input flow rate, which demonstrates a shear-enhanced diffusion.

The spatially averaged normalized effective diffusion coefficient as a function of input flow rate for the aggregating RBC with plasma is presented in Figure 4.9. Error bars represent the standard deviation of the spatial averaging of the measured diffusion coefficient, while a dashed line is presented for clarity of the data points. The effective diffusion coefficient as a function of the flow rate was observed to increase linearly with an increase in input flow rate.

4.5.3 Transport of Molecules of Increasing Molecular Weight

Another question that is raised is how the mass transport is augmented for objects of increasing molecular weight, or in other words, molecular size. The molecular size is described as the Stokes radius, which is the radius of an equivalent hard sphere that diffuses at the same rate as that solute. The spatially averaged normalized effective diffusion coefficient versus the Stokes radius of dextran of increasing molecular weight between 10 kDa and 2000 kDa in a 30% nominal feeding hematocrit solution at different total input flow rates is presented in Figure 4.10 . The inset of the figure presents the effective diffusion coefficient as a function of Stokes radius of the increasing molecular weight dextran without the presence of cells.

The effective diffusion coefficient decreases with increasing Stokes radius in the absence of cells (observed in the inset of figure 4.10), as expected from the Stokes-Einstein relationship ($D = k_b T/6\pi\eta R_{hyd}$) which describes the inverse relationship between the diffusion coefficient of spherical particles and its size in a liquid at low Reynolds number. However, in the presence of cells (at which 30% is selected for the observed optimality), the spatially averaged normalized effective diffusion coefficients increase with increasing Stokes radii. The presence of RBCs in the microcirculation appears to minimize the effect of slower diffusive properties with increasing molecular size. The normalized effective diffusion coefficient not only is affected by the shear but it also depends on the molecular weight as well.

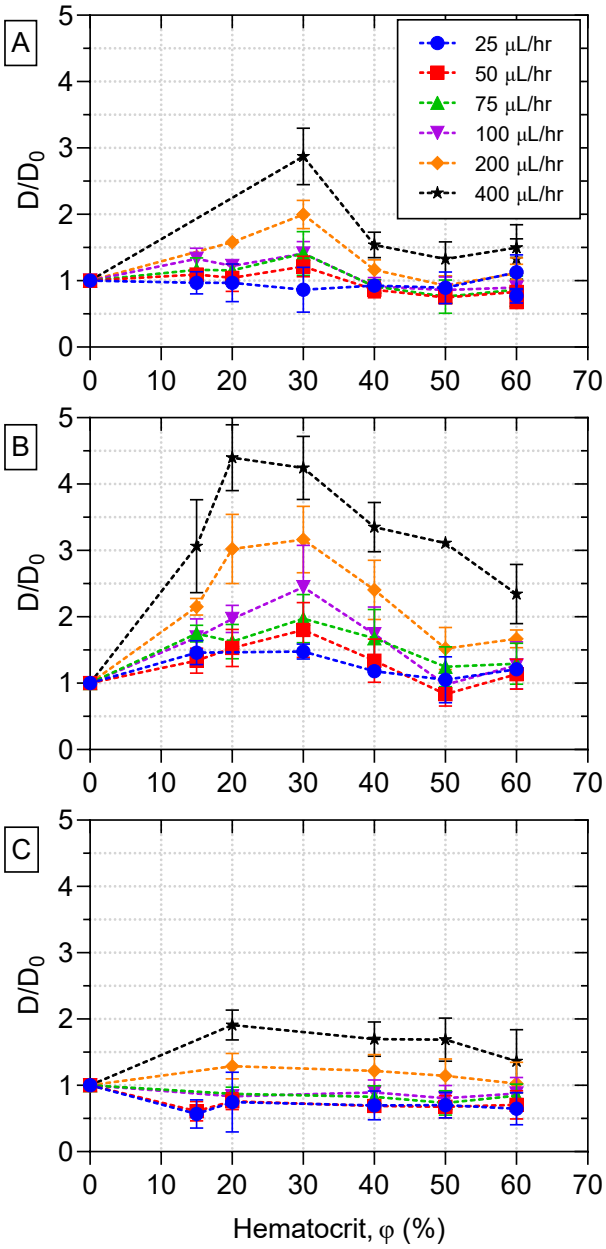


Figure 4.8: Spatially averaged normalized effective diffusion coefficient (D/D_0) between three positions (i.e. 3729 µm, 5429 µm, and 7129 µm) downstream from channel junction function of feeding hematocrit (ϕ) at different total input flowrates for (A) non-aggregating RBCs, (B) aggregating RBCs with plasma, and (C) aggregating RBCs with dextran-70. Error bars represent the standard deviation of the spatial averaging, while the dashed lines are connecting data points for clarity.

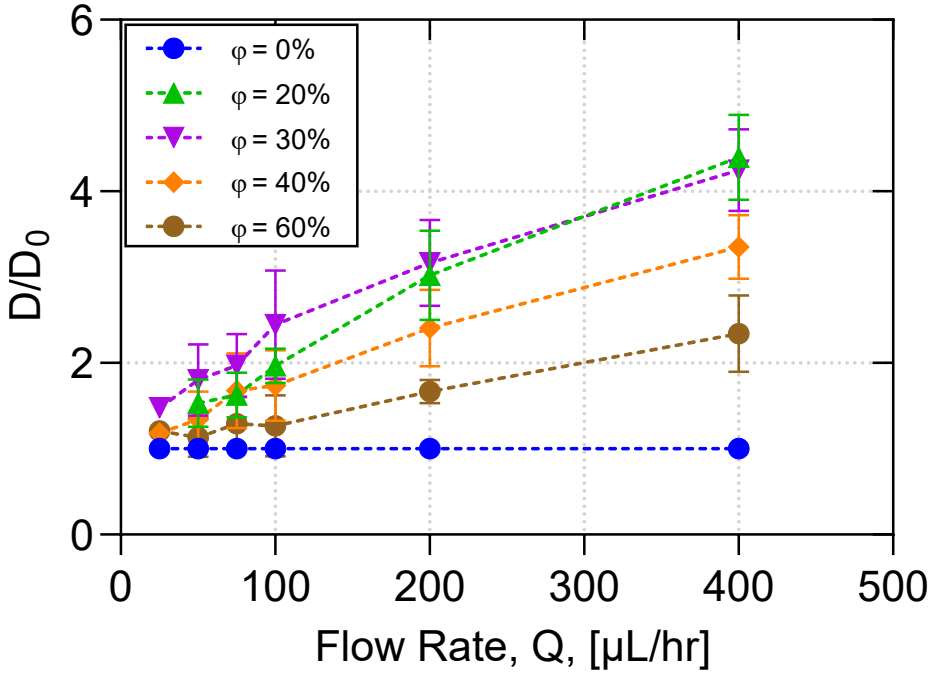


Figure 4.9: Spatially averaged normalized effective diffusion coefficient (D/D_0) between three positions (i.e. 3729 µm, 5429 µm, and 7129 µm) downstream from channel junction as a function of total input flow rates (Q) for aggregating RBCs in plasma. Error bars represent the standard deviation of the spatial averaging, while the dashed line are connecting data points for clarity.

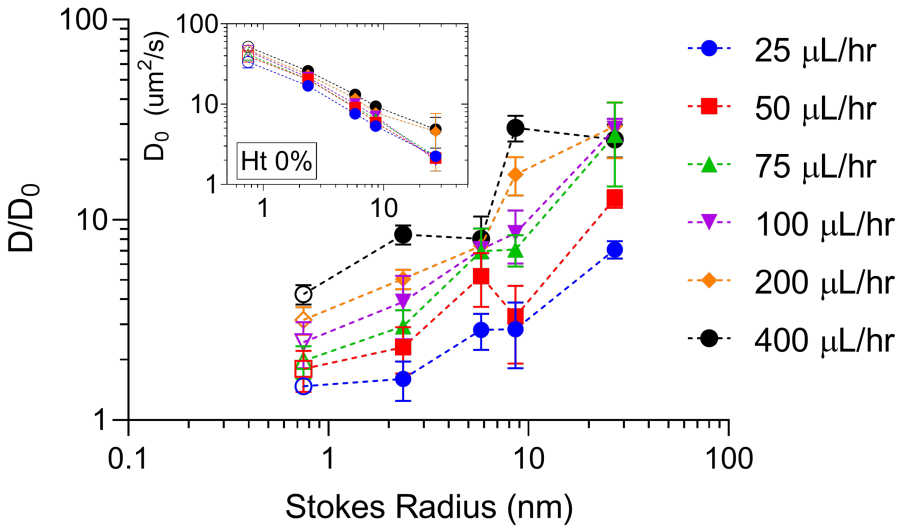


Figure 4.10: Spatially averaged effective diffusion coefficient (D/D_0) versus the Stokes radius of Alexa 647 (hollow points) and Dextran (solid points) at 1% dilution for increasing molecular weight Dextran (Dextran 10 kDa, 70 kDa, 150 kDa and 2000 kDa) for 30% hematocrit sample. The spatially averaged diffusion coefficient (D_0) with the inset of the 0% hematocrit experiments. Error bars represent the standard deviation of the spatial averaging, while the dashed line are connecting data points for clarity.

4.5.4 Cell Axial Diffusivity

One possible mechanism behind an augmentation of the diffusion coefficient may simply be an effect of axial migration of the cells crossing streamlines. To test this hypothesis, the cell membrane is stained to observe the transport of cells from one side of the channel to the other. Figure 4.11 depicts the spatially averaged effective diffusion coefficient for increasing nominal feeding hematocrit samples for both non-aggregating and aggregating samples using dextran-70. For each data point, the diffusion coefficient is averaged between three positions along the length of the channel at 3729 µm, 5429 µm and 7129 µm away from the junction.

Unlike the spatially averaged normalized effective diffusion coefficient of molecules, the cell mask representing both non-aggregating and aggregating RBCs does not show an optimality with hematocrit but instead a minimum. Furthermore, the absolute diffusivity of the cell mask is significantly lower than that of molecules in the suspending fluid, indicating that increased molecular diffusivity is not necessarily driven by large-scale cell diffusivity. Figure 4.11 illustrates the effective diffusion of red blood cells, averaged along the central channel position, confirming this trend.

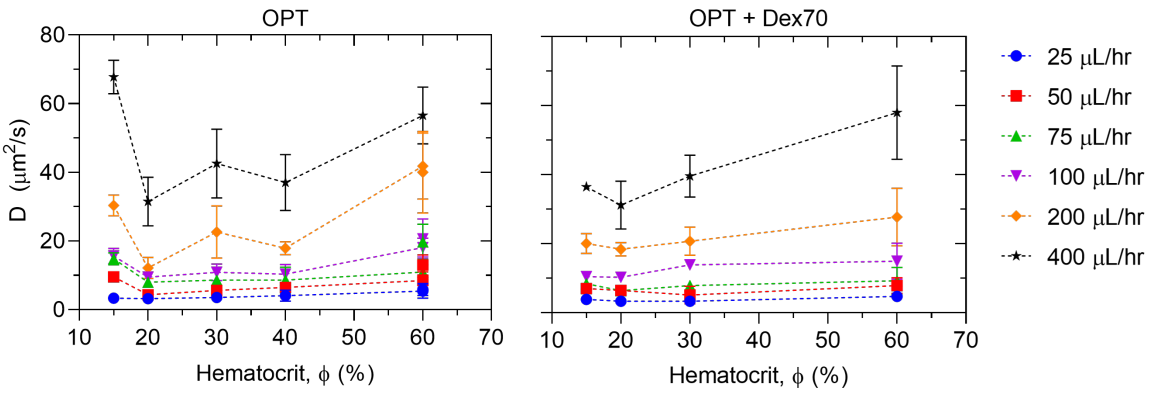


Figure 4.11: Spatially averaged effective diffusion coefficient (D) as a function of the nominal feeding hematocrit (ϕ) for non-aggregating (OPT) and aggregating (OPT + Dextran-70 solution) RBC samples. Error bars represent the standard deviation of the spatial averaging, while the solid lines are connecting data points for clarity.

4.5.5 Interface Location (3:1 vs 1:1)

A secondary mechanism behind an augmentation of the diffusion coefficient may be an effect of an increased shear rate from the position of the interface. To test this hypothesis, the position of the interface is changed by modifying the flow ratio feeding into the channel. Figure 4.12 shows the spatially averaged normalized diffusion coefficient of Alexa 488 as a function of RBC volume fraction for the 1:3 flow ratio as observed previously to an example of 1:1 flow ratio for non-aggregating RBC sample at increasing hematocrit. Comparing the normalized effective diffusion coefficient, the previously observed optimality that was observed in a 1:3 flow ratio is instead replaced by a monotonic decrease in the normalized diffusion coefficient.

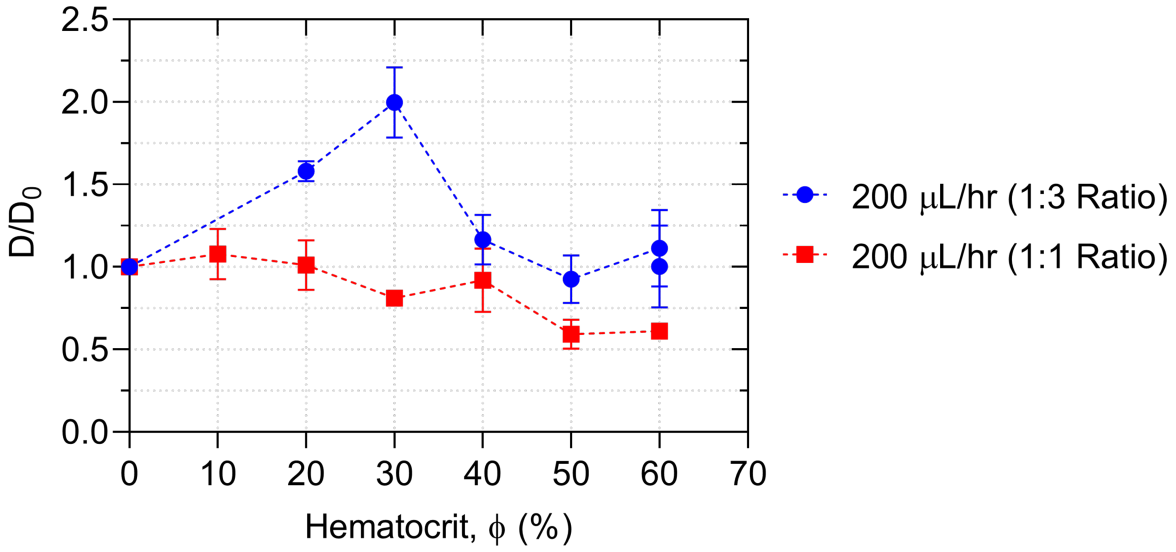


Figure 4.12: Normalized effective diffusion coefficient (D/D_0) of Alexa 488 as a function of the feeding hematocrit (ϕ) at flow ratio of 1:3 and 1:1. Dashed lines is placed between data points for clarity.

4.6 Discussion

4.6.1 Diffusion Length Scale

The diffusion length (δ) as a function of the mean advection time (t) is found to follow a power-law scaling. From the scaling parameter in Figure 4.7(left), an optimal scaling is observed for non-aggregating RBC and aggregating RBC with plasma at approximately 30% hematocrit. In contrast, aggregating RBC in dextran-70 shows decreasing scaling with increasing hematocrit. This difference between aggregation with plasma and aggregation with dextran-70 may be associated with the type of clustering. In the work of Chen and colleagues on monitoring RBC aggregate morphology under flow, RBC aggregates with dextran-70 have been reported to form clusters compared to plasma, which forms rouleau aggregate structures [103]. Since aggregation is a reversible process, how different sizes of aggregates distribute in the channel and how they may migrate axially may then also augment the mixing process in flow. This mechanism of cell motion will be further explored later in this work.

For the diffusion length scaling with time as observed in Figure 4.7, the power-law index for the no-cell condition is approximately 0.462 across the non-aggregating, plasma-aggregating, and dextran-70-aggregating cases. This scaling aligns with the expected magnitude for simple diffusive transport between single-phase fluids away from a solid boundary. As described by Ismagilov et al., in a co-flow device with two single-phase fluids at equal flow ratios, the diffusion region width scales to the power of $1/2$ at the channel mid-plane [101]. The discrepancy of the scaling to be lower than a power of $1/2$ could be due to the flow ratio being 1:3 which places the initial interface of the two fluids closer to the channel wall. As observed by Ismagilov et al., the scaling of the width of the diffusion region follows to the power of $1/3$ in the region adjacent to the wall.

What is interesting, however, is that the power-law index decreases with increasing hematocrit to approximately 0.268 for the three fluid configurations as observed in Figure 4.7(right). This trend of the power-law index shows that the scaling of the mixing transport in a RBC suspension deviates from a standard diffusive process with the addition of cells. Furthermore, the rate of spread decreases with time, and after one second, the mixing is less efficient.

4.6.2 Aggregability

Figure 4.8 reveals a non-monotonic relationship between hematocrit and spatially averaged normalized effective diffusivity in the suspending fluid, with optimal diffusivity around 30% hematocrit. Higher flow rates amplify this effect, particularly in aggregating samples in plasma compared to non-aggregating samples. The augmentation with shear rate indicates a shear-enhanced diffusion process that occurs in a suspension environment. This non-monotonic increase in the augmented mass transport follows a similar trend to the study reported by Cha and Beissinger, which found that in ghost cells the mass transport increased to a maximum at 45%, which subsequently decreased with a further increase in hematocrit [98]. Under low-shear conditions, RBC form linear rouleaux structures, but these aggregates disaggregate under flow, leading to size variations influenced by input flow rate. Aggregation, induced by suspending cells in plasma, enhances mixing, especially in denser suspensions, suggesting a potential physiological adaptation to improve mixing efficiency in blood.

Interestingly, the scaling of the augmented mass transport was found to increase approximately linearly with the input flow rate. Typically, in suspension flow, the augmentation of the diffusion should be correlated to the characteristic Péclet number as $a^2\dot{\gamma}/D$, where a is the effective radius of the particle, $\dot{\gamma}$ is the shear rate, and D is the diffusion coefficient of the solute. Therefore, the increase in the augmentation of the spatially averaged normalized diffusion coefficient is found to scale linearly with the Péclet number.

4.6.3 Transport of Molecules of Increasing Molecular Weight

Results show that, in 0% hematocrit, the spatially averaged diffusion coefficient of dextran decreases with increasing molecular size as expected from the Stokes-Einstein relationship. What is interesting, however, is that when the dextran is placed in 30% hematocrit, this trend is regulated. In the presence of cells, larger molecules diffuse faster, becoming comparable to smaller molecules. Additionally, the mean shear rate, influenced by flow rate variations, plays a significant role in the presence of cells, an effect less prominent without cells. These findings suggest that the presence of cells modulates the mass transport of molecules, diminishing the influence of molecular size and highlighting the interaction between cells, flow, and shear rate. This also further establishes that the normalized effective diffusion coefficient is not a purely diffusive mechanism and must be associated with an advective phenomenon that may manifest from the presence of cells. This brings up the question of what exactly is the mechanism behind the mass transport of solutes present in the liquid phase.

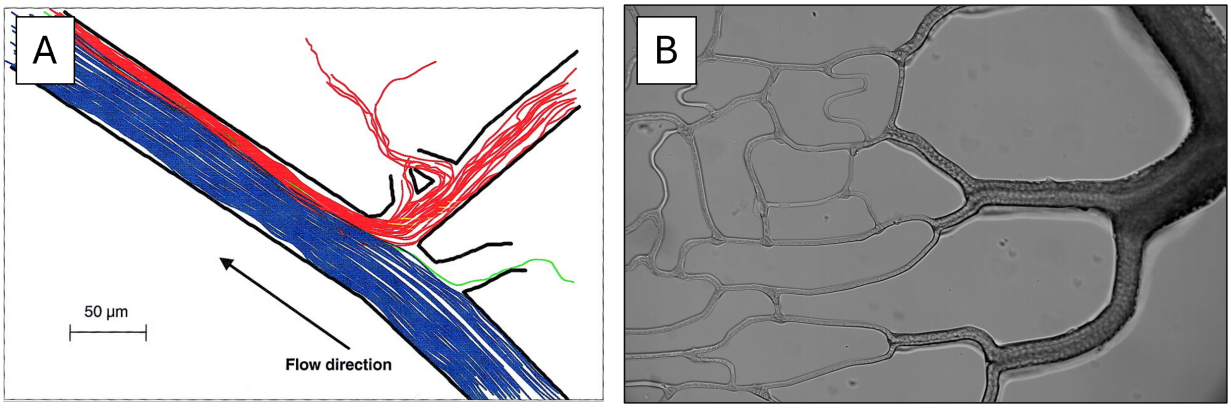


Figure 4.13: (A) Composite diagram of trajectories of individual cells reflecting the branch origin indicate absence of mixing between flow stream (Reproduced from [104]). (B) An in vitro illustration of a microcirculatory network of branching channels illustrates the minimal extent of cell diffusion, as indicated by the prolonged traces of heterogeneous distribution (Reproduced from [93]).

4.6.4 Mechanisms

Radial diffusion

Unlike the spatially averaged normalized effective diffusion coefficient of molecules, the cell mask representing both non-aggregating and aggregating cells does not show an optimal hematocrit but instead a minimum. Furthermore, the absolute diffusivity of the cell mask is significantly lower than that of molecules in the suspending fluid, indicating that increased molecular diffusivity is not necessarily driven by large-scale cell diffusivity. Figure 4.11 illustrates the effective diffusion of RBCs, averaged along the central channel position, confirming this trend.

Measurements of RBC trajectories in the venular network of the rat spinotrapezius muscle, with and without aggregation, further support these findings. Bishop and colleagues demonstrated minimal lateral diffusion when channels converge in vivo [104]. Cells tracked near the wall of an unbranched venular segment migrated approximately 1% of the longitudinal path length without aggregation, with slightly greater migration during aggregation [104]. Similarly, our in vitro observations reveal that cells tend to remain in lateral positions within channels while traversing multiple collecting junctions, as shown in Figure 4.13.

Red blood cell rotation

Insights from granular suspensions, which consist of solid non-Brownian particles larger than cells, may shed light on mechanisms observed in blood flow. Metzger and colleagues demonstrated that particles enhance thermal diffusivity in suspensions up to an optimal point, after which steric effects hinder particle movement and reduce diffusivity [105]. Similarly, the dense packing of red blood cells in blood may contribute to reduced diffusion at higher volume fractions. Souzy and colleagues observed dye dispersion in suspensions of non-Brownian particles, finding that flows between particles spread through gaps in mixing patterns that show stretched fluid interfaces that decreases length scales for mixing to occur, as illustrated in Figure 4.14 [106]. Furthermore, in their work, particles located against the wall rotate within the shear flow, which further induces disturbances within the fluid. These localized shear increases likely augment the effective diffusivity of solutes

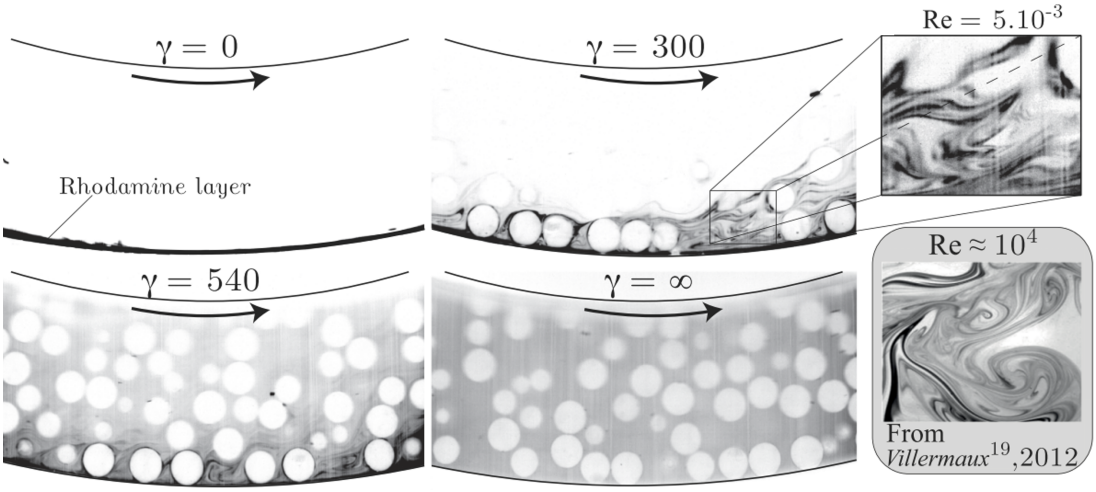


Figure 4.14: Successive snapshots of the suspension illustrate the mixing process driven by shear. Initially, a thin layer of Rhodamine 6G dye (in black) coats the outer cylinder. As the suspension is sheared, the dye gradually disperses across the gap until the mixture becomes homogeneous. The particles appear as white discs. A closer look at the flow pattern reveals mixing patterns with stretched fluid interfaces that decreases length scales for mixing to occur. (Reproduced from [106])

in the suspending phase, a phenomenon potentially relevant to blood. However, unlike granular suspensions, having a time- and space-resolved visualization of the flow between densely packed red blood cells, even at 20% volume fraction, is challenging using a confocal

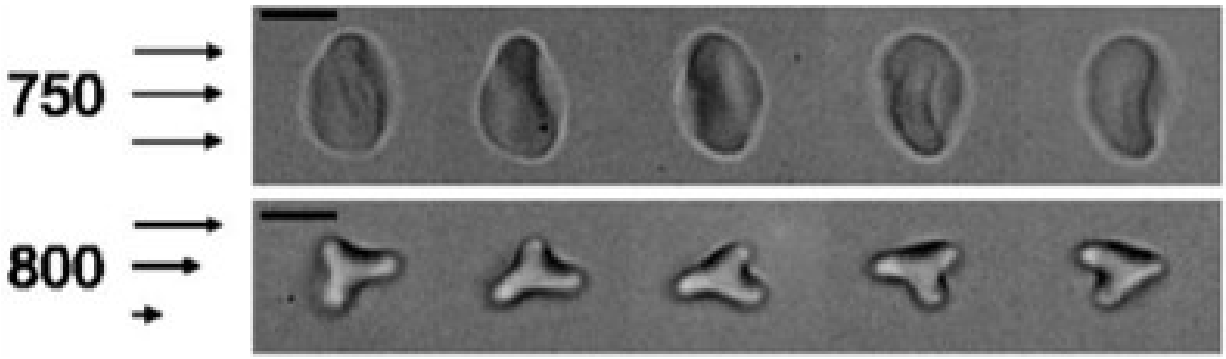


Figure 4.15: Sequence of RBC deformation at two shear rates (top view and side view) show casing trilobe morphology and rotation in the microfluidic channel. (Reproduced from [17])

laser scanning setup. Nevertheless, it is plausible that collisions and deformations of cells within channels generate localized shear rate increases, influencing solute diffusion.

Through observation of RBCs in shear flow, a plethora of cell dynamics such as tumbling, rolling, and tank-threading/swinging appear to all play a role in the dynamics of the transport of solutes between cells in an increase in hematocrit. In the work of Lanotte et al. a rich diversity of shapes and dynamical states of RBC are observed with increasing shear rates [17]. Solid-like rotation of the cells is observed at high shear rates, where RBC forms three lobes that rotate around the center of mass, which is represented in a time sequence in Figure 4.15 [17]. These observations in glass round capillaries indicate that rotation is present in flow, and so, analogous to observations in granular suspension, the augmentation of the mass transport must be strongly associated with the dynamics in flow.

Interface position

An interesting aspect of the augmentation of mass transport is that the enhancement of mixing diminishes when the co-flow interface is centered in the channel, rather than offset as in the 3:1 ratio configuration. This reduction in optimality is hypothesized to arise from several factors: shear-rate gradient, hematocrit distribution, or changes to the RBC interactions.

In pipe flow, shear rate peaks near channel walls and drops to zero at the center. A centrally located interface experiences lower shear-rate gradients, reducing the "stirring"

effect that enhances mixing. Alternatively, RBC concentration increases from the wall toward the center, as noted by Sherwood et al. [107]. When the co-flow interface coincides with lower shear regions where RBC density is higher, flow-driven mixing may become less efficient because the RBCs move more coherently, offering fewer opportunities for fluid to be perturbed in the transverse direction to the flow. Lastly, the ability for the cell to deform and collide may differ between the wall where rotation and collisions may promote rapid transport of the fluid phase compared to the channel center where the RBCs may move more uniformly, generating fewer disturbances to the flow.

4.7 Conclusions

In this work, the effects of the presence of RBC on the augmentation of the mass transport of solutes in the suspending phase are explored. In order to improve the mixing of proteins, glucose, and all the other constituents in the microcirculation, the presence of RBC and high flow rates are required. However, not only does fast circulation improve the observed mass transport, there appears to be an optimal cell volume fraction around 30% hematocrit for both non-aggregating and aggregating blood samples. Peculiarities were observed in aggregating samples in dextran-70; however, this may be a result of differences in the aggregate morphologies between physiological linear arrays and clusters. The optimality around 30% hematocrit, which is close to microcirculatory hematocrit, and cell aggregability in itself may not be a coincidence as they both represent a real physiological phenomenon of blood rheology and are indicative of mechanisms that help improve mixing in microcirculation.

Another intriguing finding is that the augmentation of the mass transport is significantly improved for macromolecules of increasing molecular weight. This finding is of particular interest in the context of drug delivery via blood flow, as it suggests that the delivery of drugs using nanomedicine and nanoparticles should be comparable for drugs with Stokes radii ranging from 1 to 100 nm. From a mass transport perspective, nanoparticles of different sizes can be rapidly transported through the microcirculatory system, since their effective transport behaves similarly. Enhanced mixing of larger macromolecules could improve the uniform distribution of therapeutic agents within microcirculatory networks, potentially aiding drug delivery.

In certain pathological conditions, such as sickle cell disease (which often involves both reduced hematocrit and altered RBC deformability), heightened RBC adhesion or aggregation could partially compensate for lower hematocrit by maintaining or enhancing local

mixing and transport under specific flow conditions. Similarly, in pregnant women, elevated RBC aggregation might contribute to improved mixing and nutrient delivery within the placenta, potentially ensuring that essential molecules reach the fetal circulation more effectively. Although further investigation is needed to fully understand these phenomena, these examples underscore how alterations in the degree of RBC aggregation and hematocrit can influence blood rheology and transport processes to potentially provide an adaptive benefit in otherwise challenging physiological or pathological states.

Lastly, it should be noted that the level of aggregability is uniform across all animal species. Higher levels of aggregation are commonly observed in animals that are considered "athletic", such as horses and humans [108]. This suggests an evolutionary adaptation linked to efficient blood transport under high physiological demands. Enhanced aggregation may increase local flow perturbation, improving mixing and aiding rapid nutrient and oxygen distribution. So what we may be observing is an adaptation that may be related to improving the mixing in our blood, reflecting an evolutionary strategy to improve cardiovascular efficiency.

4.8 Key Takeaways

Aggregability Effects

Non-aggregating RBC and aggregating RBC in plasma were found to enhance relative effective diffusion, peaking at a hematocrit of 30%, which further increases at higher flow rates. This may be indicative of a physiological adaptation of blood to optimize the mixing process of the constituents of blood in the microcirculatory system to be in a well-mixed state.

Mass Transport of Large Molecules

The presence of blood is found to enhance the mixing process of molecules of increasing molecular weight such that they have similar effective mass transport through the suspension. This would suggest that the transport of molecules in the suspending phase through the suspension is not purely diffusive.

Mass Transport Mechanism

The mass transport of the constituents in the suspending phase was found to be unrelated to the axial migration of cells across streamlines, which was found to be minimal. It is more probable that the transport is augmented due to other mechanisms, such as cell rotation and cell–cell collisions instead.

Chapter 5

Two-Foci Fluorescence Correlation Spectroscopy

Chapter Abstract

Conventional optical methods struggle to measure velocity fields in dense suspensions because of signal loss at higher hematocrits. To address this, two-foci fluoresence correlation spectroscopy (2f FCS) is proposed as a technique to measure velocity profiles in dense turbid red blood cell (RBC) suspensions (up to 40% hematocrit) within glass capillary microchannels. 2F FCS is validated for both transparent Newtonian and non-Newtonian fluids and extended to non-aggregating and aggregating RBCs at physiological hematocrit levels. Results show that velocity profiles are obtainable across this range: phosphate buffered saline (PBS) solution and non-aggregating RBCs (40% hematocrit) exhibit parabolic (Newtonian-like) flow, while polyethylene oxide (PEO) and aggregating RBCs (40% hematocrit) display plug flow (shear-thinning). A secondary flow condition, induced by translating the device at a constant speed, verifies the 2f FCS measurements. This study also explores two approaches for integrating local velocity and hematocrit measurements: mean fluorescent intensity and cross-correlation amplitude. While neither method provides a direct measure of local hematocrit, cross-correlation amplitude offers insights into the limitations of measurement depth. Several challenges are identified, including depth of measurement and calibration inconsistencies, underscoring the need for further research to refine the technique and achieve reliable pairing of velocity and hematocrit measurements. Despite these hurdles, 2f FCS emerges as a powerful tool for probing local velocity fields in dense RBC suspensions, driving progress in blood rheology research.

5.1 Introduction

The rheology of blood dictates the efficiency of the circulation (the power needed to maintain flow) and is therefore crucial to quantify. However, unlike simple Newtonian fluids like water, blood is a concentrated suspension of cells in a protein-rich solution. It is only because water complies with a simple rheological constitutive law with a constant viscosity, called the Newtonian law, that those fluids can be described by the Navier-Stokes equations and simulated in any flow situation. In contrast, blood lacks such a constitutive model that directly relates the local stress tensor to the strain rate tensor.

Classical rheological studies have provided valuable insights into the rheological properties of blood, particularly its non-Newtonian shear thinning behavior. These studies have employed a range of rheological measurement techniques, including capillary rheometers, Couette rheometers, and cone-plate rheometers [5, 11, 12]. The advent of microfluidics has enabled the study of intricate details of blood flow at the microscale. However, the relationship between local microstructure and local flow characteristics remains a subject of active investigation [3, 107, 109]. These research studies showcasing the relationship of the local velocity profile and the local microstructure of red blood cells in microfluidic devices raise a question of the validity of the commonly assumed linear velocity profile across the width of the rheometer gap. This phenomenon is illustrated in Figure 5.1.

At present, there is a lack of a complete constitutive law that connects the microscopic structure of blood flow with the bulk macroscopic rheological measurements of blood. To further our understanding of the complex nature of blood in both the macroscopic and microscopic scales, new experimental approaches need to be explored.

5.2 Background

An accurate method of measuring local velocity fields in fluid solutions is essential for the development of a constitutive law of a material which describes the relationship between the external forces imposed on a material and the resulting deformation at a macroscopic level. In the case of a fluid that flows and deforms continuously under the influence of an applied shear stress (τ), the deformation resulting from the shear stress is a function of the local shear rate ($\dot{\gamma}$) and the local hematocrit (ϕ). The shear rate is defined as the velocity gradient in the direction perpendicular to the plane of shear.

The viscosity of a fluid is regarded as an inherent property of the fluid itself, which describes the relationship between the shear stress applied to the fluid and its response

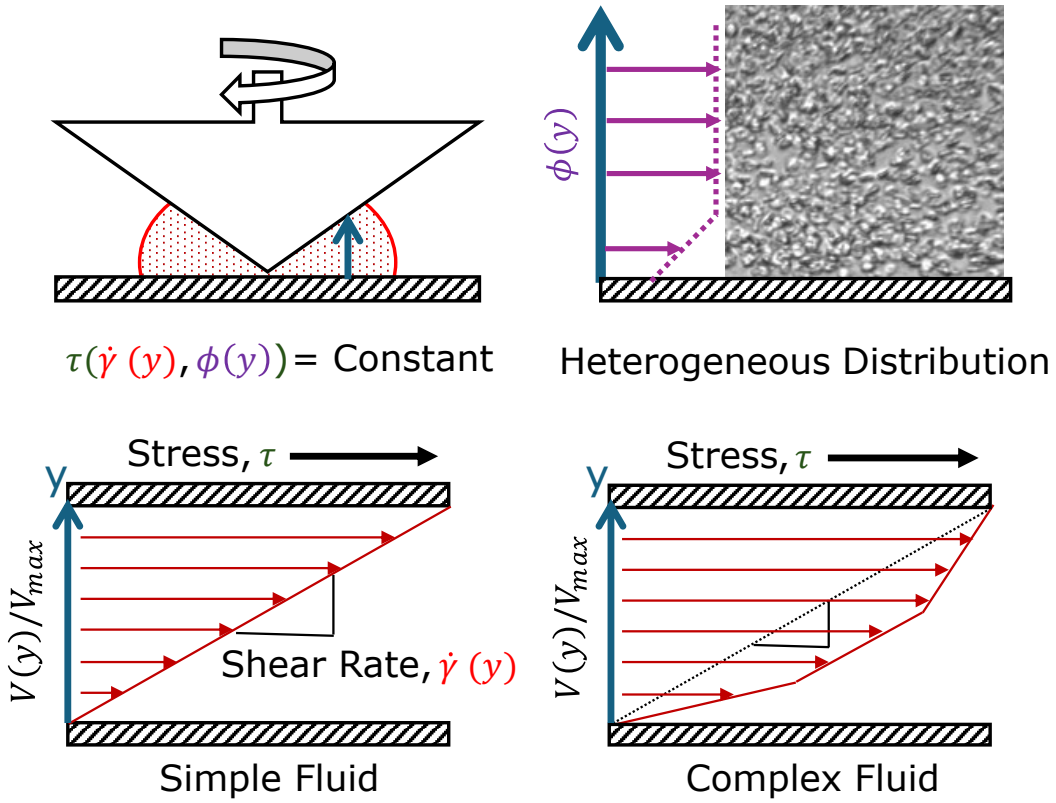


Figure 5.1: Using a rotational rheometers, a constant shear stress (τ) is applied to the bulk fluid (indicated as dotted red area and enlarged for clarity) in which the shear rate is assumed to be constant and the distribution of the fluid is assumed homogeneous. The heterogeneous distribution of blood cells however modifies the velocity field. Therefore, to deduce a true constitutive law, measuring the local distribution of cells (ϕ) and local shear rate ($\dot{\gamma}$) is required. (Adapted from [110])

to shear rate. Conventional rheometric measurements of fluid viscosity typically rely on the assumption that the fluid is a continuum, which is valid for single-phase homogeneous materials. However, in the case of suspensions comprising multiple phases, such as blood cells, the necessary condition to assume a continuum material is only valid when the characteristic length scales of the particle sizes are much smaller than the characteristic length scale of the strongest gradients of flow [111].

In measurement devices such as rotational rheometers or capillary rheometers, it is crucial to recognize that the dimensions of the gap or channel may not be appreciably larger than the size of the particles. Furthermore, even when particles are considerably smaller than the gap, the continuum assumption of a homogeneous suspension is invalid near solid surfaces due to the differing distribution of particles near a surface compared to that in the bulk, which is a consequence of excluded-volume effects [111]. A heterogeneous distribution of red blood cells (RBCs) is observed in blood microflow in the form of a cell free layer or cell depleted layer (CFL), which results in a lower concentration of RBCs at the wall and a dense concentration of RBCs in the core of the channel. The depleted layer of cells at the surface wall has a lower viscosity than that of the bulk, which leads to a higher shear rate. This is commonly described as an apparent wall-slip velocity of the suspension [111, 112]. Consequently, in order to ascertain the viscosity of an unbounded RBC suspension and to re-examine the shear-thinning behavior of blood, it is necessary to complete a direct measurement of the velocity profile throughout the gap of the rheometer in order to obtain the true local strain rate as well as simultaneously the local hematocrit field and link it to the shear stress applied by the rheometer and constant throughout the gap.

5.2.1 Techniques in Blood Rheology to Measure Velocity

A number of image-based optical techniques have been developed for the characterization of velocity profiles in micro-flows. These are summarized in a published mini-review, which can be found in Appendix D [113]. The mini-review explores the use of cell tracking, kymography, micro-particle image velocimetry (μPIV), and dual slit photometry, and considers their specific applications and limitations for the purpose of measuring velocity profiles. The principal technical challenge of these image-based techniques is the measurement of high hematocrit conditions, where the tracking of tracer particles or the differentiation of individual cells becomes increasingly difficult to identify in flow conditions that approach physiological levels. It should be noted that other techniques have been employed to characterize RBC suspension velocity profiles that are not image-based, including magnetic resonance microscopy [114], x-ray PIV [115], and pulsed Doppler ultrasound systems [116]

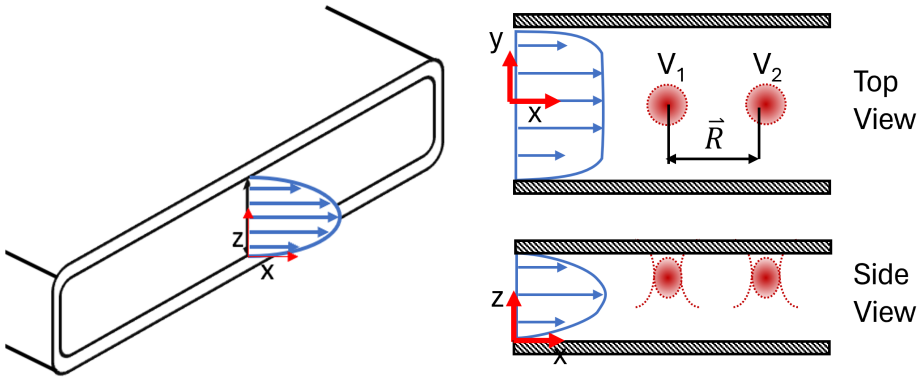


Figure 5.2: Schematic of cross-section of microfluidic channel with fluid flow exhibiting a parabolic velocity profile indicated in blue. Measurement of the velocity profile are taken at the center width of the channel taking the bottom surface as the datum. Top and side view showcase the two spatially separated beams (at distance $\vec{R}$) aligned with the direction of the flow in which the passage of low concentration fluorescent molecules or particles are measured. (Adapted from [110])

and although these techniques have been demonstrated to have the ability to complete measurements through dense suspensions, they do require highly specialized instrumentation while also having resolutions that are typically in the range of 50 to 500 µm [117]. Currently, there still needs further exploration in the development of velocity measurement techniques that are easily accessible and able to penetrate through dense RBC suspensions.

To address the limitation of measuring flow conditions at higher hematocrit concentrations, two-foci fluoresence correlation spectroscopy (2f FCS), a technique initially characterized during the master's thesis, is further explored as a novel application of deep RBC suspension velocity measurement in this work. This approach draws upon fluoresence correlation spectroscopy (FCS), a technique utilized to investigate the dynamics of molecular processes by observing the spontaneous fluorescence fluctuations caused by the passage of low concentration labeled particles through a small detection volume realized using a confocal experimental setup [118–120]. In the context of 2f FCS, two spatially separated confocal volume elements are created with a known distance apart. This enables the independent measurement of fluorescence fluctuations induced by fluid flow, which transports low concentration fluorescence from the upstream confocal volume to the downstream focal volume. Figure 5.2 provides a visual representation of the configuration of the confocal volumes.

The completion of a cross-correlation of fluctuation data between the two confocal volumes results in the identification of a peak lag time, which is associated with the time that fluorescent particles pass from one focal volume through the next. With the known distance between the focal volume and the lag time, a local velocity can be calculated. The advantage of employing 2f FCS is that it offers a rapid and straightforward approach for determining the flow velocity, spanning from 10 µm/s to 10 cm/s, with a reasonable detection time of 10 to 100 seconds [118,119]. Secondly, in dense suspensions where the presence of RBCs may block or interfere with fluorescence signals, the fact that 2f FCS requires a low concentration of fluorescent particles would assist in the completion of measurements in physiological hematocrit. Preliminary results have indicated that measurements in RBC suspensions were achievable at least 60 µm into the channel at 40% hematocrit [110].

5.2.2 Velocity Measurement from 2f FCS

Brinkmeier and colleagues outline a theoretical model that can be used to fit the fluorescent intensity fluctuation normalized cross-correlation [118]. The generalized solution of the cross-correlation of fluorescence fluctuation between two spatially separated confocal volumes is given as follows:

$$G_C(\tau) = \frac{1}{N} \frac{1}{(1+\frac{\tau}{\tau_D})(\ 1+\frac{\omega_0^2}{z_0^2}\frac{\tau}{\tau_D})^{0.5}} \exp\left\{ -\frac{|V_p|^2(\tau^2+\tau_F^2-2\tau\tau_F\cos\alpha)}{\omega_0^2(1+\frac{\tau}{\tau_D})} \right\} \tag{5.1}$$

where N is the average molecule number in the detection volume, ω_0 and z_0 are the beam waist radius and height of the foci volume. $\tau_D = \omega_0^2/4D$ is the characteristic diffusion time (τ_D) for a given diffusion coefficient D, τ_F is the flow time which is the ratio of $\vec{R}$ distance between the foci and the in-plane flow velocity (V_p), and α is the angle between the direction of the flow and the connecting vector of the two foci. In the limiting case where the characteristic diffusion time is vanishingly small (slow diffusion), the equation further simplifies to:

$$G_C(\tau) = \frac{1}{N} \exp\left\{ \left[-\frac{R^2}{w_o^2} \left(\frac{\tau^2}{\tau_F^2} + 1 - 2\frac{\tau}{\tau_F} cos\alpha \right) \right] \right\}. \tag{5.2}$$

The characteristic curves of the simplified flow dominated system are represented in Figure 5.3. The fundamental parameter that is of interest is the peak lag time, which can simply be extracted at the peak correlation from Equation (5.2) . While the asymmetry of the fits and amplitude of the correlation function for this model are primarily dictated

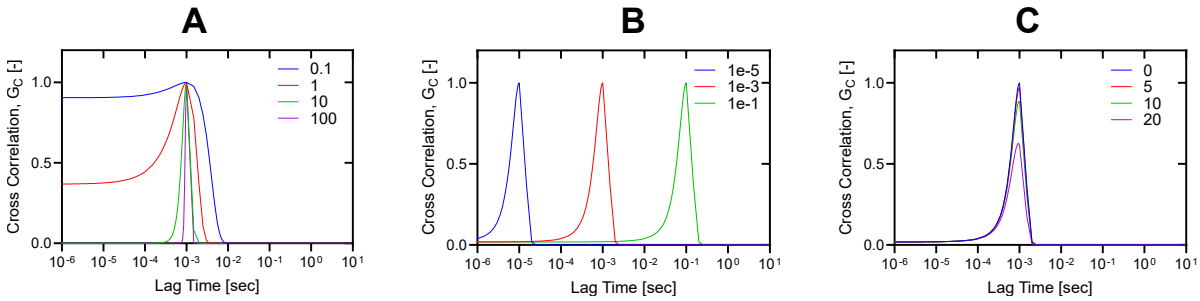


Figure 5.3: Cross-correlation function for simplified 2f FCS model where (A) R^2/w_0^2 varied with fixed flow time and angle, (B) flow time varied with fixed R^2/w_0^2 and angle, and (C) angle varied with fixed R^2/w_0^2 and flow time.

by the beam waist and distance ratio, and relative beam angle, respectively.

5.2.3 Velocity Measurements of Blood in Vitro

A widely used technique to measure velocity in vitro in microfluidic devices is through μPIV, where measurements have been completed in a variety of geometries from rectangular, square, or circular channel designs with either a non-aggregating solution or an aggregating solution. Typically, measurements using μPIV rarely supersede 25% hematocrit, with exceptions when utilizing more specialized techniques such as X-ray PIV [115]. Velocity measurements using μPIV have primarily been completed in the transverse plane of the channel, which should produce a plug flow velocity profile in low aspect ratio channel designs [3, 121].

Velocity profile measurements of RBC flow reported in the literature present conflicting results regarding the behavior of blood flow in vitro for both aggregating and non-aggregating RBCs. Sugii et al. observed parabolic velocity profiles for both non-aggregating and aggregating RBCs at approximately 20% hematocrit, flowing through circular bore microcapillaries (100 µm) using fluorescent particles and high-speed μPIV [122]. Similarly, Lima et al. reported parabolic profiles in non-aggregating RBCs flow within a 100 µm square microchannel and in rectangular microchannels (300 µm by 45 µm) at hematocrit levels of 17% and 20%, respectively, using confocal μPIV and fluorescent particles [109, 123].

Parabolic profiles were also noted by Bukowska et al., who used joint spectral and time-domain optical coherence tomography in channels 40 µm deep with widths ranging

from 50 µm to 300 µm for samples at 40% hematocrit [124]. Conversely, Bitsch et al. reported plug-like velocity profiles for a 60% hematocrit sample flowing through a 32.5 µm by 360 µm capillary, using μPIV with red blood cells serving as natural particle tracers [125]. Similarly, Passos et al. observed a decrease in velocity profile bluntness with reduced RBC deformability in a 50 µm square channel, measuring 5%, 10%, and 25% hematocrit using μPIV and RBCs as flow tracers [126]. Additionally, the velocity profile reported by Passos et al. demonstrates that there potentially exists a distance within the solid boundary where the linear extrapolation of the velocity profile vanishes, suggesting a slip condition that influences the flow behavior [126]. The presence of a slip length may be indicative of the CFL as discussed earlier in Section 1.2.3.

Park et al. used X-ray PIV techniques with carbon dioxide microbubbles to measure pulsatile velocity profiles of human blood at 40% hematocrit in vitro. They found blunted velocity profiles under these conditions [115]. Bishop et al., using an in vivo rat model with lower RBC aggregability compared to humans, showed that non-aggregating blood displayed nearly parabolic velocity profiles under both control and reduced flow rates. However, dextran-induced RBC aggregation caused slight flattening of the profiles under control flow rate and significant flattening under reduced flow conditions [104]. A compilation of these diverse velocity profile measurements is shown in Figure 5.4.

The variability in reported blood velocity profiles raises an important question: are these differences due to the complex and still poorly understood nature of blood flow, or are they a consequence of limitations in the measurement techniques? μPIV, a widely used technique for velocity measurements, has its resolution influenced by several factors, including the presence of out-of-focus particle images, the density and size of tracer particles, and the overall imaging quality [127–129]. These challenges are further compounded by inconsistencies in microchannel dimensions, optical characteristics, and fluid preparation protocols across studies.

For blood with non-aggregating RBCs, velocity profiles have been reported to exhibit both parabolic [109, 122, 123] and plug-like characteristics [125, 126]. The observed profile often depends on the hematocrit level and the depth of correlation associated with the measurement technique. In contrast, aggregating RBCs displays more diverse behaviors, with some studies reporting parabolic velocity profiles [122], while others observe blunted, plug-like profiles [104, 115, 130]. The primary factors contributing to the development of a flattened, plug-like velocity profile are an increase in hematocrit and a reduction in flow velocity. This behavior can be described mathematically using the following equation:

$$V(z) = V_{max}\left(1 - \left|\frac{z}{h}\right|^{K}\right) \tag{5.3}$$

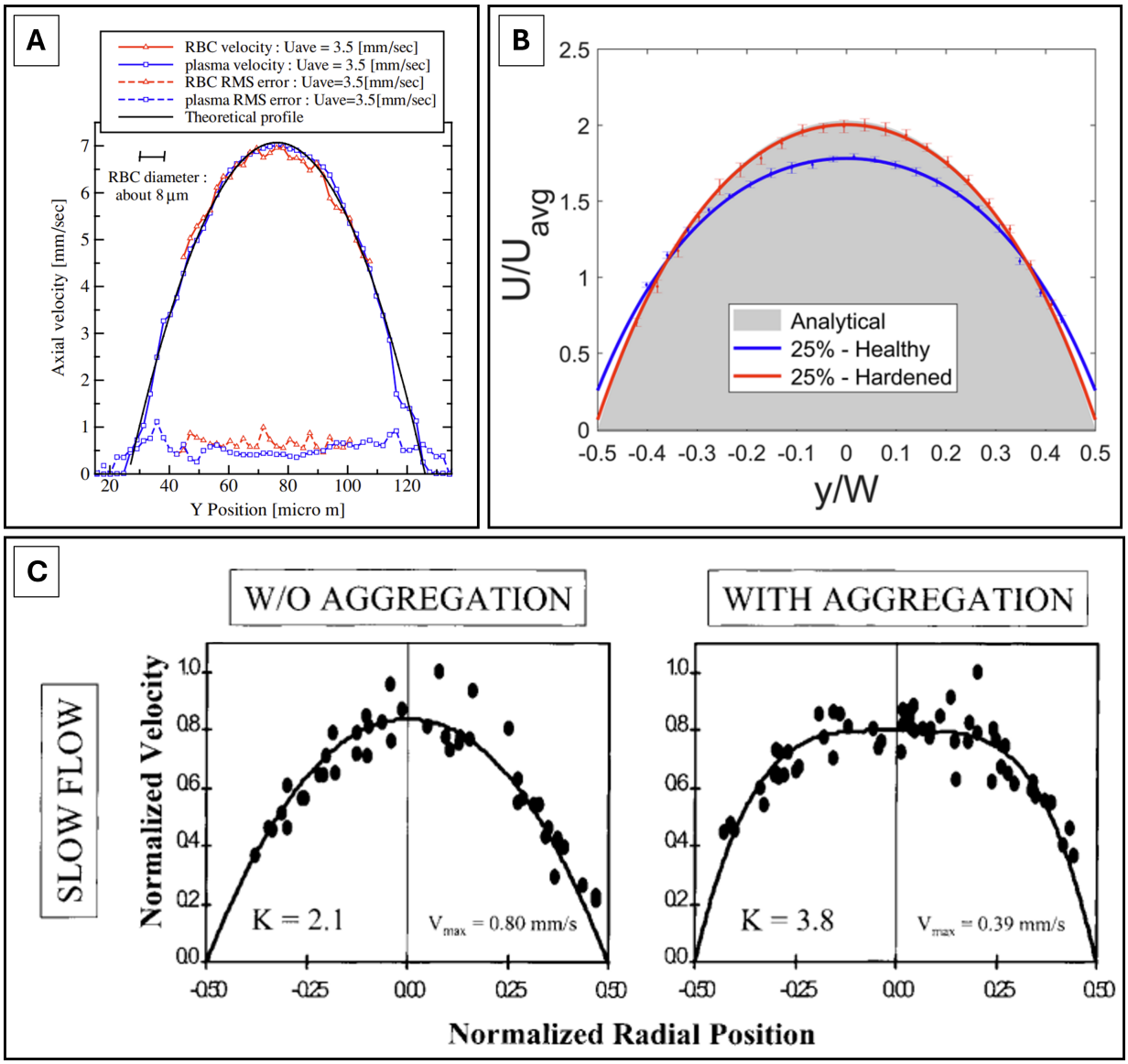


Figure 5.4: A compilation of velocity profiles from various studies reveals mixed results for both non-aggregating and aggregating RBCs. (A) Sugii et al. observed parabolic profiles for both non-aggregating and aggregating samples at 20% hematocrit in 100 µm circular bore microcapillaries [122]. (B) Passos et al. observed plug-like flow in non-aggregating samples at 25% hematocrit using micro-PIV in a 50 µm square channel [126]. (C) Bishop et al. demonstrated a plug-like velocity profile in a rat in vivo study with induced aggregation [104].

where V_{max} is the max velocity, h is the height of the channel, z is the height position in the channel taken at the mid-plane as the reference, and K is the bluntness factor. For aggregated plug flow, Bishop et al. reported a K-value of approximately 3.8 [104], while Park et al. reported a slightly lower K-value of 3.6 [115]. A representative example of the blunted, plug-like profile is shown in Figure 5.4(B).

5.2.4 Viscosity Models of Whole Blood in Bulk

The most well-studied non-Newtonian characteristic of blood is its diminishing viscosity with increasing shear rate. Classically, this has been demonstrated by Chien's coaxial cylinder rheometer experiment, where the viscosity of aggregating samples decreases by a factor of approximately 45 as the shear increases from 0.01 to 500 s^{-1}, while non-aggregating samples decrease by a factor of approximately 3.5 [5]. The characteristic property of blood is observed in Figure 1.5 for healthy aggregating RBC suspension, normal non-aggregating samples, and hardened cells.

Several shear thinning constitutive models for blood viscosity have been proposed [23]. The simplest of these models assumes a constant viscosity, which can be approximated by either the constant infinite shear viscosity, η_∞ or an intermediate shear rate at which aggregates of RBCs are dispersed. In contrast, generalized Newtonian models of bulk blood viscosity are also common in modeling the shear thinning behavior of blood. A generalized Newtonian fluid is an idealized fluid for which the shear stress is a function of shear rate at the particular time and is independent of a history of deformation. Although non-Newtonian, its constitutive equation is a generalized form of a Newtonian fluid that satisfies $\tau = \eta_{eff}(\dot{\gamma})\dot{\gamma}$.

The power-law is frequently used to model blood viscosity [23]:

$$\eta(\dot{\gamma}) = k\dot{\gamma}^{(n-1)} \tag{5.4}$$

where n is the power-law index and k is the consistency. For a shear-thinning fluid, the power-law index is less than one. Hussain et al. [131] reported an average power-law index of 0.703 with a 2.9% error and a normalized consistency of 0.980 with a 9.138% error for fresh blood samples. In contrast, Walburn and Schneck [20] observed an average power-law index of 0.785 and a consistency of 134 mPas^n, while Robertson et al. [23] reported a lower average power-law index of 0.628 but a significantly higher consistency of 20.2 mPas^n. The power-law model for shear-thinning fluid predicts an unbounded zero-shear viscosity while zero viscosity as the shear rate tends to infinity, and so there is a limitation on shear rates over which the model is valid.

Other viscosity models for blood have finite values for zero shear rate viscosity conditions and infinite shear rate viscosity in the form of:

$$\eta = \eta_\infty + (\eta_0 - \eta_\infty) f(\dot{\gamma}). \tag{5.5}$$

A general model is the Carreau-Yasuda model, which contains several other models as special cases, and is as follows:

$$\frac{\eta - \eta_\infty}{(\eta_0 - \eta_\infty)} = f(\dot{\gamma}) = \frac{1}{[1 + (\lambda\dot{\gamma})^a]^{(1-n)/a}} \tag{5.6}$$

where shear thinning models have power-law exponent $n < 1$. The special cases of the Carreau-Yasuda model include Simplified Cross ($a = 1$, $n = 0$), Cross-model ($a = 1 - n$), and Carreau model ($a = 2$). An analytical solution for the Carreau-Yasuda and Cross models in both pipe flow and flow over infinitely thin plates has been reported by Sochi [132]. However, in this work, the power-law model was implemented primarily for simplicity to extract the power-law index.

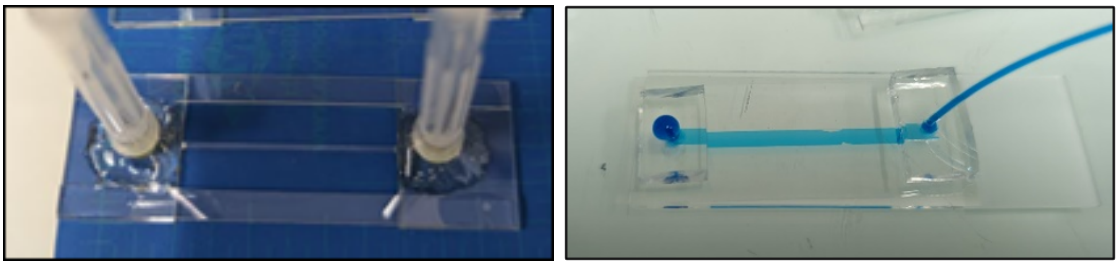
5.3 Objective

The hypothesis put forth is that 2f FCS is a viable technique for measuring micro blood flow velocity profiles. To demonstrate this, the specific objectives of this work are as follows:

- Validate the accuracy of the 2f FCS technique in measuring velocity profile in rectangular glass capillaries first flowing Newtonian fluid and then subsequently RBC suspension of increasing hematocrit.
- Assess the possibility of using 2f FCS to measure local hematocrit by analyzing parameters such as raw signal intensity fluctuation.
- Lastly, examine the limitations and considerations that should be made when using 2f FCS for micro blood flow velocity measurements.

5.4 Material and Methods

This section describes the two different types of microfluidic devices utilized, the preparation of fluid samples flowing through such devices, the experimental setup of the 2f FCS and the analysis methodologies.



(a) Glass Capillary (b) Glass-PDMS Sandwich

Figure 5.5: Example (a) glass capillary microfluidic device with nominal rectangular cross-sectional area of 100 µm by 1000 µm and (b) glass-PDMS sandwich microfluidic device with nominal rectangular cross-sectional area of 100 µm by 3000 µm.

5.4.1 Microfluidic Device

Glass capillary and glass-polydimethylsiloxane (PDMS) sandwich microfluidic devices are used for this project to characterize the ability to measure velocity profiles through dense RBC suspensions in which the fabrication is described in Section 2.1.2 and Section 2.1.3, respectively. The microfluidic devices are single straight channels with a constant rectangular cross-sectional area with a nominal height of either 100 µm or 200 µm. These devices are used primarily for their wide aspect ratio (of 1:10 and 1:30 for the glass capillary and glass-PDMS device, respectively) to produce velocity profiles in the center of the channel that are minimally affected by wall effects and for the thinness of the glass walls to observe through the full height of the channel while using a high numerical aperture objective lens. An example capillary microfluidic device and glass-PDMS sandwich microfluidic device are presented in Figure 5.5.

5.4.2 Sample Preparation

In this study, healthy human RBCs are used in both non-aggregating and aggregating states, which are prepared as described in Section 2.2 at a nominal feeding hematocrit between 10% and 40%. In addition to using blood samples, phosphate buffered saline (PBS) is flowed as a reference transparent Newtonian fluid, and polyethylene oxide (PEO) is flowed as a reference transparent non-Newtonian fluid for comparison. Two types of tracers were tested in this project, which are dark red FluoSpheres and Alexa 647 dye.

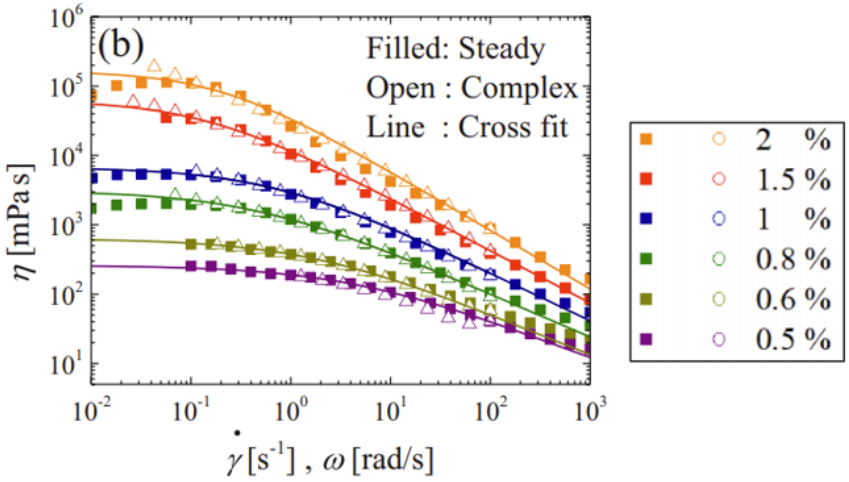


Figure 5.6: Steady shear viscosity as a function of shear rate (indicated by filled symbols) for samples of increasing PEO concentration using a MCR302 stress-controlled rheometer (Anton Paar, Austria). Data is fitted with cross-fit viscosity model indicated by solid line. (Reproduced from [133])

Polyethylene oxide

PEO solution is made by mixing 8000 kDa PEO powder (372781, Sigma-Aldrich, Germany) with Mili-Q water at a weight by weight concentration of 0.5% . Mixing is completed using a magnetic stirrer while avoiding light. The solution is then placed in the fridge to ensure a homogeneous solution due to having a better dilution coefficient with lower temperature for several hours to a few days. The concentration of the PEO was created and selected by Tristan Xabada for its zero shear viscosity to be approximately 150 mPa s at 20 °C representing 0.5% concentration by weight. A characteristic viscosity curve of the steady shear viscosity is reported by Louhichi et al. at various PEO concentrations and is presented in Figure 5.6. The solution is stored in a darkened falcon tube and at room temperature before measurement.

Tracer particles

Prior to mixing the RBC pellet with the suspending fluid, fluorescent dye (Alexa 647, Thermo Fisher Scientific Inc., USA) or 0.04 µm dark red FluoSpheres (Thermo Fisher Scientific Inc., USA) are added to the suspending fluid. Achieving robust measurements and identifiable peak correlation times necessitates very low concentrations of fluorescing

molecules in practice. Final concentration between 0.01 nmol/L – 10 nmol/L concentration of Alexa 647 is achieved by sequential dilution using a mother solution of Alexa 647 at 50 µmol/L. While concentrations of 0.0005% - 0.005% solids of the FluoSpheres were used from a mother solution of 5% solids that has been sonicated for 1 h.

5.4.3 Experimental Setup

The 2f FCS system is an in-house-built optical setup that is situated on an optical table. It comprises an inverted microscope (Axio Observer A1, Carl Zeiss AG, Germany) equipped with a water immersion 63x objective lens (Objective C-Apochromat, Carl Zeiss AG, Germany). The microfluidic device is affixed to the microscope on a two-axis manual control stage. The vertical position is fixed at the bottom, while the relative focus position of the objective lens is adjusted using a lens positioner system (Nano-F200 Series, Mad City Labs Inc., USA). The microfluidic device is held in place using a slide holder (MLS203P2, Thorlabs Inc., USA) and rotated manually in order to align two parallel beams of the 2f FCS with the direction of flow. A visualization of the general in-house-built optical setup is demonstrated in Figure 5.7.

The two foci for 2f FCS are created with a single 5 mW Red HeNe Laser (Melles Griot, USA) which emits at a wavelength of 633 nm to illuminate the fluorescent dye or beads. The laser is first passed through a round continuously variable neutral density filter (NDC-50C-2, Thorlabs Inc., USA) to regulate the laser power and then condensed into an optical fiber to clean the laser beam and obtain a Tem00 mode, perfectly Gaussian profile in intensity. To generate the two parallel beams using a single laser line, two cube beam splitters are utilized. A waveplate is positioned prior to the split to ensure equalized beam intensity. The position of the beams is adjusted with two kinematic mirror mounts before being coupled into the microscope objective lens's back aperture. Each beam individually forms the foci to excite fluorescent dye or beads. The resulting fluorescent emission is collected through the same objective lens, passing through a dichroic mirror and light filter into individual fiber optics openings of a 1-to-4 fan-out fiber optic bundles (BF42HS01, Thorlabs, USA), spaced 400 µm apart at their centers. The distance of the center of the fiber and magnification of the 63x objective lens dictate that the distance between the beams ($\vec{R}$) is approximately 6.34 µm if they are placed directly in the center of the fiber. Each fiber leads to an avalanche photodiode (APD) (Photon Counting Module, Excelitas Technologies Corp., USA) that is employed for photon counting of emitted photons from fluorescent molecules or particles in the measurement volume. Data acquisition is conducted via ISS VistaVision software (ISS Medical DBA ISS Inc., USA) which utilizes the FFS module for auto-correlation and

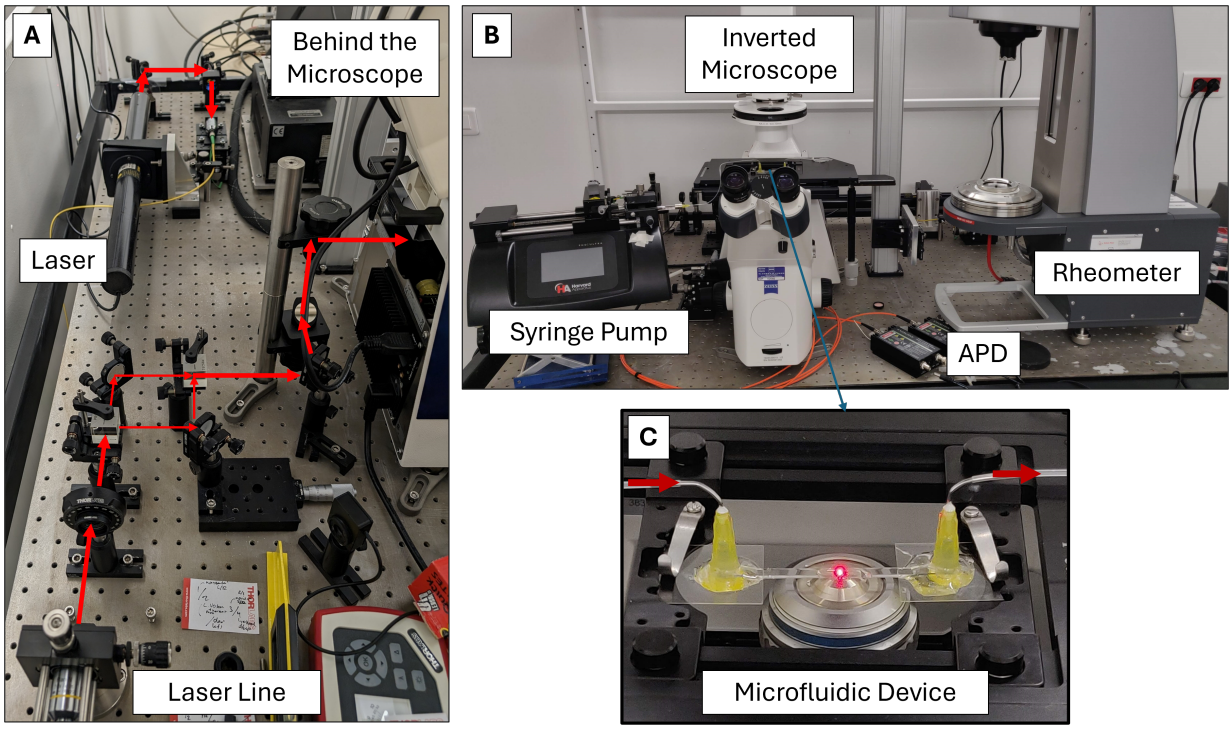


Figure 5.7: (A) Behind the inverted microscope is the optical setup to produce the two foci using a single red HeNe laser which is back fed into the inverted microscope. The laser line path is highlighted by the directional arrows. (B) The front end consist of the inverted microscope which holds the microfluidic device on the x-y stage. Output signals is measured from the side-optical output into two avalanche photo diodes (APD). Alternatively, the rheometer can be placed in lieu of the microscope to measure the local velocity while in operation. (C) Example attached glass capillary microfluidic device with feeding tubes for flowing samples from the syringe pump.

cross-correlation in FCS and 2f FCS, respectively. The schematic of the 2f FCS system is represented in the following Figure 5.8.

Fluctuation data acquisition

To complete a velocity measurement using the 2f FCS setup, it is first necessary to have the laser and laser system primed for data acquisition for a minimum of an hour prior to acquisition. This is to ensure that the laser intensity does not vary during data acquisition. Once the system has been primed, the distance between the measurement volume location is calibrated such that the measured fluorescent intensity is at the maximum for each fiber optic. This is accomplished by employing a standard solution of Alexa 647 at a 10 nmol/L dilution on a glass slide and adjusting the laser power to achieve a total photon count per second of approximately 50,000 to 100,000 with the focus positioned within the drop of the standard solution.

The first step aligns the initial focal volume with the first optical fiber while blocking the second focal volume, by translating the optical fiber stage until a maximum photon count is observed on the acquisition program. Next, the second focal volume is aligned to the second optical fiber by adjusting the main mirror to maximize the photon count reading while minimizing cross-talk (light leakage to the opposing fiber). Finally, the two foci must align with the channel's flow direction, which may require rotating the fiber optics or channel and repeating the previous steps. The goal of the calibration step is to align the center of the two foci to their respective fiber optics center. The distance between the foci is then presumed to be 6.34 µm as dictated by the distance between the center of the fiber and the magnification of the objective lens.

Once the 2f FCS system is set up, the microfluidic device is prepared. The device is pre-filled with the working fluid, and any bubbles in the channel, tubing, or syringe are removed prior to setting up the microfluidic device on the inverted microscope. The calibration glass slip is replaced with the channel and secured loosely with the clip of the slide holder. The channel is aligned with the direction of the two foci manually by rotating the device. The tubing attached to the channel is secured loosely to the microscope platform with tape to prevent any additional movement of the microfluidic device during injection. The velocity profile in the z-direction is measured at the center of the channel, where the effects of the channel walls on the velocity profile are minimal. The general procedure is then to set the flow conditions and take a sequence of measurements at different heights in the channel relative to the bottom surface wall, as illustrated in Figure 5.9(a). For each measurement taken, fluorescent fluctuation data is recorded between 5 s to 60 s (see Figure 5.9(b)).

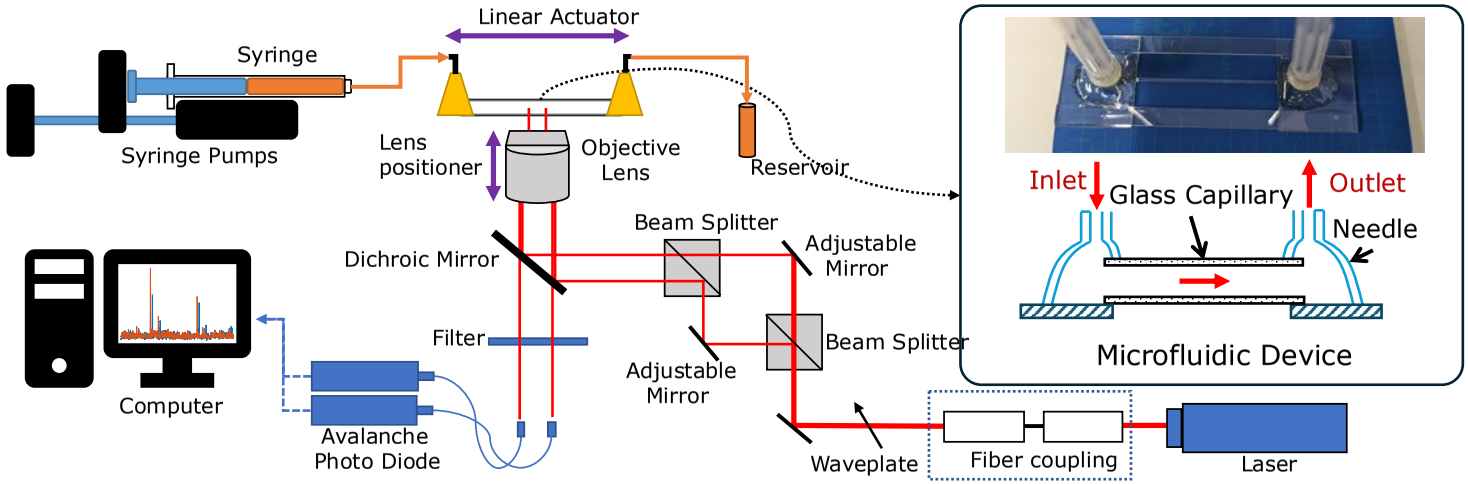
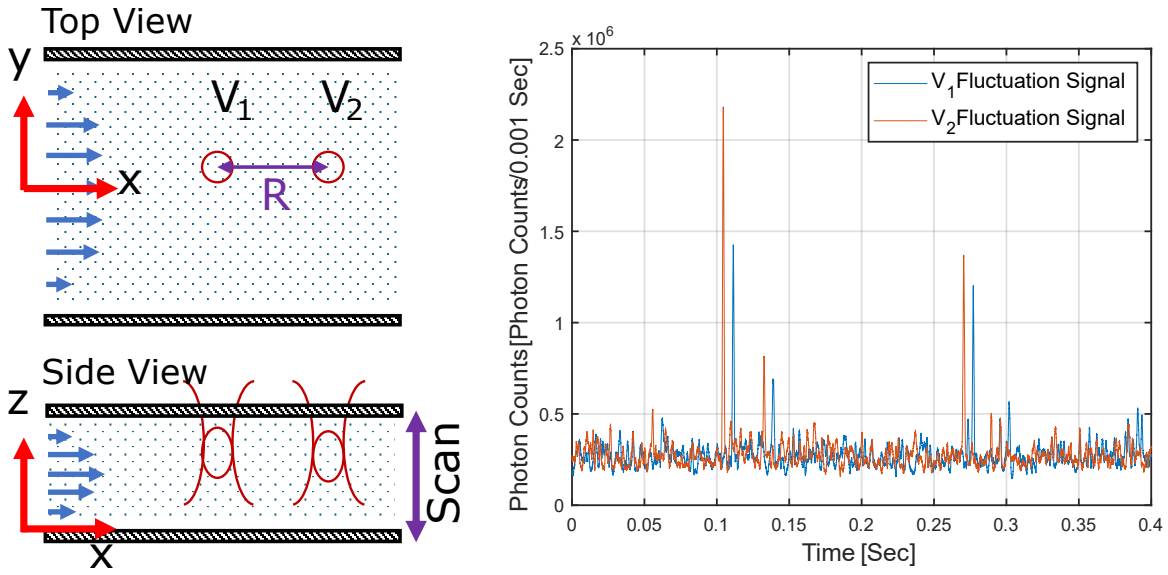


Figure 5.8: 2f FCS experimental setup consists of a pair of beam splitters to separate a single HeNe laser, 63x objective lens to focus the beam into the microfluidic device, dichroic mirror to separate the excitation from emitted light, and fiber optics to avalanche photo diode (APD) to measure the fluorescence fluctuations. Fluid samples are inoculated with low concentration of Alexa 647 dye (<10 nmol/L) or fluorescent beads (<0.005% solids).



(a) Acquisition Position (b) Sample Signal Acquisition

Figure 5.9: Photon fluctuation through two confocal volumes (indicated by red circles denoted V_1 and V_2) separated at a known distance $\vec{R}$ at a given height in a microchannel is cross correlated to determine the lag time for fluorescent molecules or beads to pass from the first foci to the second. The local velocity is determined as the ratio of the known distance and the measured lag time. (a) Schematic of the two confocal volume. (b) Example fluorescent fluctuation trace obtained from the two confocal volume.

The data acquired from the APD is the number of photons counted per second in each focus. This data is then cross-correlated between the two volumes in order to determine the time it takes for the same group of fluorescent molecules or fluorescent particles to pass from one volume to the next. Once the time required to traverse the distance between the two volumes is known, the velocity at that point can be calculated by dividing the two values. The raw data is extracted from the ISS VistaVision software as a text file and processed through a MATLAB script to complete the cross-correlation between the focal volume, fit the data with the model or a Gaussian function, and extract the peak correlated time. Subsequently, the velocity can be determined by calculating the ratio of the distance between the focal volume and the peak correlated time.

Velocity field generation

Two modes of velocity generation are employed to validate the 2f FCS system for the purpose of measuring velocity through a dense RBC suspension. The first is through a flow rate controlled injection into the microfluidic device using a syringe pump (PHD ULTRA, Harvard Apparatus, USA) with manual input of the flow condition. Prior to measurement of the fluorescent trace, the syringe pump is held for 1 min to ensure that the flow produced by the syringe pump is steady. The working fluid is contained within a 500 µL Hamilton glass syringe (Hamilton, USA) that is connected to the glass capillary microfluidic device via rigid tubing (FEP tubing, Fluigent, France). The resulting flow rate of a Newtonian fluid is anticipated to exhibit a parabolic profile along the center of the channel, consistent with Poiseuille's law (see Figure 5.10(a)).

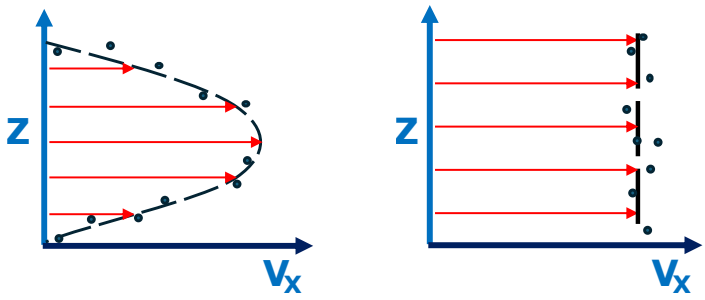
The secondary flow condition is a linear actuation of the microfluidic device itself without any flow. This is accomplished by pushing the x-y stage at fixed flow rates with a metal plunger attachment to the syringe pump acting in this case as an 'actuator'. The syringe pump is secured to the optical table and the metal plunger is aligned to the x-y stage to only push in the x-direction. With the entire channel moving in unison with the stage, the displacement of the fluid within the channel is equivalent to the stage displacement and should be constant across the height of the channel (see Figure 5.10(b)). The velocity of the stage displacement can be approximated by considering the geometry of the pre-programmed syringe and the set flow rate, which can be expressed as the following: $V \approx Q/A$. The theoretical velocity approximated from the pre-programmed syringe and flow setting is compared to a direct measurement of the velocity of the stage using a high-speed camera and calibration grid, and the velocity measurement extracted using 2f FCS with results summarized in Figure C.3 in Appendix C.

5.4.4 Analysis Methods

Peak time extraction

The peak cross-correlation time can be extracted using either the ISS VistaVision software, which employs a multi-tau cross-correlation scheme, or a secondary program with the raw text file. For this project, a MATLAB 2019a script and graphical user interface (GUI) are utilized to determine the peak lag time from the raw text file, following the methodology outlined by Brinkmeier and colleagues [118].

A MATLAB script was developed to calculate the instantaneous fluctuations from the time-tagged fluorescence data, conduct forward and backward cross-correlation of the flu-



(a) Syringe Pump (b) Linear Actuation

Figure 5.10: Theoretical velocity profile of a Newtonian fluid in a wide-aspect ratio channel taken at the the mid-width is (a) parabolic in a flow control condition and (b) constant along the height when in a linear translation condition.

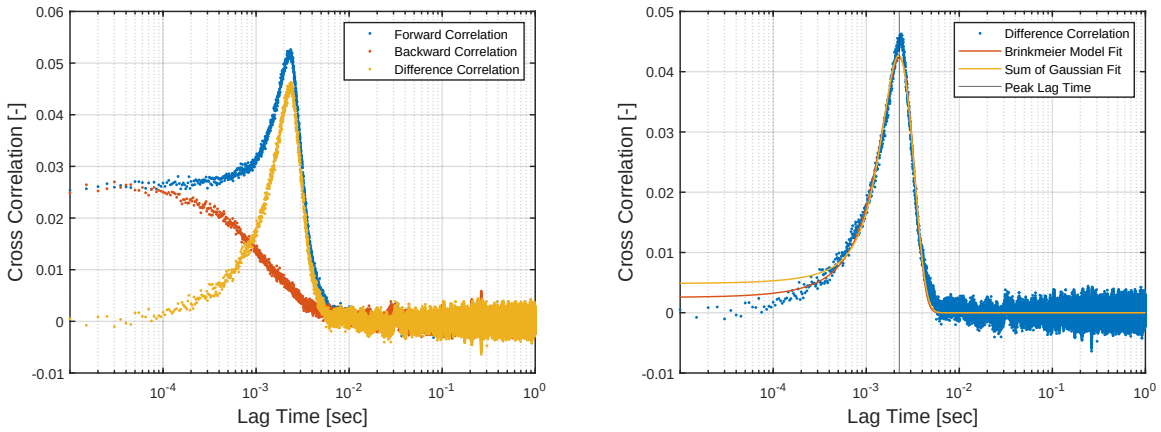
orescence fluctuation data, and calculate the difference between the forward and backward cross-correlations, representing the pure cross-correlation. The difference cross-correlation is fitted with either the model equation (Equation (5.2)) or a sum of Gaussian functions. The peak time where the maximum value of the fitted cross-correlation function occurs is extracted and taken as the value at which particles are most likely to have passed from the first focal volume to the next. The velocity is then computed as the ratio of the distance between the two foci obtained from the distance between the centers of the two optical fibers (reduced by the magnification factor of the objective) and the peak lag time extracted from the correlation curve. A representative sample of the cross-correlation curves and the fits is depicted in Figure 5.11.

Uncertainty approximation

To approximate a measurement uncertainty, each data acquisition which spans between 5 s to 60 s is split into 0.5 s increments and cross-correlated. Negative correlation fits and outliers defined as values three scaled median absolute deviations away are removed. Error bars represented in velocity measurements are defined as one standard deviation of 0.5 s cross-correlated segmented acquisition.

Velocity fit

Velocity measurements are taken at the center of the channel's width. As described in the introduction, the Hele-Shaw interpretation of the channel as infinite plates is a good



(a) Normalized Correlation (b) Fitting Difference Cross-Correlation

Figure 5.11: (a) Cross-correlation of the forward (blue), backward (orange), and difference (yellow) data are presented against time. (b) Fitting model are completed over the difference curve data to obtain the peak lag time (solid black vertical line) by either using the Brinkmeier model equation (orange solid line) or approximated with a sum of Gaussian (yellow solid line).

approximation for measurements that are completed far from the side walls of a low-aspect ratio channel. A constant viscosity model and power-law model velocity curve are fit over the measured velocity profile. The analysis for determining the velocity profile in a rectangular channel is outlined in Appendix C. Combining Equation (C.4) and Equation (C.5), the following approximation is made on the velocity profile for a Newtonian fluid:

$$V_x(z) = \frac{6Q}{(h^3 w)(1 - 0.63\frac{h}{w})} z(h - z) \tag{5.7}$$

where $V_x(z)$ is the velocity as a function of the positional height z, Q is the input flow rate, h is the height, and w is the width. In this work, the solution of the velocity profile of a power-law fluid across two narrow infinite plates is considered, which is:

$$V_x(z) = \left(\frac{h}{2k}\frac{\delta p}{\delta x}\right)^{1/n} \frac{hn}{2(n+1)} \left[1 - \left(\frac{|z - h/2|}{(h/2)}\right)^{\frac{n}{n+1}}\right] \tag{5.8}$$

5.5 Results

5.5.1 Velocity Profile Measurements

The first component of developing a true constitutive law of blood requires the measurement of the velocity profile to determine the local shear rate. In this section, a proof of concept of 2f FCS is demonstrated and a validation through a secondary flow generation is presented.

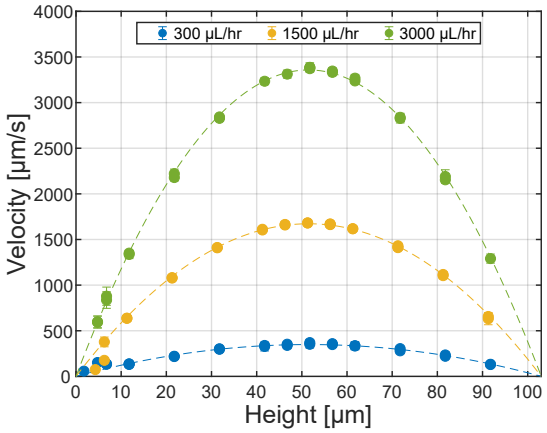
Measurement through different solutions

Velocity profiles for a transparent Newtonian fluid (Figure 5.12(a)), a non-aggregating RBC suspension (Figure 5.12(b)) at 40% hematocrit, a transparent non-Newtonian fluid (Figure 5.12(c)), and an aggregating RBC suspension (Figure 5.12(d)) at 40% hematocrit are presented. The velocity profiles presented are for increasing input flow rates where the error bars represent one standard deviation of 0.5 s length segment of the full acquisition. Figure 5.12(a,c,d) is measured in a glass-PDMS microfluidic device with a cross-sectional area of 103 µm by 3 mm, while Figure 5.12(b) is measured in a glass capillary microfluidic device with a cross-sectional area of 107 µm by 1 mm. A Newtonian model is fitted for the PBS while a power-law model is fitted over the 40% hematocrit non-aggregating sample, PEO sample, and 40% hematocrit aggregating sample, which has been summarized in Table 5.1. The relative error of the absolute values of the velocity measurements for the theoretical Newtonian fluid was approximately -28.9% and was consistent when testing different input flow rates on the same experimental day. This discrepancy between theoretical and measured values will be further reported in Section 5.5.3.

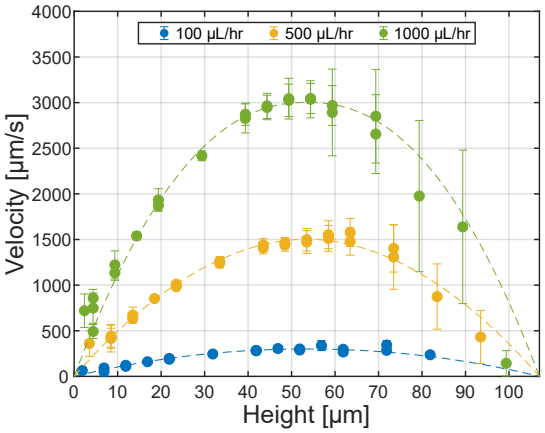
Velocity measurements using 2f FCS are not only applicable for transparent solutions but also dense RBC up to at least 40%. In this work, the velocity profile of the non-aggregating RBC is found to be relatively parabolic, reminiscent of a Newtonian fluid, but with the difference of an elevated velocity close to the wall of the channel indicating a slip length which is similarly observed for the aggregating RBC sample as well. Measurement through a dense RBC suspension at a nominal feeding hematocrit of 40% was surprising, and so the accuracy of the velocity profile shape needed to be verified.

Measurement validation through secondary flow conditions

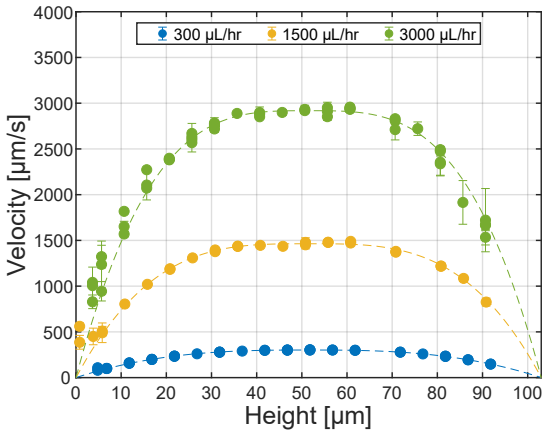
To verify the validity of the measurement technique using 2f FCS in a dense suspension, two velocity measurement methods are employed with non-aggregating RBC samples in glass



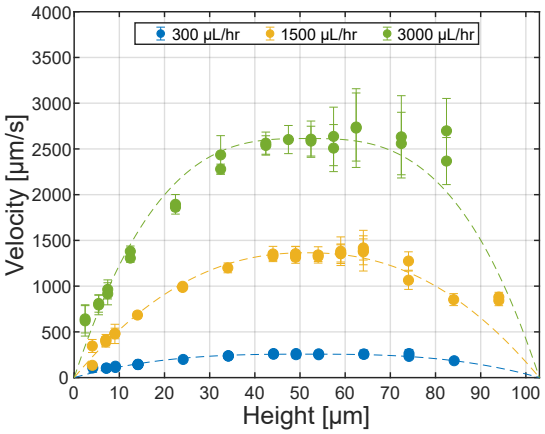
(a) PBS



(b) 40% hematocrit RBC in PBS OptiPrep



(c) PEO



(d) 40% hematocrit RBC in Plasma OptiPrep

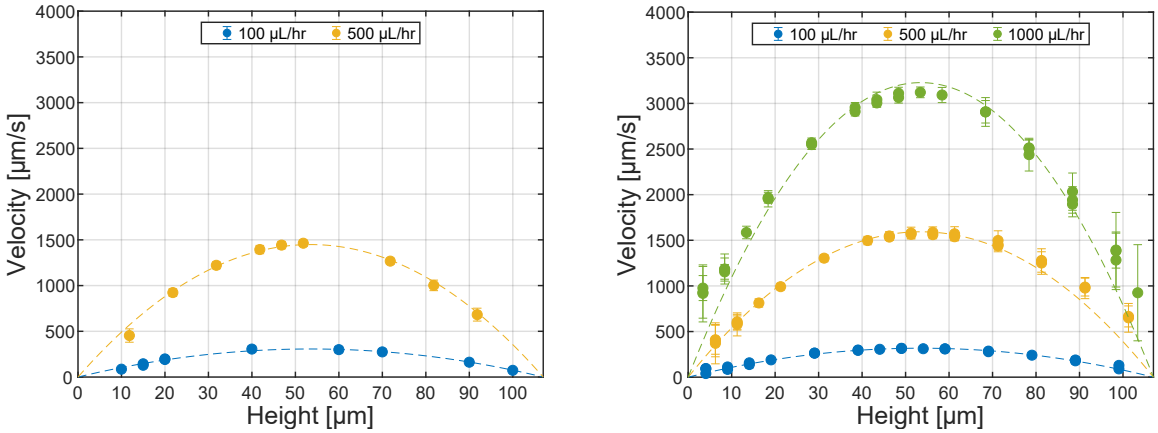
Figure 5.12: Velocity profiles through different solutions for increasing input flow rates. Flowing a (a) transparent Newtonian fluid, (b) non-aggregating RBC sample, (c) transparent non-Newtonian fluid, and (d) aggregating RBC sample. Blood data presented are for nominal feeding hematocrit of 40%. Dashed line represents a fitted Poiseuille's law model (a) and power-law model for (b-d). Each data point represents a unique trace in which the error bars represent one standard deviation of the cross-correlation peak lag time of sub-sampled 0.5 s length segment of the full acquisition.

Table 5.1: Fitted power-law index for Figure 5.12

	power-law Index		
Fluid	100 µL/h	500 µL/h	1000 µL/h
40% RBC in PBS	0.965	1.077	0.806
	300 µL/h	1500 µL/h	3000 µL/h
PEO	0.570	0.445	0.437
40% RBC in Plasma	0.559	0.811	0.515

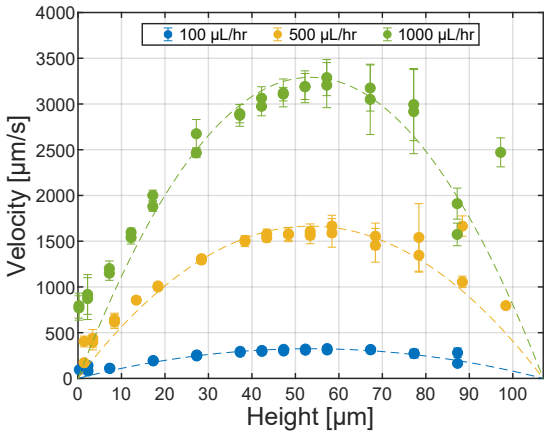
capillary channels with 107 µm channel height for nominal feeding RBC hematocrits of 0%, 10%, 20%, and 40%. The first is through flow rate control (Figure 5.13) using a syringe pump with an input flow rate of 100 µL/h, 500 µL/h, and 1000 µL/h. The second method is the linear actuation (Figure 5.14) for nominal displacement rates of 33.3 µm/s, 150.6 µm/s and 321.1 µm/s. Parabolic fits (which are expected for a Newtonian fluid) are fit over the volume control flow condition as dashed lines while the mean velocity profile of the channel is fitted over the linear actuation flow condition as a dashed line. Experimental conditions for 0% and 40% were measured on the same day, while 10% and 20% were measured the following day using the same washed RBC from the same donor sample. Furthermore, the fluid samples are prepared in the capillaries and tested in both flow conditions before switching samples to avoid changing the bulk fluid RBC hematocrit.

Similarly to the previous result, velocity profiles using the syringe pump demonstrate relatively parabolic velocity profiles reminiscent of a Newtonian fluid with the additional presence of a slip length at the wall that depends on the hematocrit and the flow rate. In contrast, velocity profiles found using the constant velocity method produced flat profiles as expected for a constant translation of the stage. Furthermore, in the constant velocity measurement, a clear lag in velocity is observed between the measured velocity and applied velocity using the syringe pump as an actuator. The discrepancy will be explored further in the limitations and considerations under theoretical experimental mismatch (see Section 5.5.3).

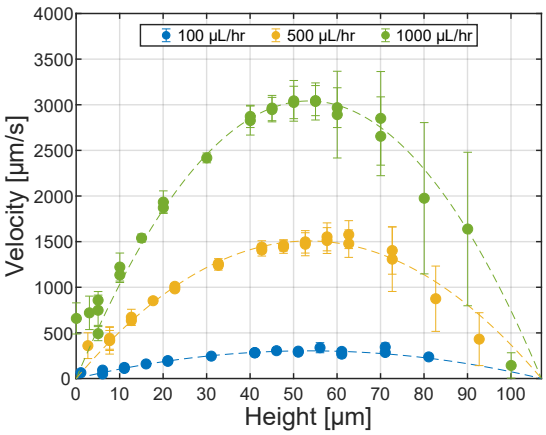


(a) PBS

(b) 10% RBC in PBS OptiPRep

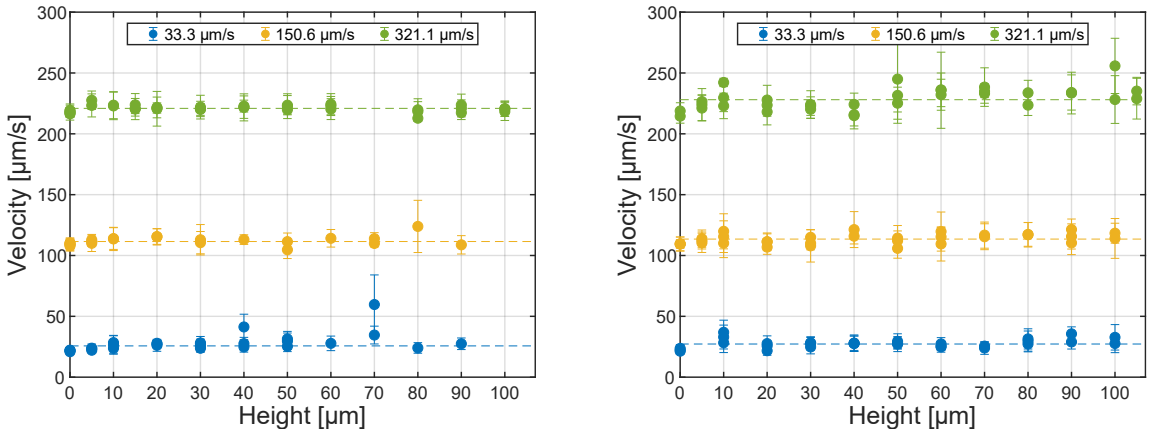


(c) 20% RBC in PBS OptiPRep



(d) 40% RBC in PBS OptiPRep

Figure 5.13: Flow rate control flow condition with three flow rates. Example of a (a) PBS Newtonian solution and non-aggregating RBC sample at increasing nominal feeding hematocrit. Dashed line represents a Poiseuille's law velocity model with no-slip condition. Each data point represents a unique trace of the fluorescent fluctuation in which the error bars represent one standard deviation of the cross-correlation peak lag time of sub-sampled 0.5 s length segment of the full acquisition.



(a) PBS

(b) 10% RBC in PBS OptiPRep

(c) 20% RBC in PBS OptiPRep

(d) 40% RBC in PBS OptiPRep

Figure 5.14: Constant velocity condition with three linear translation speed. Example of a (a) PBS Newtonian solution and non-aggregating RBC sample at increasing nominal feeding hematocrit of (b) 10%, (c) 20%, and (d) 40%. Dashed line represents the mean measured velocity. Each data point represents a unique trace of the fluorescent fluctuation in which the error bars represent one standard deviation of the cross-correlation peak lag time of sub-sampled 0.5 s length segment of the full acquisition.

5.5.2 Hematocrit Approximation

The second component of developing a true constitutive law of blood requires the measurement of the local hematocrit distribution. Two approaches for integrating local velocity and hematocrit measurements are explored: mean fluorescent intensity and cross-correlation amplitude.

Fluorescent intensity

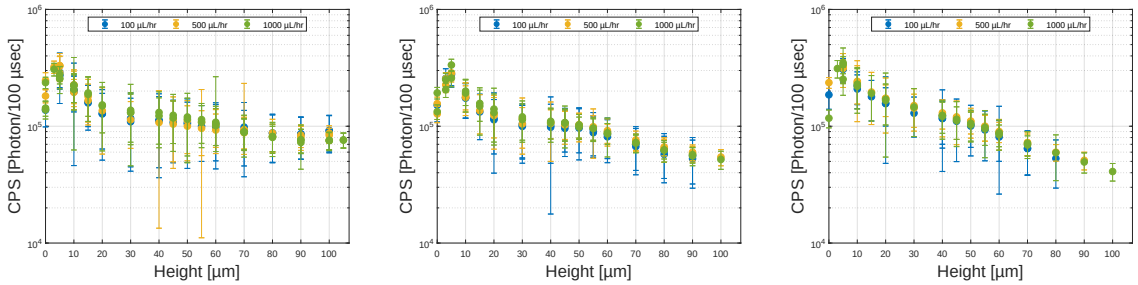
In examining the local hematocrit, it was hypothesized that the local volume fraction of cells may be determined by the fluorescent intensity data itself, thus allowing a measurement of the proportion of cells in the local volume of interest. This is characterized by a fluorescent intensity defined as the mean photon counts per 100 microseconds plotted, which is plotted as a function of height for 10%, 20%, and 40% hematocrit samples for flow control flow condition (Figure 5.15(a)) and constant velocity condition (Figure 5.15(b)). Error bars represent one standard deviation of the photon counts per 100 microseconds.

The absolute value of fluorescent intensity was found to not be correlated to the nominal feeding hematocrit in the channel in which a proportional increase in the hematocrit did not result in a decrease in the mean photon count. Interestingly, a sharp increase in the counts per second is observed at the entrance of the channel (defined as position 0, taken from the bottom of the channel). This initial increase is followed by a non-linear decay in the photon counts for the flow control flow condition, while a non-linear decay and then increase is observed at the 10% and 20% hematocrit sample fo the constant velocity flow condition. This initial increase may be understood as the height of the beam entering the channel itself.

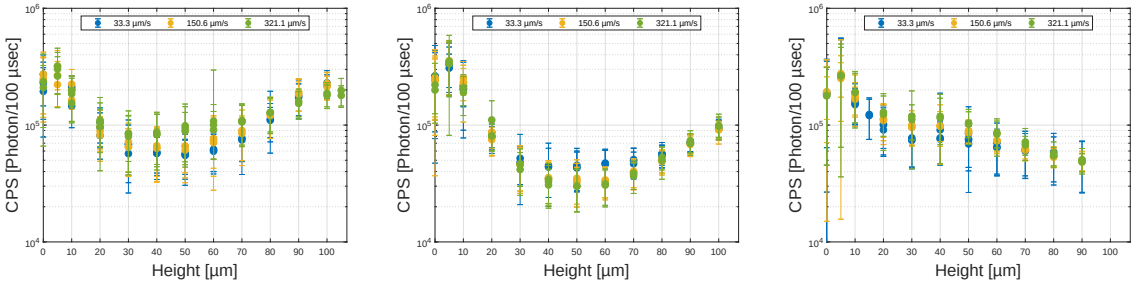
Cross-correlation amplitude

A second approach in measuring the local hematocrit is tested with the amplitude of cross-correlation that dictates the local velocity measured. This is characterized by the average peak amplitude of the cross-correlation function (described in Equation (5.2)) of the segmented trace in 0.5 s plotted as a function of height for 10%, 20%, and 40% hematocrit samples for the flow control condition (Figure 5.16(a)) and the constant velocity condition (Figure 5.16(b)).

The response of the cross-correlation amplitude was observed to be different between the two flow conditions. In the case of the flow control condition, a peak is observed in the

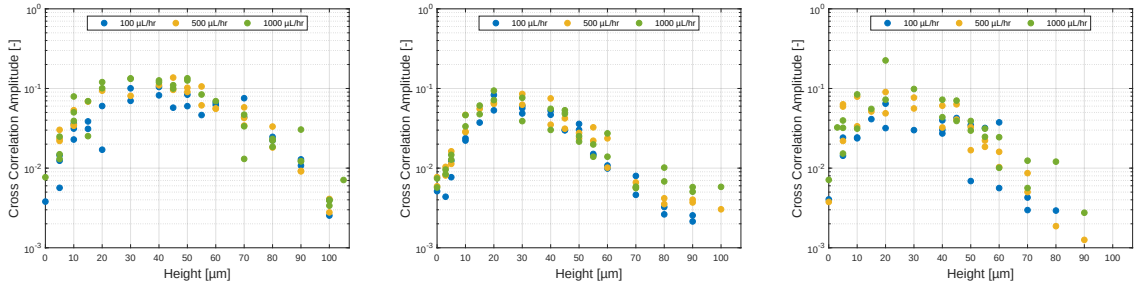


(a) Flow rate control flow condition

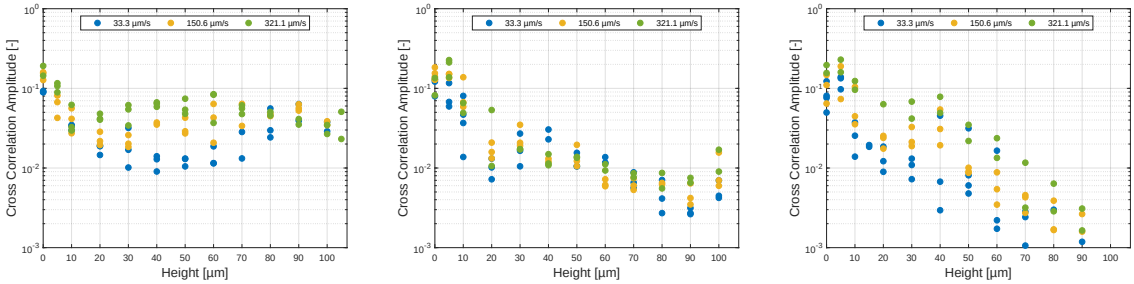


(b) Constant velocity condition

Figure 5.15: Photon counts per second measurement for non-aggregating RBC for 10% (left), 20% (center) and 40% (right) nominal feeding hematocrit across the height of the channel. Each data point represents a unique trace in which the error bars represent one standard deviation of the photon counts per 100 microseconds.



(a) Flow rate control flow condition



(b) Constant velocity flow condition

Figure 5.16: Correlation amplitude for non-aggregating RBC for 10% (left), 20% (center) and 40% (right) nominal feeding hematocrit across the height of the channel. Each data point represents the cross-correlation amplitude to a unique trace.

cross-correlation amplitude that shifts closer to the bottom channel surface with increasing RBC hematocrit. In contrast, for the constant velocity condition, the amplitude of the cross-correlation is observed to decrease exponentially with increasing penetration of the 20% and 40% hematocrit samples, while plateauing is observed for the 10% hematocrit samples.

5.5.3 Limitations and Considerations

In the following section, measurement depth, multiple lag time, and theoretical mismatch are explored. While additional considerations on tracer selection and velocity profile symmetry are reported in Appendix C.

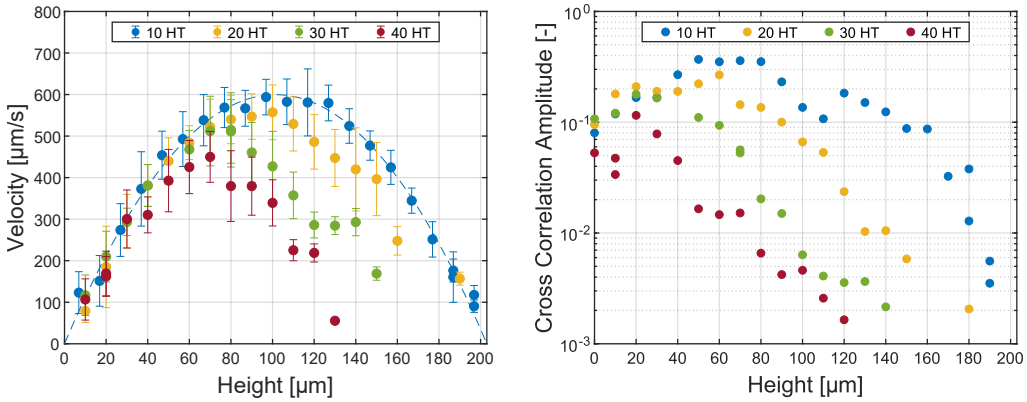
Measurement depth penetration

One key limitation of 2f FCS to consider is the depth at which signals can produce reliable cross-correlation and lag time. The velocity measurements and cross-correlation amplitude are presented in Figure 5.17(a) for 0%, 10%, 20%, 30%, and 40% feeding hematocrit with 0.005% solid of fluorescent particles at an input flow rate of 500 µL/h for a glass capillary channel height of 203 µm (these measurements were completed by Maya Salame during her master's internship under supervision). The dashed blue line is a Poiseuille law for the 10% hematocrit sample if it is considered Newtonian, knowing the geometry of the capillary. It is observed that as the hematocrit increases, the depth of measurement into the suspension decreases as the cross-correlation amplitude decreases. Furthermore, it is observed that the magnitude of the velocity measurement of the RBCs decreases progressively sooner for increasing hematocrit.

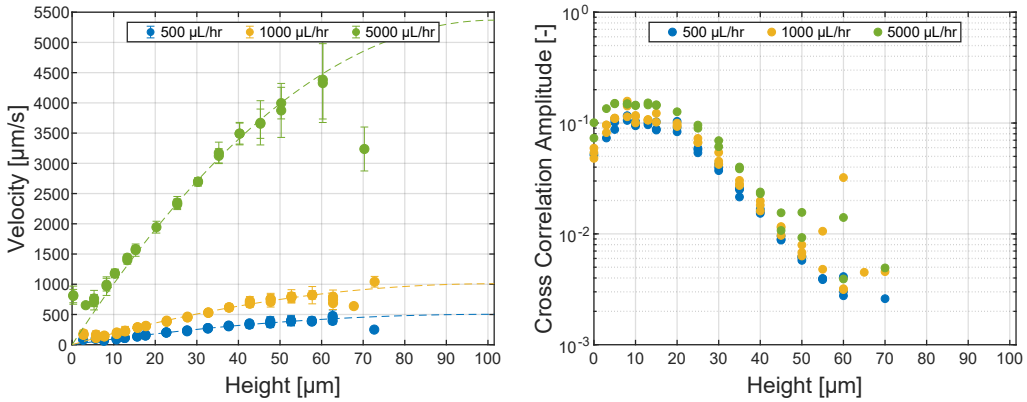
The velocity measurement and cross-correlation amplitude for volume-control injection (see Figure 5.17(b)) were conducted at 40% feeding hematocrit with 0.1 nmol/L of Alexa 647 at an input flow rate of 500 µL/h, 1000 µL/h, and 5000 µL/h in the same glass capillary channel. Similarly, the velocity measurement and cross-correlation amplitude for the constant flow condition (see Figure 5.17(c)) were conducted at 40% feeding hematocrit with 0.0005% of fluorescent beads at a displacement rate of 150.6 µm/s, 321.1 µm/s and 635.5 µm/s. The depth of penetration of which velocity is measurable can be observed to be independent of input flow rate between the range tested where measurements after 60 µm begin to decay.

Wall effects and multiple lag time

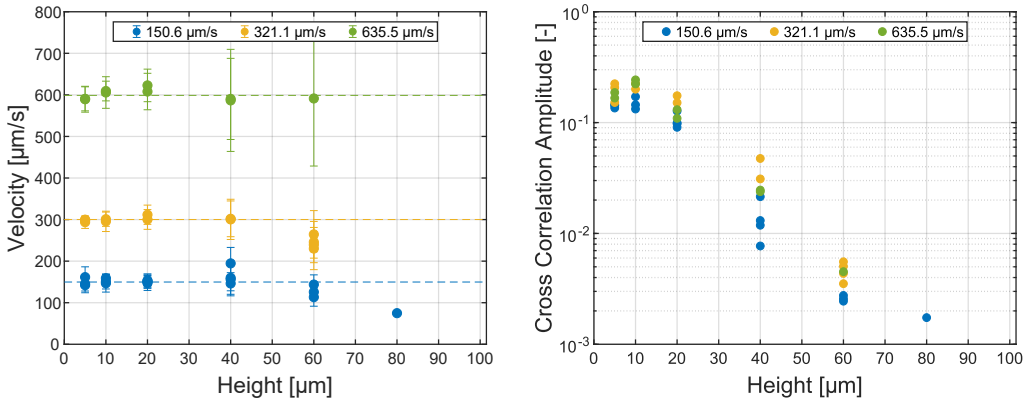
An interesting phenomenon is observed close to the channel wall, where typically a CFL is present in blood flow. Cross-correlation of segmented trace into 0.5 second traces (Figure 5.18) between heights of 0 µm and 60 µm is presented for 40% hematocrit at 1000 µL/h. Close to the surface wall up to 10 µm, multiple peak lag times can be observed that span up to two orders of magnitude difference in time. After 10 µm, the peak lag times of the individual segments converge to a single value; however, the correlation amplitude decreases the further into the suspension a velocity is measured. This decrease in correlation amplitude is observed in the exploring hematocrit interpretation of the data.



(a) Feeding hematocrit variation



(b) Volume control injection



(c) Linear Actuation

Figure 5.17: Velocity and cross-correlation amplitude measurements in 203 µm glass capillary channels. (a) Hematocrit variation with 0.005% solid of fluorescent particles at an input flow rate of 500 µL/h. (b) Volume-control injection for 40% feeding hematocrit with 0.1 nmol/L of Alexa 647. (c) Linear actuation for 40% feeding hematocrit with 0.0005% of fluorescent beads.

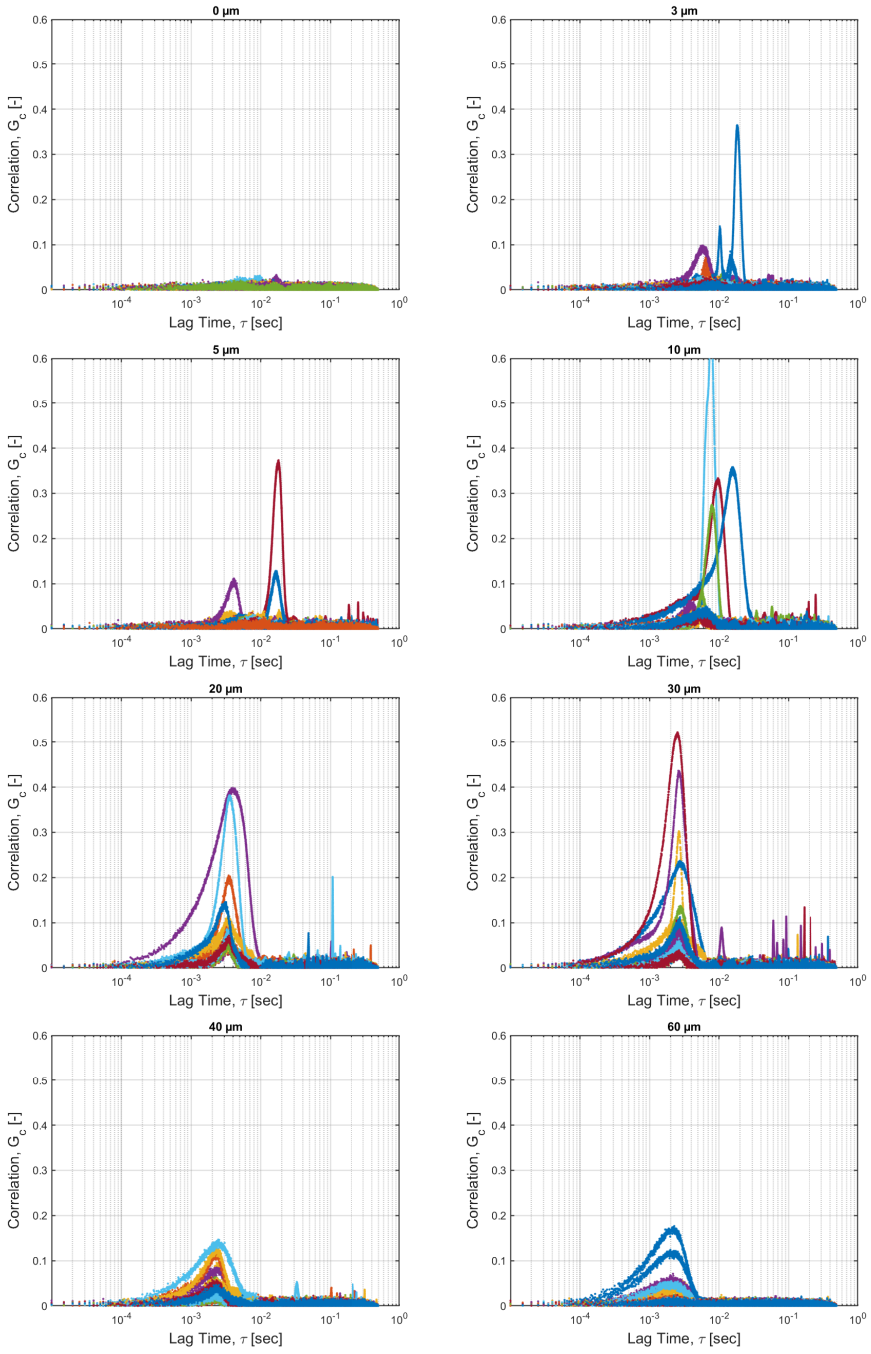


Figure 5.18: Cross-correlation function of non-aggregating 40% hematocrit sample taken from the bottom wall to 60 µm with input flow rate of 1000 µL/h.

Theoretical and experimental mismatch

An important point to consider is the discrepancy between the theoretical maximum velocity and the actual maximum velocity values. Table 5.2 presents a summary of the measurements completed over the span of four months using the 2f FCS for PBS, and non-aggregating RBC of 10%, 20%, and 40% hematocrit. Prior to using the 2f FCS, measurements completed on different days were calibrated by centering the beams such that the photon counts per second in a standard solution of Alexa 647 at a concentration of 10 nmol/L on a glass slip are at a maximum for both optical fibers. The mean relative error defined as $(V_{max}^{Theoretical} - V_{max}^{Experimental})/V_{max}^{Theoretical})$ spans between -0.293 to 0.169, where the largest variations of relative error occur between weeks and minimal variations are observed when doing measurements on the same day.

Table 5.2: Relative measurement error over different experimental days

Date	Fluid	Condition	100 µL/h	500 µL/h	1000 µL/h	Mean Relative Error
25/10/23	PBS	S.P.		0.981		- 0.019
11/1/23	10% HT	S.P.		1.169		0.169
14/2/24	PBS	S.P.	0.713	0.697		- 0.295
14/2/24	PBS	L.A.	0.702	0.742	0.687	- 0.289
14/2/24	40% HT	S.P.	0.716	0.721	0.723	- 0.28
14/2/24	40% HT	L.A.	0.653	0.753	0.715	- 0.293
15/2/24	20% HT	S.P.	0.776	0.800	0.794	- 0.21
15/2/24	20% HT	L.A.	0.689	0.745	0.700	- 0.289
15/2/24	10% HT	S.P.	0.768	0.757	0.776	- 0.233
15/2/24	10% HT	L.A.	0.723	0.743	0.694	- 0.28
			300 µL/h	1500 µL/h	3000 µL/h	
7/3/2024	PBS	S.P.	1.011	0.944	0.935	- 0.036
14/3/2024	PBS	S.P.	0.753	0.709	0.736	- 0.267
26/3/2024	PBS	S.P.	0.848	0.811	0.810	- 0.177

S.P. = Syringe Pump, control flow rate condition, L.A. = Linear Actuation, constant velocity profile condition, HT = Hematocrit

5.6 Discussion

5.6.1 Velocity Profile Measurement

Flowing PBS solution (Figure 5.12(a)) through the low aspect ratio microfluidic device exhibited a parabolic velocity profile characteristic of a Newtonian fluid in Poiseuille flow that is measurable over the full height of the microfluidic channel (Equation (5.7)). This demonstrates as a baseline that 2f FCS is a technique capable of measuring velocity fields in a transparent medium similarly demonstrated in previous works [110, 118]. Velocity measurements, of course, are not limited to Newtonian fluids and parabolic profiles, as flowing PEO solution, which is a transparent fluid that has known shear-thinning behavior, even at low concentrations, produced an expected plug flow (Section 5.5.1). Fitting a simple power-law model (Equation (5.8)) of the PEO solution produced a power-law index ranging between 0.437 to 0.570, which is a comparatively lower value than reported values ranging from 0.981 for 1.2% concentration of PEO in water at 20 °C down to 0.736 for 4.8% concentration of PEO in water at 20 °C completed in a rotational viscometer Haake VT 550 [134]. The concentration of PEO of the tested sample was 0.5% w/w with MilliQ water, in which the zero shear viscosity of the fabricated PEO solution is approximately 150 mPa sec at 20 °C. However, as the solution was a few weeks old, there may be some level of evaporation of the solution over time that would have an increasing effect on the viscosity of the fluid.

2f FCS was found to not be limited to transparent fluids, flowing both non-aggregating RBCs (Figure 5.12(b)) and aggregating RBCs (Figure 5.12(d)) at 40% hematocrit both produced measurable velocities. The non-aggregating sample produced a relatively parabolic profile with elevated velocities close to the walls as measured. This is observed by fitting a power-law model over the non-aggregating sample where the extracted power-law indices found are 0.965, 1.077, and 0.806 for input flow rates of 100 µL/h, 500 µL/h and 1000 µL/h, respectively. In contrast, plug flow was observed for the aggregating RBCs at 40% hematocrit, which when fitted with a power-law model resulted in the extracted power-law indices of 0.559, 0.811, and 0.515 for input flow rates of 300 µm/s, 1500 µm/s and 3000 µm/s, respectively. However, from a qualitative inspection of the curve itself, a simple power-law model does not adequately capture the velocity profile of the non-aggregating sample. Furthermore, similarly to the non-aggregating sample, measured velocities close to the walls are elevated compared to the fitted power-law model.

To confirm the validity and accuracy of the velocity measurements using the 2f FCS method, two flow generation methodologies were completed. The first flow generation methodology was a flow control system using syringe pumps, which produces a parabolic

velocity profile when flowing a Newtonian fluid. While the second flow generation methodology was a linear translation of the stage, which produces a constant velocity profile. A constant velocity profile is expected because at this scale the Reynolds number and Stokes number are much less than 1 and minimal relative motion of the RBCs is expected between the RBC and the channel walls. A constant velocity profile is observed in both the Newtonian PBS sample and RBC suspension between 10% to 40% hematocrit (Figure 5.14). These two distinct flow conditions demonstrate that the measurements completed using 2f FCS capture the features that describe the relative motion of the RBC suspension in flow.

Velocity profile in literature has shown contradictory results regarding the response of blood flow in vitro from works reporting parabolic velocity profile [109, 122–124] which is in contrast to plug velocity profiles [104, 115, 125, 126]. From literature it is unclear whether the range of reported differences in expected velocity profile is a consequence of the complex and not yet fully understood character of blood flow or the limitations of the technique utilized in these reports.

Slipping length

In this work, a more detailed examination of the non-aggregating RBC sample in the flow control system (Figure 5.13) indicates an interesting feature that deviates away from a transparent Newtonian fluid. Close to the channel wall, the measured velocity is elevated in contrast to the center of the channel where the velocities are found to be slower than an equivalent Newtonian fluid. Furthermore, when comparing the increasing hematocrit, it is observed that the overall magnitude of the elevated velocity close to the channel wall appears to decrease. This elevated velocity in proximity to the channel wall, however, is not present in the constant velocity configuration, which may indicate that there may be a coupling of the velocity measurements using 2f FCS to that of the local distribution of the cells.

The results of an elevated velocity close to the channel wall may be an indication that there is a slip length that should be considered when flowing RBC. Qualitatively, this phenomenon of increased velocity appears to be dependent on the hematocrit, which appears to dampen the velocity, and the input flow rate through the channel. This slip length is most likely to be a result of the fact that the velocity of the RBCs at the wall will not necessarily tend towards zero at the wall as assumed by a no-slip condition. This may then be related to the CFL which is known to be dependent on the hematocrit [135] or a general effect of the local hematocrit distribution.

5.6.2 Hematocrit Approximation

To understand the connection of local velocity dynamics simultaneous to having local hematocrit variation, two approaches were considered with the objective of extracting meaningful information about the local hematocrit of the sample. The initial approach was to examine the mean fluorescent intensity as a function of the height into the channel at different sample hematocrits. In the case of the fluorescent intensity, it was hypothesized that with increasing hematocrit, the mean fluorescent intensity would decrease as a consequence of the absorption of light from the presence of a greater number of cells if the concentration of tracer particles is maintained in the surrounding suspending fluid.

This hypothesis was found to not hold true in practice, as the results of the mean fluorescent intensity are found to minimally change with the input flow rate for all RBC hematocrits (Figure 5.15). Furthermore, the magnitude was not necessarily found to be correlated with the RBC hematocrit, as doubling of the RBC hematocrit did not result in a proportional reduction of the mean intensity. While in terms of flow rate control and flow condition, the mean fluorescent intensity was found to behave similarly close to the initial channel surface where an increase in intensity is observed, followed by a decay. However, the fluorescent intensity increased after the center of the channel for the 10% and 20% hematocrit samples in a constant velocity condition.

The question arises then on what exactly the fluorescent intensity represents. In modeling the system, the fluorescent fluctuation function is assumed to be proportional to the molecule concentration and the time independent emitted excitation profile. It is known that close to the channel wall there is a CFL where there is a lower concentration of RBCs which then increases approaching the center of the channel and so if the local hematocrit of RBC is increasing the deeper into the channel then the less volume the fluorescent beads can occupy. This may be further convoluted by the fact that the beams at the walls are also not fully immersed in the channel as the center of the beam foci is focused at the wall. Therefore, the initial increase in intensity can be understood as the process where the bottom half of the foci is entering the channel (represented in Figure 5.19). Consequently, as a preliminary attempt at determining a local hematocrit structure, the process proved to be more intricate than anticipated.

The second method that was explored was looking at the change in cross-correlation amplitude, which is defined as the mean amplitude of the segmented peak cross-correlation function. There is a correlation to the velocity magnitude as slower velocities tend to have lower correlation amplitude, and this may be associated with the idea that the ratio of the diffusion characteristic time is not insignificant from the characteristic flow time. Comparing the trend of the correlation amplitude of a transparent medium to a dense

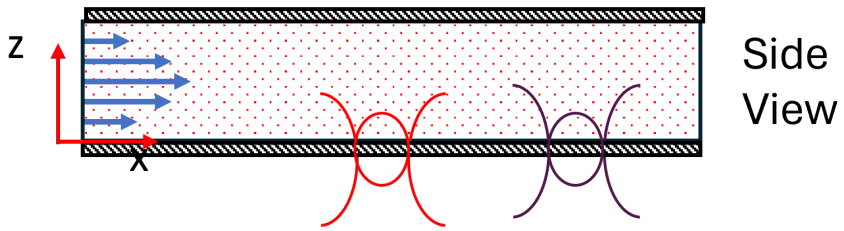


Figure 5.19: A schematic shows two focal volumes, colored red and purple, positioned within a channel containing a low concentration of fluorescent beads or dyes, viewed from the side. When the two foci are directed at the channel, the excitation volume near the wall is reduced to approximately half of what is typically used deeper in the channel.

medium consisting of a translucent object, the correlation amplitude decays the deeper into the channel the velocity is measured. What is noticed between the three tested hematocrits of 10%, 20%, and 40% is that the start of the decay of the correlation amplitude occurs at a lower depth the greater the feeding hematocrit. The rate of the decay of the correlation amplitude also appears to change depending on the sample hematocrit.

5.6.3 Considerations and Limitations

Measurement depth penetration

A key question is how deep the velocity can be measured in dense suspensions. In 107 µm channels, velocity measurements span the full height under both flow control and constant velocity conditions, aligning with theoretical profiles (Figure 5.13, Figure 5.14). However, this is not the case in larger capillaries (203 µm height), where increasing hematocrit causes the velocity profile to plateau and decrease at lower heights (Figure 5.17(a) left). This plateauing and decay correlate with the cross-correlation amplitude, which diminishes sooner and rapidly at higher hematocrit levels. The reduced penetration depth for the same hematocrit in larger tubes is likely linked to the Fåhræus effect, where smaller tube diameters decrease the average RBC concentration. Thus, penetration depth in dense suspensions is strongly influenced by both the tube hematocrit and the diameter.

The measurement penetration depth, however, appears to be minimally affected by the flow condition or input flow rate as for both the volume control injection (Figure 5.17(b) left) and linear actuation (Figure 5.17(c) left) for a given fixed input RBC hematocrit. The resulting measurement in velocity profiles conforms with the expected theoretical profile up to the same height, after which the measured velocities deviate from the expected velocity.

Wall effects and multiple lag time

From the velocity profiles of non-aggregating RBC samples, it is observed that the velocities close to the wall are often elevated compared to the expected velocity of those of a Newtonian fluid. In closer inspection of the correlation of the individual 0.5 s segment, what emerges is the presence of multiple peak lag times which can range in magnitude of value for a given height, which eventually converges to a singular value the further the channel is penetrated. Multiple peak lag times may arise from several sources. The first possible source of variation of multiple lag times to consider is due to the heterogeneous distribution of RBCs and the formation of a CFL. Close to the channel walls, infrequent cell passage due to the presence of a CFL could result in a time scale that is associated with both the cell velocity through the focal point and the velocity of fluorescent beads in the suspending fluid. Furthermore, RBC dynamics close to the wall, such as rolling, tumbling, and sudden cell-cell interactions, may further induce temporal variations that result in multiple time lags during cell passage through the focal points. While progressing deeper into the channel, the amount of voids between cells which contain a low concentration of fluorescent particles in the suspending fluid is expected to decrease because the cells are more packed, and what is observed is a merging of the peak lag times. A secondary source of variation of multiple lag times to consider is that there is a distribution of sizes of fluorescent particles, as the batch used was already a few years old. Although the fluorescent bead suspension was ultra-sonicated for a period of 45 min prior to further dilution, large aggregates may be present, which would flow slower than the surrounding fluid if their inertia were to become significant. Lastly, a third source of variation could be a result of the fact that the beam foci is finite and in a region of high velocity gradient. Measuring close to the wall, where no-slip conditions are expected, to a region with non-zero velocity would produce what would be expected to capture two time scales that are distinct. This is reminiscent of having a large depth of correlation when looking at μPIV.

Theoretical and experimental mismatch

Comparing the theoretical and experimental values of Newtonian fluid. There is a bias that is not accounted for in the presentation of this work. Measurements completed on the same day on the same sample were found to produce similar relative error for different flow speeds and flow configurations (Table 5.2). The relative error is also found to be of the same magnitude when comparing different samples completed on the same day as well.

At the time of this report, further verification is required to resolve the discrepancies. It is hypothesized that these discrepancies in relative measurement error stem from the day-

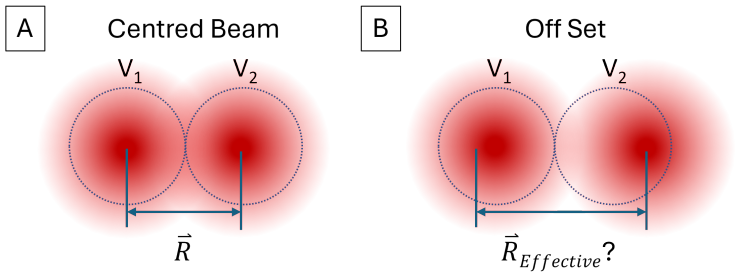


Figure 5.20: Dotted line represents the area of the fiber optics that the beams are focused on, where as the gradient red circles represent the top view projection of the focal beam. The hypothesis of the source of error is associated to the placement of the two foci (A) the placement of the foci are centered to the fiber (B) the placement of the foci are off centered to the fiber.

to-day calibration procedure. Calibrating the 2f FCS apparatus involves aligning the two foci with the fiber optics to maximize photon counts per second while minimizing cross-talk between the two foci. This manual three-step process includes adjusting the fiber optics, main mirror, and beam splitters to align the beam foci parallel to each other and perpendicular to the channel. It is challenging due to the second foci's non-linear movement during mirror adjustments and the difficulty in identifying the true global maximum photon count.

In the presented velocity measurements, the distance between the foci (i.e., the length scale for velocity measurement) is assumed to be the central distance between the fiber optics, magnified by the objective lens and fixed across measurements, as shown in Figure 5.20 A. This assumption holds if the beam foci are centered on the fiber optics, but it is unclear what occurs when the beam foci are off-center, potentially causing the foci to be too close or too far apart. While the first foci is likely well-aligned with the first optical fiber due to the straightforward alignment via the fiber stage translation, the second foci may be biased to be further from the fiber center to minimize cross-talk. This misalignment is hypothesized to alter the effective distance between the foci, as fluorescent particles would either be excited sooner (if the foci are closer) or later (if farther apart). Further verification is needed to assess the length scale and address this issue. Possible solutions to ensure the proper length scale is used are incorporating optical calibration tools, such as a microscope reference scale and camera system, or conducting a pre-experiment calibration test with stage translation at a known velocity to determine the effective length scale prior to completing experiments.

5.7 Conclusions and Future Work

In this work, the hypothesis put forth is that 2f FCS is a viable technique for measuring the micro blood flow velocity profile. It has been demonstrated that the velocity fields of transparent fluid mediums are achieved for both Newtonian and non-Newtonian fluids. Although that has been demonstrated in similar works of Brinkmeier and colleagues [118], our study further shows that the velocity profiles through dense suspension media, specifically RBCs, around physiological hematocrit, can be effectively measured. The velocity profiles are verified by comparing two flow conditions: flow control using syringe pumps and a constant velocity profile by translating the stage. When flowing non-aggregating RBCs in glass capillaries at the scale of 107 µm the velocity close to the walls is elevated and the center region lowered compared to a Newtonian fluid, which is similar to plug flow velocity profiles demonstrated in some μPIV literature. Additionally, a slip length is observed in the velocity profile of blood flow as the velocity of the cells at the wall is never zero. These first results demonstrate the power that the novel application of an established technique can bring to understanding micro-blood flow.

With the future goal of pairing local velocity measurement with local hematocrit measurement using the same technique, this work assesses two possibilities of using 2f FCS: mean fluorescent fluctuation intensity and cross-correlation amplitude. In the former, the magnitude of the mean intensity was not found to be proportional to the hematocrit of the sample. However, differences in the decay of the mean fluorescent fluctuation intensity do appear between sample hematocrit and also the flow configuration. The latter method exploring the cross-correlation amplitude proved to be more about the efficacy of the depth of velocity measurements than a means of measuring local hematocrit. The cross-correlation amplitude as a function of the height similarly does not scale with the volume fraction of the RBC however, the depth at which correlation amplitude begins to decay occurs at lower height with increasing hematocrit. As an assessment at determining a local hematocrit structure, the process proved to be more intricate than anticipated. Further exploration will need to be completed in order to truly pair local velocity measurements with local hematocrit, which is essential in re-exploring rheological measurements in rotational rheometers.

Several limitations and considerations that should be made regarding measurements using 2f FCS for micro blood flow velocity measurements regarding depth of measurement and calibration. Measurement depth penetration through a dense suspension was found to depend both on the feeding hematocrit and the tube diameter, while independent of the tested flow rate or flow configuration. At physiological hematocrit of around 40%, a measurement depth of approximately 60 µm was achieved in a 100 µm tall channel. Lastly,

theoretical and experimental mismatch is explored in which relative error was found to be similar when measurements are completed on the same day after which calibration was completed. As it currently stands, the calibration methodology of trying to place the beam foci at the maximum position of the fiber optics is not a sufficient requirement. Further exploration on the effects of the center of the beam relative to the center of the fiber optics should be explored to determine the discrepancies of day-to-day measurements. Despite these challenges, 2f FCS proves to be a valuable tool in re-examining local velocity fields in dense suspensions, paving the way for future advancements in blood rheology research.

5.8 Key Takeaways

Velocity Measurements

Normalized velocity profiles demonstrate that the velocity profile characterization across the microfluidic device is achievable for both transparent fluids and dense suspensions of RBC of at least 40% feeding hematocrit. Both aggregating and non-aggregating samples exhibit slip length that may be indicative of a CFL and the fact that the velocity of the cells at the wall is never zero.

Hematocrit Approximation

Hematocrit approximation of RBC suspension is still in contention. The measurements of the intensity by mean fluorescent intensity did not correlate directly with hematocrit, as an increase in the feeding hematocrit did not result in a proportional decrease in the intensity. While measurement using the cross-correlation amplitude also did not scale with the feeding hematocrit, the amplitude was indicative of the depth at which measurements could be made.

Considerations and Limitations

To successfully achieve measurements in a dense suspension, several considerations need to be made regarding tracer selection, depth of penetration, and calibration. The selection of tracer particles should have a characteristic diffusion time that is slower than the flow rate tested. The depth of penetration needs to be verified as it is dependent on the feeding hematocrit and the geometry at which the suspension is flowed. Lastly, to ensure accurate velocity measurement, a reference velocity calibration measurement is recommended.

Chapter 6

General Conclusions and Perspectives

This work makes several contributions to the field of blood rheology by combining bulk rheological measurements of blood flow with the characterization of local microstructural phenomena occurring when blood flows through both simple and complex geometries. Three key questions were proposed and explored in this dissertation, which are outlined as follows:

- Firstly, at the capillary scale of the microcirculation, where nutrient and gas exchanges occur. **How does the cells interact with individual nodes and channels of a microfluidic network and how this contributes to the overall transport through the network?**
- Secondly, at the arteriolar level, the mixing process in blood is not fully understood, despite its primary function being the transport of nutrients and gases in a well-mixed state to the capillary field. **How does the presence of red blood cells (RBCs) affect mixing at the scale of microcirculation?**
- Lastly, in bulk, where blood suspensions are typically measured using classical rheometric methods such as plate-cone rheometers, linear velocity profiles are assumed when measuring the viscosity of the fluid of interest. **Is the velocity profile still true for the case of dense suspension such as blood?**

At the capillary scale, the transport dynamics of RBCs in uniform microvascular networks were explored, emphasizing how interactions between cells and network nodes correlate with perfusion efficiency. First, looking at the macroscopic rheological response

through three different network channels, a non-linear relationship between the excess relative resistance and capillary number was observed. The excess relative resistance as a function of capillary number was found to scale with a simple power law with parameters that are dependent on the hematocrit and the porosity.

The excess relative resistance magnitude was found to increase linearly at low volume fraction and non-linearly at high volume fraction. Furthermore, it was not found to be directly correlated to the velocity or cell morphology variation, and cluster-size distributions remained largely unchanged across all channels. However, larger hematocrit increased cluster formation and which could influence excess resistance of channels with differing porosity differently. The power-law exponent was found to decrease with increasing hematocrit, converging to a constant value. Differences in the power-law exponent were found to primarily be associated with the difference in morphological distribution in the channels observed. At the high capillary number regime, the power-law exponent was found to be lowered, which was found to be associated with the plateauing of the RBC elongation.

Rigidified RBCs with glutaraldehyde showed higher excess relative resistance but, when flow rates were rescaled by a capillary number reflecting their increased shear modulus, the excess relative resistance magnitude aligned with healthy controls. These rigidified cells also had a lower power-law exponent, suggesting deformability may have hit a limit. In contrast, rigidified RBCs with diamide changed the RBC surface area-to-volume ratio, altering flow resistance in ways not fully captured by adjusting the shear modulus alone. Overall, while capillary-number scaling appeared to capture changes to surface shear modulus, caution is advised if treatments also shift a cell's geometry.

This work established a framework for linking the local transport of RBCs in microfluidic networks to their overall macroscopic transport properties. While blood disorders such as sickle cell disease, spherocytosis, and thalassemias all affect RBC deformability, their underlying mechanisms differ. As a result, it remains uncertain whether these conditions lead to comparable changes in bulk transport or similar local RBC dynamics; an issue with implications for developing microfluidic-based diagnostic tools. This direction of exploring the effects of deformability in the network would complement the preliminary exploration of the use of chemically treated cells and the effects on the macroscopic transport. A second avenue of exploration is examining the role of RBC aggregability in confined microcirculatory flows. As aggregation can increase cell-cell interaction, it could have an effect on how cells form clusters and trains in the network. Exploration of network flow with aggregability could offer critical insights into how aggregation influences perfusion efficiency at the microcirculatory scale.

At the arteriolar level, the impact of mixing of fluorescent macromolecules in the sus-

pending phase was explored under the presence of a concentrated suspension of RBCs. Using a polydimethylsiloxane (PDMS) microfluidic co-flow device, experiments were conducted under varying RBC aggregability, volume fraction, and flow rates. We found that in order to improve mixing of proteins, glucose and all the constituents in the microcirculation, the presence of RBCs and high flow rates are paramount. Notably, an optimal hematocrit near 30% emerged for both non-aggregated and aggregated samples with plasma, suggesting a physiological phenomenon that enhances transport efficiency under typical microcirculatory conditions. Another intriguing result was that the enhancement of the mass transport was significantly improved for macromolecules of increasing molecular weight. This result underscores an important consideration for the design of nanoparticle-based drug delivery systems: in the microcirculatory regime, macromolecules and nanoparticles of varying sizes can exhibit similar transport behavior, leading to enhanced mixing and potentially more uniform distribution within microcirculatory networks.

To elucidate the mechanism behind the augmentation of the mass transport through the suspending phase, axial migration of the cell and the position of the interface are explored. Unlike the normalized effective diffusion coefficient of molecules, non-aggregated and aggregated cells did not show an optimal hematocrit but instead a minimum, indicating that increased molecular diffusivity is not necessarily driven by large-scale cell diffusivity. Insight from granular suspension suggests that particle rotation can play a large role in augmenting the effective diffusivity by inducing disturbances within the fluid. Observation of RBCs in glass capillaries indicates rotation is present in flow and, so, analogous to observations in granular suspension, the augmentation of the mass transport must be strongly associated with the dynamics in flow. Lastly, results of placement of the interface to the center of the channel resulted in a reduction in the mass transport rather than optimality observed when placed at the 1:3 position. This reduction in optimality is hypothesized to arise from several factors: shear-rate gradient, hematocrit distribution, or changes to the RBC interactions.

A potential next step in understanding the mass transport at the scale of microcirculation is to observe the influence of channel geometry. As physiological microcirculation tends to not be simple straight rectangular channels as indicated in the previous work on networks, the effect of curvature, tortuosity, and network bifurcation may be critical to further understanding the general dynamics behind the mass transport through dense suspension.

Lastly, in bulk, a novel approach using two-foci fluoresence correlation spectroscopy (2f FCS) is presented as a method to measure velocity fields in dense RBC suspensions within glass capillary microchannels. 2f FCS is validated using both transparent Newtonian and non-Newtonian fluid and extended in non-aggregated and aggregated RBCs at nominal

feeding hematocrit of 40%. The velocity profiles are verified by comparing two flow conditions: flow control using syringe pumps and a constant velocity profile by translating the stage. When flowing non-aggregated RBCs in glass capillaries at the scale of 107 µm the velocity close to the walls is elevated and the center region lowered compared to a Newtonian fluid, which is similar to plug flow velocity profiles demonstrated in some micro-particle image velocimetry (μPIV) literature. The initial results demonstrate the effectiveness of applying established techniques to enhance our understanding of micro blood flow.

This work assessed two possibilities of using 2f FCS to measure local hematocrit, which was the mean fluorescent fluctuation intensity and cross-correlation amplitude. The first method revealed that mean intensity was not proportional to sample hematocrit. However, the decay of mean fluorescent fluctuation intensity varied with both hematocrit levels and flow configurations. The second method, which analyzed cross-correlation amplitude, did not correlate with RBC volume fraction as well; however, the height at which the amplitude began to decay decreased with increasing hematocrit. Assessing local hematocrit structure was more complex than anticipated. Further research is necessary to accurately correlate local velocity measurements with local hematocrit, which is essential for revisiting rheological measurements in rotational rheometers.

The limitations and considerations using 2f FCS for micro blood flow velocity measurements were explored, which included the selection of tracer, depth of measurement, and calibration. However, despite these challenges, 2f FCS proves to be a valuable tool in re-examining local velocity fields in dense suspensions, paving the way for future advancements in blood rheology research. To further improve this measurement technique as a method to develop a true constitutive law for blood, further exploration needs to be made in characterizing the local hematocrit of blood flow. This may entail further controlled experiments on correlating the fluctuation data with the feeding hematocrit or the development of auxiliary techniques that can be completed simultaneously to 2f FCS. Ultimately, the future of this work will be in coupling the state-of-the-art rheometer with the 2f FCS system to couple the stress-strain measurement of the rheometer with the local measurement of the velocity and cell volume fraction.

References

[1] M. Fenech and L. Haya. Blood Flow Mechanics. In M. Labrosse, editor, *Cardiovascular Mechanics*, chapter 3, pages 63–89. CRC Press, 9 2018.

[2] M. Abkarian and A. Viallat. On the Importance of the Deformability of Red Blood Cells in Blood Flow. In *Fluid–Structure Interactions in Low-Reynolds-Number Flows*, chapter 10. RSC Publishing, 2016.

[3] R. Mehri, C. Mavriplis, and M. Fenech. Red blood cell aggregates and their effect on non-Newtonian blood viscosity at low hematocrit in a two-fluid low shear rate microfluidic system. *PLoS ONE*, 2018.

[4] E. Kaliviotis, J. M. Sherwood, and S. Balabani. Partitioning of red blood cell aggregates in bifurcating microscale flows. *Scientific Reports 2017 7:1*, 7:1–13, 3 2017.

[5] S. Chien. Shear dependence of effective cell volume as a determinant of blood viscosity. *Science*, 1970.

[6] T. W. Secomb. Blood Flow in the Microcirculation. *Annual Review of Fluid Mechanics*, 49:443–461, 1 2017.

[7] K. B. Chandran, S. E. Rittgers, and A. P. Yoganathan. *Biofluid Mechanics: The Human Circulation*. CRC Press, 2nd edition, 2012.

[8] F. C. Mokken, M. Kedaria, C. P. Henny, M. R. Hardeman, and A. W. Gelb. The clinical importance of erythrocyte deformability, a hemorrheological parameter. *Annals of Hematology*, 64:113–122, 1992.

[9] D. E. Discher, N. Mohandas, and E. A. Evans. Molecular maps of red cell deformation: Hidden elasticity and in situ connectivity. *Science*, 1994.

[10] R. M. Hochmuth, E. A. Evans, H. C. Wiles, and J. T. McCown. Mechanical measurement of red cell membrane thickness. *Science*, 1983.

[11] A. S. Popel and P. C. Johnson. Microcirculation and hemorheology. *Annual Review of Fluid Mechanics*, 2005.

[12] R. Fåhræus and T. Lindqvist. The viscosity of the blood in narrow capillary tubes. *American Journal of Physiology-Legacy Content*, 1931.

[13] L. Waite and J. Fine. *Applied Biofluid Mechanics*. Taylor and Francis group, 1st edition, 2007.

[14] T. G. Mezger. *The Rheology Handbook : 4th Edition*. Vincentz Network, 4th edition, 2012.

[15] C. J. Pipe, T. S. Majmudar, and G. H. McKinley. High shear rate viscometry. *Rheologica Acta*, 47:621–642, 7 2008.

[16] P. Guillot, P. Panizza, J. B. Salmon, M. Joanicot, A. Colin, C. H. Bruneau, and T. Colin. Viscosimeter on a microfluidic chip. *Langmuir*, 22:6438–6445, 7 2006.

[17] L. Lanotte, J. Mauer, S. Mendez, D. A. Fedosov, J. M. Fromental, V. Claveria, F. Nicoud, G. Gompper, and M. Abkarian. Red cells' dynamic morphologies govern blood shear thinning under microcirculatory flow conditions. *Proceedings of the National Academy of Sciences of the United States of America*, 113:13289–13294, 11 2016.

[18] P. Vennemann, R. Lindken, and J. Westerweel. In vivo whole-field blood velocity measurement techniques. *Experiments in Fluids*, 2007.

[19] A. L. Zydney, J. D. Oliver, and C. K. Colton. A constitutive equation for the viscosity of stored red cell suspensions: Effect of hematocrit, shear rate, and suspending phase. *Journal of Rheology*, 35:1639–1680, 11 1991.

[20] F. J. Walburn and D. J. Schneck. A constitutive equation for whole human blood. *Biorheology*, 13:201–210, 1976.

[21] E. W. Merrill. Rheology of Blood. *Physiological Reviews*, 49:863–888, 1969.

[22] R. L. Whitmore. *Rheology of the Circulation*. Pergamon Press, 1st edition, 1968.

[23] G. P. Galdi, A. M. Robertson, R. Rannacher, and S. Turek. *Hemodynamical Flows: Modeling, Analysis and Simulation*, volume 37. Die Deutsche Bibliothek, 2008.

[24] S. Lorthois. Blood suspension in a network. In A. Viallat and M. Abkarian, editors, *Dynamics of Blood Cell Suspensions in Microflows*, chapter 8. CRC Press, 1st edition, 2019.

[25] T Secomb. Mechanics of red blood cells and blood flow in narrow tubes. In C. Pozrikidis, editor, *Hydrodynamics of Capsules and Cells*, pages 163–196. Chapman & Hall/CRC Press, 2003.

[26] H. L. Goldsmith. Red cell motions and wall interactions in tube flow. *Federation Proceedings*, 1971.

[27] Gwennou Coupier, Badr Kaoui, Thomas Podgorski, and Chaouqi Misbah. Noninertial lateral migration of vesicles in bounded poiseuille flow. *Physics of Fluids*, 2008.

[28] B. Kaoui, G. H. Ristow, I. Cantat, C. Misbah, and W. Zimmermann. Lateral migration of a two-dimensional vesicle in unbounded poiseuille flow. *Physical Review E - Statistical, Nonlinear, and Soft Matter Physics*, 2008.

[29] D. L. and A. Acrivos. The shear-induced migration of particles in concentrated suspensions. *Journal of Fluid Mechanics*, 1987.

[30] A. R. Pries, T. W. Secomb, P. Gaehtgens, and J. F. Gross. Blood flow in microvascular networks. experiments and simulation. *Circulation Research*, 67:826–834, 1990.

[31] A. R. Pries, D. Neuhaus, and P. Gaehtgens. Blood viscosity in tube flow: Dependence on diameter and hematocrit. *American Journal of Physiology - Heart and Circulatory Physiology*, 263, 1992.

[32] A. R. Pries and T. W. Secomb. Rheology of the microcirculation. *Clinical Hemorheology and Microcirculation*, 29:143–148, 2003.

[33] D. Quemada. Hydrodynamique sanguine : Hémorhéologie et Écoulement du sang dans les petits vaisseaux. *Le Journal de Physique Colloques*, 37:C1–9, 1 1976.

[34] S. P. Sutera, V. Seshadri, P. A. Croce, and R. M. Hochmuth. Capillary blood flow ii. deformable model cells in tube flow. *Microvascular Research*, 2:420–433, 1970.

[35] Robin Fåhraeus. The suspension stability of the blood. *Physiological Reviews*, 9(2):241–274, April 1929.

[36] G. D.O. Lowe, editor. *Clinical Blood Rheology*. CRC Press, June 2019.

[37] J. J. Bishop, A. S. Popel, M. Intaglietta, and P. C. Johnson. Rheological effects of red blood cell aggregation in the venous network: A review of recent studies. *Biorheology*, 2001.

[38] W. Reinke, P. Gaehtgens, and P. C. Johnson. Blood viscosity in small tubes: effect of shear rate, aggregation, and sedimentation. *American Journal of Physiology - Heart and Circulatory Physiology*, 1987.

[39] S. Chien and K. M. Jan. Ultrastructural basis of the mechanism of rouleaux formation. *Microvascular Research*, 1973.

[40] J. K. Armstrong, H. J. Meiselman, and T. C. Fisher. Evidence against macromolecular "bridging" as the mechanism of red blood cell aggregation induced by nonionic polymers. *Biorheology*, 1999.

[41] H. J. Meiselman. Red blood cell role in rbc aggregation: 1963-1993 and beyond. *Clinical Hemorheology and Microcirculation*, 1993.

[42] J. Wu and M. Gu. Microfluidic sensing: state of the art fabrication and detection techniques. *Journal of Biomedical Optics*, 16:080901, 8 2011.

[43] A. Merlo, S. Losserand, F. Yaya, P. Connes, M. Faivre, S. Lorthois, C. Minetti, E. Nader, T. Podgorski, C. Renoux, G. Coupier, and E. Franceschini. Influence of storage and buffer composition on the mechanical behavior of flowing red blood cells. *Biophysical Journal*, 122:360–373, 1 2023.

[44] V. Clavería, O. Aouane, M. Thiébaud, M. Abkarian, G. Coupier, C. Misbah, T. John, and C. Wagner. Clusters of red blood cells in microcapillary flow: hydrodynamic versus macromolecule induced interaction. *Soft Matter*, 12:8235–8245, 10 2016.

[45] P. Vaupel. Tumor microenvironmental physiology and its implications for radiation oncology. *Seminars in Radiation Oncology*, 14:198–206, 7 2004.

[46] S. Novais, D. Pinho, D. Bento, E. Pinto, T. Yaginuma, C. S. Fernandes, V. Garcia, A. I. Pereira, J. Lima, M. Mujika, R. Dias, S. Arana, and R. Lima. Cell-Free Layer (CFL) Measurements in Complex Geometries: Contractions and Bifurcations. In R. Lima, Y. Imai, T. Ishikawa, and M.S.N. Oliveira, editors, *Visualization and Simulation of Complex Flows in Biomedical Engineering*, pages 119–132. Springer Netherlands, November 2013.

[47] A. Merlo, M. Berg, P. Duru, F. Risso, Y. Davit, and S. Lorthois. A few upstream bifurcations drive the spatial distribution of red blood cells in model microfluidic networks. *Soft Matter*, 18:1463–1478, 2 2022.

[48] W. Reinke, P. C. Johnson, and P. Gaehtgens. Effect of shear rate variation on apparent viscosity of human blood in tubes of 29 to 94 um diameter. *Circulation Research*, 59:124–132, 1986.

[49] T. W. Secomb, R. Skalak, N. Özkaya, and J. F. Gross. Flow of axisymmetric red blood cells in narrow capillaries. *Journal of Fluid Mechanics*, 163:405–423, 1986.

[50] C. Quéguiner and D. Barthès-Biesel. Axisymmetric motion of capsules through cylindrical channels. *Journal of Fluid Mechanics*, 348:349–376, 10 1997.

[51] R. Skalak and H. Tozeren. Flow mechanics in the microcirculation. *Mathematics of Microcirculation Phenomena*, 1980.

[52] J. S. Lee and Y. C. Fung. Modeling experiments of a single red blood cell moving in a capillary blood vessel. *Microvascular Research*, 1:221–243, 4 1969.

[53] P. S. Lingard. Capillary pore rheology of erythrocytes: V. the glass capillary array—effect of velocity and haematocrit in long bore tubes. *Microvascular Research*, 17:272–289, 5 1979.

[54] T. W. Secomb. Red blood cell mechanics and capillary blood rheology. *Cell Biophysics*, 18:231–251, 6 1991.

[55] H. Noguchi and G. Gompper. Shape transitions of fluid vesicles and red blood cells in capillary flows. *Proceedings of the National Academy of Sciences of the United States of America*, 102:14159–14164, 10 2005.

[56] A. M. Djojosugito, B. Folkow, B. ÖBerg, and S. White. A comparison of blood viscosity measured in vitro and in a vascular bed. *Acta Physiologica Scandinavica*, 78:70–84, 1970.

[57] P. Baeckström, B. Folkow, E. Kendrick, B. Löfving, and B. ÖBerg. Effects of vasoconstriction on blood viscosity in vivo. *Acta Physiologica Scandinavica*, 81:376–384, 1971.

[58] H. Stauber, D. Waisman, N. Korin, and J. Sznitman. Red blood cell (rbc) suspensions in confined microflows: Pressure-flow relationship. *Medical engineering & physics*, 48:49–54, 2017.

[59] A. Mantegazza, F. Clavica, and D. Obrist. In vitro investigations of red blood cell phase separation in a complex microchannel network. *Biomicrofluidics*, 14:14101, 1 2020.

[60] D. Obrist, B. Weber, A. Buck, and P. Jenny. Red blood cell distribution in simplified capillary networks. *Philosophical Transactions of the Royal Society A: Mathematical, Physical and Engineering Sciences*, 368:2897–2918, 6 2010.

[61] Z. Shen, F. Plouraboue, J. S. Lintuvuori, H. Zhang, M. Abbasi, and C. Misbah. Anomalous diffusion of deformable particles in a honeycomb network. *Physical Review Letters*, 2023.

[62] G. Tomaiuolo. Biomechanical properties of red blood cells in health and disease towards microfluidics. *Biomicrofluidics*, 8, 9 2014.

[63] M. Abkarian, M. Faivre, R. Horton, K. Smistrup, C. A. Best-Popescu, and H. A. Stone. Cellular-scale hydrodynamics. *Biomedical Materials*, 3:034011, 9 2008.

[64] G. Tomaiuolo, M. Simeone, V. Martinelli, B. Rotoli, and S. Guido. Red blood cell deformation in microconfined flow. *Soft Matter*, 2009.

[65] Y. Suzuki, N. Tateishi, M. Soutani, and N. Maeda. Deformation of erythrocytes in microvessels and glass capillaries: Effects of erythrocyte deformability. *Microcirculation*, 3:49–57, 1996.

[66] M. Abkarian, M. Faivre, and H. A. Stone. High-speed microfluidic differential manometer for cellular-scale hydrodynamics. *Proceedings of the National Academy of Sciences*, 103:538–542, 1 2006.

[67] A. Guckenberger, A. Kihm, T. John, C. Wagner, and S. Gekle. Numerical–experimental observation of shape bistability of red blood cells flowing in a microchannel. *Soft Matter*, 14:2032–2043, 3 2018.

[68] S. M. Recktenwald, K. Graessel, F. M. Maurer, T. John, S. Gekle, and C. Wagner. Red blood cell shape transitions and dynamics in time-dependent capillary flows. *Biophysical Journal*, 121:23–36, 1 2022.

[69] B. Kaoui, G. Biros, and C. Misbah. Why do red blood cells have asymmetric shapes even in a symmetric flow? *Physical Review Letters*, 2009.

[70] H. Bruus. *Theoretical Microfluidics*. Oxford University Press, 2023.

[71] A. M. Forsyth, J. Wan, W. D. Ristenpart, and H. A. Stone. The dynamic behavior of chemically "stiffened" red blood cells in microchannel flows. *Microvascular Research*, 80:37–43, 7 2010.

[72] I. Safeukui, P. A. Buffet, G. Deplaine, S. Perrot, V. Brousse, A. Sauvanet, B. Aussilhou, S. Dokmak, A. Couvelard, D. Cazals-Hatem, O. Mercereau-Puijalon, G. Milon, P. H. David, and N. Mohandas. Sensing of red blood cells with decreased membrane deformability by the human spleen. *Blood Advances*, 2:2581, 10 2018.

[73] A. Abay, G. Simionato, R. Chachanidze, A. Bogdanova, L. Hertz, P. Bianchi, E. V. D. Akker, M. V. Lindern, M. Leonetti, G. Minetti, C. Wagner, and L. Kaestner. Glutaraldehyde - a subtle tool in the investigation of healthy and pathologic red blood cells. *Frontiers in Physiology*, 10:450377, 5 2019.

[74] A. Drochon. Rheology of dilute suspensions of red blood cells: Experimental and theoretical approaches. *EPJ Applied Physics*, 22:155–162, 2003.

[75] R. E. Kalman. A new approach to linear filtering and prediction problems. *Journal of Basic Engineering*, 82:35–45, 3 1960.

[76] H. W. Kuhn. The hungarian method for the assignment problem. *Naval Research Logistics (NRL)*, 52:7–21, 2 2005.

[77] X. Li, K. Wang, W. Wang, and Y. Li. A multiple object tracking method using kalman filter. *2010 IEEE International Conference on Information and Automation, ICIA 2010*, pages 1862–1866, 2010.

[78] D. Ershov, M. S. Phan, J. W. Pylvänäinen, S. U. Rigaud, L. L. Blanc, A. Charles-Orszag, J. R.W. Conway, R. F. Laine, N. H. Roy, D. Bonazzi, G. Duménil, G. Jacquemet, and J. Y. Tinevez. Trackmate 7: integrating state-of-the-art segmentation algorithms into tracking pipelines. *Nature Methods 2022 19:7*, 19:829–832, 6 2022.

[79] C. Cortes, V. Vapnik, and L. Saitta. Support-vector networks. *Machine Learning 1995 20:3*, 20:273–297, 9 1995.

[80] J. M. Sosa, N. D. Nielsen, S. M. Vignes, T. G. Chen, and S. S. Shevkoplyas. The relationship between red blood cell deformability metrics and perfusion of an artificial microvascular network. *Clinical Hemorheology and Microcirculation*, 57:275–289, 2014.

[81] T. Gervais, J. El-Ali, A. Günther, and K. F. Jensen. Flow-induced deformation of shallow microfluidic channels. *Lab on a Chip*, 6:500–507, 2006.

[82] A. Raj and A. K. Sen. Flow-induced deformation of compliant microchannels and its effect on pressure–flow characteristics. *Microfluidics and Nanofluidics*, 20:1–13, 2 2016.

[83] P. S. Lingard. Capillary pore rheology of erythrocytes. i. hydroelastic behaviour of human erythrocytes. *Microvascular Research*, 8:53–63, 7 1974.

[84] A. Koponen, M. Kataja, and J. Timonen. Permeability and effective porosity of porous media. *Physical Review E*, 56:3319, 9 1997.

[85] M. Matyka, A. Khalili, and Z. Koza. Tortuosity-porosity relation in porous media flow. *Physical Review E - Statistical, Nonlinear, and Soft Matter Physics*, 78, 8 2008.

[86] J. L. Mcwhirter, H. Noguchi, and G. Gompper. Flow-induced clustering and alignment of vesicles and red blood cells in microcapillaries. *Sciences*, 106, 2009.

[87] K Schulte, U. Kunter, and M. J. Moeller. The evolution of blood pressure and the rise of mankind. *Nephrology Dialysis Transplantation*, 30:713–723, 5 2015.

[88] B. J. Kirby. *Micro- and Nanoscale Fluid Mechanics: Transport in Microfluidic Devices*. Cambridge University Press, 6 2010.

[89] J. Crank. *The Mathematics of Diffusion*. Oxford University Press, 1975.

[90] N-H L. Wang and K. H. Kellert. Augmented transport of extracellular solutes in concentrated erythrocyte suspensions in couette flow. *Journal of Colloid and Interface Science*, 1985.

[91] J. K. Patra, G. Das, L. F. Fraceto, E. V. R. Campos, M. D. P. Rodriguez-Torres, L. S. Acosta-Torres, L. A. Diaz-Torres, R. Grillo, M. K. Swamy, S. Sharma, S. Habtemariam, and H. S. Shin. Nano based drug delivery systems: recent developments and future prospects. *Journal of Nanobiotechnology 2018 16:1*, 16:1–33, 9 2018.

[92] P. J.A. Kenis, R. F. Ismagilov, and G. M. Whitesides. Microfabrication inside capillaries using multiphase laminar flow patterning. *Science (New York, N.Y.)*, 285:83–85, 7 1999.

[93] M. Fenech, V. Girod, V. Claveria, S. Meance, M. Abkarian, and B. Charlot. Microfluidic blood vasculature replicas using backside lithography. *Lab on a Chip*, 2019.

[94] G. C. Hsu, R. G. Lindgren, Y-C Chung, and W. H. Corcoran. Dialysis study of diffusion in a flowing suspension. *AIChE Journal*, 22:691–695, 7 1976.

[95] C. K. Colton, K. A. Smith, E. R. Merrill, and S. Friedman. Diffusion of urea in flowing blood. *AIChE Journal*, 17:800–808, 1971.

[96] A. L. Zydney and C. K. Colton. Augmented solute transport in the shear flow of a concentrated suspension. *PCH PhysicoChemical Hydrodynamics*, 10:77–96, 1988.

[97] D. Kim and R. L. Beissinger. Augmented mass transport of macromolecules in sheared suspensions to surfaces. *Journal of Colloid and Interface Science*, 159:9–20, 8 1993.

[98] W. Cha and R. L. Beissinger. Augmented mass transport of macromolecules in sheared suspensions to surfaces b. bovine serum albumin. *Journal Of Colloid and Interface Science*, 178:1–9, 1996.

[99] T. E. Diller and B. B. Mikic. Oxygen diffusion in blood: A translational model of shear-induced augmentation. *Journal of Biomech Engineering*, 1983.

[100] C. Kotsalos, F. Raynaud, J. Lätt, R. Dutta, F. Dubois, K. Z. Boudjeltia, and B. Chopard. Shear induced diffusion of platelets revisited. *Frontiers in Physiology*, 13:2148, 10 2022.

[101] R. F. Ismagilov, A. D. Stroock, P. J.A. Kenis, G. Whitesides, and H. A. Stone. Experimental and theoretical scaling laws for transverse diffusive broadening in two-phase laminar flows in microchannels. *Applied Physics Letters*, 76:2376, 4 2000.

[102] A. E. Kamholz and P. Yager. Theoretical analysis of molecular diffusion in pressure-driven laminar flow in microfluidic channels. *Biophysical Journal*, 80:155–160, 2001.

[103] S. Chen, B. Gavish, S. Zhang, Y. Mahler, and S. Yedgar. Monitoring of erythrocyte aggregate morphology under flow by computerized image analysis. *Biorheology*, 32:487–496, 1995.

[104] J. J. Bishop, A. S. Popel, M. Intaglietta, and P. C. Johnson. Effects of erythrocyte aggregation and venous network geometry on red blood cell axial migration. *American Journal of Physiology - Heart and Circulatory Physiology*, 281, 2001.

[105] B. Metzger, O. Rahli, and X. Yin. Heat transfer across sheared suspensions: role of the shear-induced diffusion. *Journal of Fluid Mechanics*, 724:527–552, 6 2013.

[106] M. Souzy, X. Yin, E. Villermaux, C. Abid, and B. Metzger. Super-diffusion in sheared suspensions. *Physics of Fluids*, 27, 4 2015.

[107] J. M. Sherwood, E.Kaliviotis, J. Dusting, and S. Balabani. Hematocrit, viscosity and velocity distributions of aggregating and non-aggregating blood in a bifurcating microchannel. *Biomechanics and Modeling in Mechanobiology*, 13:259–273, 11 2014.

[108] O. Baskurt, B. Neu, and H. J. Meiselman. Red blood cell aggregation. *Red Blood Cell Aggregation*, pages 1–288, 9 2011.

[109] R. Lima, S. Wada, S. Tanaka, M. Takeda, T. Ishikawa, K. Tsubota, Y. Imai, and T. Yamaguchi. In vitro blood flow in a rectangular pdms microchannel: Experimental observations using a confocal micro-piv system. *Biomedical Microdevices*, 10:153–167, 4 2008.

[110] A. V. Le. Blood Microflow Characterization Using Micro-Particle Image Velocimetry and 2-Beam Fluorescence Cross-Correlation Spectroscopy. Master's thesis, Université d'Ottawa / University of Ottawa, 12 2020.

[111] S. Gallier and E. Lemaire. Dynamics of suspensions of rigid particles. In A. Viallat and M. Abkarian, editors, *Dynamics of Blood Cell Suspensions in Microflows*, chapter 2. CRC Press, 1st edition, 2019.

[112] S. C. Jana, B. Kapoor, and A. Acrivos. Apparent wall slip velocity coefficients in concentrated suspensions of noncolloidal particles. *Journal of Rheology*, 39:1123–1132, 11 1995.

[113] A. V. Le and M. Fenech. Image-based experimental measurement techniques to characterize velocity fields in blood microflows. *Frontiers in Physiology*, 13:766, 4 2022.

[114] G. R. Cokelet, J. R. Brown, S. L. Codd, and J. D. Seymour. Magnetic resonance microscopy determined velocity and hematocrit distributions in a couette viscometer. *Biorheology*, 42:385–399, 2005.

[115] H. Park, E. Yeom, S. J. Seo, J. H. Lim, and S. J. Lee. Measurement of real pulsatile blood flow using x-ray piv technique with co2 microbubbles. *Scientific Reports 2015 5:1*, 5:1–7, 3 2015.

[116] P. J. Brands, A. P. G. Hoeks, L. Hofstra, and R. S. Reneman. A noninvasive method to estimate wall shear rate using ultrasound. *Ultrasound in Medicine & Biology*, 21:171–185, 1 1995.

[117] S. Aumann, S. Donner, J. Fischer, and F. Müller. Optical coherence tomography (oct): Principle and technical realization. *High Resolution Imaging in Microscopy and Ophthalmology*, pages 59–85, 2019.

[118] M. Brinkmeier, K. Dörre, J. Stephan, and M. Eigen. Two-beam cross-correlation: A method to characterize transport phenomena in micrometer-sized structures. *Analytical Chemistry*, 1999.

[119] R. Rigler and E. Elson. *Fluorescence Correlation Spectroscopy: Theory and Applications*. Springer Berlin, Heidelberg, 2001.

[120] K. Bacia, S. A. Kim, and P. Schwille. Fluorescence cross-correlation spectroscopy in living cells. *Nature Methods*, 2006.

[121] E. Kaliviotis, J. Dusting, J. M Sherwood, and S. Balabani. Quantifying local characteristics of velocity, aggregation and hematocrit of human erythrocytes in a microchannel flow. *Clinical Hemorheology and Microcirculation*, 63:123–148, 2016.

[122] Y. Sugii, R. Okuda, K. Okamoto, and H. Madarame. Velocity measurement of both red blood cells and plasma of in vitro blood flow using high-speed micro piv technique. *Measurement Science and Technology*, 16:1126, 3 2005.

[123] R. Lima, S. Wada, M. Takeda, K. Tsubota, and T. Yamaguchi. In vitro confocal micro-piv measurements of blood flow in a square microchannel: The effect of the haematocrit on instantaneous velocity profiles. *Journal of Biomechanics*, 2007.

[124] D. M. Bukowska, L. Derzsi, S. Tamborski, M. Szkulmowski, P. Garstecki, and M. Wojtkowski. Assessment of the flow velocity of blood cells in a microfluidic device using joint spectral and time domain optical coherence tomography. *Optics Express, Vol. 21, Issue 20, pp. 24025-24038*, 21:24025–24038, 10 2013.

[125] L. Bitsch, A. L. H. Olesen, A. C. H. Westergaard, H. Bruus, A. H. Klank, and A. J. P. Kutter. Micro particle-image velocimetry of bead suspensions and blood flows. *Experiments in Fluids*, pages 505–511, 2005.

[126] A. Passos, J. M. Sherwood, E. Kaliviotis, R. Agrawal, C. Pavesio, and S. Balabani. The effect of deformability on the microscale flow behavior of red blood cell suspensions. *Physics of Fluids*, 31:91903, 9 2019.

[127] B. Chayer, K. L. Pitts, G. Cloutier, and M. Fenech. Velocity measurement accuracy in optical microhemodynamics: Experiment and simulation. *Physiological Measurement*, 2012.

[128] K. L. Pitts, R. Mehri, C. Mavriplis, and M. Fenech. Micro-particle image velocimetry measurement of blood flow: validation and analysis of data pre-processing and processing methods. *Measurement Science and Technology*, 23:105302, 8 2012.

[129] K. L. Pitts and M. Fenech. High speed versus pulsed images for micro-particle image velocimetry: a direct comparison of red blood cells versus fluorescing tracers as tracking particles. *Physiological Measurement*, 34:1363, 9 2013.

[130] Y. Sugii, S. Nishio, and K. Okamoto. In vivo piv measurement of red blood cell velocity field in microvessels considering mesentery motion. *Physiological Measurement*, 2002.

[131] M. A. Hussain, S. Kar, and R. R. Puniyani. Relationship between power law coefficients and major blood constituents affecting the whole blood viscosity. *Journal of Biosciences*, 24:329–337, 9 1999.

[132] T. Sochi. Analytical solutions for the flow of carreau and cross fluids in circular pipes and thin slits. *Rheologica Acta*, 54:745–756, 8 2015.

[133] A. Louhichi, C. A. Charles, T. Phou, D. Vlassopoulos, L. Ramos, and C. Ligoure. Biaxial extensional viscous dissipation in sheets expansion formed by impact of drops of newtonian and non-newtonian fluids. *Physical Review Fluids*, 5:053602, 5 2020.

[134] R. Wójtowicz, K. Kocewiak, and A. A. Lipin. Identification of rheological properties of poly(ethylene oxide) - water solutions. *ChemChemTech*, 63:82–87, 2020.

[135] S. Kim, P. K. Ong, O. Yalcin, M. Intaglietta, P. C. Johnson, P. K. Ong, O. Yalcin, M. Intaglietta, and P. C. Johnson. The cell-free layer in microvascular blood flow *. *Biorheology*, 46:181–189, 1 2009.

[136] D. Tiab and E. C. Donaldson. Porosity and permeability. *Petrophysics*, pages 87–202, 1 2004.

[137] K. M. Graczyk and M. Matyka. Predicting porosity, permeability, and tortuosity of porous media from images by deep learning. *Scientific Reports*, 10:1–11, 12 2020.

[138] A. Stathoulopoulos, C. S. König, S. Ramachandran, and S. Balabani. Statin-treated rbc dynamics in a microfluidic porous-like network. *Microvascular Research*, 158:104765, 3 2025.

[139] M. Bathe-Peters, P. Gmach, P. Annibale, and M. J. Lohse. Linescan microscopy data to extract diffusion coefficient of a fluorescent species using a commercial confocal microscope. *Data in Brief*, 29:105063, 4 2020.

[140] J. K. Armstrong, R. B. Wenby, H. J. Meiselman, and T. C. Fisher. The hydrodynamic radii of macromolecules and their effect on red blood cell aggregation. *Biophysical Journal*, 87:4259–4270, 12 2004.

[141] R. R. Walters, J. F. Graham, R. M. Moore, and D. J. Anderson. Protein diffusion coefficient measurements by laminar flow analysis: method and applications. *Analytical Biochemistry*, 140:190–195, 7 1984.

[142] H. A. Sober and E. K. Sober. *Handbook of Biochemistry : Selected Data for Molecular Biology*. CRC Press, 1973.

APPENDICES

Appendix A

Blood Flow Through a Uniform Network

A.1 Approximating Channel Resistance

From the Hagen-Poiseuille law, the relationship between pressure and flow rate for an incompressible Newtonian fluid flowing through a cylindrical tube can be written as follows:

$$\Delta P = \frac{8\eta l}{\pi r^4} Q = RQ \tag{A.1}$$

where η is the viscosity, l is the length of the channel, r is the radius of the tube, ΔP is the pressure drop, and Q is the flow rate through the channel. Analogous to an electric system, a hydraulic resistance (R) can be written that consists of the viscosity and geometric parameters of the cross-sectional area. Furthermore, in the hydraulic analogy, a system of interconnecting tubes can be written and broken down similarly to an electric circuit. In this section, the equivalent hydrodynamic resistance (R_{equ}) is formulated.

A simplified breakdown of the subsections of the hexagonal networks into three sections, which are henceforth denoted as A, B, and C, as seen in Figure A.1.

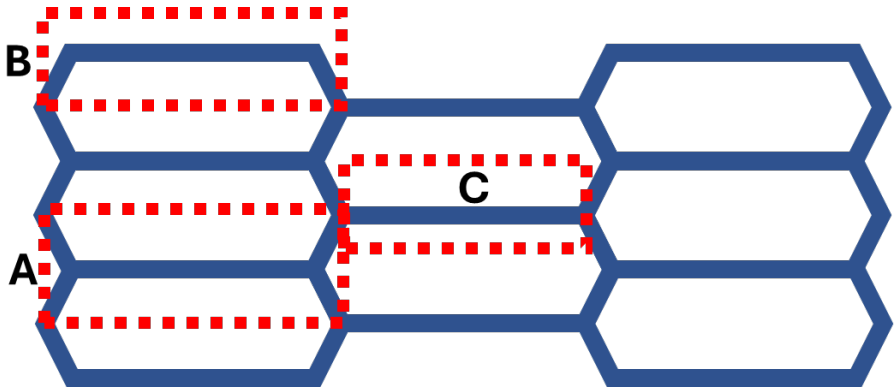


Figure A.1: Simplified schematic of hexagonal network partitioned into fundamental building blocks denoted as subsection A, B and C. Each subsection equivalent resistance is calculated to determine overall hydrodynamic resistance considering the pressure gradient decreases along the length of the network.

We first define the hydraulic resistance of each subsection as follows:

$$Subsection \quad A: \quad R_A = \frac{R_1}{2} + R_2 + \frac{R_1}{2} = R_1 + R_2 \tag{A.2}$$

$$Subsection \quad B: \quad R_B = 2R_1 + R_2 \tag{A.3}$$

$$Subsection \quad C: \quad R_C = R_2 \tag{A.4}$$

where R_1 and R_2 are the hydraulic resistance through the 45° and 0° aligned channels, respectively. The equivalent resistance of the column of parallel channels consisting of subsection A and subsection B is denoted as $R^{col}_{A//B}$ and written as follows:

$$R^{col}_{A//B} = \left(\frac{n}{(R_1 + R_2)} + \frac{m}{(2R_1 + R_2)} \right)^{(-1)} = \frac{(2R_1 + R_2)(R_1 + R_2)}{(n(2R_1 + R_2) + m(R_1 + R_2))} \tag{A.5}$$

where there are n rows of subsection A, and m rows of subsection B. While the column of parallel channels that consists of only subsection C is denoted as R^{col}_C and is simplified as follows:

$$R^{col}_C = \left(\frac{n+1}{R_2} \right)^{-1} = \frac{R_2}{n+1}. \tag{A.6}$$

The equivalent hydraulic resistance of the network then may be written as a series sum-

mation of the columns of parallel channels which reduces to the following equation:

$$R_{equ} = k(R_{AB}\ ) + (k-1)\ R_c^{col} \tag{A.7}$$

$$R_{equ} = k\left(\frac{(2R_1+R_2)\,(R_1+R_2)}{n\,(2R_1+R_2)+m\,(R_1+R_2)}\right) + \frac{(k-1)\,R_2}{(n+1)} \tag{A.8}$$

where there are k columns of parallel channels to be summed.

For a rectangular channel, the hydraulic resistance can be written as [70]:

$$R_{rectangle} = \left(\frac{12\eta l}{h^3 w}\right) \cdot \frac{1}{1-\frac{192h}{\pi^5 w}\sum_{j=0}^{\infty}\frac{1}{(2j+1)^5} tanh((2j+1)\pi\frac{w}{2h})} \tag{A.9}$$

where η is the viscosity, l is the length of the channel, h is the height of the channel, and w is the width. If the cross-sectional area of individual channels can be approximated to be consistent throughout the network, the equivalent hydraulic resistance can be considered to be a linear equation of the length of the two-channel branch and the configuration of the rows and columns.

In doing so, an equivalent hydraulic resistance can be written, separating the viscosity, width, and height from the linear arrangement of the channel lengths. The following equations highlight the separation of the length term (denoted as R_l) from the equivalent hydraulic resistance:

$$R_l = k\left(\frac{(2l_1+l_2)\,(l_1+l_2)}{n\,(2l_1+l_2)+m\,(l_1+l_2)}\right) + \frac{(k-1)\,l_2}{(n+1)} \tag{A.10}$$

$$R_{equ} = \left(\frac{12\eta}{h^3 w}\right) \cdot \frac{1}{1-\frac{192h}{\pi^5 w}\sum_{j=0}^{\infty}\frac{1}{(2j+1)^5} tanh((2j+1)\pi\frac{w}{2h})} \cdot R_l. \tag{A.11}$$

A.2 Porosity, Permeability and Tortuosity

In this study, the objective is to understand the transport of RBCs through a network and the local dynamics of the passage of cells. Taking inspiration from the field of petrophysics [136], in which understanding flow through porous media is well studied, the network topology can be considered analogous to a porous structure through which blood must pass. In a low Reynolds number regime, the flow through a matrix is governed by Darcy's law that relates the flow through a porous media with the pressure gradient by a linear relation and is described by the following formulation:

$$V = \frac{Q}{A_c} = \frac{-k}{\eta}\frac{\Delta P}{l} \tag{A.12}$$

where V is the mean velocity, Q is the mean flow rate through the porous medium, A_c is the cross-sectional area of the material, k is the permeability, η is the viscosity, and ΔP is the pressure gradient across the porous medium over a given l length [136]. A relationship of the flow through a porous medium depends on the physical properties of the porous media; it is therefore essential to define the physical parameters of the system, such as porosity, permeability, and tortuosity [84, 85, 137].

Porosity

Porosity (ϱ) is defined as the fraction of the bulk volume of a porous medium that is not occupied by the solid framework. In a porous medium, the space between aggregates is commonly irregular in shape and therefore never fits together perfectly. This allows the fluid to pass through. The definition of porosity can therefore be described by the following formulation:

$$\varrho = \frac{\mathbb{V}_{bulk} - \mathbb{V}_{grains}}{\mathbb{V}_{bulk}} = \frac{\mathbb{V}_{pores}}{\mathbb{V}_{bulk}} \tag{A.13}$$

where $\mathbb{V}_{bulk}$ is the total bulk volume of the material, $\mathbb{V}_{grains}$ is the volume of the grains, and $\mathbb{V}_{pores}$ is the volume of the space between the grains that the fluid can occupy. For a general porous system, developed pore spaces become isolated from other spaces due to several factors, such as clogging. Therefore, two definitions of porosity may be defined: absolute porosity, which is the ratio of total pore space to bulk volume regardless of interconnecting spaces, and effective porosity, which is the ratio of total usable pore space to the bulk volume. The absolute porosity from the geometric designs can be approximated from the computer-aided design presented in Figure A.2 and the results are summarized in Table A.2.

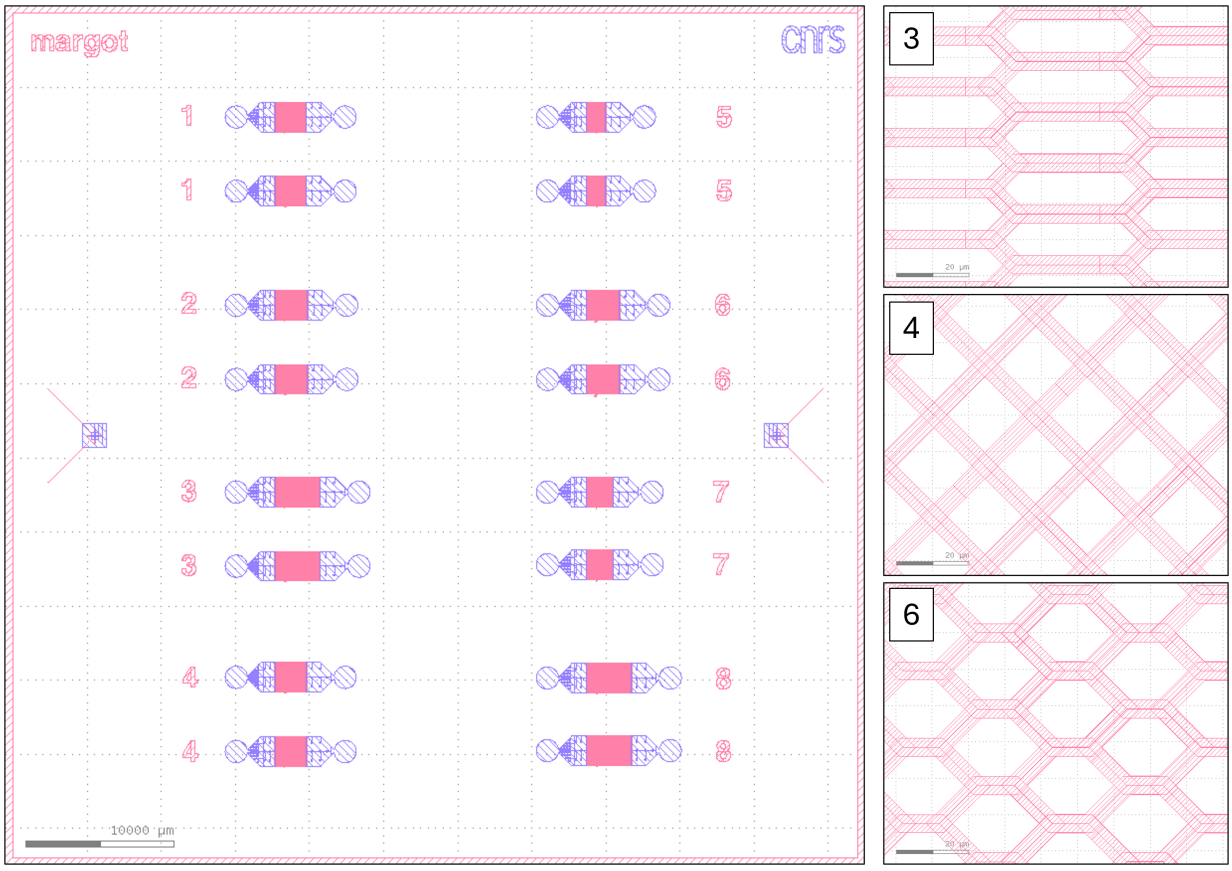


Figure A.2: (Left) CAD schematic file of the mask used to manufacture SU8 master wafer for PDMS channels. (Right) Expanded view of Channels 3, 4, and 6 which have length ratio of 1:3, 1:0, and 3:2, respectively.

Porosity can also then be approximated from the local imaging as well, which benefits from accounting for manufacturing variability that may result in wider channels and is simply the ratio of projected channel area to total projected area of the region of interest. This approximation of the mesh represented in Figure A.3 results in a mean porosity measurement of 0.392 ($\pm$ 0.001), 0.404 ($\pm$ 0.001), and 0.332 ($\pm$ 0.004), for channels 3, 4, and 6, respectively.

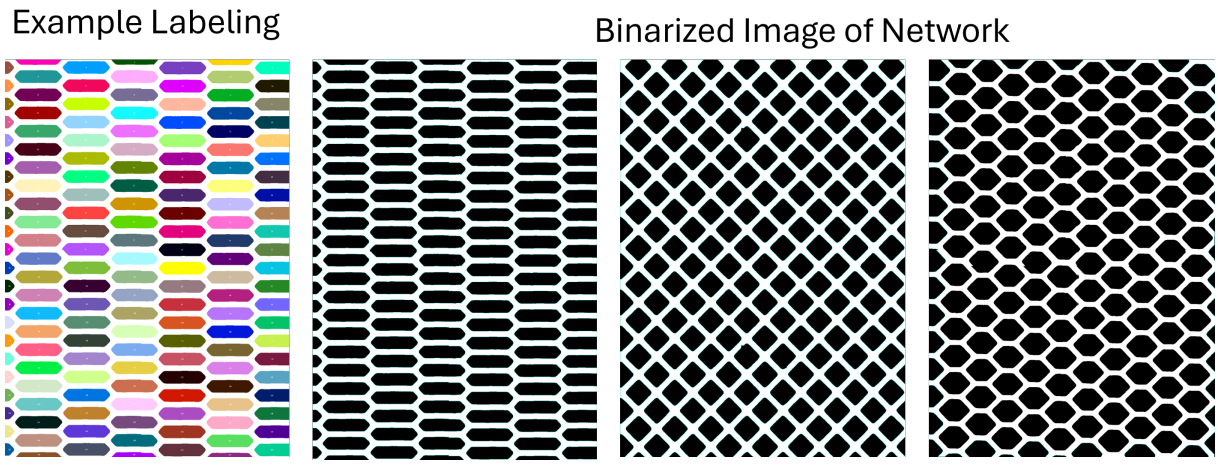


Figure A.3: Porosity approximation from the region of interest completed on Fiji for Channels 3 (1:3), 4 (1:0), and 6 (3:2). Resulting in mean porosity measurement of 0.392 (±0.001) and 0.404 (±0.001), and 0.332 (±0.004), respectively.

Tortuosity

Tortuosity (T) characterizes the general path of particle transport through the medium and can then be written as follows:

$$T = \frac{l_{travelled}}{l_{parallel}} \tag{A.14}$$

where $l_{travelled}$ is the length traveled along the tortuous path of the network and $l_{travelled}$ is the length projected along the axis in the direction of the flow.

The minimum tortuosity of the system can then be approximated from the designed geometry:

$$T_{min} = \frac{k(2l_1 + l_2) + (k-1)l_2}{k(2l_1 cos(45) + l_2) + (k-1)l_2} \tag{A.15}$$

where k is the number of columns in the network, and l is the length of the individual channels. Two approximations of the tortuosity can be described depending on how the length is defined for the passage of the objects through the network: the center path line and the inner path line as represented in the schematic in Figure A.4 (B, C). A modification of the general tortuosity equation to account for a path that slides along the inner walls of

the channel for a hexagonal topology is as follows:

$$l'_{1x} = l_1 cos(45) + w cos(45) \tag{A.16}$$

$$l'_{1y} = l_1 sin(45) - w \tag{A.17}$$

$$l'_2 = l_2 - w cos(45) \tag{A.18}$$

where l' is the inner length, and w is the width of the individual channel. This is in contrast to the square topology (Channel 4), where the length of the channel can be modified as follows:

$$l'_{1x} = l_1 cos(45) \tag{A.19}$$

$$l'_{1y} = l_1 sin(45) - w. \tag{A.20}$$

This calculation of tortuosity can only be described as the minimum bound of the tortuosity through which a cell can traverse the network channel. Given the degree of interconnectedness of the channels, the general trajectories of the cells through the network are hypothesized to be close to the minimum such that they are primarily moving from the entrance of the network to the exit. The rare occasion at which cells briefly travel in the reverse direction to the bulk flow may be the result of localized clogs that inhibit the flow of cells' passage. The order of increasing tortuosity for channels 1 to 6 is presented in Figure A.5 and the tortuosity is tabulated in Table A.1.

Permeability

Permeability (k), on the other hand, is another property of interest that describes the ability of fluid to flow through interconnected pores. This ability for fluid flow is called the permeability, which depends on the effective porosity. In the context of Darcy's law of flow through a porous medium, the proportionality constant is known as permeability. Permeability is affected by the shape and size of the grains that make up the porous media. For example, large, flat, uniformly arranged grains in the horizontal direction will have high permeability in the horizontal direction, while the vertical permeability will be minimal. In contrast, rounded grains will result in high permeability in both directions [136].

The relationship between porosity (ϱ) and permeability (k) is not always clear; however, one of the most popular empirical correlations expressing permeability as a function of porosity and specific surface area is the Kozeny-Carman equation [84, 85]. The general

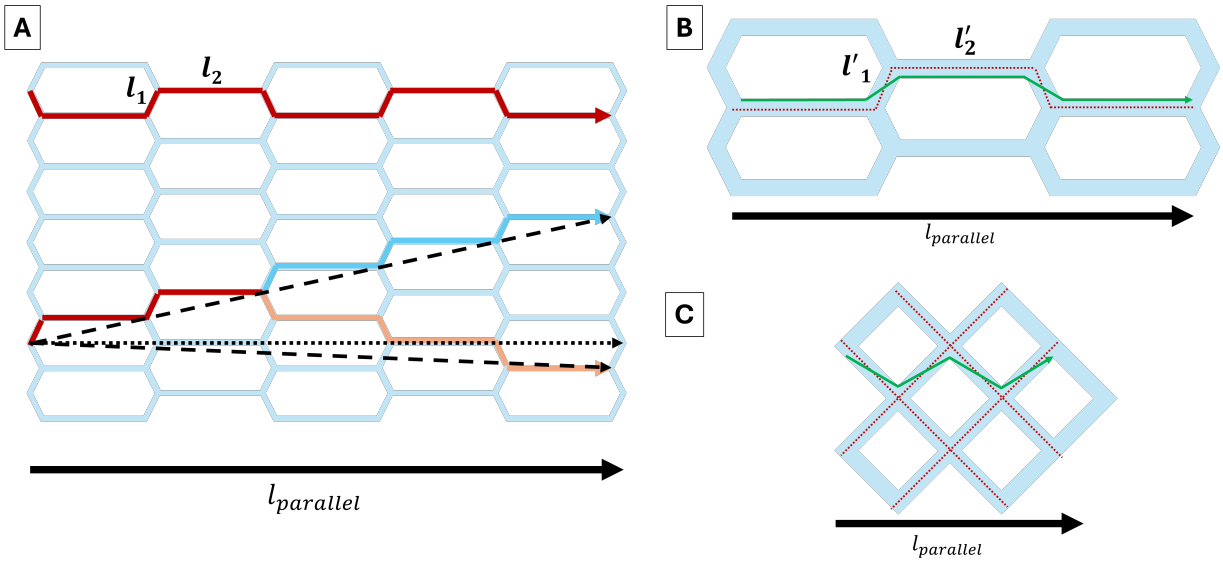


Figure A.4: (A) Schematic of the general calculation of the tortuosity through the network assuming a center-line passage of the cell through the network. (B) and (C) Schematic of an inner path can also be used to calculate a minimum tortuosity.

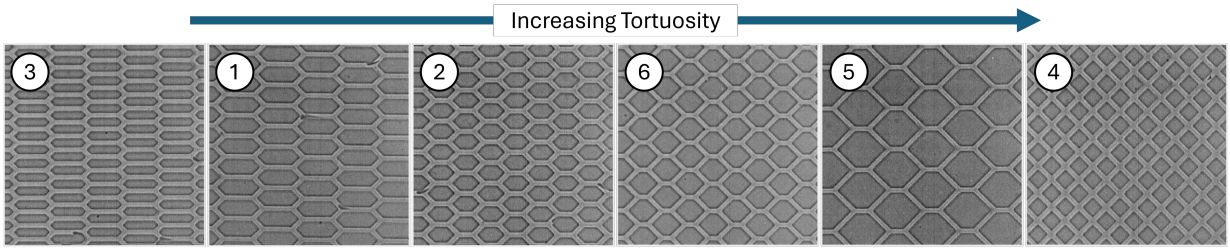


Figure A.5: Ordering of the network topologies with increasing minimum tortuosity.

form of the Kozeny-Carman equation is:

$$k = \frac{\varrho^3}{cS^2T^2} \tag{A.21}$$

where c is the Kozeny coefficient or shape factor, S is the specific surface area which is the ratio of total pore surface volume and the total void area, and T is the tortuosity which is the elongation of the flow path in the pore space. The application of the Kozeny-Carman correlation is tabulated in Table A.2 using a Kozeny coefficient of two, which is typically used for cylinders [84]. In the work of Koponen and colleagues, the simplest way to modify the Kozeny-Carman equation to include the effect of nonconducting pores is to replace the porosity with an effective porosity which will be less than the absolute porosity [84]. In their work in simulating creeping flow through a 2D porous medium using the lattice-gas method, effective porosity as well as tortuosity was found to be a function of porosity.

As an aside, equating Darcy's law with Poiseuille's law, the permeability from the relationship related to the hydraulic resistance is as follows:

$$Q = \frac{-kA_c}{\eta}\frac{\Delta P}{l} = \frac{1}{R_{Equ}}\Delta P \tag{A.22}$$

$$\frac{kA_c}{l_{parallel}} \propto \frac{1}{R_{equNorm}}. \tag{A.23}$$

A mean cross-sectional area (A_c) can then be defined as $A_c = \varrho hw$ since the porosity of the network results in regions of periodically changing cross-sectional area. Using the relation between permeability and hydraulic resistance, the results are tabulated in Table A.2, where it can be observed that the permeability magnitude extracted using the Kozeny-Carman correlation is an order of magnitude lower than that from the hydraulic resistance. The excess relative resistance then can be framed as the change in permeability as well:

$$R_{exc} = \frac{R_{RBC}}{R_{Opt}} - 1 = \frac{k_{Opt}}{k_{RBC}} - 1 = \frac{\varrho_{Opt}^3}{cS^2T^2}\frac{cS^2T^2}{\varrho_{RBC}^3} - 1. \tag{A.24}$$

Assuming that the mean cross-sectional area and the length of the system are to remain the same.

Table A.1: Summary of geometric tortuosity of network designs for different network length ratio

	Centre Path Line					**Inner Path Line**				
Channel	l_1	l_2	$l_{travelled}$	$l_{parallel}$	T	l'_1	l'_2	$l'_{travelled}$	$l'_{parallel}$	T
1	15	30	2220	2000	1.11	15.18	26.55	2059	2004	1.03
2	15	15	2505	2135	1.17	15.18	11.55	2233	2139	1.04
3	10	30	3170	2935	1.08	10.75	26.55	2957	2939	1.01
4	20	0	2840	2008	1.41	16.91	0.00	2400	2008	1.20
5	30	15	1515	1216	1.25	29.58	11.55	1386	1220	1.14
6	15	10	2690	2215	1.21	15.18	6.55	2340	2219	1.05
7	20	10	2150	1466	1.47	19.88	6.55	1896	1732	1.10
8	10	25	3265	2818	1.16	10.75	21.55	3014	2993	1.01

Table A.2: Summary of geometric porosity and permeability approximation from Kozeny-Carman correlation (k_{K-C}) and hydraulic resistance (k_R)

Channel	$SA_{Pore}(10^6)$ (µm^2)	$V_{Pore}(10^6)$ (µm^3)	$V_{bulk}(10^6)$ (µm^3)	ϱ	S (µm)	T	k_{K-C} (µm^2)	k_R (µm^2)
1	5.48	6.68	19.4	0.344	0.430	1.11	0.089	0.613
2	6.95	8.47	20.7	0.409	0.566	1.17	0.077	0.542
3	11.0	13.4	28.5	0.470	0.727	1.08	0.085	0.658
4	7.98	9.74	19.6	0.498	0.814	1.41	0.047	0.418
5	2.38	2.90	12.0	0.242	0.261	1.25	0.067	0.487
6	7.95	9.70	21.5	0.451	0.673	1.21	0.069	0.508
7	5.01	6.11	14.3	0.429	0.615	1.47	0.049	0.352
8	11.6	14.2	27.3	0.519	0.883	1.16	0.067	0.567

A.3 Network Clogging

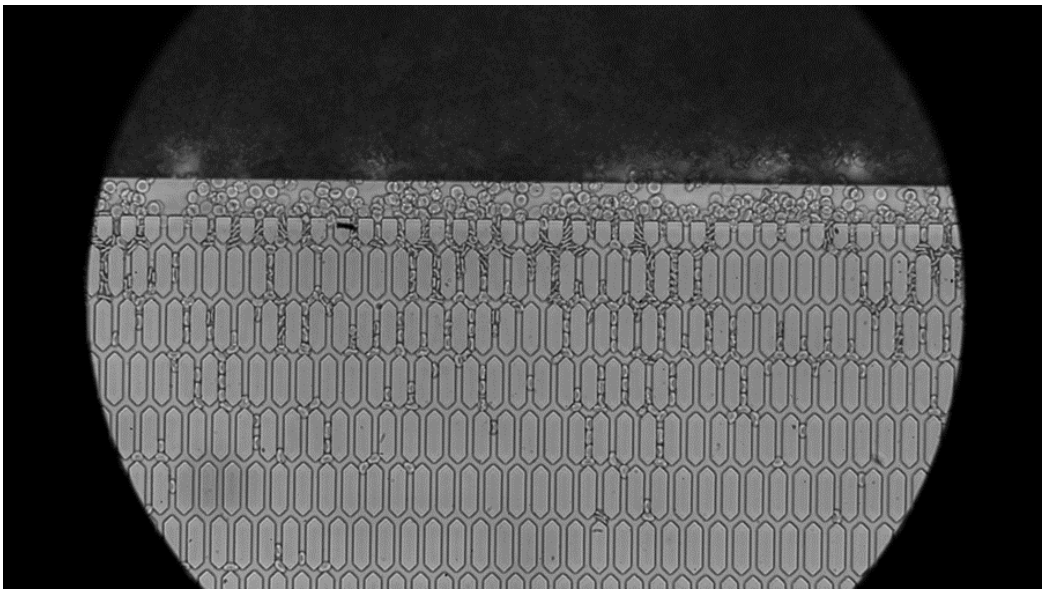
An array of glutaraldehyde treatment concentrations and incubation times was tested to ensure that treated RBCs did not result in clogged channels that artificially increase the relative resistance of the network. The tested conditions are summarized in Table A.3. The microfluidic network tended to fail by clogging the entrance, forming a pellet of RBCs (see Figure A.6 (a)) which is primarily due to cells not being able to deform to enter the entrance of the channels, or by localized clogging in the channels (see Figure A.6 (b)) which arises primarily when multiple cells jam through individual channels, resulting in a permanent clog. Furthermore, localized clogging quickly cascades into more localized clogging as all cells begin to slow down.

A region of the incubation map was found where there is a potential increase in the rigidity of the cells and the ability to flow through the network. However, the exact modification of the surface shear modulus and shape is not measured. Future work using ektacytometry, micro-pipettes, or extensional flow measurements will be essential in measuring the change in RBC deformation. A note should be made that the incubation map should be re-measured to ensure that a change in glutaraldehyde batch still allows for the passage of cells.

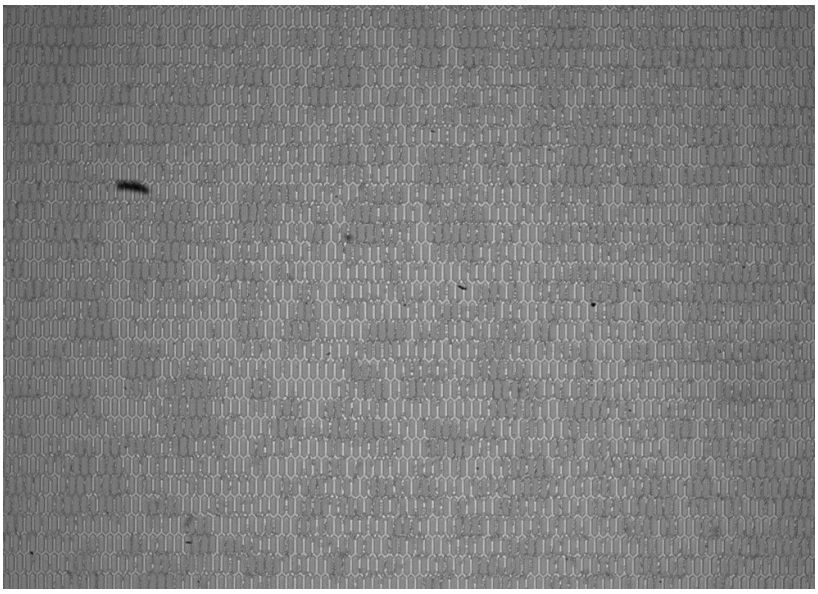
Table A.3: Glutaraldehyde treatment incubation map of cells' incubation time as a function of glutaraldehyde concentration in buffer solution

	Glutuaraldehyde Concentration (%)					
Incubation (min)	0.5	0.1	0.05	0.01	0.005	0.001
5	x	x	x	o	o	o
10		x		/	/	
15		x		x		
30						
60				x		o

x: clogged network, /: localized clogged network, o: flowing treatment



(a) Clogging Pellet at Entrance of Channel



(b) Localized Clogging in Channel

Figure A.6: Example of types of clogging pathways due to treatment of RBCs with glutaraldehyde.

A.4 Velocity Field Matrix

Variations in network geometry can be expected to result in differences in velocity distributions during single-cell passage that may correlate to the differences we see between channels. To investigate this, the normalized cell velocity distributions for healthy, untreated RBC samples were analyzed under nominal feeding hematocrit of 10% and 20%. These results are presented in Figure A.7, Figure A.8, Figure A.9, Figure A.10, Figure A.11,and Figure A.12 for channels 3 (1:3), 4 (1:0), and 6 (3:2), respectively. The figures are organized by input pressure drop to facilitate comparison. The experiments were conducted over three days using samples from the same donor to ensure consistency. In this study, the term "normalized cell velocity" is defined as the ratio of the cell velocity measured using the Fiji plug-in TrackMate to the mean convective velocity, which is calculated as the ratio of the measured flow rate to the cross-sectional area of the straight channel section aligned with the flow direction (0°). The data are separated by channel path, which includes aligning to the flow direction (0°), at the angled split (45°), or at the channel bifurcation.

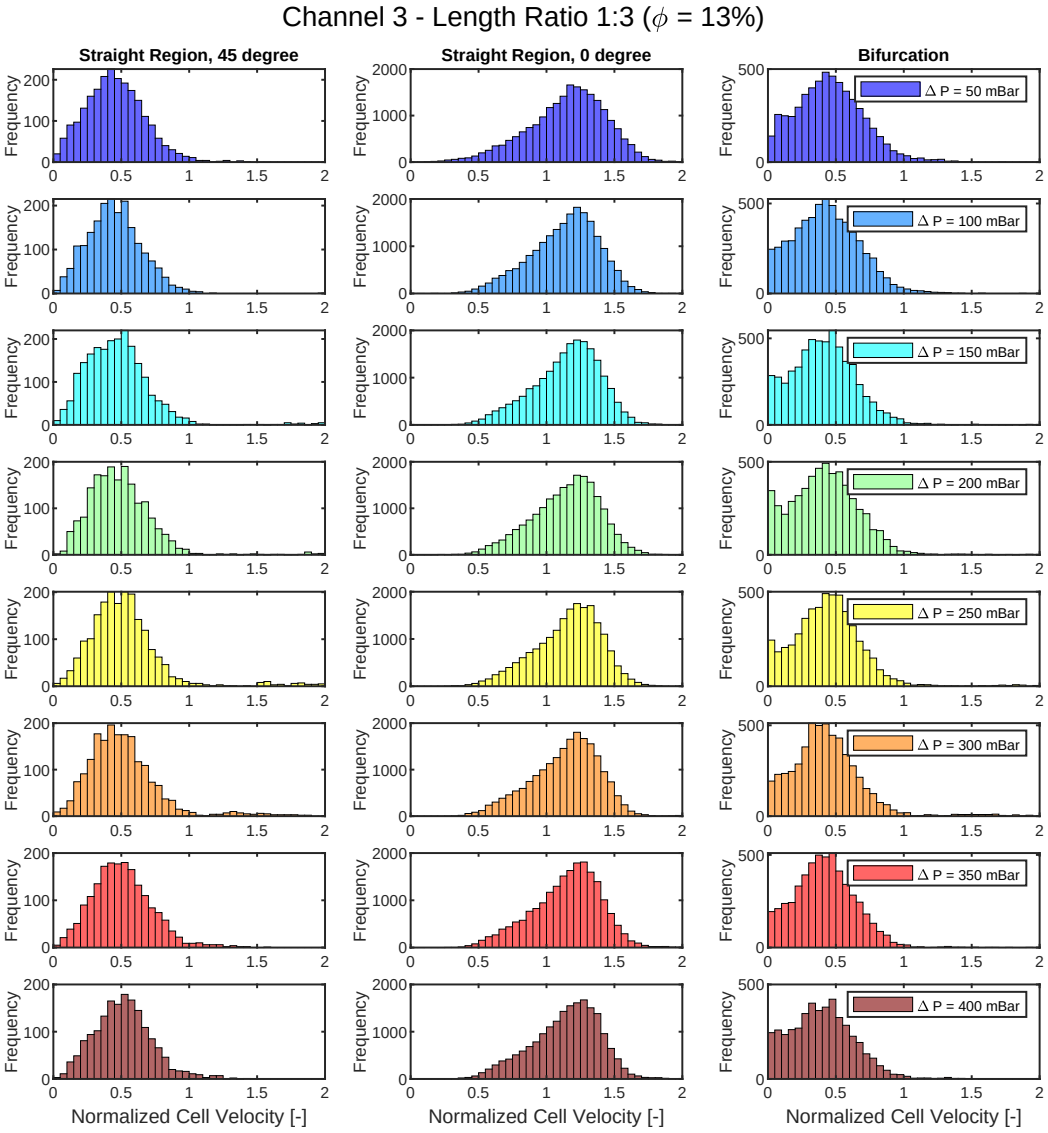


Figure A.7: Normalized cell velocity distribution at increasing pressure drops in Channel 3 (1:3) flowing RBC at nominal feeding hematocrit of 10% (with a measured projected hematocrit of 13%). Distribution are taken in individual channels either aligned to the flow indicated by 0°, 45° or at the bifurcation. The distribution encompasses the velocity of all tracked cells over the time period of acquisition.

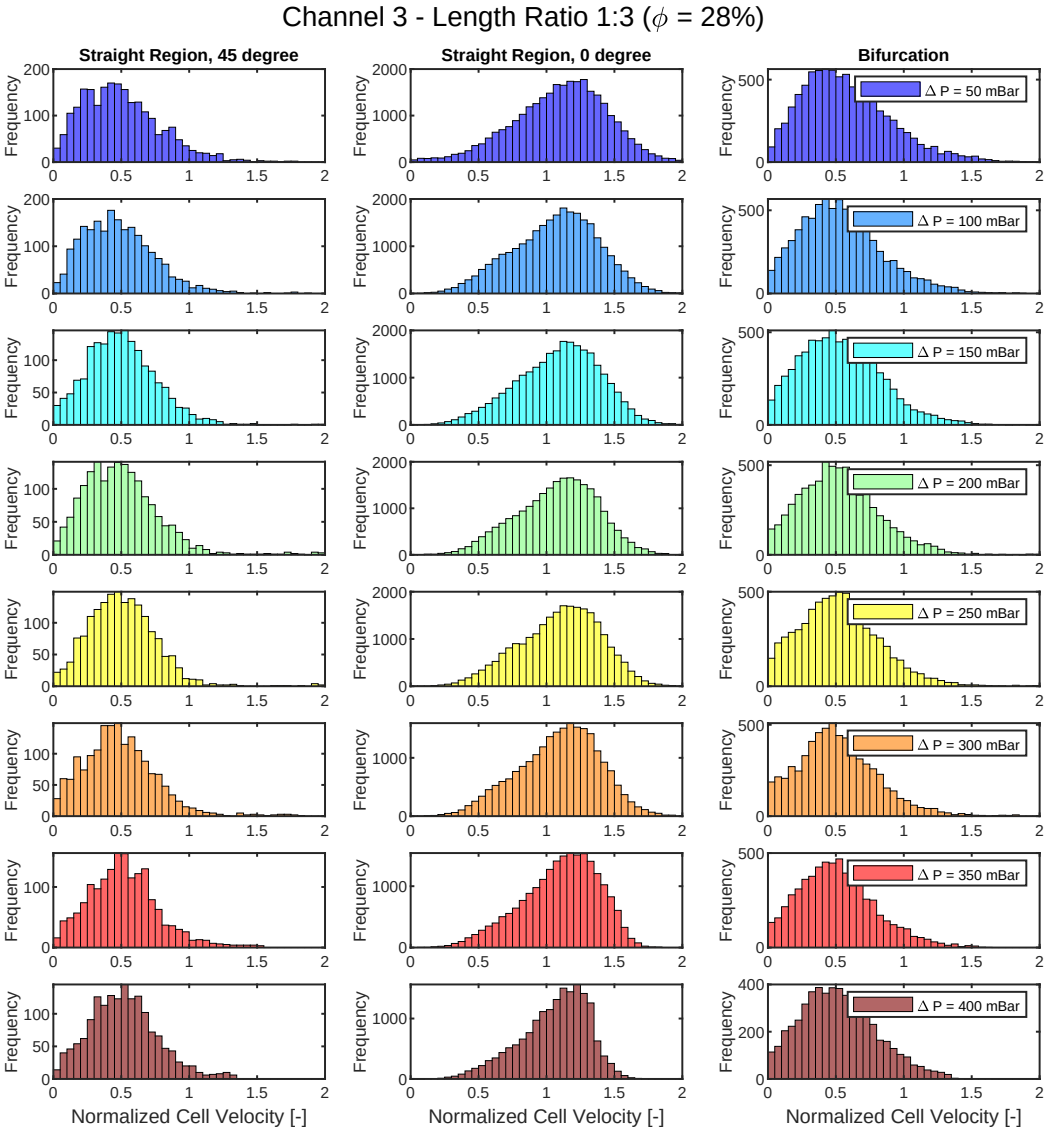


Figure A.8: Normalized cell velocity distribution at increasing pressure drops in Channel 3 (1:3) flowing RBC at nominal feeding hematocrit of 20% (with a measured projected hematocrit of 28%). Distribution are taken in individual channels either aligned to the flow indicated by 0°, 45° or at the bifurcation. The distribution encompasses the velocity of all tracked cells over the time period of acquisition.

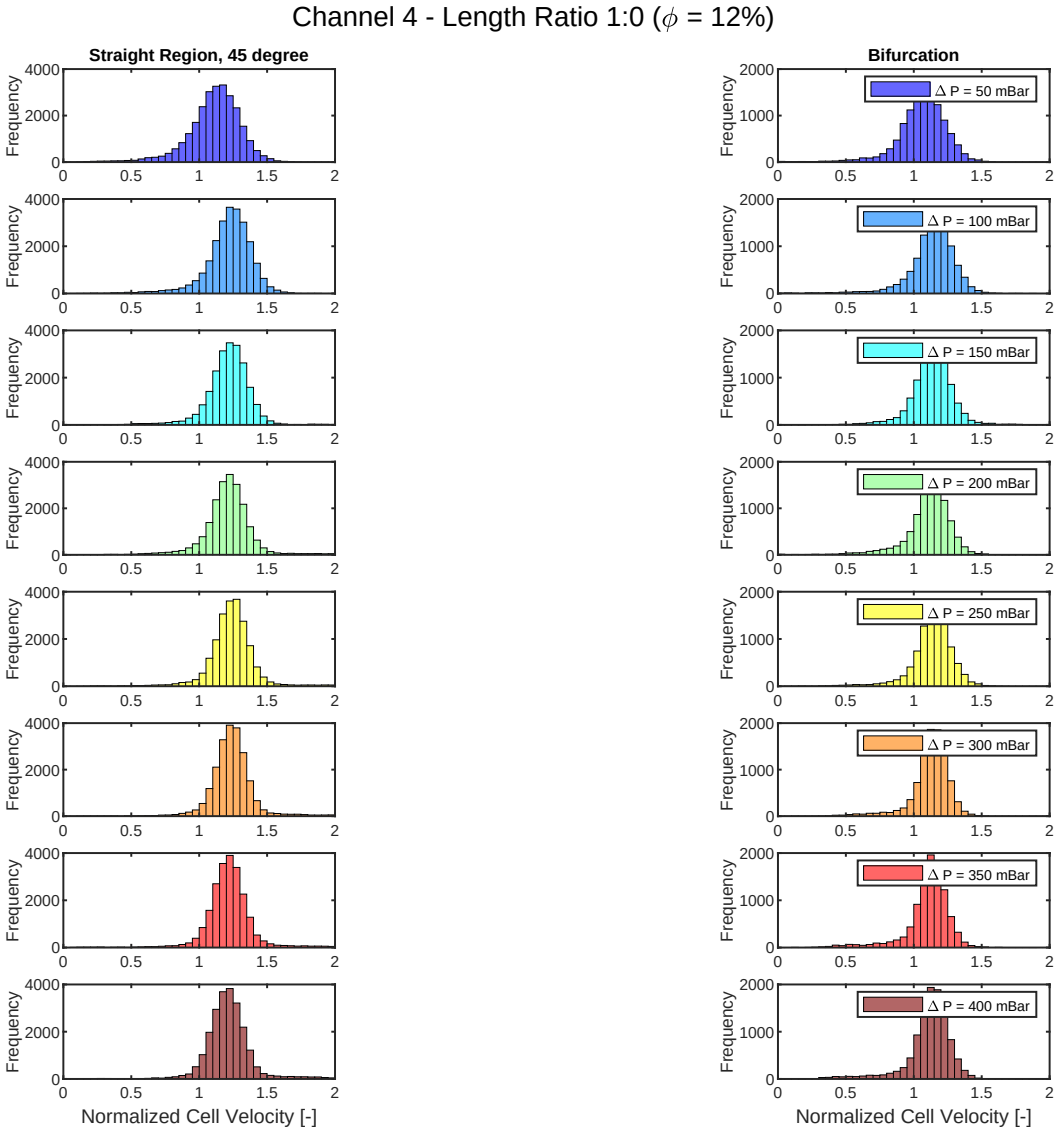


Figure A.9: Normalized cell velocity distribution at increasing pressure drops in Channel 4 (1:0) flowing RBC at nominal feeding hematocrit of 10% (with a measured projected hematocrit of 12%). Distribution are taken in individual channels either aligned to the flow indicated by 0° or at the bifurcation. The distribution encompasses the velocity of all tracked cells over the time period of acquisition.

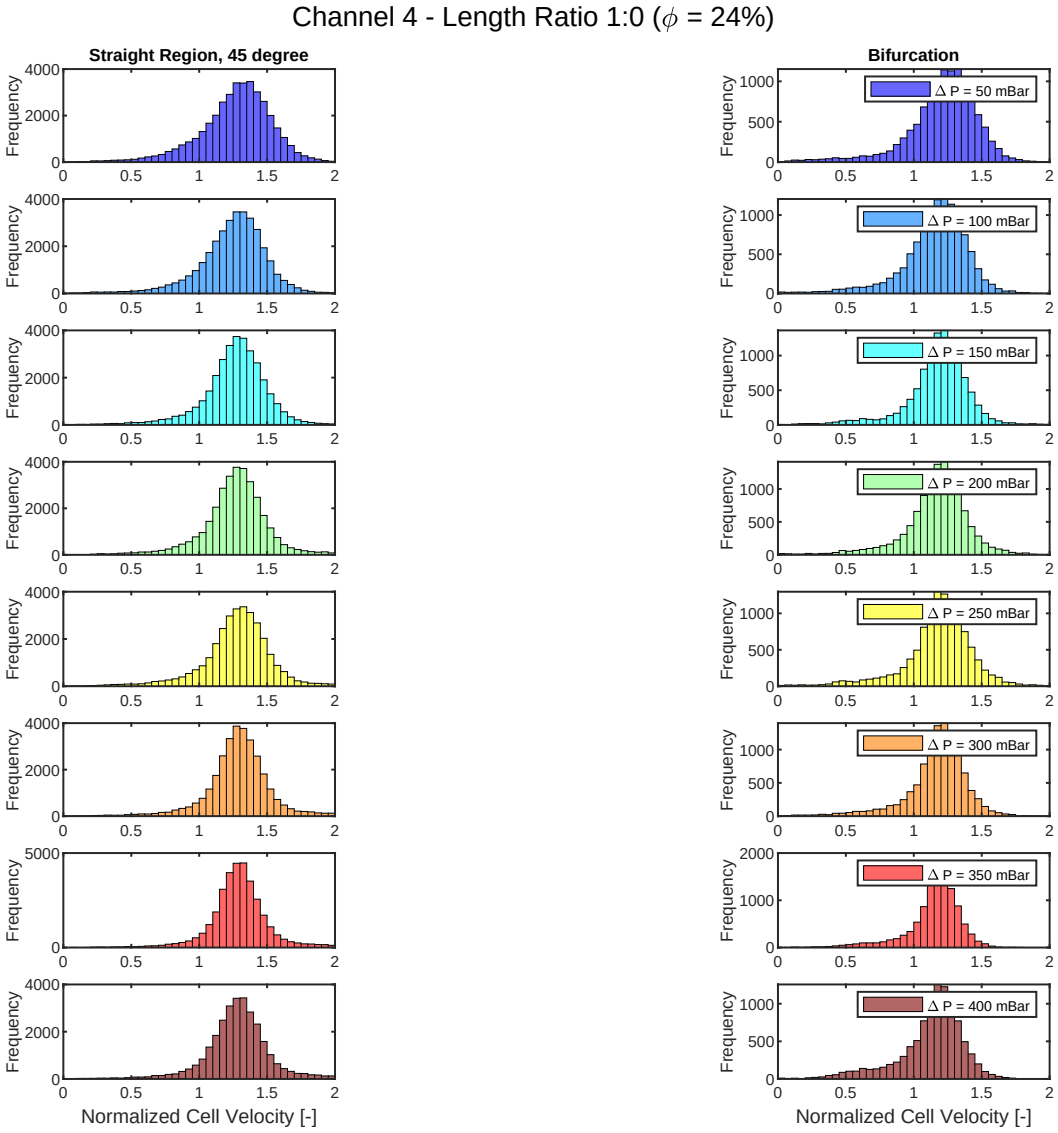


Figure A.10: Normalized cell velocity distribution at increasing pressure drops in Channel 4 (1:0) flowing RBC at nominal feeding hematocrit of 20% (with a measured projected hematocrit of 24%). Distribution are taken in individual channels either aligned to the flow indicated by 0° or at the bifurcation. The distribution encompasses the velocity of all tracked cells over the time period of acquisition.

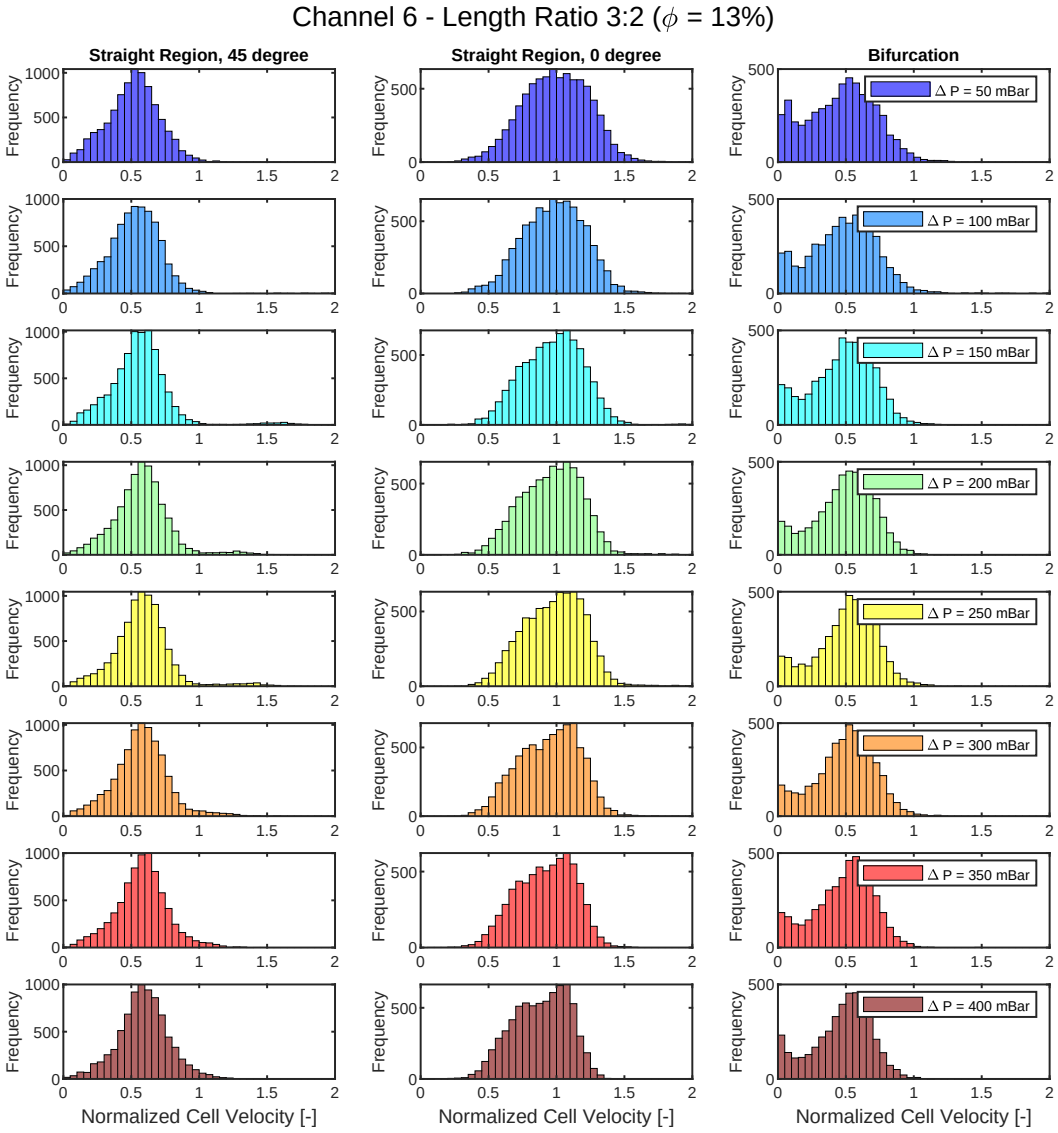


Figure A.11: Normalized cell velocity distribution at increasing pressure drops in Channel 6 (3:2) flowing RBC at nominal feeding hematocrit of 10% (with a measured projected hematocrit of 13%). Distribution are taken in individual channels either aligned to the flow indicated by 0°, 45° or at the bifurcation. The distribution encompasses the velocity of all tracked cells over the time period of acquisition.

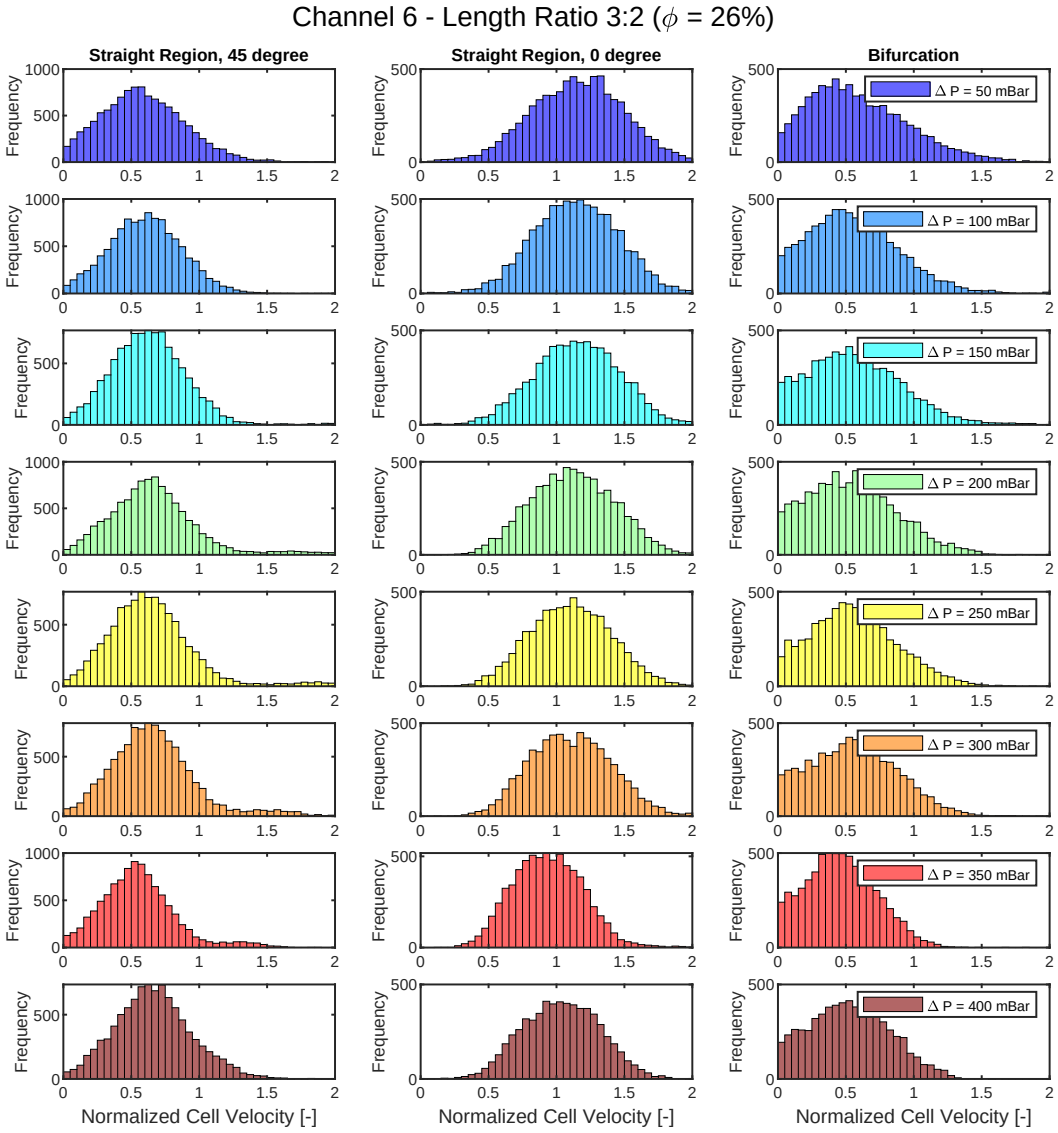


Figure A.12: Normalized cell velocity distribution at increasing pressure drops in Channel 6 (3:2) flowing RBC at nominal feeding hematocrit of 20% (with a measured projected hematocrit of 26%). Distribution are taken in individual channels either aligned to the flow indicated by 0°, 45° or at the bifurcation. The distribution encompasses the velocity of all tracked cells over the time period of acquisition.

A.5 Cell Trajectories

To better understand the flow dynamics through the network, the trajectories of cell passage through various network topologies were analyzed for two nominal feeding hematocrit: 10% and 40%. Representative trajectories are presented in Figure A.13 and Figure A.14, respectively. The analysis highlights the effect of hematocrit and pressure conditions on cell motion and flow characteristics. For the 10% nominal hematocrit, cell trajectories were tracked using Kalman filtering, while for the 40% nominal hematocrit, cell trajectories were manually tracked through the network. Manual tracking was used primarily due to the increased density of the cells and loss of trajectories on cell occlusion.

The time required for cells to traverse the width of the region of interest varied among individual cells, reflecting differences in their trajectories and flow conditions. To quantitatively characterize the flow, the tortuosity, which is the ratio of the cell traveled length to the length parallel to the flow, and the trajectory angle, which is defined as the angle between the starting position and the final position to the line parallel to the flow direction, are reported in Figure A.15 and Figure A.16 for nominal feeding hematocrit of 10% and 40%.

The lateral displacement of the RBC can be approximated by the trajectory angles. In this work, the trajectory angles were found to trend towards zero in the low hematocrit sample for the three tested network geometries, indicating that in this regime of hematocrit low lateral displacement is observed. What is observed in the level of confinement tested can be described as a zig-zag motion which is similarly observed in the work of healthy RBCs flowing in microfluidic micro-pillar arrays [58, 138]. In porous media, tortuosity is a commonly used term to augment the permeability through the medium besides the specific area and the porosity of the medium. However, in the case of an ordered system of pillars, the tortuosity was found to not significantly deviate from the geometric tortuosity at this degree of cell confinement. This is in contrast to the work of Shen and colleagues in modeling transport of deformable particles in honeycomb networks, where soft particles exhibit short memory between bifurcations, with transport resembling random partitioning leading to diffusion-like behavior [61]. In this work, the trajectories of the cells' passage in the network appear to strongly follow a zig-zag trajectory within the region of interest. To further explore long-scale dispersion, a wider imaging will be required while simultaneously consistent measurement of the same object through its trajectory.

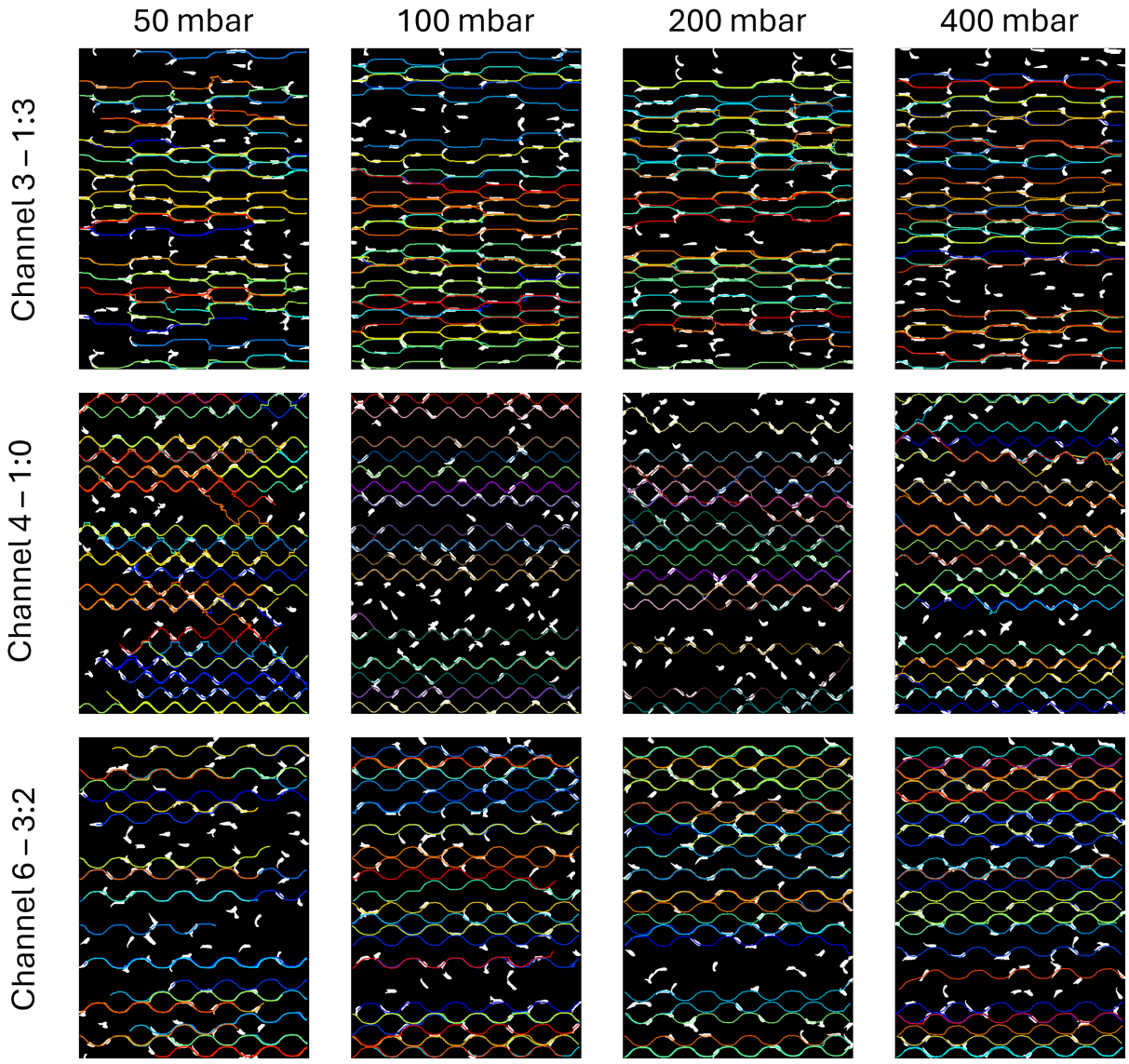


Figure A.13: Sample trajectories of cells passage in the different network topologies taken at increasing pressure for nominal feeding hematocrit of 10%. Tracks are overlaid over binary image with pillars removed and tracks are completed using Kalman filtering through MATLAB. Different color trajectories indicate unique tracks of individual cell passage for clarity.

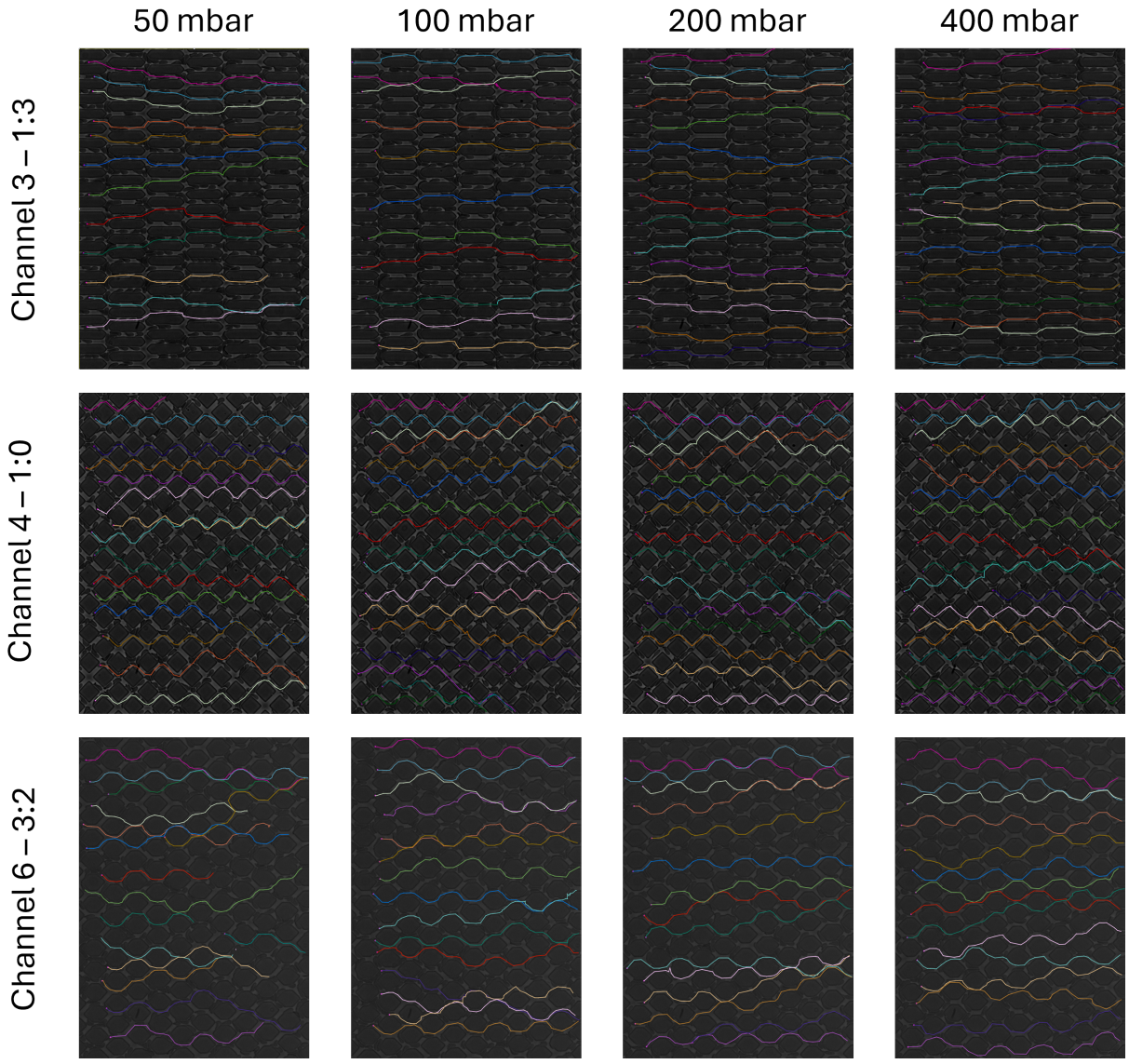


Figure A.14: Sample trajectories of cells passage in the different network topologies taken at increasing pressure for nominal feeding hematocrit of 40%. Tracks are overlaid over raw image and tracks are completed manually using the ImageJ plugin TrackMate. Different color trajectories indicate unique tracks of individual cell passage for clarity.

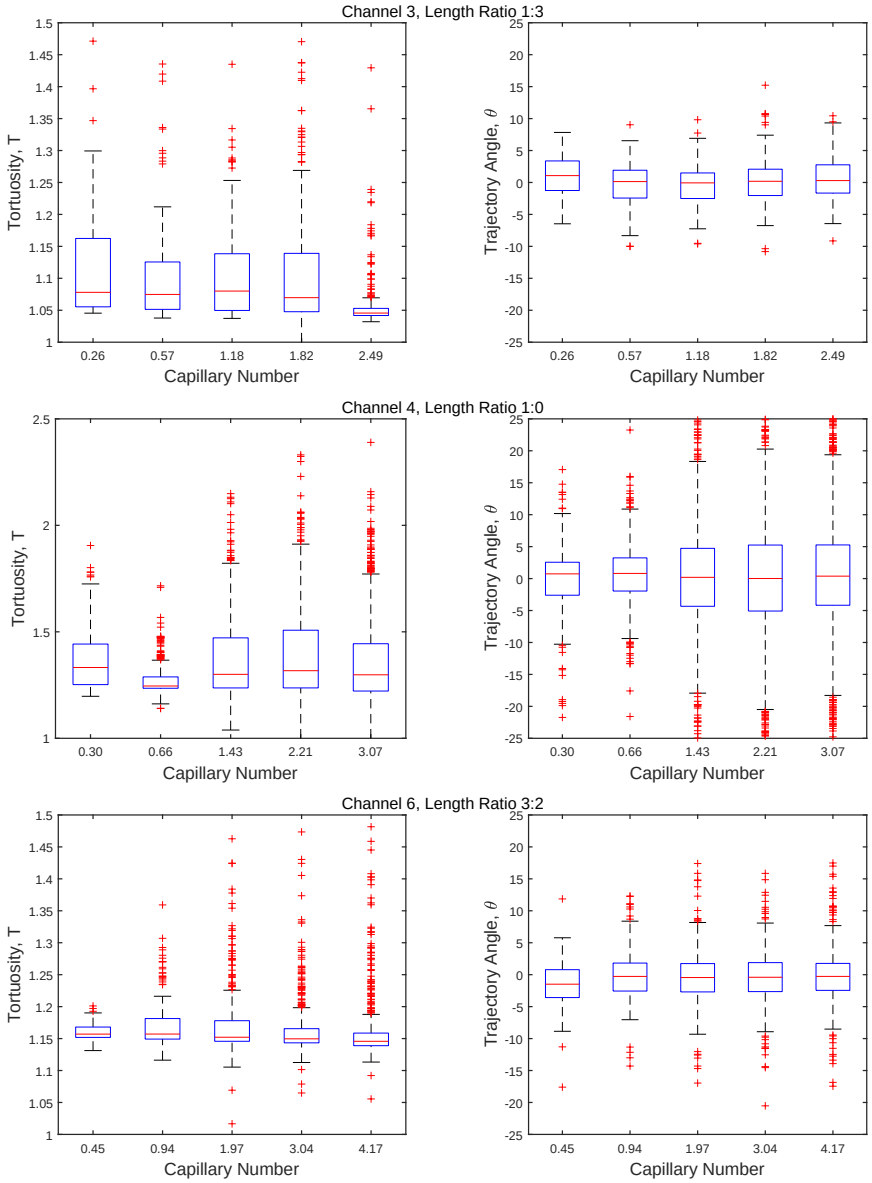


Figure A.15: Box plot of calculated tortuosity and track angles that extend over 3 mesh lengths are plotted for Channel 3 (1:3), 4 (1:0), and 6 (3:2) at a nominal feeding hematocrit of 10%.

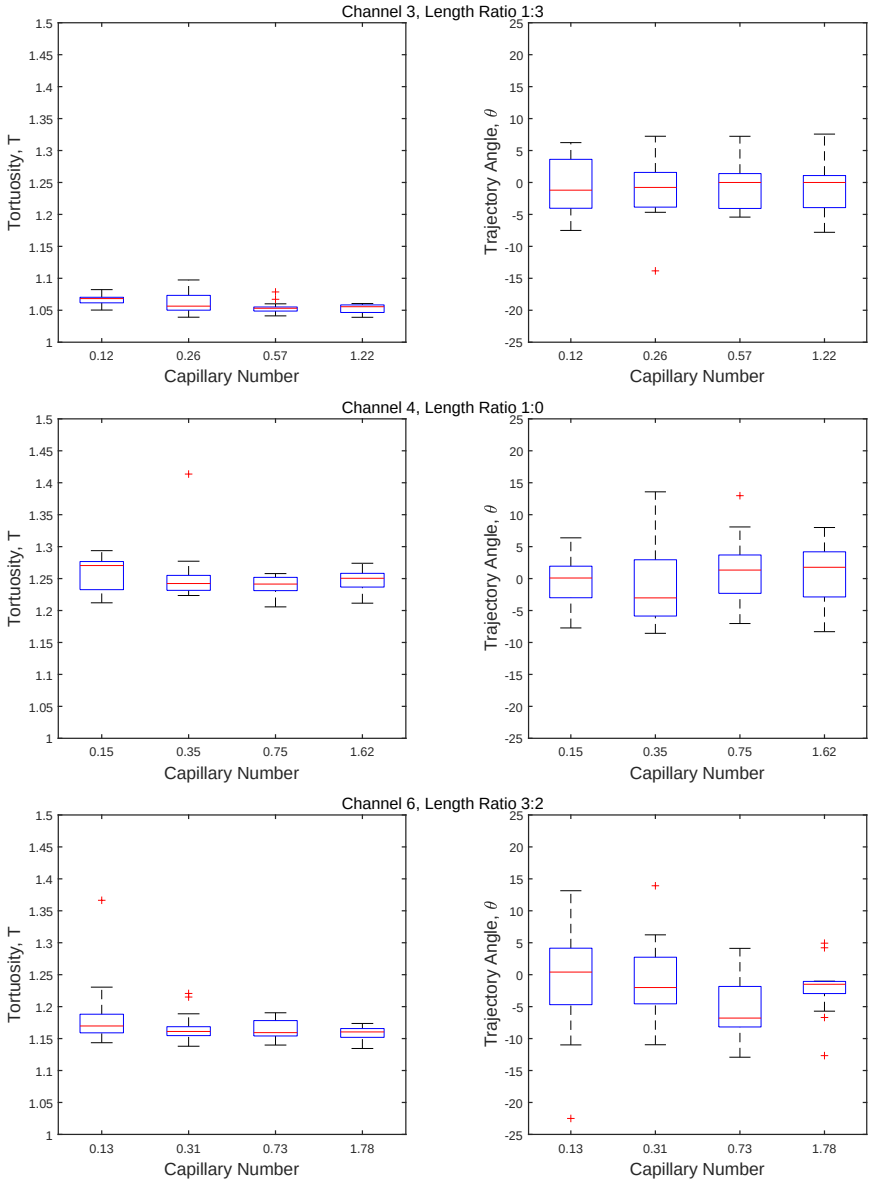


Figure A.16: Box plot of calculated tortuosity and track angles that extend over 3 mesh lengths are plotted for Channel 3 (1:3), 4 (1:0), and 6 (3:2) at a nominal feeding hematocrit of 40%.

A.6 Cell Cluster Distribution

The change in the average cluster size of cell passage as a function of capillary number across different network geometries is analyzed for increasing cell volume fractions. Histograms illustrate the total normalized projected cell area for healthy, untreated RBCs, with insets showing the relative proportion of cell area binned into clusters of 1, 2, 3, and 4 or more cells over time. These distributions are presented for nominal feeding hematocrit levels of 10%, 20%, and 40% in channels 4 and 6 at various capillary numbers in Figure A.18, and Figure A.19, respectively. The normalized projected cell area is defined as the ratio of the measured projected cell area to the first peak of the projected cell area distribution. Histograms are smoothed using a kernel density estimator to identify peaks. The absolute value of the first peak of the projected cell area is plotted as a function of pressure drop in Figure A.17, providing insight into the relationship between pressure and cell behavior within the network.

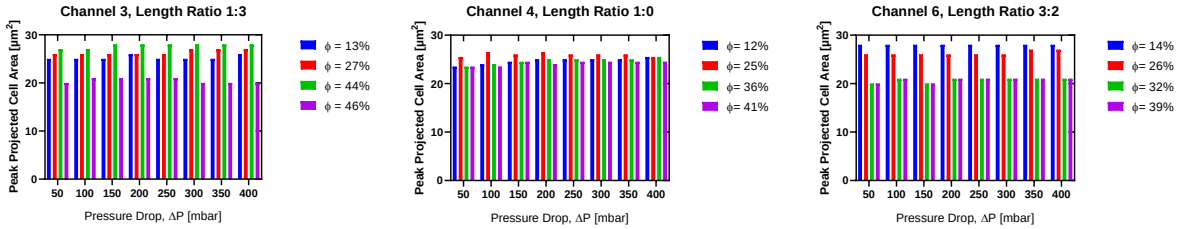


Figure A.17: Absolute value of peak projected cell area of the first mode of cell cluster histogram for each pressure drop measurement.

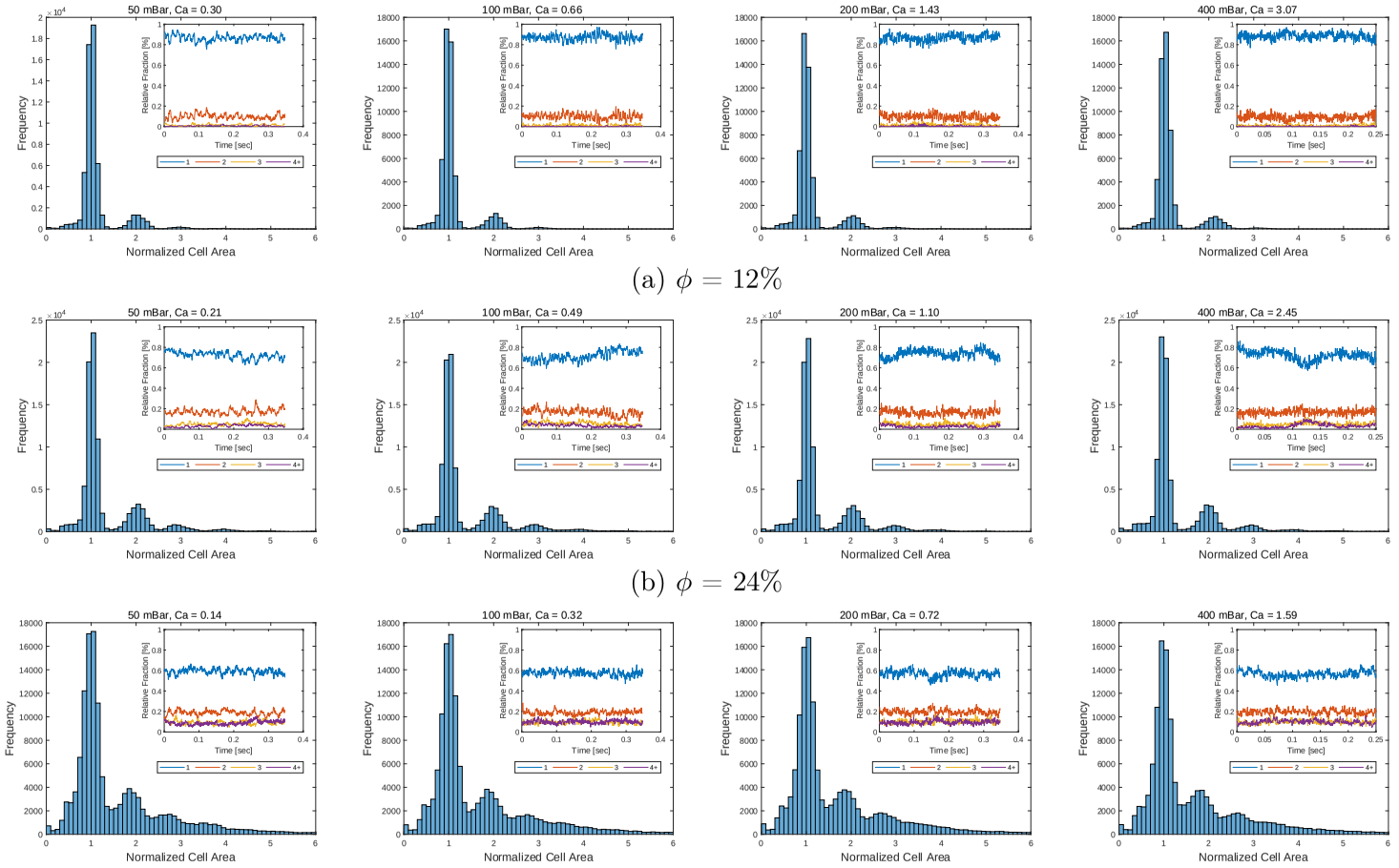


Figure A.18: Channel 4 (1:0) projected cell area distribution for increasing pressures of healthy untreated RBC for increasing nominal feeding hematocrit of (a) 10%, (b) 20%, and (c) 40% (with a measured projected hematocrit of (a) 12%, (b) 24%, and (c) 41%). Inset is the relative fraction of cell sizes binned by cluster size of 1, 2, 3, or 4 or more cells as a function of acquisition time.

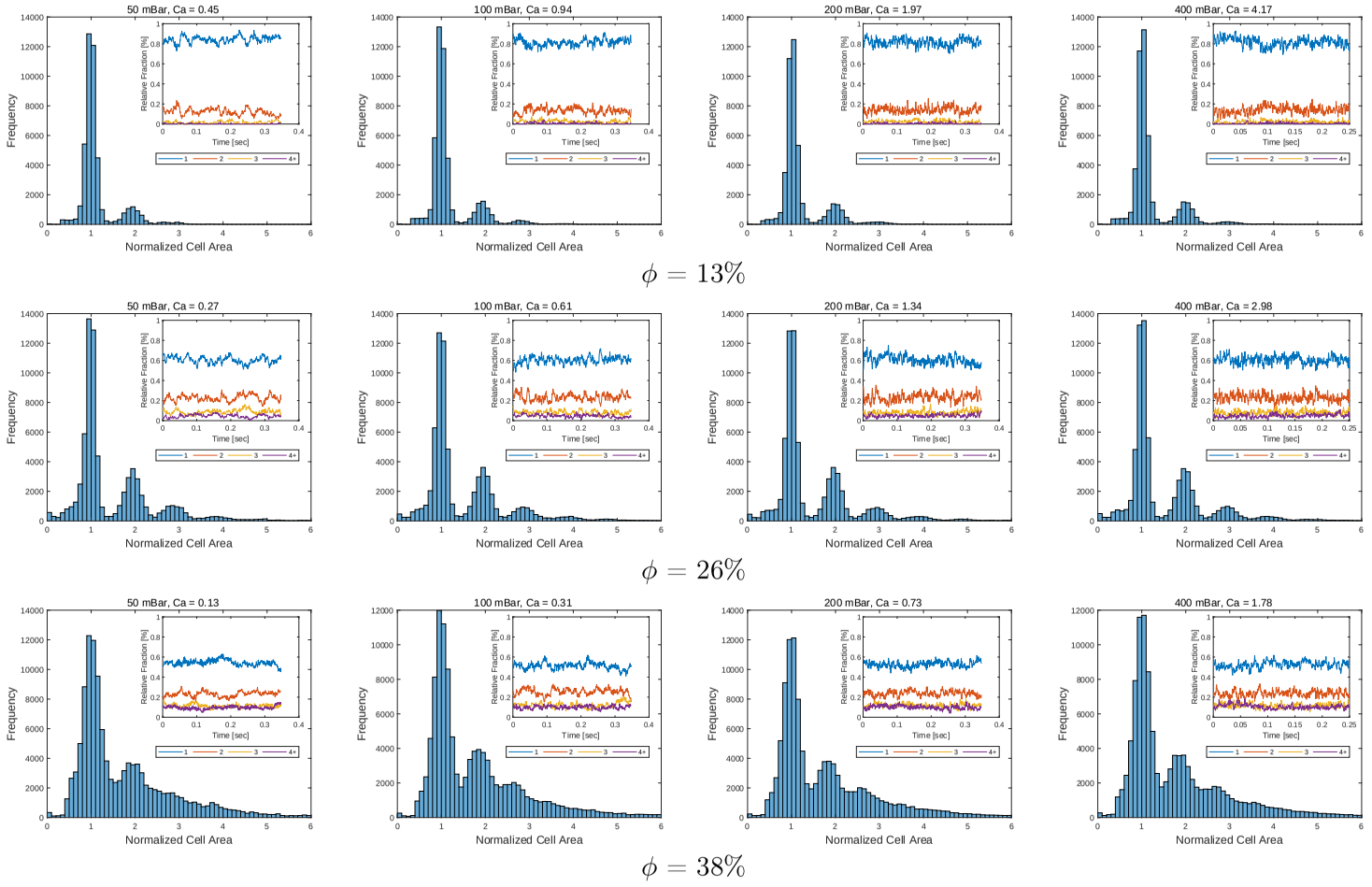


Figure A.19: Channel 6 (3:2) projected cell area distribution for increasing pressures of healthy untreated RBC for increasing nominal feeding hematocrit of (a) 10%, (b) 20%, and (c) 40% (with a measured projected hematocrit of (a) 13%, (b) 26%, and (c) 38%).Inset is the relative fraction of cell sizes binned by cluster size of 1, 2, 3, or 4 or more cells as a function of acquisition time.

A.7 Morphological Variations

Compared to the macroscopic interpretation of the elongation index as a function of Ca (Figure 3.34), each individual data point can be interpreted as an individual cell which has an individual associated Ca as there is a distribution of cell velocity for a given pressure.

To further investigate the elongation index, a heat map of the frequency of single cell elongation index for a given normalized measured cell velocity is presented in Figure A.20 and Figure A.21 for the three analyzed network geometries at a nominal feeding hematocrit of 10% and 20%. For each network geometry, the rows are divided according to the passage of cells in specific regions of interest: the straight 45-degree region (top row), the straight aligned region (middle row), and the bifurcation region (bottom row). Higher configuration occurrences are indicated by yellow, while regions lacking occurrences are indicated by black. As observed in the velocity distribution, the hot spots of higher concentration

Heat map comparisons reveal qualitative differences between channels. In Channel 3 (1:3), cell elongation patterns vary by network region, with a higher occurrence in the straight, flow-aligned section (middle row). Notably, two distinct clusters appear in elongation index and normalized velocity, suggesting velocity-dependent morphological variation. In contrast, Channel 4 (1:0) shows a narrower distribution of elongation and velocity. Comparing Channel 3 (1:3) and Channel 6 (3:2) in their straight, flow-aligned regions indicates lower variance in the 3:2 configuration, merging previously separate velocity regimes into a single broader distribution. As feeding hematocrit rises, velocity distributions expand, further widening these clusters. These differences highlight the potential for more detailed morphological analysis to pinpoint how cells adapt under varying network geometries.

The heat map analysis suggests that multiple distinct RBC morphologies coexist in the network, traveling at different speeds and appearing in varying frequencies. As illustrated in Figure A.22 and Figure A.23, RBC shapes in Channel 3 (length ratio 1:3) differ between straight and bifurcation regions. These examples, recorded at 200 mBar (mean capillary number 1.18), feature a white outline denoting each cell's binary-imaged perimeter.

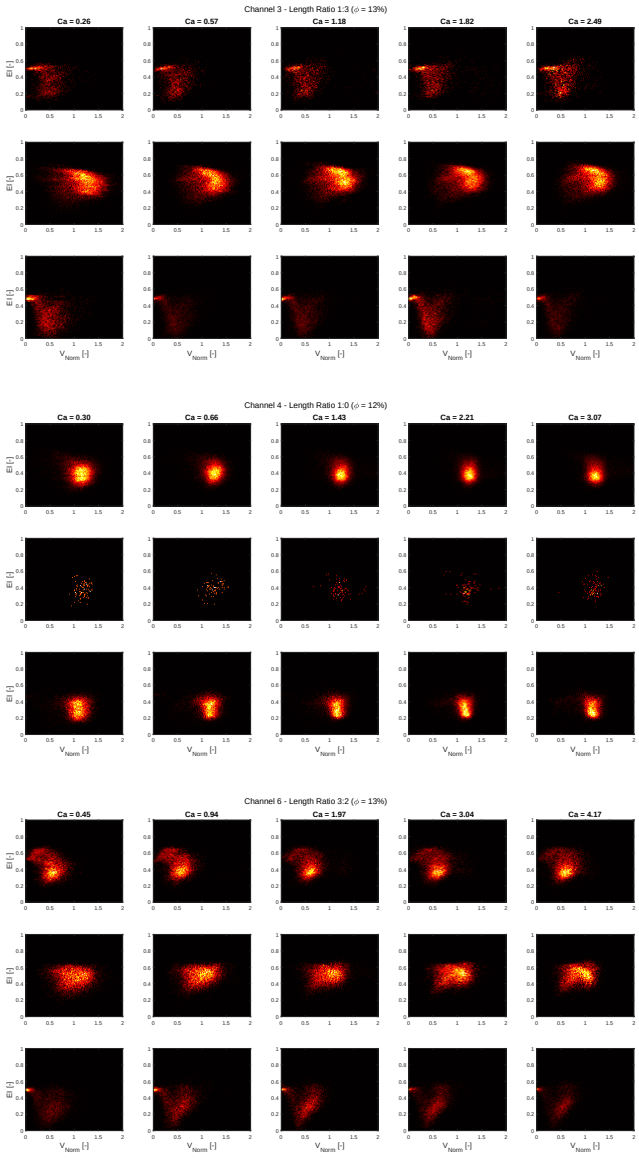


Figure A.20: Heat map of elongation index as a function of normalized cell velocity at a given average capillary number derived from global measurements of blood flow. Low hematocrit samples are presented at nominal feeding hematocrit of 10%. For each of the network geometry, the rows are split by the passage of cells in specific region of interest which are the straight 45 degrees (top row), straight aligned (middle row) and bifurcation (bottom row).

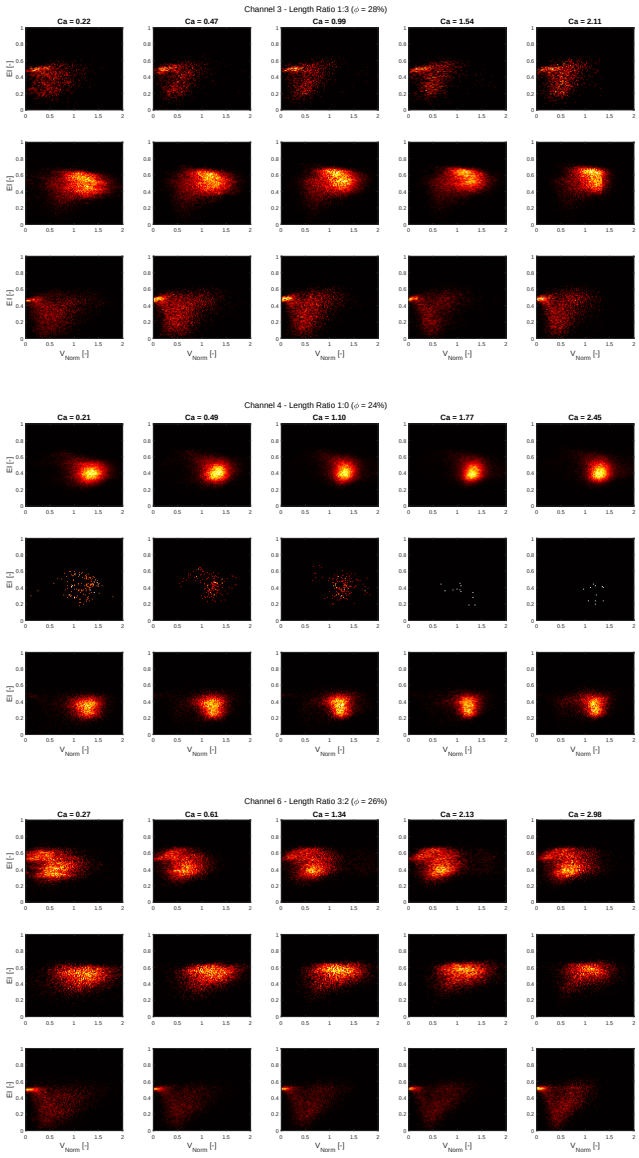
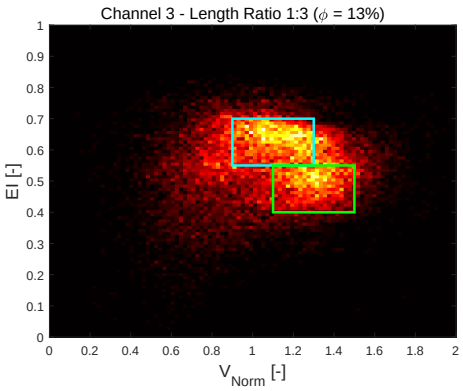
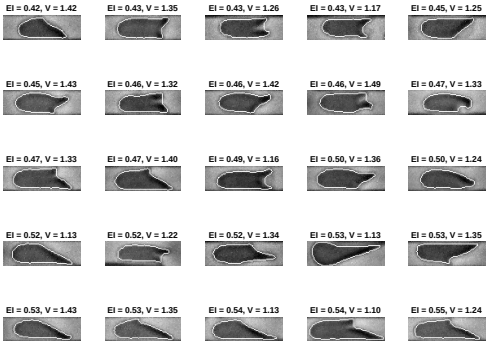


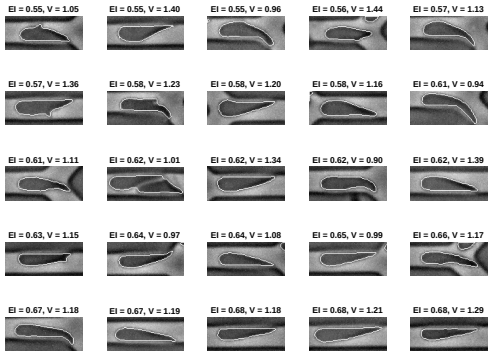
Figure A.21: Heat map of elongation index as a function of normalized cell velocity at a given average capillary number derived from global measurements of blood flow. Low hematocrit samples are presented at nominal feeding hematocrit of 20%. For each of the network geometry, the rows are split by the passage of cells in specific region of interest which are the straight 45 degrees (top row), straight aligned (middle row) and bifurcation (bottom row).



(a) EI to Normalized Velocity Heat map

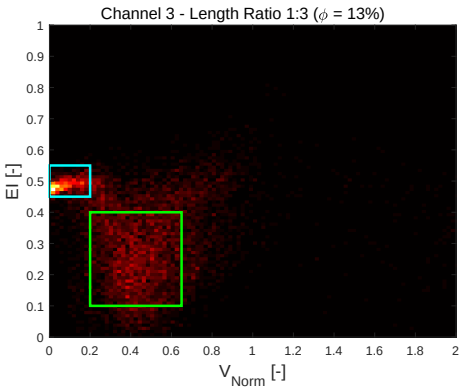


(b) Sample indicated by green rectangle

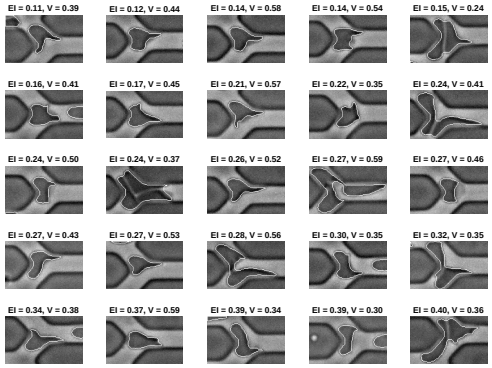


(c) Sample indicated by cyan rectangle

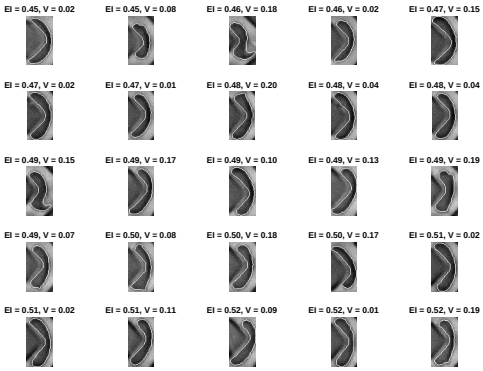
Figure A.22: Example of RBC morphology in Channel 3 (1:3) in the straight channel aligned to the flow taken at a mean capillary number of 1.18 (pressure drop 200 mBar). Samples are taken from the high incidence region observed by the yellow area. Both parachute and slipper like morphologies are observed.



(a) EI to Normalized Velocity Heat map



(b) Sample indicated by green rectangle



(c) Sample indicated by cyan rectangle

Figure A.23: Example of RBC morphology in Channel 3 (1:3) in the bifurcation region at a mean capillary number of 1.18 (pressure drop 200 mBar). Samples are taken from the high incidence region observed by the yellow area and broad region. Bumping cases are a specific subset observed in the heat map (a) indicated by the cyan rectangle.

A.8 Hematocrit Measurement Errors

Upon initial observation of the relative resistance scaling factor in Figure 3.26, it appears that the magnitude in question exhibits a rightward shift as a function of hematocrit. This discrepancy may be first attributed to the methodology employed to ascertain the local projected hematocrit, which involves calculating the projected area of the cells relative to the total area of the network. The two-dimensional projected area of a single axisymmetric cell is expected to be an overestimation of the true hematocrit. If a first-order approximation of the error is considered where the cell can be assumed a cylinder compared to that of a rectangular prism, the total sum of relative error of the hematocrit associated with the projection can be described as the following:

$$Error_{\phi} = \frac{\sum(\pi r^2 l - 4r^2 l)}{2r(TotalChannelArea)} \tag{A.25}$$

where r is the radius of the cell which is assumed to span the full width and height of the channel, and l is the length of the cell. In the low hematocrit regime, where cells are dispersed in the network and cell-cell interactions are minimal, the relative error is low as the proportional volume composed of cells is low compared to channel volume. While the relative error is expected to increase with increasing cell count as more cells occupy the volume of the channel observed in the region of interest. This first approximation, however, does not necessarily account for errors where cells are observed to flow side by side or in trains, such that the volume conforms more closely to the channel geometry. In addition, heterogeneity of the flow within the network, location of data acquisition and the size of the region of interest may play a role on the accuracy of sampling the local hematocrit as well. Furthermore, there are image quality variations that would contribute to the approximation error of the projected hematocrit.

For example, variation of the height of the focus plane and lighting of the network contributes to small changes in the measured cell area. While in the condition of a higher hematocrit regime, the segmentation of cells from the channel using the outlined methodology of a simple threshold became increasingly challenging, primarily due to the similarity in gray scale regime of the cells and the pillar. The results are binary images that occasionally exhibited ghost objects and light fluctuations, which contributed to an increased uncertainty in hematocrit measurement.

The feeding hematocrit as a function of the local projected hematocrit in Figure A.24 which exhibits the elevated hematocrit expected to be primarily associated with the projection error. All to say that the error associated with the hematocrit is dependent on

many factors, and the shift at low hematocrit would not account for the shift observed in the scaling of the relative resistance.

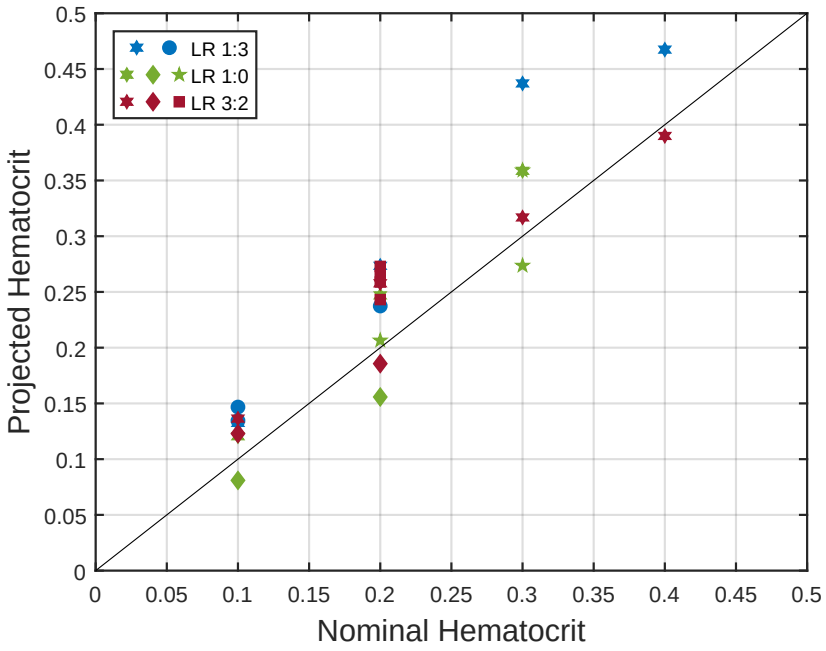


Figure A.24: Projected hematocrit as a function of nominal feeding hematocrit for healthy cells in channel geometry of 3 (1:3), 4 (1:0), and (3:2). Matched markers represent the same blood sample used between measurements completed on different channels.

A.9 Experimental Matrix

In the following section, a tabulation of all the completed experiments for the blood flow through the uniform network project is presented in Table A.4, Table A.5, and Table A.6 for the healthy untreated, diamide treated, and glutaraldehyde treated RBCs, respectively. For each set of trials, there is one trace of the Newtonian fluid run and either one or two traces of blood samples. Experiments that were skipped due to fiber or clogs were not included. Categories do not distinguish network pairs.

Table A.4: Trials for completed healthy RBC samples

	Nominal Feeding Hematocrit			
Channel	10%	20%	30%	40%
1	0	9	1	0
2	1	1	3	1
3	9	9	2	1
4	9	13	4	2
5	0	1	1	0
6	6	7	2	2

Table A.5: Trials for diamide treated RBC samples at 10% hematocrit

	Diamide Treatment [µM]		
Channel	50	100	200
3	1	1	1
4	1	1	1
6	1	1	1

Table A.6: Trials for glutaraldehyde treated RBC samples.

	GlutaraldehydeTreatment [%]		
Ht	0.001	0.005	0.01
10			2
20	1	1	3

Appendix B

Mixing in Microcirculation

B.1 Alternative Experimental Setup

A secondary experimental setup that utilizes a pressure control system and flow meter is used in contrast to the syringe-controlled system as represented in Figure B.1. The two-input reservoirs are pressurized using a single pressure controller (Flow EZ LU-FEZ-1000, Fluigent, France) and the output with another independent pressure controller. The relative input flow rate through the two-branch channel is primarily controlled by changing the relative length of the tubing from the reservoir to the input port. By varying the relative length of the tubing inputting the port, the resistance of the two branches is unequal for a given pressure drop. To achieve a flow ratio of 1:3 between the fluorescent and non-fluorescent samples, the length ratio is set to be 3:1 in length, while a flow ratio of 1:1 between the fluorescent and non-fluorescent samples requires a 1:1 length ratio. To further control the relative input flow rate of the two branches, the input reservoirs are placed on an optical rail placed vertically attached to the optical table of the microscope setup to allow for adjustment of the relative height of the reservoir. Doing so, the pressure difference between the entrance can be fine-tuned to adjust the position of the interface.

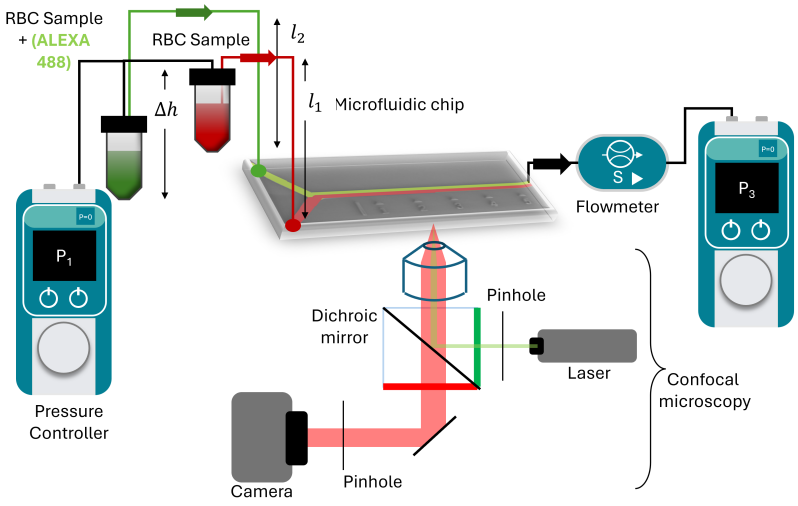


Figure B.1: A PDMS microfluidic coflow channel with a rectangular cross section area to quantify mixing in blood at different cell volume fraction are used. Two samples of identical volume fraction of RBCs with one dyed with alexa 488 that is flowed together in the channel and measure the fluorescent intensity profile at different positions along the length using a confocal microscopy setup.

B.2 Fitting Models to Characterize Flow

The advection-diffusion equation is a fundamental mathematical model used to describe the transport of any conserved property that is carried along with a fluid flow and does not affect the fluid. It combines two key processes: advection, which represents the transport due to the motion of the medium, and diffusion, which accounts for the spread of substances driven by random thermal fluctuations of the system. To formulate an understanding of mixing in microcirculation, the general differential form of the scalar advection-diffusion equation can be written for a uniform diffusion coefficient as follows:

$$\frac{\partial \mathbb{C}}{\partial t} + \nabla \left(V\mathbb{C} \right) = \nabla \left(D\nabla\mathbb{C} \right) + \mathbb{R} \tag{B.1}$$

where $\mathbb{C}$ is the concentration of the solute in the fluid, V is the velocity field, D is the diffusion coefficient, and $\mathbb{R}$ are changes due to reactions. To simplify the general transport equation, the system is assumed to be incompressible, steady-state with no additional reactions and a constant diffusion coefficient. The simplified equation results in terms that describe the advective terms and diffusive terms:

$$V\nabla\mathbb{C} = D\nabla^2\mathbb{C}. \tag{B.2}$$

In a non-dimensional form, the following equation is derived:

$$V^*\nabla^*\mathbb{C}^* = \frac{1}{Pe}\nabla^{*2}\mathbb{C}^* \tag{B.3}$$

where the starred properties are the non-dimensionalized parameters and Pe is the Peclet number. The ratio of the product of the characteristic length scale with the characteristic velocity and the diffusion coefficient is known as the Peclet number and can be understood as the ratio of advective mass transport and diffusive mass transport.

$$Pe = \frac{l\,|V|}{D} \tag{B.4}$$

where l is the characteristic length scale of the system, V is the characteristic velocity, and D is the diffusion coefficient.

To simplify the mass transport equation, the following assumptions are applied. In a shallow microfluidic device where the width is much larger than the depth of the channel, the flow can be approximated as a Hele-Shaw flow, and so velocity variation is only dependent on the depth. While the solute diffusion in the direction of the flow can be ne-

glected in an advection-dominated regime in the stream-wise direction. Furthermore, for long time scales, the solute concentration is sufficiently diffused across the channel depth and becomes independent of the depth. Thus, the mass transport equation simplifies to:

$$V\frac{\partial \mathbb{C}}{\partial x} = D\frac{\partial^2 \mathbb{C}}{\partial y^2}. \tag{B.5}$$

For parallel co-flowing channels where the fluorescent dye occupies a portion of the channel width, the initial condition is $\mathbb{C}\left(x=0,y\right)=\mathbb{C}_1+\left(\mathbb{C}_2-\mathbb{C}_1\right)\ H\left(y\right)$, where H is the Heaviside step function and the boundary condition of no-flux through the surface walls. The solution of the simplified mass transport can be solved using the method of images, also known as the method of reflection and superposition, discussed in the works of Crank for a finite system under an enclosed boundary [89].

$$\mathbb{C}\left(x,y\right)=\mathbb{C}_1+\frac{\mathbb{C}_2-\mathbb{C}_1}{2}\sum_{k=-\infty}^{\infty}\left[erf\left(\frac{y-\frac{w}{4}+2wk}{\sqrt{\frac{4\ \mathbf{D}x}{V_x}}}\right)-erf\left(\frac{y-\frac{3w}{4}+2wk}{\sqrt{\frac{4\ \mathbf{D}x}{V_x}}}\right)\right] \tag{B.6}$$

where $\mathbb{C}$ is the local concentration, w and h are the width and height of the channel, D is the diffusion coefficient, and V is the velocity in the x direction. In this study, the fluorescent intensity is assumed to be proportional to the concentration field.

B.3 Diffusion Length Function of Time

The dispersion of the fluorescent intensity profile represented by the diffusion length (δ) is presented as a function of the mean advection time, defined as the ratio of the position measured and velocity, for three distinct scenarios in Figure B.2: non-aggregated RBCs, aggregated RBCs with plasma, and aggregated RBCs with Dextran 70 at all nominal feeding hematocrit tested between 0% and 60%. The increase in δ is found to scale with the advective time reminiscent of a power law.

B.4 Relative Effective Diffusion Coefficient Function of Position

The evolution of the relative effective diffusion coefficient for various feeding hematocrit, measured at different positions along the channel after the bifurcation, is shown in Figure B.3. At each channel position, the effective diffusion coefficient is individually fitted and normalized using the 0% hematocrit sample as a baseline, representing diffusion without cells. In Figure B.3, rows correspond to different fluid configurations, and columns represent various flow rates. These measurements were taken for RBCs suspended in phosphate buffered saline (PBS), OptiPrep (density-controlled plasma), and a mixture of PBS, OptiPrep, and Dextran 70 (OPT + Dex70). As the total input flow rate increases, the effective diffusion coefficient initially rises in all cases but subsequently decreases along the channel's length. This trend becomes more pronounced with higher input flow rates, while the feeding hematocrit and RBC aggregation further influence the diffusion behavior.

The normalized diffusion coefficient increases with the presence of cells but decreases along the channel length. In some cases, sub-diffusive behavior occurs at downstream positions, resulting in diffusion coefficients lower than those for the 0% hematocrit samples. Additionally, the effect of cell size—whether individual cells or aggregated particles (in plasma or Dextran)—on the diffusion coefficient is non-monotonic with hematocrit changes. While the exact causes of the observed decrease in diffusion are uncertain, it is speculated to result from entrance effects and the limitations of fitting a 2D model to the data. In all cases, an increase in the effective diffusion coefficient with the presence of the cells is observed, followed by a decrease along the length of the channel. While this effect is amplified with an increasing input flow rate into the channel, it is modulated by the feeding hematocrit and affected by the morphology of the RBCs.

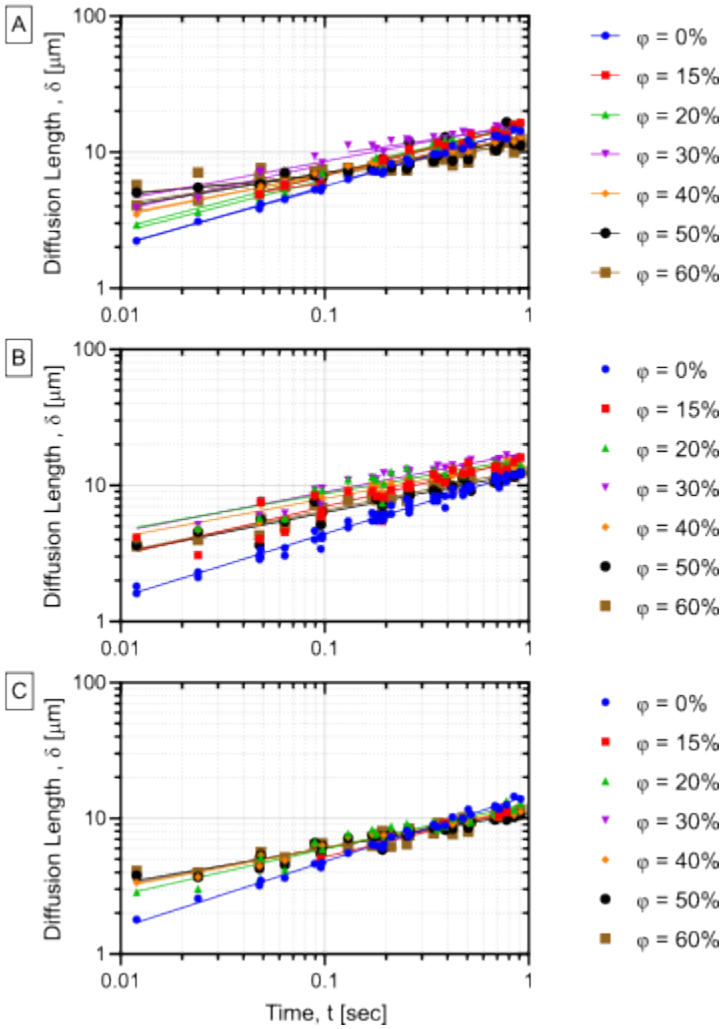


Figure B.2: The total spread as a function of advection time for the suspending fluid and RBC suspension for all tested hematocrit for (A) non-aggregated, (B) aggregated in plasma and (C) aggregated RBC in Dextran 70. Each hematocrit data set is a cumulation of measurements taken at six positions along the length of the straight channel and six input flow rates, which is collectively fitted with a power-law model indicated by a solid line.

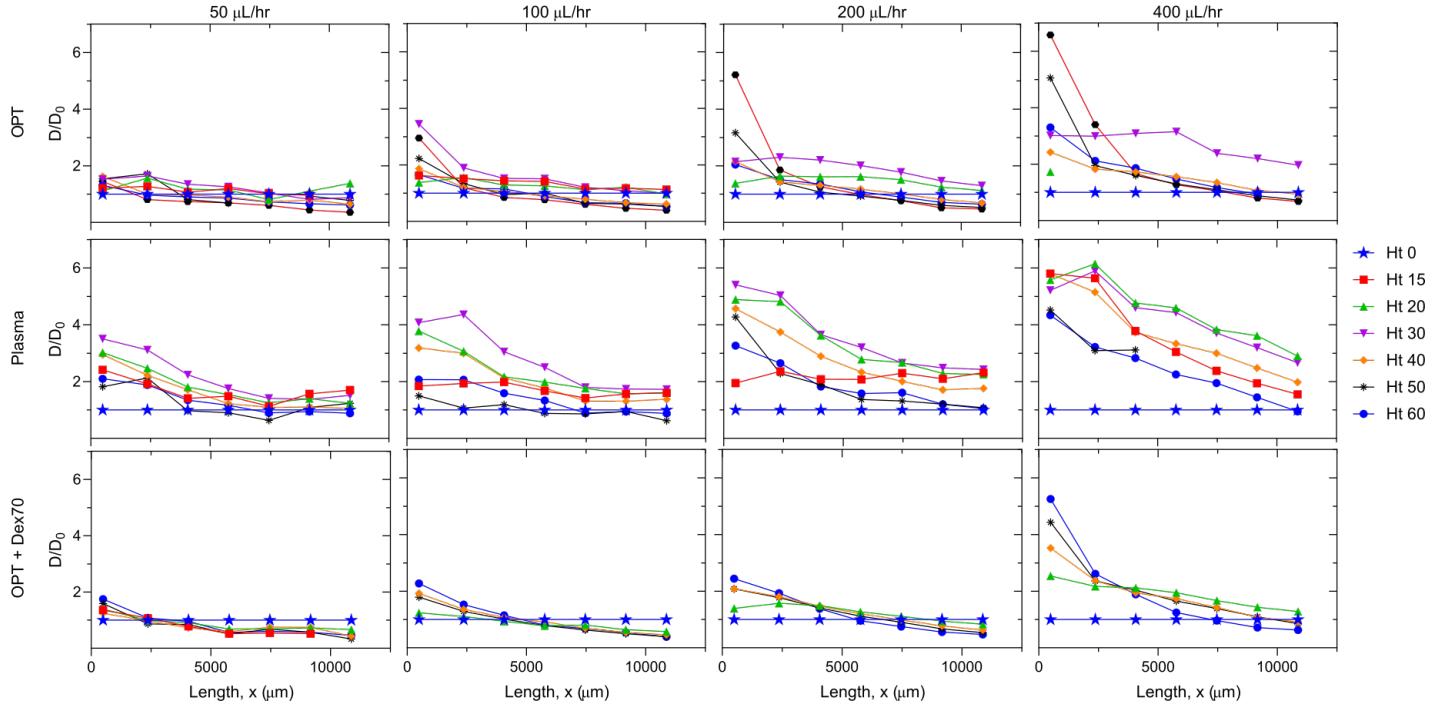


Figure B.3: Evolution of the normalized effective diffusion coefficient (D/D_0) of different nominal feeding hematocrit (Ht) taken at different positions along the length of the channel after the bifurcation for non-aggregated RBC suspension in OptiPrep (OPT), aggregated RBC suspension in Plasma, and aggregated RBC suspension in OptiPrep and Dextran 70 (OPT + Dex70). Total input flow rate for 50 µL/h, 100 µL/h, 200 µL/h and 400 µL/h are separated by column.

B.5 Experiment Matrix

In the following section, tabulation of the completed experiments for the mixing in the microcirculation project is presented in the Table B.1 and Table B.2 for the augmentation of mixing from aggregation and the effects on the transport of molecules of increasing molecular weight, respectively. For each set of trials, there are approximately seven positional measurements (Table B.3) and six flow conditions (Table B.4).

Table B.1: Trials for the different fluids (number indicates how many sets either partial or complete in input flow rate and position) using syringe pump (imposed flow)

Test	Alexa 647, Aggregability			Cell Mask Experiment	
ϕ (%)	OPT	OPT Dex-70	Plasma	OPT	OPT Dex70
0	1	1	1		
15	1	1	1	2	1
20	1	1	1	1	1
30	1		1	1	1
40	1	1	1	1	
50	1	1	1		
60	2	1	1	2	1

Table B.2: Dextran trial configurations for exploring augmentation of solutes of increasing molecular weights using syringe pump (imposed flow)

Test	OPT				Plasma			
ϕ (%)	Dex10	Dex70	Dex150	Dex2000	Dex10	Dex70	Dex150	Dex2000
0	1	1	1	1	1	1	1	1
30	1	1	1	1	1	1	1	1

Table B.3: Measurements taken along the length of channel at different positions (x)

Grad.	Position from Bifurcation, x (µm)
0	500
5	2030
10	3730
15	5430
20	7130
25	8830
30	10530

Table B.4: Measurement flow rate conditions that are tested using syringe pump (imposed flow) and associated Péclet number

Q total (µL/h)	Q fluorescent (µL/h)	Q dark (µL/h)	Péclet number
25	6.25	18.75	156
50	12.5	37.5	312
75	18.75	56.25	623
100	25	75	1246
200	50	150	1870
400	100	300	2493

Appendix C

Two-Foci Fluorescence Correlation Spectroscopy

Velocity Profile in Rectangular Channel

A theoretical velocity profile is a fundamental tool for comparing and verifying experimental results. In the context of pressure-driven flow, also known as Poiseuille flows, the flow is driven by a pressure gradient along the length of the channel. The flows are assumed to be parallel and limited to fluids that are incompressible. The fluid velocity at the channel boundaries is assumed to exhibit no slip condition. Starting from the Navier-Stokes equation and assuming that the flow profile is time independent ($\partial/\partial t = 0$), parallel flow ($V_y = 0, V_z = 0$) and the pressure gradient is solely along the length of the channel, the simplified Navier-Stokes equation results in Equation (C.1):

$$\frac{\partial P}{\partial x} = \eta \left(\frac{\partial^2 V_x}{\partial y^2} + \frac{\partial^2 V_x}{\partial z^2} \right) \tag{C.1}$$

where $\frac{\partial P}{\partial x}$ is the pressure gradient driving the flow, and $\eta(\frac{\partial^2 V_x}{\partial y^2} + \frac{\partial^2 V_x}{\partial z^2})$ are the viscous forces. Analytical solutions to Poiseuille flow for the commonly encountered channel geometries in microfluidics such as circular and rectangular cross-sectional profiles are known. In the case of rectangular cross-sectional channels, the solution necessitates the use of Fourier series to represent the velocity profile. This is given by the following formulation when the

coordinate is taken as the bottom of the channel (see Figure 5.2) [70]:

$$V_x(y,z) = -\frac{4}{\eta}\frac{h^2}{\pi^3}\frac{\partial p}{\partial x}\sum_{n=0}^{\infty}\frac{1}{(2n+1)^3}\left(1-\frac{cosh((2n+1)\pi\frac{y}{h})}{cosh((2n+1)\pi\frac{w}{2h})}\right)sin\Big((2n+1)\pi\frac{z}{h}\Big) \quad \text{(C.2)}$$

where V is the velocity in the direction of the channel x, $\partial p/\partial x$ is the pressure gradient along the length of the channel, h is the height of the channel, and w is the width of the channel. The flow rate, Q is then calculated by taking the surface integration across the cross-sectional area [70]:

$$Q = -\frac{h^3 w}{12\mu}\frac{\partial p}{\partial x}\left(1-\frac{192h}{\pi^5 w}\sum_{n=0}^{\infty}\frac{1}{(2n+1)^5}tanh\Big((2n+1)\pi\frac{w}{2h}\Big)\right). \quad \text{(C.3)}$$

The flow rate can be approximated for channels with low aspect ratio (h/w) where $tanh((2n+1)\pi\frac{w}{2h}) \to 1$ when $w/h \to \infty$. This further simplifies the flow rate in a rectangular cross-sectional channel to be approximated as Equation (C.4).

$$Q = -\frac{h^3 w}{12\mu}\frac{\partial p}{\partial x}\left(1-0.63\frac{h}{w}\right) \quad \text{(C.4)}$$

For low aspect ratio the results of Equation (C.2), the velocity profile at the center of the width of the channel begins to approach the case of flow between two infinite parallel plates as the aspect ratio of the channel approaches zero. The velocity profile in low aspect ratio can then be approximated by the velocity field of a Hele-Shaw flow Equation (C.5).

$$V_x(z) = -\frac{1}{2\eta}\frac{\partial P}{\partial x}z(h-z) \quad \text{(C.5)}$$

A comparison of the analytical solution and approximation using the Hele-Shaw flow interpretation is presented in Figure C.1 for different positions along the width of the channel taking 10 n iterations of the Fourier sum. The approximation of the velocity profile at the center along the width of the channel produces a relative error below 0.1%, and remains a good approximation until measurements are completed close to the channel's side wall.

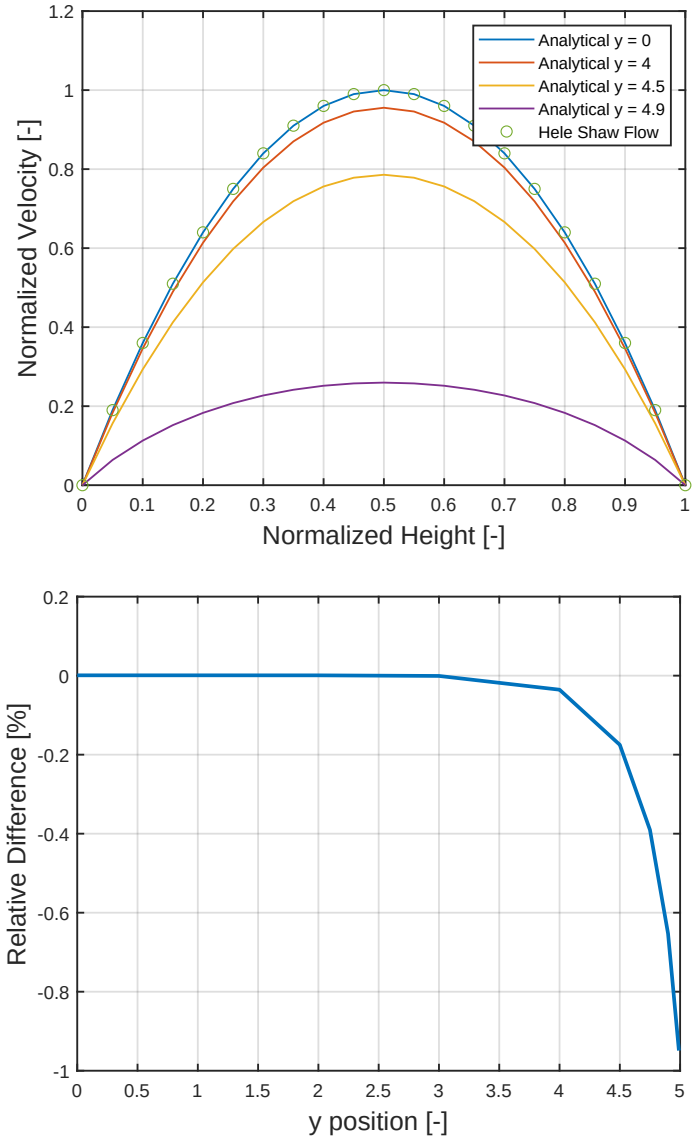


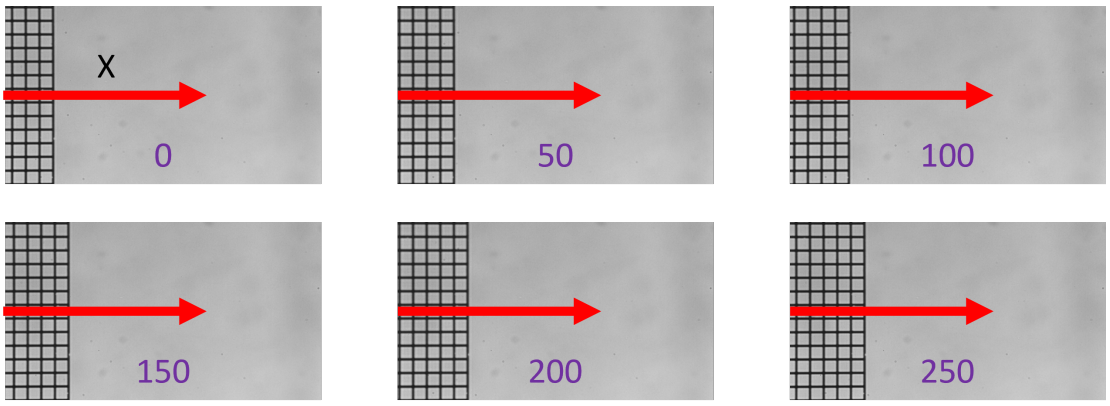
Figure C.1: (Top) For a rectangular channel with aspect ratio of 0.1 for positions taken at different width position of a rectangular channel using the analytical equation (Equation (C.2)) and the Hele-Shaw approximation (Equation (C.5)). (Bottom) Relative error comparing the Hele-Shaw approximation to the analytical solution over the width position of a rectangular channel.

C.1 High Speed Camera Imaging of Linear Actuation

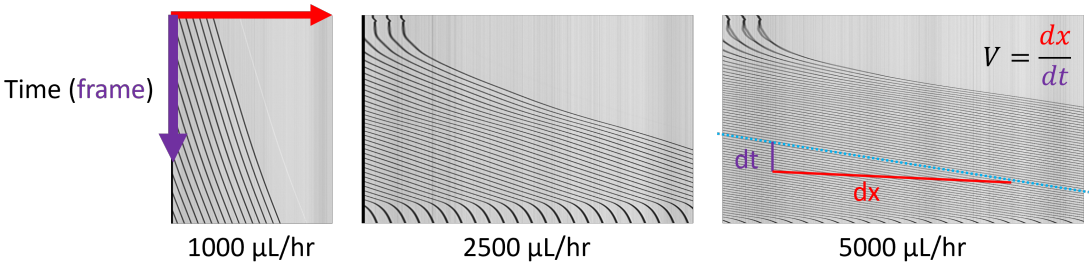
The linear actuation of the x-y stage for the secondary flow condition is verified by a direct measurement of the displacement of a microscope calibration grid and a high-speed FASTCAM NOVA R5-4K camera (Photron, Japan). The microscope calibration grid is placed in position instead of a glass capillary microfluidic device, and the displacement of the grid is measured at different input flow rates of the syringe pump. The velocity measurement is completed using a kymograph. In Figure C.2 (a), the image of the calibration grid is depicted in frames 0, 50, 100, 150, 200, and 250. The gray scale value along a pixel line, as indicated by the red arrow, is plotted over all frames, producing what is known as a kymograph Figure C.2 (b). The lines are produced from the passage of multiple grid lines, whereas the slope that it produces on the kymograph changes depending on the speed at which an object passes along the pixel line. The slope of the line is itself the velocity measurement of the grid's passage. The theoretical velocity approximated from $V \approx Q/A$ is compared to the direct measurement of the stage velocity using the high-speed camera and the kymograph technique, which is summarized in Table C.1 and Figure C.3. Velocity measurements from the high-speed camera indicate that the theoretical velocity measurement is greater than what is the true displacement of the x-y stage. This may simply be due to the unaccounted-for effect that the additional force required to overcome the frictional forces to displace the mass of the x-y stage compared to the typical syringe to which the pump is designed to move.

Table C.1: Theoretical linear actuation velocity compared to velocity from high-speed camera imaging and kymograph measurement

Q (μL/hr)	Theoretical (μm/s)	Measured (μm/s)	Std V (μm/s)
1000	33.28	32.33	1.29 (3.8%)
2500	83.20	77.87	3.40 (4.3%)
5000	166.40	150.68	7.76 (5.1%)
10000	332.80	321.12	10.33 (3.2%)
15000	499.19	478.44	18.68 (3.9%)
20000	665.58	635.53	27.23 (4.2%)



(a) Image sequence of calibration progression at different time frame



(b) Example Kymograph at different input flow rates

Figure C.2: Velocity measurement of linear acquisition using kymograph technique on high-speed camera imaging of microscope calibration grid displacement. The grid velocity can be derived from the slope of the trace created by the movement of the microscope grid lines.

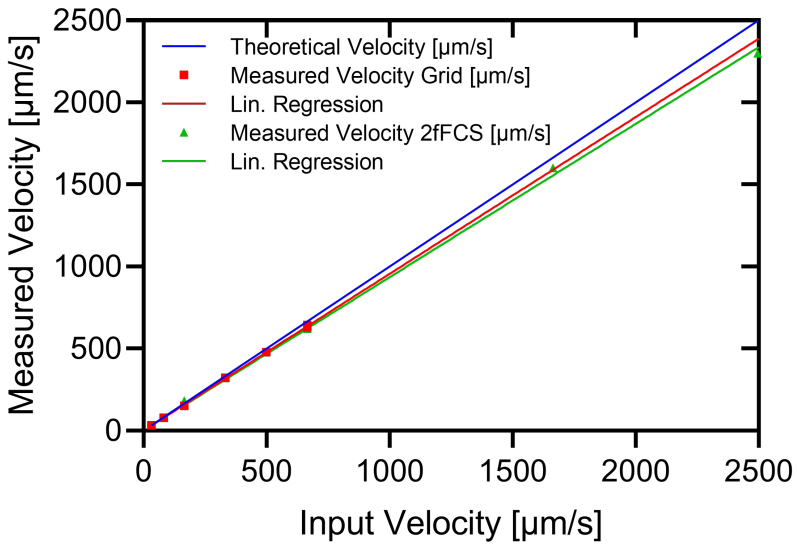


Figure C.3: Linear actuation measurement comparison between theoretical velocity measurement (approximated by $V \approx Q/A$), measured velocity grid using the high-speed camera, and measured velocity using 2f FCS.

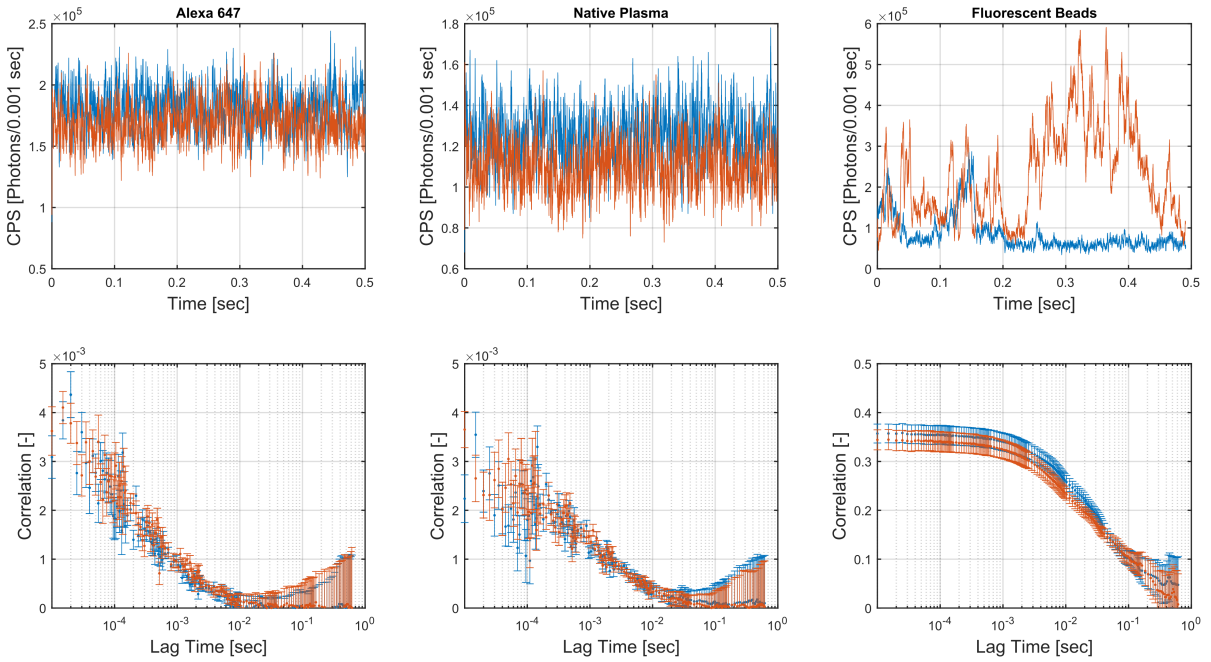


Figure C.4: (Top row) Fluctuation intensity data of Alexa 647, diluted native plasma, and fluorescent beads in water where each color represents the results from the two foci. (Bottom row) Auto-correlation data extracted from ISS Vistavision of fluctuation intensity data.

C.2 Tracer Selection

In order to select an appropriate tracer to complete velocity measurements, the characteristic time scale of diffusion of the tracer should be lower than the characteristic time of flow. The result of the fluorescence fluctuation data and auto-correlation taken in a stationary liquid droplet on a glass slide of Alexa 647, diluted native plasma with PBS, and fluorescent particles is shown in Figure C.4 for both focal points. With measurements taken at a rate of 200,000 Hz, the results for Alexa 647 and native plasma are found to be noisy at short time scales. The 2f FCS experimental setup was not calibrated to determine the observation volume, which is required for direct measurement of the diffusion coefficient. It can be observed that the characteristic time scale of diffusion of the beads is a magnitude slower than that of native plasma and that of Alexa 647.

When modeling diffusion-flow in 2f FCS (Equation (5.2)), two key time scales are the diffusion time of the measured molecule and the fluid flow time between the foci. This

study uses Alexa 647 and dark red fluorescent particles, chosen for their emission in the red wavelength spectrum [110]. Alexa 647 has a diffusion coefficient of $330 \pm 0.1\,\mu m^2/s$ [139], while dark red FluoSpheres (nominal diameter) have an approximate diffusion coefficient of $9.5\,\mu m^2/s$, calculated using the Stokes-Einstein equation. Native plasma proteins exhibit diffusion coefficients between $19.8\,\mu m^2/s$ and $61\,\mu m^2/s$ [140–142], consistent with preliminary tracer measurements, where diffusion times decrease from fluorescent beads to plasma to Alexa 647.

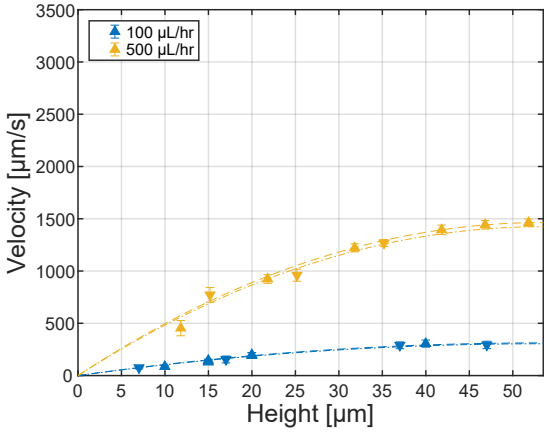
To separate these time scales, tracer particles should ideally diffuse slower than the tested flow rates. This is influenced by fluid viscosity, as diffusion scales inversely with viscosity per the Stokes-Einstein equation. Fluorescent beads are ideal for this purpose, but larger particles may capture slower velocities, provided their inertia is negligible. Excessive particle inertia can cause velocity lag, where particles gradually adjust to changes in fluid direction.

The native plasma results were obtained without Alexa 647 or fluorescent beads, measuring velocities for non-aggregated 40% hematocrit RBC at two input flow rates. Achieving these measurements required input laser power two orders of magnitude higher than for fluorescent beads ($10\,\mu W$ to $2\,mW$) to produce a peak correlation time. This raises the question of what fluctuations are being measured to generate the peak lag time with RBCs alone. It is hypothesized that either the RBCs scatter light, creating fluctuations similar to single-molecule passage, or trace amounts of fluorescent molecules naturally present on or around the cells produce signals akin to those from Alexa 647 or fluorescent beads. The exact source of fluctuation is not conclusive and will need further work to explore, but it can be said that in the presence of plasma there are constituents that are measurable in the 2f FCS setup used in these experiments.

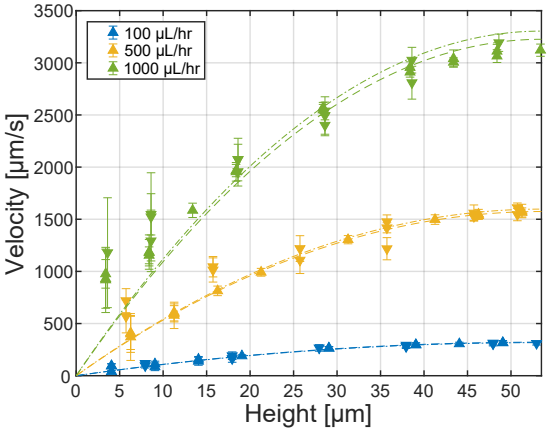
C.3 Symmetry Across Channel Height

Velocity profiles of the transparent and dense RBC suspensions are plotted with increasing flow rates which have been folded along the center position of the channel (Figure C.5). Upward triangles indicate measurements made on the bottom half of the channel and downward triangles indicate measurements made on the top half of the channel. Parabolic fits are completed over individual halves of the velocity profile to contrast differences in the velocity measurement. Velocity profiles are symmetrical for transparent solutions where minimal change is found regarding the standard deviation of measurements in the top half of the fluid and the fit of the flow. In contrast, for the RBC fluid samples, the velocities also appear to be symmetric; however, the standard deviation of the measurements increases with increasing cell penetration.

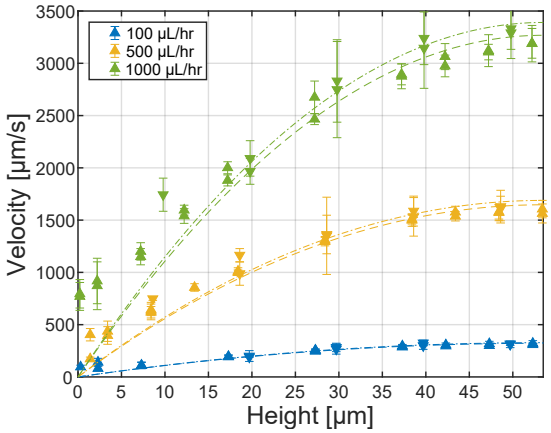
Velocity profile measured in the 107 µm channel was found to be symmetrical for the case of transparent fluids (Figure C.5(a)). This, however, does not necessarily appear to be the case for when RBC is introduced into the mix. The velocity measurement on the top half of the channel tends to have a wider correlation function than its counterpart on the bottom half of the channel. The deeper you try to measure into the channel, the more RBC that you are passing through, first in the distance for the laser to travel for excitation and the same distance back for observation of the fluctuation at a given height. Multiple lag times are observable close to the bottom wall, which are not observed when looking at the top surface, which results in a wall velocity that tends to always be greater than expected.



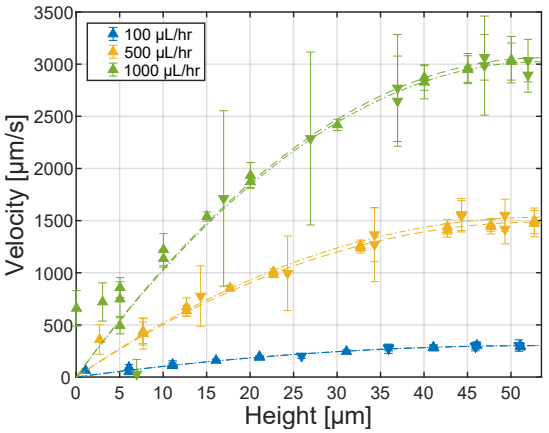
(a) PBS



(b) 10% HT RBC in PBS OptiPrep



(c) 20% HT RBC in PBS OptiPrep



(d) 40% HT RBC in PBS OptiPrep

Figure C.5: Velocity profiles folded along midplane of channel through increasing hematocrit of non-aggregated samples. Upward triangles are velocities of the bottom half and downward triangles are velocities of the top half. (- -) and (- .) are fits of bottom and top velocity profile using a constant viscosity model, respectively.

Appendix D

Mini Review

In this work, the published mini-review on image-based experimental measurement techniques may be of use to readers of this work [113].

frontiers | Frontiers in Physiology

MINI REVIEW
published: 29 April 2022
doi: 10.3389/fphys.2022.886675

Image-Based Experimental Measurement Techniques to Characterize Velocity Fields in Blood Microflows

Andy Vinh Le[1,2] *and Marianne Fenech*[1]*

[1]Department of Mechanical Engineering, University of Ottawa, Ottawa, ON, Canada, [2]Centre de Biochimie Structurale, CNRS UMR 5048—INSERM UMR 1054, University of Montpellier, Montpellier, France

Predicting blood microflow in both simple and complex geometries is challenging because of the composition and behavior of the blood at microscale. However, characterization of the velocity in microchannels is the key for gaining insights into cellular interactions at the microscale, mechanisms of diseases, and efficacy of therapeutic solutions. Image-based measurement techniques are a subset of methods for measuring the local flow velocity that typically utilize tracer particles for flow visualization. In the most basic form, a high-speed camera and microscope setup are the only requirements for data acquisition; however, the development of image processing algorithms and equipment has made current image-based techniques more sophisticated. This mini review aims to provide a succinct and accessible overview of image-based experimental measurement techniques to characterize the velocity field of blood microflow. The following techniques are introduced: cell tracking velocimetry, kymographs, micro-particle velocimetry, and dual-slit photometry as entry techniques for measuring various velocity fields either *in vivo* or *in vitro*.

Keywords: microcirculation, kymographs, micro-particle velocimetry, dual-slit photometry, cell tracking

OPEN ACCESS

Edited by:
Stavroula Balabani, University College London, United Kingdom

Reviewed by:
Georgios C. Georgiou, University of Cyprus, Cyprus

***Correspondence:**
Marianne Fenech
mfenech@uottawa.ca

Specialty section:
This article was submitted to Biophysics, a section of the journal Frontiers in Physiology

Received: *28 February 2022*
Accepted: *04 April 2022*
Published: *29 April 2022*

Citation:
Le AV and Fenech M (2022) Image-Based Experimental Measurement Techniques to Characterize Velocity Fields in Blood Microflows. Front. Physiol. 13:886675. doi: 10.3389/fphys.2022.886675

INTRODUCTION

Microcirculation, which is composed of numerous vessels with diameters typically less than 50 μm, is the main exchange site between blood and tissues. Because blood behavior in the microcirculation cannot be considered as a liquid flow, and is rather regarded as a collection of interacting particles in suspension (Secomb, 2017), the study of blood flow in the microcirculation represents a considerable challenge. Red blood cells (RBCs), which are the most abundant cells found in the blood (40% of the blood volume), may adversely affect blood viscosity (Coull et al., 1991; Baskurt and Meiselman, 2007; Silva-Herdade et al., 2016; Sloop et al., 2020). For instance, blood viscosity increases when blood cells are too abundant (as shown in Erythrocytosis (Pearson and Path, 2001) and hyperleukocytic leukemia (Sharma et al., 1992), less deformable than healthy cells (sickle cell disorders (Connes et al., 2016), hemolytic anemia (Johnson and Ravindranath, 1996), and falciparum anemia (Parrow et al., 2018)), or if they tend to aggregate abnormally (observed in a variety of clinical states such as burns (Levin and Egorihina, 2011), infections and sepsis (Baskurt and Meiselman, 2013), complicated diabetes mellitus (Le Devehat et al., 1990), and malignant and rheumatic diseases (Luquita et al., 2009)). Velocity characterization is a key measurement in numerous studies, such as those analyzing the impact on microcirculation on cellular interactions due to aggregation, blood cell congestion, or

TABLE 1 | Comparison of image-based experimental measurement techniques to characterize velocity fields in blood microflows.

	Cell tracking	Kymograph	Micro-PIV	Dual slit
Tracers	Cells	Speckles from RBC shadows	RBCs or fluorescent microparticles	Speckles from RBC shadows
Image processing algorithms	See note	Kymograph	Cross-correlation	Cross-correlation
Critical parameters	*dt*	Image stability, focus, requires a flat (2-dimensional) microcirculation bed	DOC, *dt*, size and shape of CCW	DOC, relative position of the slits, slits shape
Hematocrit	<1%	Not reported	<20%	Not reported
Provide: characteristic velocity	yes	yes	yes	yes
Provide: velocity profile	yes	no	yes	yes
Provide: 2D velocity field in the vessel	yes	no	yes	yes
Provide: 3D velocity field in the vessel	no	no	yes, e.g., using confocal microscopy	no
Associated blood structural characteristics commonly explored in conjunction with velocity field	Aggregate size Spatial distribution of red blood cells Cell depleted layer Viscosity Distribution	Cell depleted layer Microcirculation velocity distribution	Aggregate size Hematocrit Profile Cell depleted layer Viscosity Distribution	
Possibility to investigate unsteady flow	yes	Limited	limited	no
Typical Experimental equipment	a high-speed camera, a microscope	Kymograph only: a high-speed camera, a microscope *In vivo*: a portable high-speed camera with darkfield capacity coupled with an appropriate lens and a sterile disposable cap	a light sensitive and short interframe times camera (double frame or high speed), a double pulsed laser with appropriate beam coupling and guiding, an epifluorescence microscope (single channel or stereo)	Photosensor (photodiodes, phototransistors, optical fibers) or a high-speed camera, a microscope

Note: Examples of cell tracking algorithms (not necessary RBC): multiple-hypothesis tracking of extracted cell barycenters, local optimization using a cost function within spatially limited search regions, state-space diagram optimization in a greedy fashion, nearest-neighbor tracking of extracted centers of mass, and iterative spatial-temporal association based on three-dimensional connectivity for 2D data (Maška et al., 2014).

platelet migration, to provide useful insights into the mechanisms of disease or to study therapeutic solutions (Bishop et al., 2001a; Long et al., 2004; Ishikawa et al., 2011; Kaliviotis et al., 2011; Sherwood et al., 2012; Pitts and Fenech, 2013b; Kaliviotis et al., 2018; Passos et al., 2019). The advent of microfluidics technology has propelled *in vitro* studies pertaining to the flow behavior of blood or blood cells in microchannels and the development of blood lab-on-a-chip platforms (Khalid et al., 2017; Maria et al., 2017; Sebastian and Dittrich, 2018; Passos et al., 2019; Abay et al., 2020; Mantegazza et al., 2020; Kihm et al., 2021).

Blood microcirculation studies are performed either *in vivo*, using intra-vital microscopy, or in a more controlled *in vitro* environment, taking advantage of the recent development and accessibility of microfluidic chips. The methods described here are image-based measurement techniques that are used in either *in vivo* or *in vitro* context, or are sometimes used in both contexts. Over the years, with the increase in the camera sampling frequency, advances in image processing techniques, and increase in computer calculation capacity, the original image-based method (cell tracking) has evolved into more complex methods that coexist and evolve in parallel. Although the choice of the method seems to be linked to the research community (*in vivo* vs *in vitro*) or to the experience of the research group and available equipment, this mini review aims to better guide the choice of a suitable method for a desired application by highlighting the capabilities and limitations of different methods. **Table 1** summarizes key information as a quick guide.

IN VIVO VS *IN VITRO* STUDIES

Numerous methods, such as Doppler, thermodilution, and dye injection, have been used to investigate microvascular flows (Gutterman et al., 2016; Secomb, 2017). However, here, we will focus only on image-based methods.

Intravital microscopy involves the observation of phenomena occurring in living organisms through a microscope. The simplest method is to operate on a small animal and exteriorize an organ, usually in the peritoneum, to be able to image it, which offers visualization of a flat microcirculatory network. The organ is immersed in a saline solution and immobilized with stitches (Bishop et al., 2001b; Long et al., 2004). Other research groups have opted for the implementation of a viewing window, which makes it possible to keep the animal alive for several days and to observe the spatial and temporal evolution of the microcirculation (Patumraj et al., 2005; Cabrales and Carvalho, 2010; Kihm et al., 2021).

Intravital microscopy images contain several artifacts that can influence velocity calculations, such as physiological movements, dilation and contraction of vessels, superposition of vessels in the organ, and light scattering. Open-source image processing tools are available to stabilize the images (e.g., the image stabilizer plugin for ImageJ (Li and Kang, 2008)).

For *in vivo* studies, the velocity characterization methods aim for a characteristic velocity along each vessel (average velocity or maximum velocity), and the velocity field is then the map of

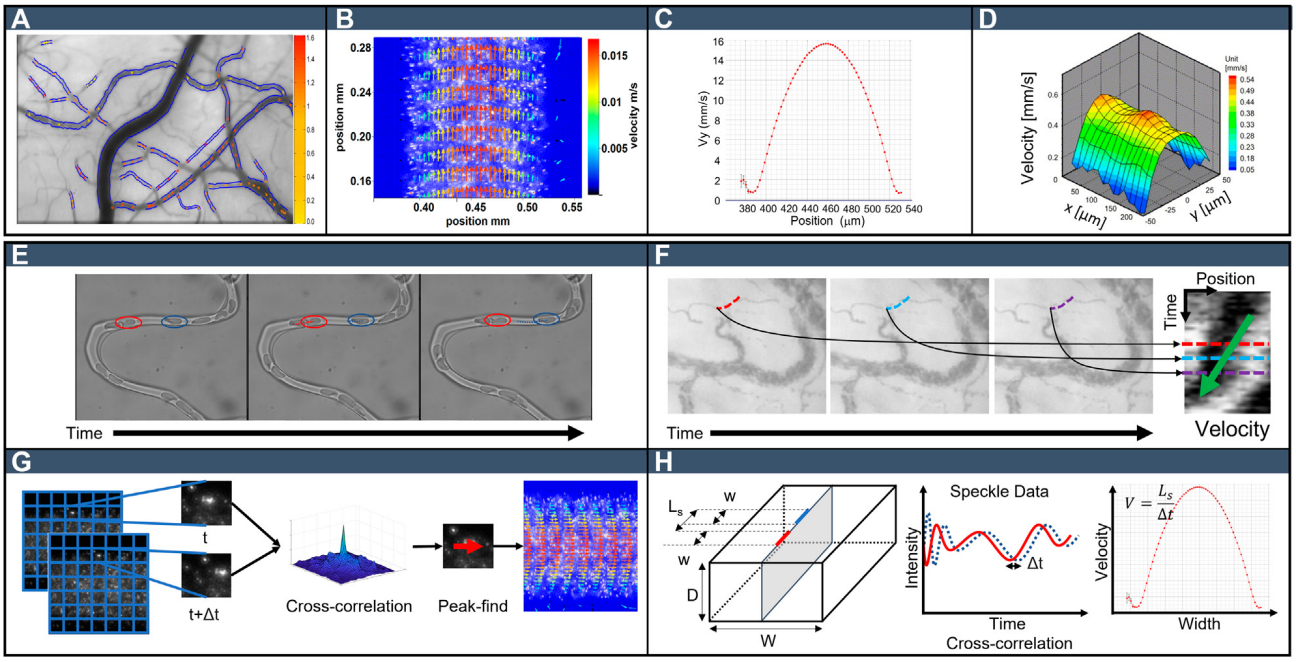


FIGURE 1 | (A-D): Visual comparison of typical velocity fields. **(A)** Color map of local velocity in a conjunctival microcirculation network. Color bar represents velocity in units of mm/s. The velocity vectors were obtained using kymographs image reused per United States government copyright (Khansari et al., 2015). **(B)** Field of 2D velocity vectors profile across a glass round 150 mm diameter capillary channel where blood, at 10% hematocrit, was flowing at a flow rate of 11.5 ml/min. The velocity vectors were obtained in our lab using micro-PIV. **(C)** Space-time averaged velocity corresponding to the field of 2D velocity vectors presenting in **(B)**. **(D)** Instantaneous 3D velocity profile of blood sample at 17% hematocrit in the central plane of a rectangular microchannel in in vitro analysis. Data were obtained using confocal micro-PIV, image reused with permission, copyright, 2022, Elsevier (Lima et al., 2007). **(E-H)**: Methods' schematic of velocity determination **(E)** Cell tracking. The image presents *in vitro* RBCs in semi-circular curved channel **(F)** Kymograph. The image presents *in vivo* Sublingual microcirculation. **(G)** Micro-PIV. Images show fluorescent particles in the blood. **(H)** Dual slit photometry.

velocities in the microcirculatory network, as shown in **Figure 1A**. In contrast, in *in vitro* studies on a single vessel, the methods seek to characterize the velocity profile along a line (**Figure 1B**) or velocity field in a cross-section (**Figure 1C**), and sometimes even the 3D velocity field (**Figure 1D**). *In vitro* studies, although less physiologically representative, offer the possibility of controlling parameters, such as geometry, flow rate, cell concentration, and pressure drop, while allowing better quantitative and qualitative velocity measurements.

All the methods presented here have a potential to be applied to *in vivo* and *in vitro* studies; however, typically, when red blood cell velocity is investigated in a single vessel, cell tracking velocimetry is used, while when a full network is to be analyzed, automatic vessel detection using the kymograph method is more popularly employed. For more detailed velocity field characterization, micro-particle image velocimetry (micro-PIV) and dual-slit methods are the reference methodologies; however, more advanced expertise is required.

CELL TRACKING VELOCIMETRY

This technique involves identifying matching particles between the frames to link the positions. The velocities of the particles are then evaluated by dividing the time taken between each consecutive frame (**Figure 1E**). The first studies using cell tracking velocimetry were published in the 1960s (Bugliarello and Hayden, 1962). This method is simple to implement and captures temporal and spatial speed variations. It is mainly used *in vivo* and *ex-vivo*, but is also used *in vitro* (Omori et al., 2015). The first analysis was performed manually, but with the advent of computer automation, simple free access algorithms are available for quick analysis (Gonciarz, 2021). However, the simplicity of this method leads to several limitations. For instance, to be able to identify individual blood cells, the hematocrit, i.e., the RBC volume fraction, must be very low, or a small fraction of the cells must be fluorescently stained for tracking. RBC staining is a simple procedure that is easy to implement *in vitro*, and it has also been used *in vivo* in small animals (Horan et al., 1990; Asai et al., 2007; Agrawal et al., 2017). Only particles in the plane of interest (or focus) should be tracked; this can be done by visual inspection, however, automatic processing considers out-of-focus particles. In addition, RBCs can group due to aggregation, resulting in the tracked objects changing in size, disappearing due to overlapping, or changing in shape due to their rotation. These occurrences affect the accuracy of the automatic image processing (Niazi et al., 2019). Despite these limitations, cell tracking is still a very efficient and accurate method that is widely used to track the passage of single blood cells in microfluidics. A review regarding the comparison of different

tracking methods was performed by Chenouard et al. (2014). Open source codes are available for simple tracking (e.g., (Tinevez et al., 2017; Gonciarz, 2021)). Some such codes include a position predictor (e.g., one based on a c) to account for cells that temporarily disappear, while more advanced tools integrate several popular machine learning algorithms to efficiently track objects from brightfield and fluorescence microscopy images (e.g., (39)).

KYMOGRAPHS

In addition to studying the velocity in a specific vessel, intravital microscopy is also used to investigate tissue perfusion under changing conditions. Typically, studies aim to capture the spatial and temporal variability of microcirculation affecting perfusion. In animal studies, all organs can be investigated, while in human studies, nail, coronary (**Figure 1A**), and sublingual microcirculation (**Figure 1F**) can be accessed non-invasively, while microcirculation at other sites, such as the brain, can also be investigated using endoscopies or during surgery.

Common imaging approaches utilize sublingual orthogonal polarization spectral (OPS) imaging, side-stream dark field (SDF) imaging, and incident dark-field (IDF) imaging (Dobbe et al., 2008; Massey and Shapiro, 2016) to record videos of microcirculation activity with enhanced contrast. In either case, high-speed image collection, typically >60 frames per second (fps), is required. For intravital microscopy, image stabilization is the first step in image analysis because of physiologically induced motions such as respiration and cardiac activity. Thus, vessel segmentation is necessary to identify the vasculature as shown in **Figure 1A**. Finally, the RBC velocities are determined using space–time diagrams, called kymographs, for every time interval and for every vascular segment. An example of a kymograph is shown in **Figure 1F**. A kymograph is obtained by plotting the intensity in the grayscale level along the vessel segment over time. On this new "image," where space is encoded along the *x*-axis while time is plotted along the *y*-axis, velocity is then deduced from red blood cell shadow (speckles) angles (Jähne, 2005).

Typically, flow characterizations are presented as a color-coded velocity map, as illustrated in **Figure 1A**. Few commercial software packages are available to complete the full procedure (image acquisition, stabilization, segmentation, and velocity characterization) such as AVA (Microvision Medical B.V., Amsterdam, Netherlands) and CapiScope (KK Research Technology Ltd., Devon, England). The procedure was also implemented in the open source image software ImageJ under the name STAFF (Clendenon et al., 2019a; Clendenon et al., 2019b).

The method is highly dependent on the image quality, particularly image contrast and image sharpness. While illumination techniques have improved, the sharpness of the image is still an important limiting factor because the focus may be difficult to obtain when adjusting the lens on soft tissues and on living subjects, especially during bedside techniques, such as sublingual microcirculation, when the patient is awake. Companies manufacturing commercial acquisition devices, such as USB3 MicroScan (Microvision Medical B.V., Amsterdam, Netherlands), are still improving their focus-monitoring options.

MICRO PARTICLE IMAGE VELOCIMETRY

Micro-PIV has been developed to determine the velocity field in microfluidics (Santiago et al., 1998), and since 2000, it has been used to characterize the velocity profiles of blood flowing through micro-channels (Okuda et al., 2003; Koutsiaris and Pogiatzi, 2004; Bitsch et al., 2005; Lima et al., 2006; Pasias et al., 2020). This technique is a particle-based flow visualization method. **Figure 1G** presents the schematic of the method. Under a microscope, two sequential images of the microflow are recorded at a known time interval (*dt*) at a fixed position. The pairs of images are used to determine the movement of a group of particles from the first image in the pair to the second image using cross-correlation within sub-regions known as cross-correlation windows (CCW). An interrogation window in the first image is compared within an interrogation window grid in the second image to find the most look-alike windows. The distance between the centers of both windows can be divided by the time elapsed between each frame to calculate the mean velocity of the particles for this position. To capture the displacement of the particles in a micrometric field of view, *dt* is set in conjunction with the size of the CCW. The average particle displacement between consecutive frames should be approximately a quarter of the size of the CCW (Scharnowski and Kähler, 2020) (from ms to μs depending on the lens magnification and flow velocity). This is a critical parameter because if *dt* is too large, the particles of the first image could pass beyond the second CCW, resulting in a loss of correlation.

Because this method is a particle-based technique, tracer particles are required. *In vivo* vs *in vitro* applications of micro-PIV require different equipment and execution choices. Traditionally, *in vivo* applications require high-speed photography using the RBCs themselves as tracers (Sugii et al., 2002; Koutsiaris and Pogiatzi, 2004; Bitsch et al., 2005; Lee et al., 2007; Kikuchi and Mochizuki, 2011), while in *in vitro* studies, artificial micro-fluorescent particles are added to the blood (Okuda et al., 2003; Lima et al., 2006; Lima et al., 2007; Lima et al., 2008; Pitts et al., 2012; Pitts and Fenech, 2013a; Mehri et al., 2015; Mehri et al., 2018; Pasias et al., 2020). Artificial tracer particles have also been used in living subjects in the chicken vitelline network, and embryonic heart (Poelma et al., 2008). Obtaining three-dimensional profiles of cell suspension flow is also possible by coupling micro-PIV with confocal microscopy (Lima et al., 2006). Micro-PIV offers a robust and accurate tool to characterize micro blood flows in 2D or 3D; however, the main disadvantage of this technique is the limitation in cell concentration, as the accuracy drops for RBC concentrations above 20% as the ability to resolve the particles decreases.

DUAL SLIT PHOTOMETRY

Dual-slit photometry is a technique developed by Wayland and Johnson (Wayland and Johnson, 1967) and is used to estimate the

flow velocity and volumetric flow rates in microchannels (Lee et al., 1983). With optimized settings, it can be used to measure maximal velocity in microchannels both *in vivo* and *in vitro* (Roman et al., 2012b). The dual slit is a photometric technique that utilizes two photo sensors (slits) positioned along the vessel. The photosensors can be either photodiode sensors or are taken as two regions of interest in a digitized image. In order to obtain a full velocity profile, the slits' width could be selected to be as small as 1 to 3 pixels, allowing for multiple velocity measurements along the cross-section of the channel (Roman et al., 2012a). **Figure 1H** presents the schematic of the method. In each slit, light fluctuations (speckles) are produced by the passage of the RBC flowing through the vessel. A time-dependent signal is captured for each slit in which the time delay between the two signals is obtained by temporal cross-correlation. The RBC velocities are then estimated by assessing the distance between the two slits.

Owing to the large number of RBCs in the channel, the difference in contrast between the cells and suspension media must be sharp to provide a good signal. Furthermore, the RBC rotation, shape, and migration in channels with larger diameters can result in two different signal outputs, preventing an accurate estimation of the velocity profile. For optimized measurement, the technique should be applied to vessels or microchannels that are linear where the slits can be placed at 5 to 10 particle size apart. Finally, the flow through the vessel must be steady, as the technique requires time averaging to ensure statistical convergence of the temporal cross-correlation (Roman et al., 2012b).

EMERGENT METHODS

Conventional methods to infer fluid velocity and pressure measurements or stress fields rely on either analyzing visual images as seen in the optical velocimetry techniques or by enforcing underlying physics without considering the visual data as completed in computational fluid dynamics (CFD). However, with the introduction of a physics-informed neural network, flow visualization image data, such as particles or injected-dye, can be used to derive quantitative information of the flow field while respecting any laws of physics described by a general partial differential equations (PDE) (Raissi et al., 2019). By encoding the Navier-Stokes equations into a neural network, the technique has been applied to flow visualization of both classical fluid problems and more complex flows such as the flow through a microaneurysm-on-a-chip (Raissi et al., 2019; Raissi et al., 2020; Cai et al., 2021). The steps for developing a physics-informed neural network include defining the underlying physical laws, configuring image data to be fed into the neural network, constructing the neural network architecture, training the neural network, verifying the robustness of the model, and finally deploying the model (Raissi et al., 2020; Cai et al., 2021).

The advantage of using a physics-informed neural network is its key property that it can be effectively trained using small datasets (Raissi et al., 2019). Furthermore, with 2D images from microfluidic experiments or from *in vivo* observations, a full estimate of the 3D velocity, pressure, and stress field of the system can be deduced, which may be challenging to measure experimentally or derive from the images alone (Raissi et al., 2019; Raissi et al., 2020; Cai et al., 2021). In contrast to traditional CFD methods, which are sensitive to boundary conditions, a physics-informed neural network can infer the flow field with the sequence of recorded data without any *a priori* knowledge of the inlet and outlet conditions. The implementation of a physics-informed neural network may also be considered more accessible as it can be implemented with open-source software such as TensorFlow (Abadi et al., 2016) on a powerful workstation or a local cluster (Raissi et al., 2020; Cai et al., 2021). However, the cost of utilizing a neural network for analysis is the computational cost of the development and training of the model itself, which is more computationally costly compared to simpler conventional optical methodologies relying only on visual images.

DISCUSSION

Table 1 presents a comparison of different methods and important parameters to inform decisions related to the method to be chosen for a specific study.

Tracer Particles

Image-based experimental measurement techniques to characterize the velocity field of blood microflow utilize some form of tracer particles to visualize the flow. *In vivo*, natural tracers from the cells themselves can be used, while *in vitro* there are more options available for tracer selection from introducing microbeads, fluorescent molecules, or even marking the cells in the fluid sample. The use of RBCs has the advantage of not requiring particle injection and, more importantly, it avoids confounding interpretation attributed to the modification of the system under study. The use of RBCs as imaging tracers has nevertheless some disadvantages because their diameter is approximately 7 μm, while the diameter of an artificial fluorescent particle is typically on the order of 1 μm. The higher RBC particle size and density are responsible for the decrease in accuracy of the measurement method, increasing the depth of correlation (DOC), i.e., the depth at which "the correlation signal of particles significantly contributes to the correlation function" (Kloostermann et al., 2009; Nguyen et al., 2010; Chayer et al., 2012; Pitts and Fenech, 2013a). To minimize the effects of out-of-focus particles, "image-overlapping post-processing" method has proven to be beneficial specifically for blood micro-PIV (Pitts et al., 2012). When it is not possible to add tracer particles, it was shown that using RBCs as tracer particles has acceptable accuracy when analyzing for the value of the flow rate, but not when assessing for the specific shape of the velocity profile (Chayer et al., 2012; Pitts and Fenech, 2013a).

Volume Fraction and Cell Contrast

Image-based techniques are severely limited by the feeding hematocrit of the system; it is difficult to distinguish cells or tracer particles introduced into the fluid medium in high hematocrit studies. This effectively limits the study of the dynamics of blood microflows using imaging techniques, as

the accuracy of measurements decreases as the hematocrit approaches values closer to the physiological values. The volume fraction is a significant factor to consider when selecting an optical measurement technique because if the cell concentration is too high, automatic cell tracking and PIV algorithms are less accurate, while the contrast of the cells can affect the accuracy of kymography and dual-slit photometry. Measuring flow fields in dense suspension of cells would require techniques that utilize sensors that can penetrate denser samples, such as ultrasound localization microscopy (Errico et al., 2015) or those with modifications to RBC opacity, such as converting RBCs into ghost cells (Jansen et al., 2016).

Type of Velocity Field

To extract a characteristic velocity, such as the mean or max velocity, any technique presented here can be utilized. However, to expand into the 2D velocity field of the vessel, cell tracking, micro-PIV, and dual-slit photometry should be considered; in micro-PIV, it is also possible to obtain 3D profiles with additional equipment. With the most basic equipment, the techniques are not necessarily independent and differ by the image processing algorithms that are applied to the acquired images; however, the optimal setting of certain factors, such as the channel configuration, lighting, and lens type, can drastically change the accuracy of the algorithm applied. To obtain more detailed velocity profiles in 3D or under a broad range of flowrates would require more sophisticated equipment such as cameras with higher acquisition rates, pulsed lasers, or filters. This can make profiling of the velocity field in blood microflow an expensive endeavor because the upfront cost of the equipment can be high.

AUTHOR CONTRIBUTIONS

AL and MF defined the scope of this mini review and contributed equally to the writing of the manuscript.

FUNDING

This work was funded by the Natural Science and Engineering Research Council of Canada (#RGPIN-2020-07020).

REFERENCES

Abadi, M., Agarwal, A., Barham, P., Brevdo, E., Chen, Z., Citro, C., et al. (2016). *TensorFlow: A system for Large-Scale Machine Learning*. In Proceedings of the 12th USENIX conference on Operating Systems Design and Implementation (OSDI'16), USENIX Association: Savannah, GA, USA, 265–283.

Abay, A., Recktenwald, S. M., John, T., Kaestner, L., and Wagner, C. (2020). Cross-sectional Focusing of Red Blood Cells in a Constricted Microfluidic Channel. *Soft Matter* 16 (2), 534–543. doi:10.1039/c9sm01740b

Agrawal, R., Balne, P. K., Tun, S. B. B., Sia Wey, Y., Khandelwal, N., and Barathi, V. A. (2017). Fluorescent Dye Labeling of Erythrocytes and Leukocytes for Studying the Flow Dynamics in Mouse Retinal Circulation. *J. Vis. Exp.* (125), e55495. doi:10.3791/55495

Asai, A., Sahani, N., Ouchi, Y., Martyn, J., and Yasuhara, S. (2007). *In Vivo* Micro-circulation Measurement in Skeletal Muscle by Intra-vital Microscopy. *J. Vis. Exp.* (4), e210. doi:10.3791/210

Baskurt, O., and Meiselman, H. J. (2007). "*In Vivo* hemorheology," in *Handbook of Hemorheology and Hemodynamics*. Editors O. K. Baskurt, M. R. Hardeman, and M. W. Rampling (Amsterdam: IOS press), 322–338.

Baskurt, O. K., and Meiselman, H. J. (2013). Erythrocyte Aggregation: Basic Aspects and Clinical Importance. *Clin. Hemorheol. Microcirc.* 53 (1–2), 23–37. doi:10.3233/CH-2012-1573

Bishop, J. J., Popel, A. S., Intaglietta, M., and Johnson, P. C. (2001b). Rheological Effects of Red Blood Cell Aggregation in the Venous Network: A Review of Recent Studies. *Biorheology* 38, 263–274.

Bishop, J. J., Popel, A. S., Intaglietta, M., and Johnson, P. C. (2001a). Effects of Erythrocyte Aggregation and Venous Network Geometry on Red Blood Cell Axial Migration. *Am. J. Physiology-Heart Circulatory Physiol.* 281 (2), H939–H950. doi:10.1152/ajpheart.2001.281.2.h939

Bitsch, L., Olesen, L. H., Westergaard, C. H., Bruus, H., Klank, H., and Kutter, J. P. (2005). Micro Particle-Image Velocimetry of Bead Suspensions and Blood Flows. *Exp. Fluids* 39 (3), 507–513. doi:10.1007/s00348-005-0967-7

Bugliarello, G., and Hayden, J. W. (1962). High-speed Microcinematographic Studies of Blood Flow *In Vitro*. *Science* 138, 981–983. doi:10.1126/science.138.3544.981

Cabrales, P., and Carvalho, L. J. M. (2010). Intravital Microscopy of the Mouse Brain Microcirculation Using a Closed Cranial Window. *J. Vis. Exp.* (45), 2184. doi:10.3791/2184

Cai, S., Li, H., Zheng, F., Kong, F., Dao, M., Karniadakis, G. E., et al. (2021). Artificial Intelligence Velocimetry and Microaneurysm-On-A-Chip for Three-Dimensional Analysis of Blood Flow in Physiology and Disease. *Proc. Natl. Acad. Sci. U.S.A.* 118 (13), e2100697118. doi:10.1073/pnas.2100697118

Chayer, B., L Pitts, K., Cloutier, G., and Fenech, M. (2012). Velocity Measurement Accuracy in Optical Microhemodynamics: Experiment and Simulation. *Physiol. Meas.* 33 (10), 1585–1602. doi:10.1088/0967-3334/33/10/1585

Chenouard, N., Smal, I., de Chaumont, F., Maška, M., Sbalzarini, I. F., Gong, Y., et al. (2014). Objective Comparison of Particle Tracking Methods. *Nat. Methods* 11 (3), 281–289. doi:10.1038/nmeth.2808

Clendenon, S. G., Fu, X., Von Hoene, R. A., Clendenon, J. L., Sluka, J. P., Winfree, S., et al. (2019a). A Simple Automated Method for Continuous Fieldwise Measurement of Microvascular Hemodynamics. *Microvasc. Res.* 123, 7–13. doi:10.1016/j.mvr.2018.11.010

Clendenon, S. G., Fu, X., Von Hoene, R. A., Clendenon, J. L., Sluka, J. P., Winfree, S., et al. (2019b). Spatial Temporal Analysis of Fieldwise Flow in Microvasculature. *J. Vis. Exp.* (153), e60493. doi:10.3791/60493

Connes, P., Alexy, T., Detterich, J., Romana, M., Hardy-Dessources, M.-D., and Ballas, S. K. (2016). The Role of Blood Rheology in Sickle Cell Disease. *Blood Rev.* 30 (2), 111–118. doi:10.1016/j.blre.2015.08.005

Coull, B. M., Beamer, N., de Garmo, P., Sexton, G., Nordt, F., Knox, R., et al. (1991). Chronic Blood Hyperviscosity in Subjects with Acute Stroke, Transient Ischemic Attack, and Risk Factors for Stroke. *Stroke* 22 (2), 162–168. doi:10.1161/01.STR.22.2.162

Dobbe, J. G. G., Streekstra, G. J., Atasever, B., van Zijderveld, R., and Ince, C. (2008). Measurement of Functional Microcirculatory Geometry and Velocity Distributions Using Automated Image Analysis. *Med. Biol. Eng. Comput.* 46 (7), 659. doi:10.1007/s11517-008-0349-4

Errico, C., Pierre, J., Pezet, S., Desailly, Y., Lenkei, Z., Couture, O., et al. (2015). Ultrafast Ultrasound Localization Microscopy for Deep Super-resolution Vascular Imaging. *Nature* 527 (7579), 499–502. doi:10.1038/nature16066

Gonciarz, K. (2021) Particle Tracker, Image J. Dresden, Germany. Available at: https://imagej.net/plugins/particle-tracker, (Accessed April 08, 2022).

Gutterman, D. D., Chabowski, D. S., Kadlec, A. O., Durand, M. J., Freed, J. K., Ait-Aissa, K., et al. (2016). The Human Microcirculation. *Circ. Res.* 118 (1), 157–172. doi:10.1161/CIRCRESAHA.115.305364

Horan, P. K., Melnicoff, M. J., Jensen, B. D., and Slezak, S. E. (1990). Chapter 42 Fluorescent Cell Labeling for *In Vivo* and *In Vitro* Cell Tracking. *Methods Cel Biol.* 33, 469–490. doi:10.1016/S0091-679X(08)60547-6

Ishikawa, T., Fujiwara, H., Matsuki, N., Yoshimoto, T., Imai, Y., Ueno, H., et al. (2011). Asymmetry of Blood Flow and Cancer Cell Adhesion in a Microchannel

with Symmetric Bifurcation and confluence. *Biomed. Microdevices* 13 (1), 159–167. doi:10.1007/s10544-010-9481-7

Jähne, B. (2005). *Digital Image Processing: 6th Revised and Extended Edition*. Berlin: Springer, 403–406. doi:10.1007/3-540-27563-0

Jansen, S. V., Müller, I., Nachtsheim, M., Schmitz-Rode, T., and Steinseifer, U. (2016). Ghost Cell Suspensions as Blood Analogue Fluid for Macroscopic Particle Image Velocimetry Measurements. *Artif. Organs* 40 (2), 207–212. doi:10.1111/aor.12511

Johnson, R. M., and Ravindranath, Y. (1996). Osmotic Scan Ektacytometry in Clinical Diagnosis. *J. Pediatr. Hematology/Oncology* 18 (2), 122–129. doi:10.1097/00043426-199605000-00005

Kaliviotis, E., Dusting, J., and Balabani, S. (2011). Spatial Variation of Blood Viscosity: Modelling Using Shear fields Measured by a μPIV Based Technique. *Med. Eng. Phys.* 33 (7), 824–831. doi:10.1016/j.medengphy.2010.09.004

Kaliviotis, E., Sherwood, J. M., and Balabani, S. (2018). Local Viscosity Distribution in Bifurcating Microfluidic Blood Flows. *Phys. Fluids* 30, 030706. doi:10.1063/1.5011373

Khalid, N., Kobayashi, I., and Nakajima, M. (2017). Recent Lab-on-chip Developments for Novel Drug Discovery. *Wires Syst. Biol. Med.* 9, e1381. doi:10.1002/wsbm.1381

Khansari, M. M., Wanek, J., E Felder, A., Camardo, N., and Shahidi, M. (2015). Automated Assessment of Hemodynamics in the Conjunctival Microvasculature Network. *IEEE Trans. Med. Imaging* 35 (2), 605–611. doi:10.1109/TMI.2015.2486619

Kihm, A., Quint, S., Laschke, M. W., Menger, M. D., John, T., Kaestner, L., et al. (2021). Lingering Dynamics in Microvascular Blood Flow. *Biophysical J.* 120 (3), 432–439. doi:10.1016/J.BPJ.2020.12.012

Kikuchi, K., and Mochizuki, O. (2011). Micro-PIV (Micro Particle Image Velocimetry) Visualization of Red Blood Cells (RBCs) Sucked by a Female Mosquito. *Meas. Sci. Technol.* 22, 064002. doi:10.1088/0957-0233/22/6/064002

Kloostermann, A., Poelma, C., and Westerweel, J. (2009). "Accuracy of the Micro-PIV Method for Biological Applications. In the proceeding of the 8th International Symposium on PIV, Melbourne, Victoria, Australia, 25–28.

Koutsiaris, A. G., and Pogiatzi, A. (2004). Velocity Pulse Measurements in the Mesenteric Arterioles of Rabbits. *Physiol. Meas.* 25, 15–25. doi:10.1088/0967-3334/25/1/002

Le Devehat, C., Vimeux, M., Bondoux, G., and Khodabandehlou, T. (1990). Red Blood Cell Aggregation in Diabetes Mellitus. *Int. Angiol* 9 (1), 11–15.

Lee, J. Y., Ji, H. S., and Lee, S. J. (2007). Micro-PIV Measurements of Blood Flow in Extraembryonic Blood Vessels of Chicken Embryos. *Physiol. Meas.* 28 (10), 1149–1162. doi:10.1088/0967-3334/28/10/002

Lee, T. Q., Schmid-Schönbein, G. W., and Zweifach, B. W. (1983). The Application of an Improved Dual-Slit Photometric Analyzer for Volumetric Flow Rate Measurements in Microvessels. *Microvasc. Res.* 26 (3), 351–361. doi:10.1016/0026-2862(83)90084-5

Levin, G. Y., and Egorihina, M. N. (2011). Aggregation of Erythrocytes in Burn Disease. *Int. J. Burns Trauma* 1 (1), 34–41. Available at: http://www.pubmedcentral.nih.gov/articlerender.fcgi?artid=PMC3415941.

Li, K., and Kang, S. (2008) The Image Stabilizer Plugin for ImageJ. Available at: http://www.cs.cmu.edu/~kangli/code/Image_Stabilizer.html (Accessed: 29 July 2021).

Lima, R., Wada, S., Takeda, M., Tsubota, K.-i., and Yamaguchi, T. (2007). *In Vitro* confocal Micro-PIV Measurements of Blood Flow in a Square Microchannel: The Effect of the Haematocrit on Instantaneous Velocity Profiles. *J. Biomech.* 40 (12), 2752–2757. doi:10.1016/j.jbiomech.2007.01.012

Lima, R., Wada, S., Tanaka, S., Takeda, M., Ishikawa, T., Tsubota, K.-i., et al. (2008). *In Vitro* blood Flow in a Rectangular PDMS Microchannel: Experimental Observations Using a Confocal Micro-PIV System. *Biomed. Microdevices* 10 (2), 153–167. doi:10.1007/s10544-007-9121-z

Lima, R., Wada, S., Tsubota, K.-i., and Yamaguchi, T. (2006). Confocal Micro-PIV Measurements of Three-Dimensional Profiles of Cell Suspension Flow in a Square Microchannel. *Meas. Sci. Technol.* 17 (4), 797–808. doi:10.1088/0957-0233/17/4/026

Long, D. S., Smith, M. L., Pries, A. R., Ley, K., and Damiano, E. R. (2004). Microviscometry Reveals Reduced Blood Viscosity and Altered Shear Rate and Shear Stress Profiles in Microvessels after Hemodilution. *Proc. Natl. Acad. Sci. U.S.A.* 101 (27), 10060–10065. doi:10.1073/pnas.0402937101

Luquita, A., Urli, L., Svetaz, M. J., Gennaro, A. M., Volpintesta, R., Palatnik, S., et al. (2009). Erythrocyte Aggregation in Rheumatoid Arthritis: Cell and Plasma Factor's Role. *Clin. Hemorheol. Microcirc.* 41 (1), 49–56. doi:10.3233/CH-2009-1154

Mantegazza, A., Ungari, M., Clavica, F., and Obrist, D. (2020). Local vs. Global Blood Flow Modulation in Artificial Microvascular Networks: Effects on Red Blood Cell Distribution and Partitioning. *Front. Physiol.* 11, 1117. doi:10.3389/fphys.2020.566273

Maria, M. S., Chandra, T. S., and Sen, A. K. (2017). Capillary Flow-Driven Blood Plasma Separation and On-Chip Analyte Detection in Microfluidic Devices. *Microfluid Nanofluid* 21, 1–21. doi:10.1007/s10404-017-1907-6

Maška, M., Ulman, V., Svoboda, D., Matula, P., Matula, P., Ederra, C., et al. (2014). A Benchmark for Comparison of Cell Tracking Algorithms. *Bioinformatics* 30 (11), 1609–1617. doi:10.1093/bioinformatics/btu080

Massey, M. J., and Shapiro, N. I. (2016). A Guide to Human *In Vivo* Microcirculatory Flow Image Analysis. *Crit. Care* 20, 35. doi:10.1186/s13054-016-1213-9

Mehri, R., Mavriplis, C., and Fenech, M. (2015). Controlled Microfluidic Environment for Dynamic Investigation of Red Blood Cell Aggregation. *J. Vis. Exp.* 2015 (100), e52719. doi:10.3791/52719

Mehri, R., Mavriplis, C., and Fenech, M. (2018). Red Blood Cell Aggregates and Their Effect on Non-newtonian Blood Viscosity at Low Hematocrit in a Two-Fluid Low Shear Rate Microfluidic System. *PLoS ONE* 13 (7), e0199911. doi:10.1371/journal.pone.0199911

Nguyen, C. V., Fouras, A., and Carberry, J. (2010). Improvement of Measurement Accuracy in Micro PIV by Image Overlapping. *Exp. Fluids* 49 (3), 701–712. doi:10.1007/s00348-010-0837-9

Niazi, E., McDonald, J. G., and Fenech, M. (2019). An Automated Method for Size and Velocity Distribution Measurement in a Particle-Laden Flow. *Adv. Eng. Softw.* 134, 10–21. doi:10.1016/j.advengsoft.2019.05.002

Okuda, R., Sugii, Y., and Okamoto, K. (2003). "Velocity Measurement of Blood Flow in a Microtube Using Micro PIV System," in In the proceedings of the 4th Pacific Symposium on Flow Visualization and Image Processing, Chamonix, France, 4–7. Available at: http://psfvip4.univ-fcomte.fr/Fpsfvip4/sources/F4084.pdf.

Omori, T., Imai, Y., Kikuchi, K., Ishikawa, T., and Yamaguchi, T. (2015). Hemodynamics in the Microcirculation and in Microfluidics. *Ann. Biomed. Eng.* 43 (1), 238–257. doi:10.1007/s10439-014-1180-8

Parrow, N. L., Violet, P.-C., Tu, H., Nichols, J., Pittman, C. A., Fitzhugh, C., et al. (2018). Measuring Deformability and Red Cell Heterogeneity in Blood by Ektacytometry. *J. Vis. Exp.* 2018 (131), 56910. doi:10.3791/56910

Pasias, D., Passos, A., Constantinides, G., Balabani, S., and Kaliviotis, E. (2020). Surface Tension Driven Flow of Blood in a Rectangular Microfluidic Channel: Effect of Erythrocyte Aggregation. *Phys. Fluids* 32 (7), 071903. doi:10.1063/5.0008939

Passos, A., Sherwood, J. M., Kaliviotis, E., Agrawal, R., Pavesio, C., and Balabani, S. (2019). The Effect of Deformability on the Microscale Flow Behavior of Red Blood Cell Suspensions. *Phys. Fluids* 31 (9), 091903. doi:10.1063/1.5111189

Patumraj, S., Yoysungnoen, P., Kachonrattanadet, P., and Wirachwong, P. (2005). Tumor Neocapillary Density in Hepatocellular Carcinoma Cells Implanted Nude Mice Model. *Clin. Hemorheol. Microcirc.* 33 (2), 137–144.

Pearson, T. C., and Path, F. R. C. (2001). Hemorheology in the Erythrocytoses. *Mt Sinai J. Med.* 68 (3), 182–191.

Pitts, K. L., and Fenech, M. (2013a). High Speed versus Pulsed Images for Micro-particle Image Velocimetry: a Direct Comparison of Red Blood Cells versus Fluorescing Tracers as Tracking Particles. *Physiol. Meas.* 34 (10), 1363–1374. doi:10.1088/0967-3334/34/10/1363

Pitts, K. L., and Fenech, M. (2013b). Micro-particle Image Velocimetry for Velocity Profile Measurements of Micro Blood Flows. *J. Vis. Exp.* (74), e50314. doi:10.3791/50314

Pitts, K. L., Mehri, R., Mavriplis, C., and Fenech, M. (2012). Micro-particle Image Velocimetry Measurement of Blood Flow: Validation and Analysis of Data Pre-processing and Processing Methods. *Meas. Sci. Technol.* 23 (10), 105302. doi:10.1088/0957-0233/23/10/105302

Poelma, C., Vennemann, P., Lindken, R., and Westerweel, J. (2008). *In Vivo* blood Flow and wall Shear Stress Measurements in the Vitelline Network. *Exp. Fluids* 45 (4), 703–713. doi:10.1007/s00348-008-0476-6

Raissi, M., Perdikaris, P., and Karniadakis, G. E. (2019). Physics-informed Neural Networks: A Deep Learning Framework for Solving Forward and Inverse Problems Involving Nonlinear Partial Differential Equations. *J. Comput. Phys.* 378, 686–707. doi:10.1016/j.jcp.2018.10.045

Raissi, M., Yazdani, A., and Karniadakis, G. E. (2020). Hidden Fluid Mechanics: Learning Velocity and Pressure fields from Flow Visualizations. *Science* 367 (6481), 1026–1030. doi:10.1126/science.aaw4741

Roman, S., Lorthois, S., Duru, P., and Risso, F. (2012a). An Optimized Technique for Red Blood Cells Velocity Measurement in Microvessels. *J. Biomech.* 45, S35. doi:10.1016/s0021-9290(12)70036-2

Roman, S., Lorthois, S., Duru, P., and Risso, F. (2012b). Velocimetry of Red Blood Cells in Microvessels by the Dual-Slit Method: Effect of Velocity Gradients. *Microvasc. Res.* 84 (3), 249–261. doi:10.1016/j.mvr.2012.08.006

Santiago, J. G., Wereley, S. T., Meinhart, C. D., Beebe, D. J., and Adrian, R. J. (1998). A Particle Image Velocimetry System for Microfluidics. *Experiments in Fluids* 25 (4), 316–319. doi:10.1007/s003480050235

Scharnowski, S., and Kähler, C. J. (2020). Particle Image Velocimetry - Classical Operating Rules from Today's Perspective. *Opt. Lasers Eng.* 135, 106185. doi:10.1016/j.optlaseng.2020.106185

Sebastian, B., and Dittrich, P. S. (2018). Microfluidics to Mimic Blood Flow in Health and Disease. *Annu. Rev. Fluid Mech.* 50, 483–504. doi:10.1146/annurev-fluid-010816-060246

Secomb, T. W. (2017). Blood Flow in the Microcirculation. *Annu. Rev. Fluid Mech.* 49, 443–461. doi:10.1146/annurev-fluid-010816-060302

Sharma, K., Puniyani, R. R., Bhat, S. V., Advani, S. H., Hegde, U., and Rao, S. (1992). Blood Viscosity Parameter Correlation with Types of Leukemia. *Physiol. Chem. Phys. Med. NMR* 24 (2), 159–164. Available at: https://pubmed.ncbi.nlm.nih.gov/1508991/ (Accessed December 13, 2021).

Sherwood, J. M., Dusting, J., Kaliviotis, E., and Balabani, S. (2012). The Effect of Red Blood Cell Aggregation on Velocity and Cell-Depleted Layer Characteristics of Blood in a Bifurcating Microchannel. *Biomicrofluidics* 6 (2), 024119. doi:10.1063/1.4717755

Silva-Herdade, A. S., Andolina, G., Faggio, C., Calado, Â., and Saldanha, C. (2016). Erythrocyte Deformability - A Partner of the Inflammatory Response. *Microvasc. Res.* 107, 34–38. doi:10.1016/j.mvr.2016.04.011

Sloop, G. D., De Mast, Q., Pop, G., Weidman, J. J., and St. Cyr, J. A. (2020). The Role of Blood Viscosity in Infectious Diseases. *Cureus* 12 (2), e7090. doi:10.7759/cureus.7090

Sugii, Y., Nishio, S., and Okamoto, K. (2002). In vivoPIV Measurement of Red Blood Cell Velocity Field in Microvessels Considering Mesentery Motion. *Physiol. Meas.* 23 (2), 403–416. doi:10.1088/0967-3334/23/2/315

Tinevez, J.-Y., Perry, N., Schindelin, J., Hoopes, G. M., Reynolds, G. D., Laplantine, E., et al. (2017). TrackMate: An Open and Extensible Platform for Single-Particle Tracking. *Methods* 115, 80–90. doi:10.1016/J.YMETH.2016.09.016

Wayland, H., and Johnson, P. C. (1967). Erythrocyte Velocity Measurement in Microvessels by a Two-Slit Photometric Method. *J. Appl. Physiol.* 22 (2), 333–337. doi:10.1152/jappl.1967.22.2.333

Conflict of Interest: The authors declare that the research was conducted in the absence of any commercial or financial relationships that could be construed as a potential conflict of interest.

Publisher's Note: All claims expressed in this article are solely those of the authors and do not necessarily represent those of their affiliated organizations, or those of the publisher, the editors, and the reviewers. Any product that may be evaluated in this article, or claim that may be made by its manufacturer, is not guaranteed or endorsed by the publisher.

Copyright © 2022 Le and Fenech. This is an open-access article distributed under the terms of the Creative Commons Attribution License (CC BY). The use, distribution or reproduction in other forums is permitted, provided the original author(s) and the copyright owner(s) are credited and that the original publication in this journal is cited, in accordance with accepted academic practice. No use, distribution or reproduction is permitted which does not comply with these terms.